Investigation of hysteresis in biobased insulation

Moisture sorption measurements and dynamic wall-scale experiment

Christoffer M. Brødsgaard, Thomas Juul

Indoor environmental and Energy Engineering, 04.06.2025

Master Thesis

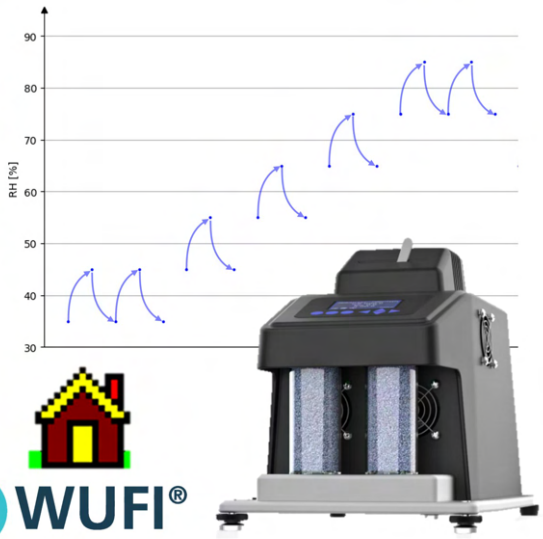

AALBORG UNIVERSITET
STUDENTERRAPPORT

The Faculty of Engineering and Science
BUILD, Department of the Built Environment
Thomas Manns Vej 23
DK-9220 Aalborg East
https://www.build.aau.dk/

Project title:

Investigation of hysteresis
in biobased insulation

Project:

Master Thesis

Project period:

September 2024 - June 2025

Project group:

IE10 -1

Authors:

Christoffer Minor Brødsgaard
Thomas Juul

Supervisor:

Rasmus Lund Jensen

Number of pages main report: 65
Number of pages appendix: 198
Number of pages total: 263

Abstract:

This thesis explores the moisture performance of biobased insulation materials, focusing on hysteresis under realistic humidity conditions.

An analysis of relative humidity inside of wall-elements found that the fluctuations are ±10% and upwards of 50 hours. Therefore, moisture sorption measurements were made at small intervals both for fast and slow durations on Aerated Autoclaved concrete, Woodfiber, and Hempfiber insulation. For these intervals, hysteresis was observed.

A climatic chamber was constructed to test wall elements with different insulation materials and vapour barriers. The results led to initial trends regarding biobased materials and vapour barriers. Measurements are compared with WUFI-simulations, where temperatures matched well but diverged on RH. The study highlights the discrepancies between reality and modelling.

The content of the report is freely available, but publication (with source reference) may only be pursued due to agreement with the authors.

Preface

This report is written by a group consisting of two Indoor Environment and Energy Engineering students on 10th semester, at Aalborg University. The report is devised from the 1st of September 2024 to the 4th of June 2025.

This thesis has been made possible with the support of several individuals, whom we would like to thank. From AAU BUILD **Lars Isbach** played a key role in preparing the climatic chamber setup and **Victor Nyborg** and **Simon Melgaard** contributed to developing the system control for the setup. **Ben Klauman Krøyer** provided essential assistance in the construction of the DewMaster boxes. **Kirstine Meyer Frandsen** for mentoring in VSA-measurements and WUFI simulations.
Lars Broder Lindgren and **Artelia** for the collaboration on the climatic chamber setup, and that their provided the wall-elements. **Simon Nygaard** and **Emil from JDH-Byg** for building the elements and help install the sensors.
We would like to extend a big thank you to the **Siemens Foundation** for their generous donation, which enables BUILD to construct an air permeameter. **Per Møldrup** arranged for us to carry out measurements at AU Viborg and provided insights into material properties. From AU Viborg **Jørgen Munksgaard Nielsen** assisted with air permeability testing, and **Michael Koppelgaard** provided valuable insights into their measurement setup. Here, **Emmanuel Arthur** on sharing his expertise with moisture sorption measurements.

Finally, we would like to thank our supervisor, **Rasmus Lund Jensen**, for his crucial guidance and feedback throughout the project.

Thomas Juul

Christoffer M. Brødsgaard

Reading Guide

References to sources will appear throughout the report, where there will be a comprehensive bibliography at the end of the report. A source reference has been used according to the numeric method, so that the text refers to a source with [Number].

Figures, tables, and equations are numbered according to chapter, i.e. the first figure in Chapter 2 is numbered 2.1, the second figure is numbered 2.2, etc. Explanatory text for figures and diagrams is found below the given figure. Explanatory text for tables is found above the given table.

At the end of the report, appendixes, consisting of calculations, results, tables and figures, which are referred to throughout the main report, are shown in letters. The appendices are divided into four parts - Determination of material properties, experimental setup, simulations, and general.

Table of contents

Chapter 1

Introduction

The building sector is one of the biggest emitters of greenhouse gases globally, and action is urgent in order to limit global warming [1]. One of the key pathways is to shift from mineral-based building materials with energy-intensive production processes to regenerative bio-based materials with low embodied carbon [2]. Biobased materials can be utilized in several areas of construction; however, they do pose certain challenges. These challenges include durability, fire, moisture, sound, and long-term performance, which must be addressed to ensure their successful integration into modern building practices. In Denmark the project Roads to biobased construction (translated title of the Danish original: "Veje til Biobaseret Byggeri") by Realdania is trying to address these challenges and provides an inspirational catalogue of construction assemblies with biobased building materials. The focus in this thesis is biobased insulation and moisture, which is investigated on a material scale and construction assembly scale.

1.1 Biobased insulation materials

Wood-frame wall with biobased insulation is a particularly ecological construction method [3] [4]. With timber framing in external walls, you can have high insulation thicknesses and reduce the operational environmental impact through reduced heating requirements during the cold seasons. Insulation makes up a large share of the building volume and the biobased insulation can act as carbon storage [2]. Unlike mineral-based materials, bio-based materials store and regulate their moisture content with regards to the relative humidity [2]. The difference in moisture sorption for typical building materials is shown on Figure 1.1, where biobased materials in general follow the curve for wood [5].

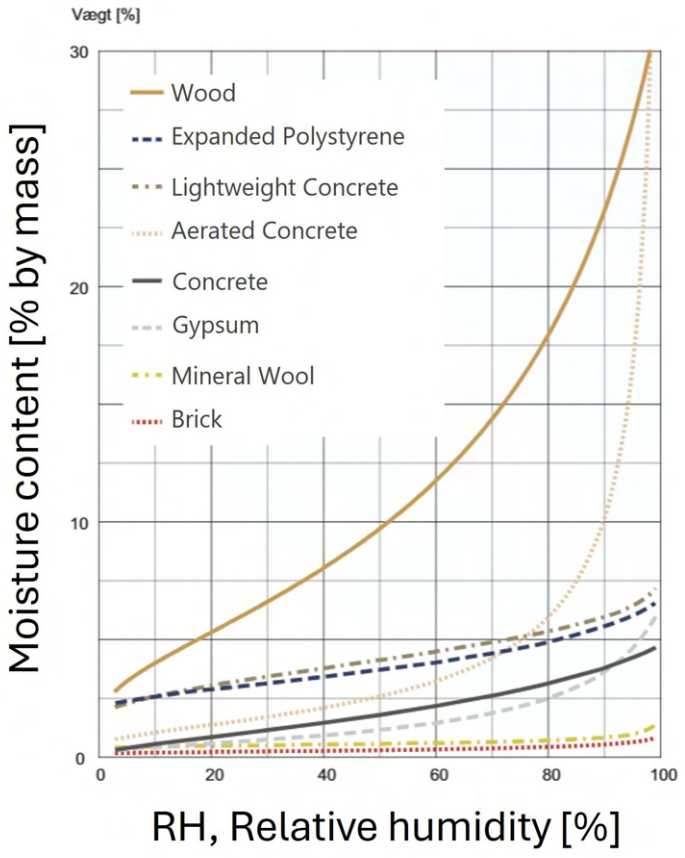

Figure 1.1. Moisture sorption isotherms for common building materials [6].

Biobased building materials cover a wide range of products, which can generally be defined as being regenerative. It is well established to build with wood and do a wood-frame construction. Wood is widely used in the building sector for boards, trusses, timber-frame structures, and fiber insulation. There is, however, a high demand for wood and wood residuals, and wood is currently imported to Denmark to fulfill the demand[2]. There is a big potential to instead locally grow and source biobased materials, which can be used in the building industry [7]. Compared to wood, alternatives like hemp, straw, flax, and grass grow fast and are also suitable as fibrous insulation with similar thermal properties as woodfiber and mineral wool. Besides their thermal conductivity, the overall performance is based on the complex relations and interaction between the material's properties, such as density, water vapour permeability, capillary suction, moisture sorption, porosity, hysteresis, and specific heat capacity. [5]. It is therefore essential to determine these material properties and use dynamic heat and moisture simulations to assess the transient performance of biobased building construction [6]. Figure 1.2 show the big difference in moisture sorption for three biobased insulation materials and mineral wool.

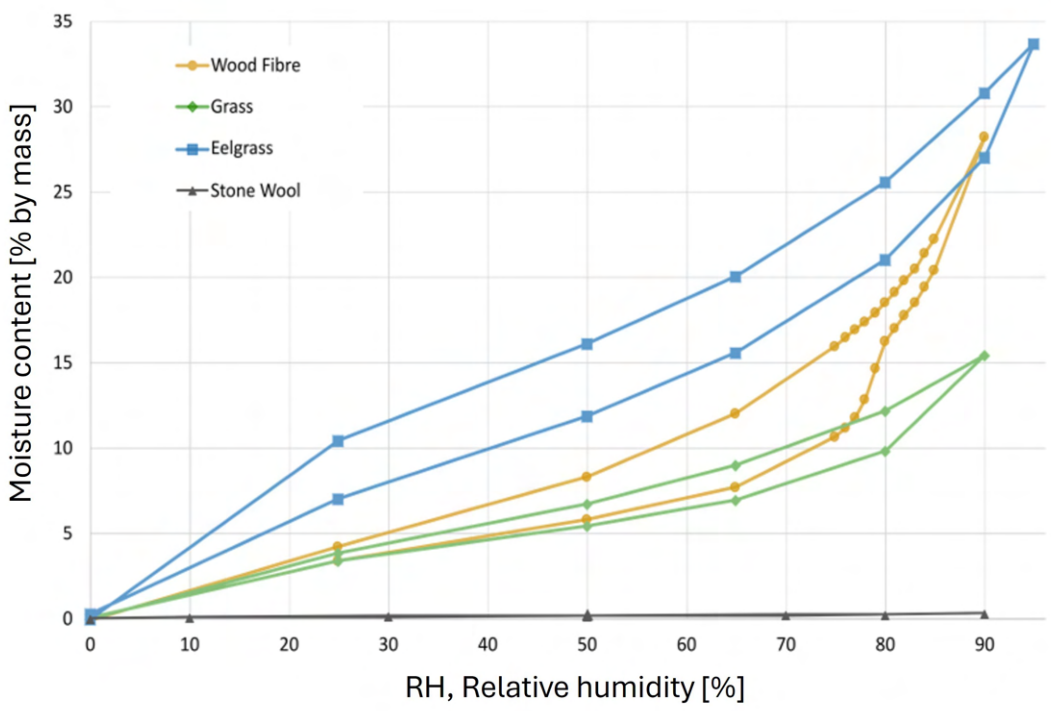

Figure 1.2. Moisture sorption isotherms for eelgrass, woodfiber, grass and mineral wool insulation [8]

1.2 Fungal mould growth

A mineral-based wall construction with concrete and mineral insulation does not have any nutrient source for mould, and is therefore more resistant against mould. By re-introducing organic materials into constructions, there is now a nutrient source for mould. Biobased building materials provide a nutrient-rich substrate, which can support the growth of mould fungi over time, if the right temperatures and humidity levels are present. The materials will naturally contain spores, which are often introduced during manufacturing, storage, or construction and can remain dormant until conditions become favourable. It is essential to avoid mould as it decomposes its substrate and releases toxins that are a major health hazard for humans [9]. The availability of moisture either in the substrate or as water vapour is the most decisive factor. At relative humidity levels above 75%, it will be possible for mould to grow. Mould growth is dependent on both the humidity and temperature, where most building-associated fungi thrive between 20–25°C, which coincides with typical indoor conditions [10]. Sedlbauer [10] provides isopleth diagrams of the relationship between temperature, relative humidity and needed time for spore germination. The dynamic independent relationship is the reason why heat and moisture simulations are needed in order to properly assess the moisture robustness of constructions. In Andersen and Rasmussen [11] they tested fungal susceptibility of some different biobased building

materials, including hemp fiber and wood fiber. Overall, the materials showed good moisture buffering capacity, without deformation or fungal growth. They find that the materials can release moisture quickly again after water damage, when the ambient relative humidity is low. However, all the samples were susceptible to fungal growth when constantly exposed to liquid water.

1.3 Moisture sources and moisture protection

Moisture is generally one of the main causes of building damage, and the different sources of moisture need to be properly managed. Here the facade cladding and roof are essential components of the building envelope, that protects against rain infiltration and direct rain exposure of the inner insulation layers [12]. For the foundation, there will be a capillary-breaking layer for protection against rising ground moisture. Besides outdoor sources of moisture, moisture can also enter the building envelope from the inside where moisture is generated from the respiration and activities of the occupants [6]. Hot indoor air can contain a lot of moisture, and can critically increase the relative humidity and pose a condensation risk if it enters inside the building envelope where the temperature drops. Moisture load classes are used to calculate the moisture load from indoor air that a building component is exposed to. It is a simplified method of describing how indoor moisture production and ventilation affect the water vapour concentration in the indoor air [13]. In Denmark, a normal dwelling will correspond to moisture class two, where moisture class three is for dwellings with unknown occupancy density. Moisture class is very unlikely to be present in dwellings [6]. The moisture classes are defined as a moisture addition to the indoor air as a function of the monthly average outdoor temperature. Using the Danish DRY 2013 weather file, the moisture class can be stated in terms of an upper boundary for the indoor relative humidity, which is shown in Table 1.1.

Month	DRY Outdoor		Indoor	Moisture class upper limits	
	Air temperature [°C]	RH [%]	Temperature [°C]	Class 2	Class 3 [%RH]
January	0.7	89	20	47	58
February	0.4	91	20	47	59
March	-0.7	87	20	44	56
April	7.1	76	20	49	57
May	11.5	76	20	56	61
June	14.2	80	22	58	61
July	17.8	77	23	61	62
August	17.9	74	23	59	60
September	14.5	78	22	57	60
October	9.8	88	20	59	65
November	3.4	91	20	50	60
December	0.7	93	20	48	59

Table 1.1. The upper indoor limit of relative humidity for moisture load class two and three, based on the monthly average outdoor temperature and relative humidity according to DRY 2013 [6]

1.3.1 Regulation of moisture diffusion

Besides energy savings, it is essential to have an air tight building envelope to avoid moisture transport by convection [12]. To avoid moisture transport by diffusion, it is typical to use a vapour barrier, which often also ensures the air tightness. The vapour barrier increases the vapour diffusion resistance and thus limits the moisture diffusion. It should be placed towards the hot indoor environment, where the temperature is high, so high relative humidity and condensation is avoided [12]. The critical areas in a construction is typically in front of the diffusion resistant layers, and area where it is cold, usually behind the wind barrier [14]. In Denmark it is Technical common knowledge, that a water vapour resistance ratio of at least 1:10, will ensure a moisture safe construction. The vapour resistance ratio is the ratio between the water vapour resistance of the wind barrier and the vapour barrier. It is standard practice to use a PE-foil, which has a high resistance of over 400 $(GPa \cdot m2 \cdot s)/kg$ (Z-value). To avoid petrochemical products, practitioners want to use other biobased alternatives, such as boards or paper-based vapour retarders which also are more permeable. Additional mounting of PE-foils is more prone to failures, and studies have found a limited lifetime [14]. The vapour resistance of the different layers are interdependent, and should be adjusted considering the moisture class load and outdoor climate [2].

1.3.2 Diffusion-open construction

When using biobased insulation, there is an interest in building wood-frame walls without a vapour barrier. This has been tried in some case buildings, such as The Breathable House (translated title of the Danish original: "Det Åndbare Hus"). Here they conclude that the

wall construction with a resistance ratio of 1:1, does not show any moisture issues, because the construction allows the permeability of water vapour [15]. They also obtain energy savings, due to a lower ventilation need with regards to moisture. The need and requirements of a vapour barrier in wood-frame walls has been more recently investigated in two simulation studies [14] [16]. Hansen et al. [14] finds that the needed ratio decreases when the wind barrier vapour resistance increases. Also, it is found that the typical ratio of 1:10 is not sufficient for some of the wood fiber insulation alternatives like grass, hemp and flax. The study however shows it can be lower with wood fiber insulation. In [4] they find that biobased insulation has a better fault tolerance compared to mineral wool insulation with air leaks, and protects the timber by absorbing and dispersing moisture. It can be concluded there is both disadvantages and advantages for biobased insulation if used properly.

1.4 Moisture transport and storage

Biobased building insulation is characterised by being porous and hygroscopic. The pore structure and size is one of the most important parameters regarding a material's water sorption. The material will have an interconnected system of pores, which impacts the transport of air, water vapour, and water. Besides its solids, the amount of liquid and air, will be dependent on the conditions. The porosity describes how big the pore volume is compared to the total volume. Fibrous insulation materials will typically have a high porosity above 90%, because the high porosity is the reason for the low thermal conductivity. Moisture in building materials is usually understood as physically bound water, and it is primarily due to absorption and capillary condensation. [6]

Water adsorption is dependent on the partial water vapour pressure and the specific surface. We typically use the relative humidity (RH) as a measure of moisture, which is the ratio between the partial and saturated water vapour pressure. When the internal surface of a porous material is in contact with water vapour, it will readily bind a layer of water molecules to the surface with considerable energy due to intermolecular forces. This binding energy decreases rapidly for each additional layer of water molecules. The layer of water molecules is transient, where some break away and others are captured. Due to cohesion and adhesion forces, there will be surface tension in the interface between the liquid, solid and gaseous phase, creating a contact angle. The contact angle impact the capillary suction of the material. [17]

The thickness of the absorbed water molecules will increase with relative humidity and eventually

opposing layers will come together and close some of the pore spaces. Here, surface tension will make the water take a curved shape. For an equilibrium situation, water will condensate on a plane liquid surface if the air reaches the water vapour saturation pressure at a given temperature, and evaporate at a partial vapour pressure. This relation is, however, different inside the material's pore structure, when the liquid surface is curved. Just above the curved surface, the water saturation pressure will be lower, and it will attract more water molecules, which is called capillary condensation. This phenomenon does not play a significant role, before the relative humidity reaches 80-90%. [6] [18]

1.4.1 Moisture sorption in biobased insulation

When combining the different effects, a moisture sorption isotherm can be drawn. A material will absorb or desorb moisture until it is eventually in equilibrium with the ambient conditions. The sorption isotherms represent the equilibrium between moisture content and the relative humidity. With changes in relative humidity, the water content will change initially fast and then slower until a new equilibrium state is reached. The relationship between the relative humidity and moisture content is very material dependent, as shown in Figure 1.1.

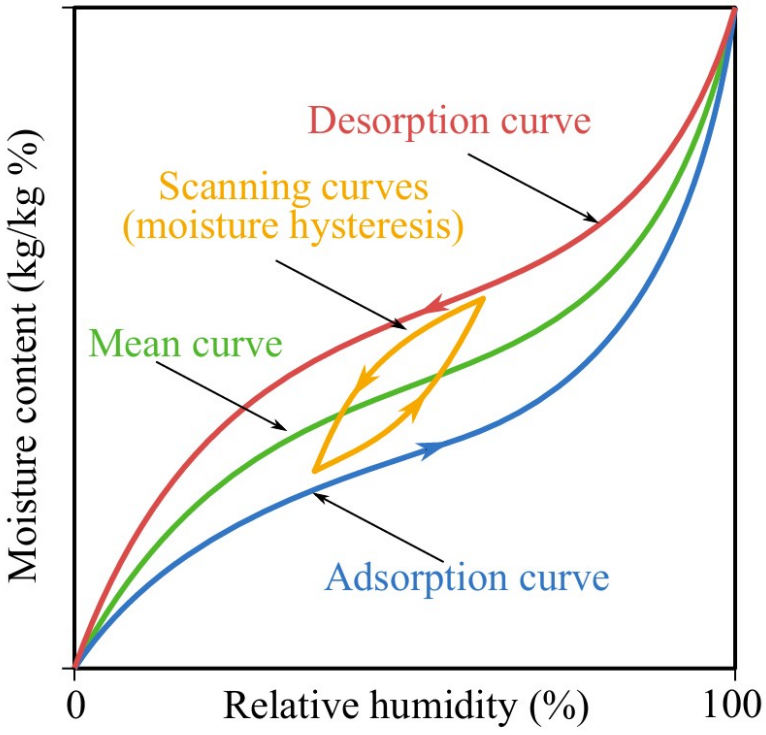

Figure 1.3. Moisture sorption isotherms [19].

The sorption curve will have a characteristic s-shape, due to the different effects. Below 20%

RH, adsorption in the first monolayer will be the dominating effect. Then the curve becomes more linear, where there is polymolecular adsorption. Above 40% RH, capillary condensation will begin and will in the end be the primary force. Above 98% relative humidity, capillary suction becomes the dominant driving force for moisture transport and this region is known as the over-hygroscopic range [17]. The moisture sorption is dependent on the material's previous moisture history, which is seen on Figure 1.2. When the material is wetted it will follow the absorption curve and when drying follow the desorption curve. The material will, however, in reality, not follow the curves, as they are the outer boundaries in equilibrium. Building materials will typically experience humidities between 20-90% in transient conditions. The materials will then follow scanning curves that lie in between the absorption and desorption curves, which is shown on Figure 1.3. Hygroscopic materials will exhibit hysteresis, which is the difference between the adsorption and desorption curves, and is stored moisture in the material. The ink-bottle effect is one of the effects causing the behaviour, where big pores during desorption first will be emptied when smaller pores, acting as a bottleneck, are emptied [17].

A lot of research is done to model moisture hysteresis and the actual scanning curves under variations in relative humidity [20, 21, 22, 23]. Moisture sorption curves are often simplified, using only the adsorption curve or an average curve, neglecting hysteresis. This is the case for the simulation software WUFI, which is considered an advanced heat and moisture transfer simulation tool. In [19] they evaluate the impact of hysteresis in a wood-frame wall with cellulose insulation, using the MATCH-software. They evaluate the risk of wood decay depending on the modelling of hysteresis using the adsorption, desorption, average curve or empirical hysteresis model. The paper concludes that using the adsorption or desorption curves leads to different results, but that the average curve and hysteresis model are quite similar and more accurate [19]. Disregarding moisture hysteresis can lead to modelling errors in the prediction of moisture content, especially with oscillating boundary conditions [22]. The hygroscopic properties also affect latent heat, where insulation will release heat, when it absorbs water [24]. This is measured for wood fiber, eelgrass, grass and mineral wool insulation, where it is clear the biobased insulations are warmer than the mineral wool [8, 24]. They also note that studies of bio-based insulation focus primarily on the material scale, and more studies on component and full scale with dynamic realistic setups are needed. With a transition to more diffusion-open constructions, our hypothesis is that it becomes more relevant to investigate hysteresis and investigate the complex dynamics for hygroscopic biobased insulation.

1.5 Problem statement

This thesis will investigate biobased insulation in both the material and wall scale. New biobased insulation calls for an exploratory approach, and more knowledge about different bio-based materials is needed, to make it easier to use in construction. There will be a focus on the material properties and hysteresis, as it is often simplified, and measurements of actual scanning curves are done. Additionally, the aim is to make a test rig that allows for testing of different wall assemblies. This leads to the following problem statement and research questions:

- **What is the moisture hysteresis for biobased insulations at realistic variations in relative humidity, and how do new biobased insulation perform in wall assemblies?**
  - What is the expected variations in relative humidity through a wall, and their time duration?
  - How are the moisture sorption isotherm at realistic relative humidity variations?
  - How can the performance of new biobased insulation be tested, and how do they perform?

To answer the above questions, the project is structured as shown on Figure 1.4.

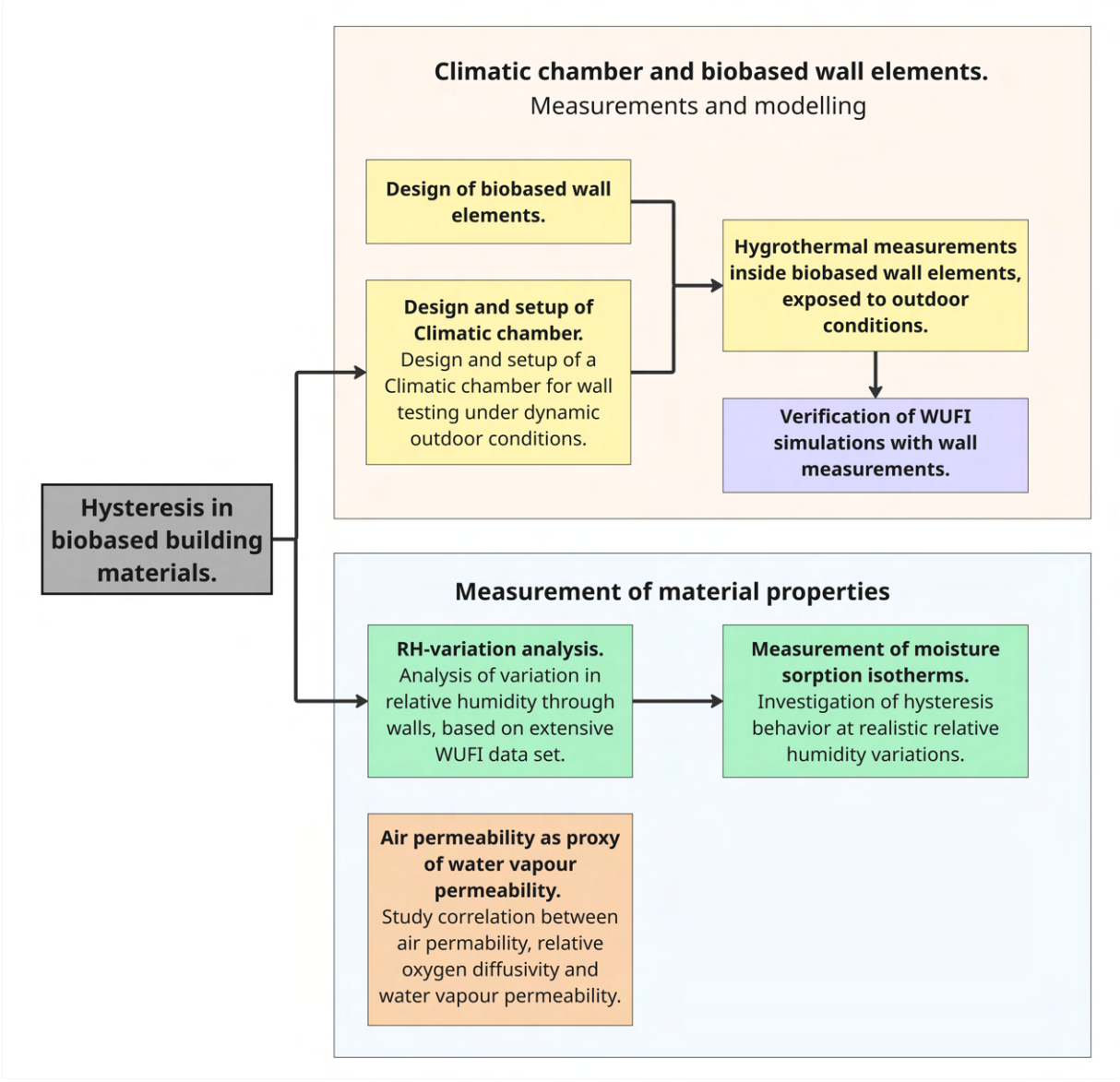

Figure 1.4. Content structure of project.

Chapter 2

Study of realistic fluctuations in relative humidity in wall assemblies

When creating moisture isotherms for building materials, the relative humidity (RH) is often varied from 10% to 90% to analyze how materials respond to different moisture levels. However, in real-world building environments, it is not investigated if the RH fluctuates within this range. Therefore, conducting an analysis of RH across multiple variations of a wall construction is essential to understand how moisture behaves throughout different layers. This type of analysis helps determine the variation of relative humidity throughout the construction, providing valuable insights into moisture control and potential risks such as mould growth or material degradation.

2.1 Variations of Relative Humidity in wall elements

The data from the variations are from a 9. semester project at Aalborg University [25]. In their project, multiple variables have been varied, including different parameters for the insulation and the type of wind and vapor barrier. Furthermore, the interior conditions are varied with both moisture class two and three. To reduce the amount of data and simplify the analysis, it has been chosen to look at a singular variation in the wind barrier and two different vapor barriers. The variations can be seen on Figure 2.1.

In addition to that, the time period has been reduced to the last year of the 10-year period. This is to secure stable conditions, as only the variations in relative humidity caused by the interior and exterior conditions, and not the initial material condition, are wanted.

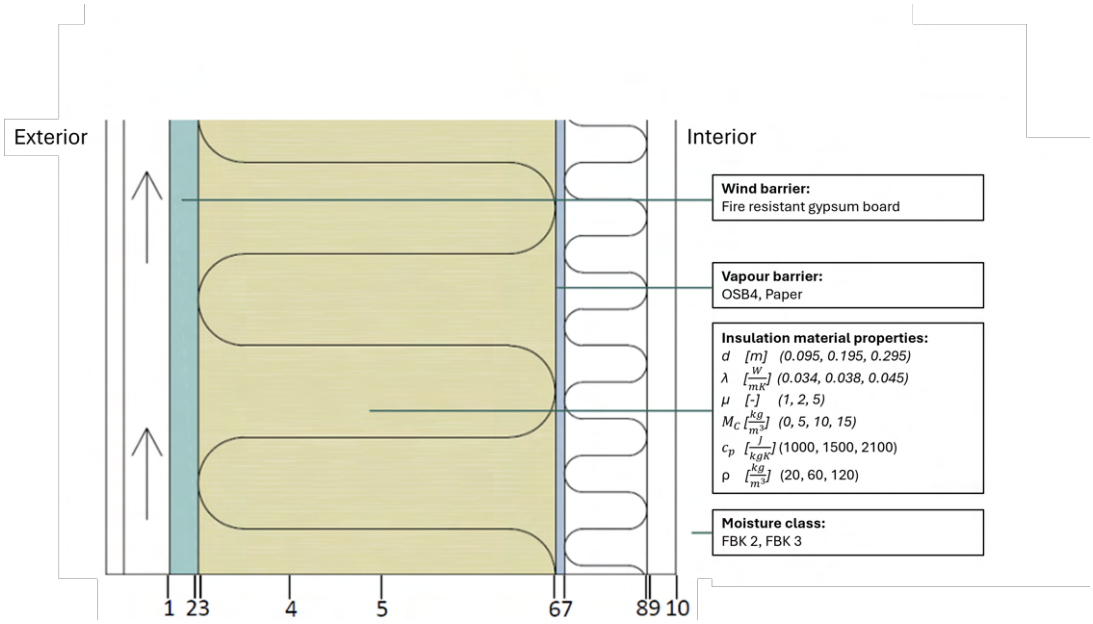

Figure 2.1. The evaluation points (1-10), and the different material parameters used in the analysis.[25, Mod.]

The data have been analysed for 5 out of the 10 points seen on Figure 2.1. The chosen points are 2 (Wind barrier), 4 (1/4 into the insulation), 5 (halfway into the insulation), 6 (insulation just before vapour barrier) and 8 (insulation close to the interior lining). The RH in these points is analysed for local extrema, and the change of RH between these is noted as well as the middle value between the extrema. The results are plotted as box plots, with the middle value grouped in intervals of 10. An example is shown in Figure 2.2 and the remaining points can be seen in Appendix U. To be able to see the larger changes in the RH, changes smaller than 3% have been removed.

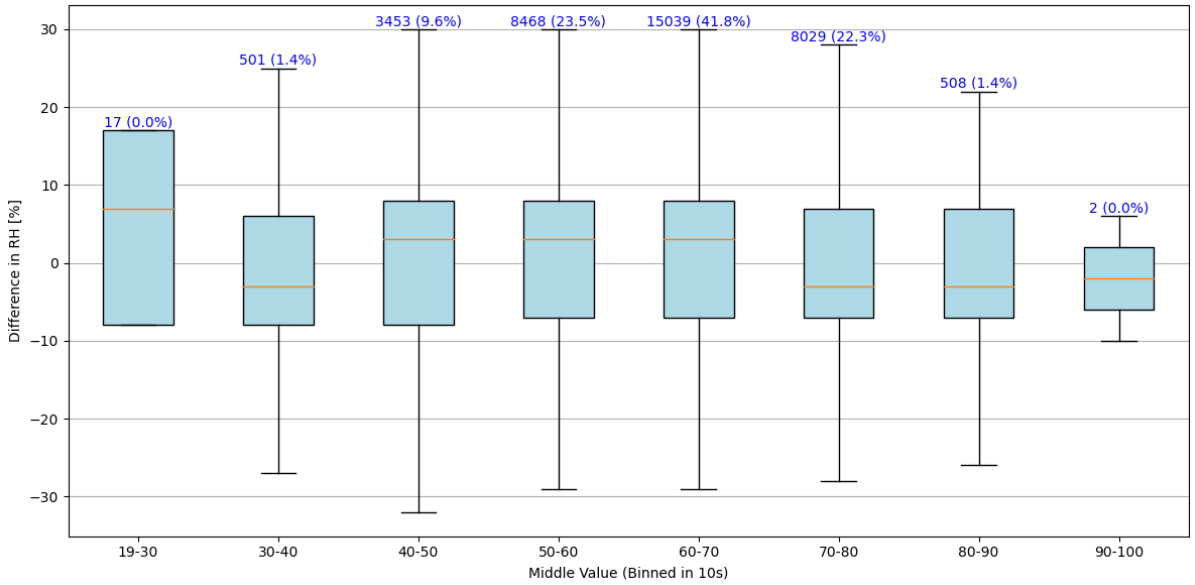

Figure 2.2. The results for the variation of RH in point 5. The distance is both positive and negative, as the direction of the variation is taken into account. The middle value intervals should be seen as [left, right[.

To focus on the core data and reduce the influence of outliers, further work is based on the results between the 1st and 3rd quartile. As seen on Figure 2.2 the RH generally varies with less than ±10% in the middle of the insulation. Furthermore, a high percentage (97%) of the total calculated differences is seen between 40 and 80% RH. This conclusion can also be seen in the other points throughout the wall.

2.1.1 Time-frame of the variations

In addition to the size of the variation in RH, it is also essential to analyse the duration of the fluctuations. The timeframe over which RH changes occur can influence how building materials absorb or release moisture and whether they reach equilibrium or remain in transient states. This is important for evaluating moisture buffering capacity and assessing risks of mold growth.

The same local extrema identified earlier are used to determine the duration of the variation. The findings are shown in Figure 2.3.

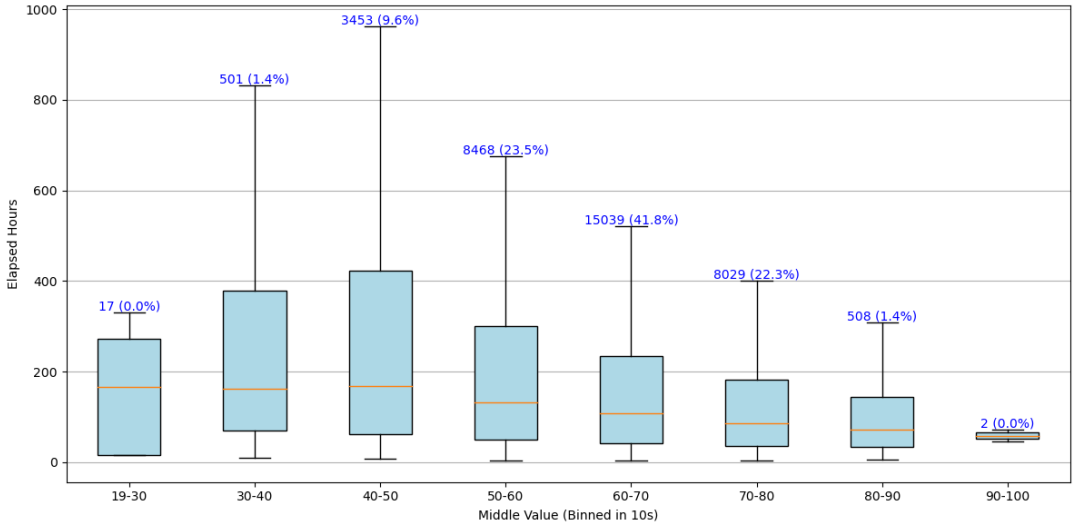

Figure 2.3. The duration of the variation in RH for point 5. The middle value intervals should be seen as [left, right[.

As seen on Figure 2.3, the duration of a change is approximately 50 to 400 hours. This can be seen for all three analysis points in the insulation. For the points surrounding the wind- and vapor barrier, the duration tends to be larger. The plots for the remaining points can be seen in Appendix U.

2.2 Variations in weather

To get an idea of the boundary conditions used in simulations, two highly used weather files are analysed. The files are HRY-REF2 and DRY_2001-2010 v3. The first parameter investigated is the size of the variation in RH. Like in the WUFI-analysis, variations smaller than 3% have been excluded. The findings are seen in Figure 2.4.

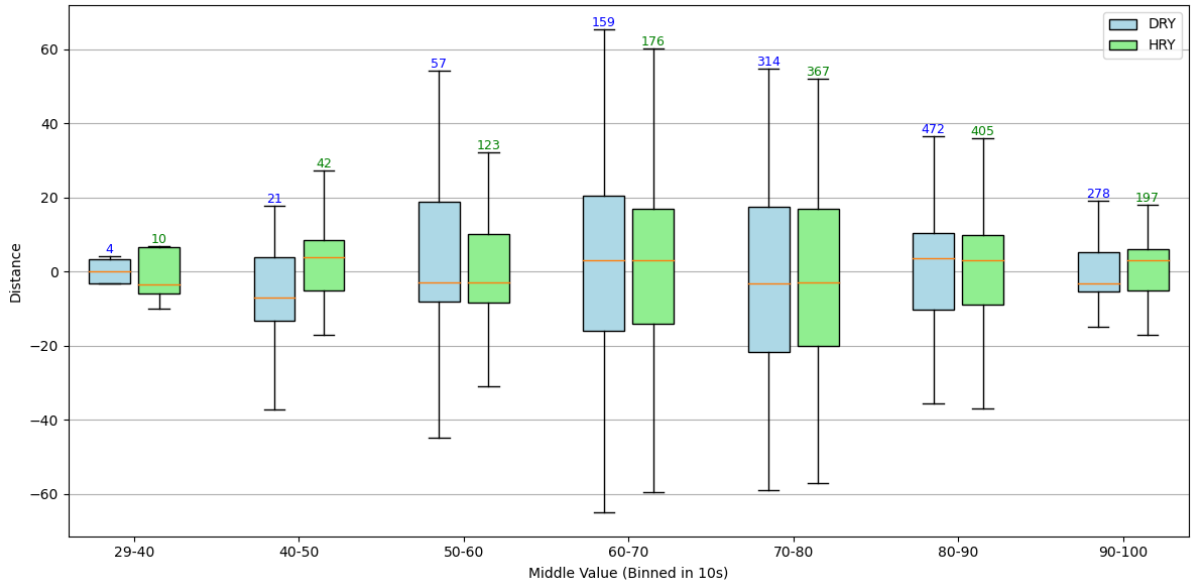

Figure 2.4. The distance of the variation of RH for the two weatherfiles. The middle value intervals should be seen as [left, right[.

As seen on the graph, there is a minor difference between the two weather files. Firstly, the variation in the DRY-file is slightly larger, especially in the lower intervals. Furthermore, the amount of variations is different. For DRY, most of the variations happen in the 60-100% range. For HRY this is also true, but there is a high amount of variations in the lower range. The size of the variations is ± 20% and it does not vary significantly between the files.

As in the WUFI-data analysis, the duration of these variations is also analysed. The duration can be seen on Figure 2.5.

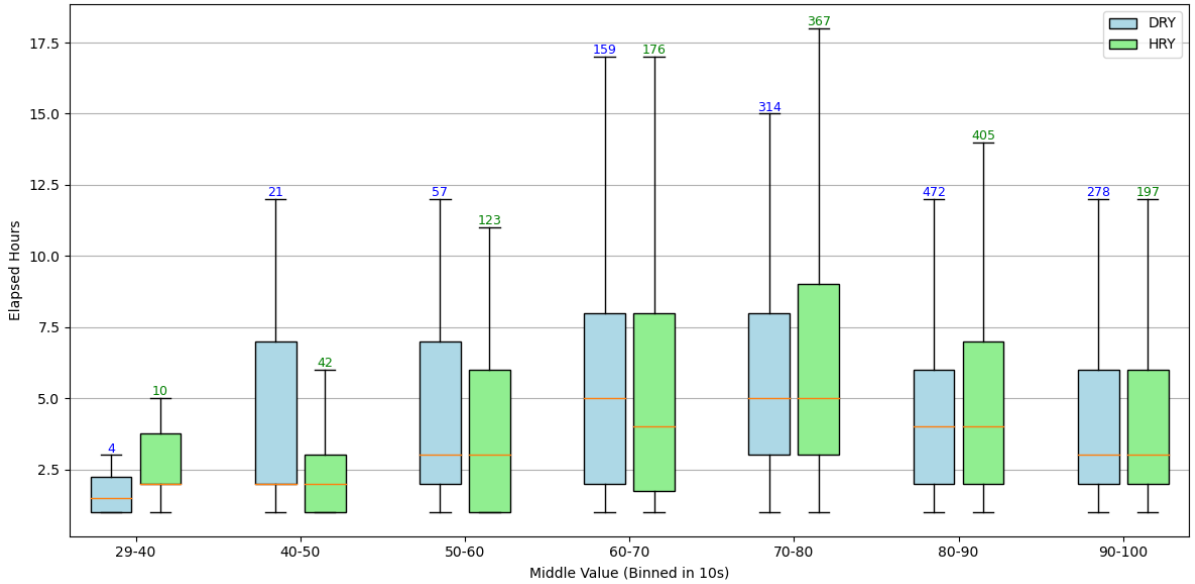

Figure 2.5. The duration of the variation of RH for the two weatherfiles. The middle value intervals should be seen as [left, right[.

The duration is much faster in the weather files than in the WUFI simulations. It is generally seen that the duration is between two and eight hours for both of the weather files.

2.3 Variations in indoor climate

For the WUFI simulations, the indoor environment is set to a specific moisture class. This results in the temperature and RH being constant and not fluctuating a lot. Therefore, data from five apartments, with multiple sensors in each, have been analysed in the same way. The distance analysis can be seen on Figure 2.6.

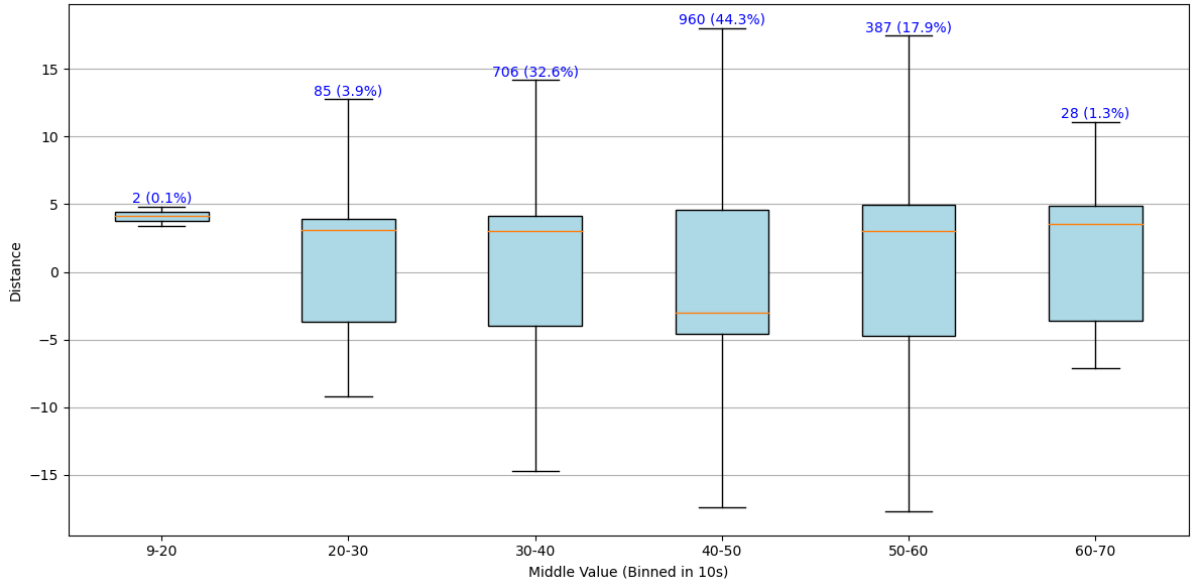

Figure 2.6. The variation in the RH for indoor environment in the 5 apartments. The middle value intervals should be seen as [left, right[.

From the analysis, it is seen that the indoor environment fluctuates within ± 5% for all of the intervals. Furthermore, most of the variations (95%) happen at a RH between 30 and 60%. The duration of the variations for the apartment measurements can be seen on Figure 2.7.

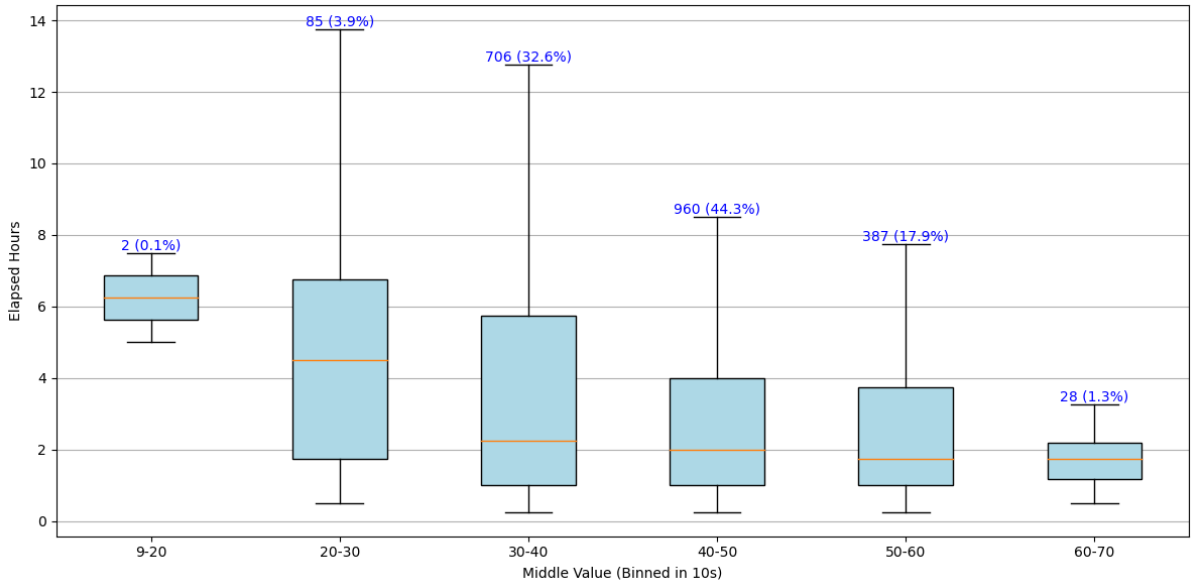

Figure 2.7. The duration of the variation in RH for indoor environment in the 5 apartments. The middle value intervals should be seen as $[\text{left}, \text{right}[$.

From this analysis, it is seen that for the lower middle value intervals (9-40%), the duration varies between one and seven hours, while for the higher intervals, the fluctuations are faster.

The findings of this chapter show that RH in wall assemblies typically fluctuates within a ±10% range, especially in the insulation layers. The RH variations most commonly occur between 40–80%, with local extrema typically separated by durations of 50–300 hours. Comparisons between simulation data, weather files, and indoor measurements highlight significant differences in both the magnitude and duration of RH variations. While weather files show larger and more rapid changes (±20% range and 2-8 hours) , indoor environments show smaller fluctuations (±5% range and 1-7 hours).

Chapter 3

Hysteresis at realistic relative humidity variations

In chapter 2, it was shown that relative humidity (RH) in wall constructions rarely fluctuates across the full 10–90% range often used in material characterization. Instead, smaller RH variations of ±10% over long durations are far more common. This discrepancy raises important questions about the accuracy of traditional sorption isotherms in representing real-world material behavior. To investigate this, the following chapter focuses on measuring hysteresis in moisture sorption under more realistic humidity conditions. By using a Vapour Sorption Analyzer (VSA), materials are tested with both large and small RH cycles to better understand how they respond to typical indoor and in-wall moisture dynamics. The results can help determine whether traditional isotherms over- or underestimate hysteresis under operational conditions.

3.1 Moisture sorption measurements

The results from the analysis are used as input for the VSA. The VSA is an automated device for generating isotherms. It offers two distinct methods for sample analysis and isotherm generation. By utilizing both methods, it can assess dynamic changes resulting from variations in water sorption and the kinetics of these changes.

A moisture sorption isotherm represents the relationship between water activity and moisture content at a specific temperature. This relationship is unique to each product due to varying interactions between water and solid components at different moisture levels. [26]

In this project, the Dynamic Dewpoint Isotherm method (DDI) is used. The DDI method

changes the relative humidity dynamically as the sample is wetted with saturated water or dried with dry air. As the DDI method isn't reliant on the sample reaching equilibrium, this method is almost 50% faster than the Dynamic Vapour Sorption method, all while the increased speed isn't causing a significant loss in measurement accuracy [27]. Furthermore, as seen in chapter 2, the RH inside of a wall construction never reaches equilibrium and therefore, reaching equilibrium with the VSA isn't deemed a necessity. Our VSA measurements consist of two measurement campaigns, where the difference is the duration of the measurements. The first measurement campaign uses the same settings as the NOWA-project [28]. These settings are:

- Resolution at 0.03 aw
- Temperature at 23℃
- Flow at 100 ml/min
- Current off
- Timeout off

3.2 Campaign 1 - Fast measurements

In the first measurement campaign, the hysteresis of two biobased materials (Wood fiber insulation (WFI) and Hemp fiber insulation (HFI)) and AAC-Ytong are evaluated. The focus is on smaller RH variations (10%), as it is seen that these variations are commonly experienced inside a wall element.

From the RH analysis, it is seen that the RH within a construction element mainly fluctuates ±10%. This conclusion is used to determine the RH cycles used in the measurements. It was also seen that a high percentage of the variations happen between 40 and 80%. Therefore, it is chosen to run variations from 35-45%, 45-55%, 55-65%, 65-75% and 75-85%. As the RH fluctuates both from high to low and low to high, these trends are also taken into account. This is done by firstly increasing the RH for each stage, and afterwards decreasing the RH for each stage. The RH stages can be seen on Figure 3.1.

Figure 3.1. The RH stages applied for the 10 % variation.

In addition to the smaller 10% variation, a larger variation from 10% to 90% is also made. This measurement is done for three repetitions, to make sure the isotherms are correct. From chapter 2 it is seen that the larger variations do not happen, but they are used in the simulation programs. Furthermore, the larger variations can help with identifying characteristics of the small isotherms.

The goal of the first measurement campaign is to try to characterise the smaller isotherms. Therefore, the small isotherms are plotted against the traditional 10-90% isotherm. For Ytong and WFI, the results are similar and the scanning curves can be seen on Figure 3.2 and 3.3.

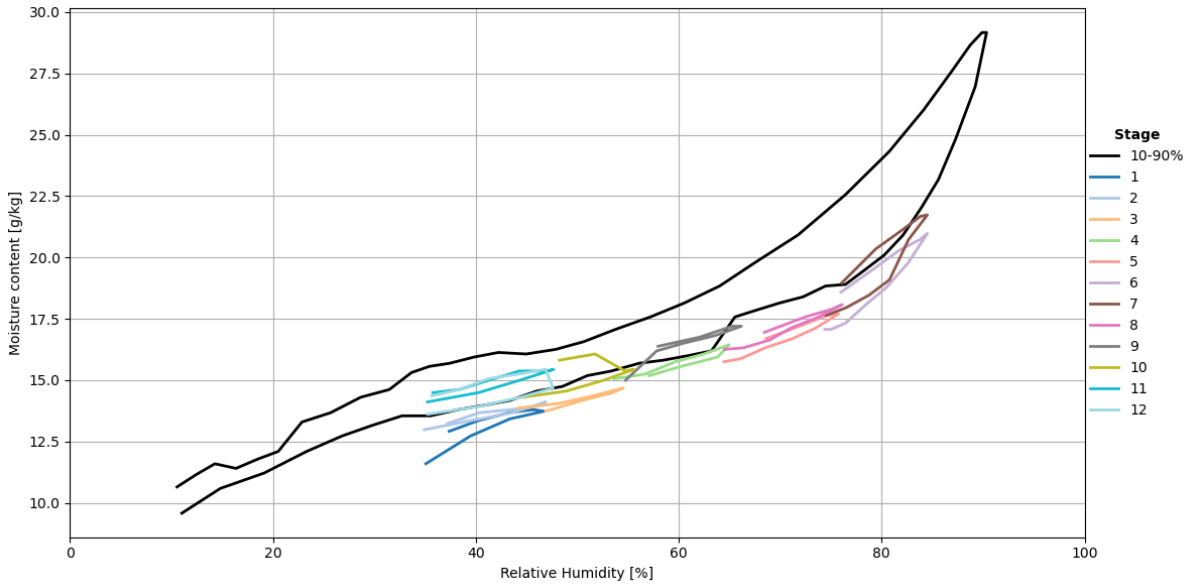

Figure 3.2. The isotherms for Ytong measured in the first measurement campaign.

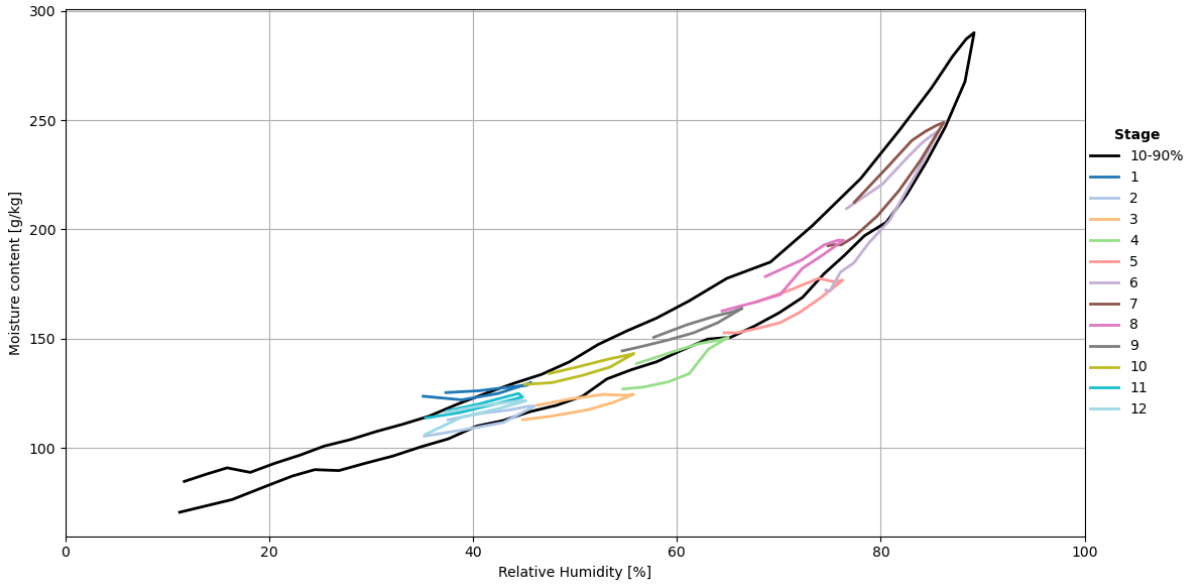

Figure 3.3. The isotherms for WFI measured in the first measurement campaign.

For Ytong, it can be observed that the small curves follow the adsorption branch of the 10–90% isotherm. Additionally, these small curves are grouped into two distinct bands: the first six appear lower, while curves 6–12 are positioned higher. This pattern aligns with expectations, as adsorption curves typically lie below desorption curves. The lower set corresponds to the first six curves, which is where the sample is in an adsorption process. For WFI, the same tendencies are seen. The third material used in this campaign, HFI, can be seen on Figure 3.4.

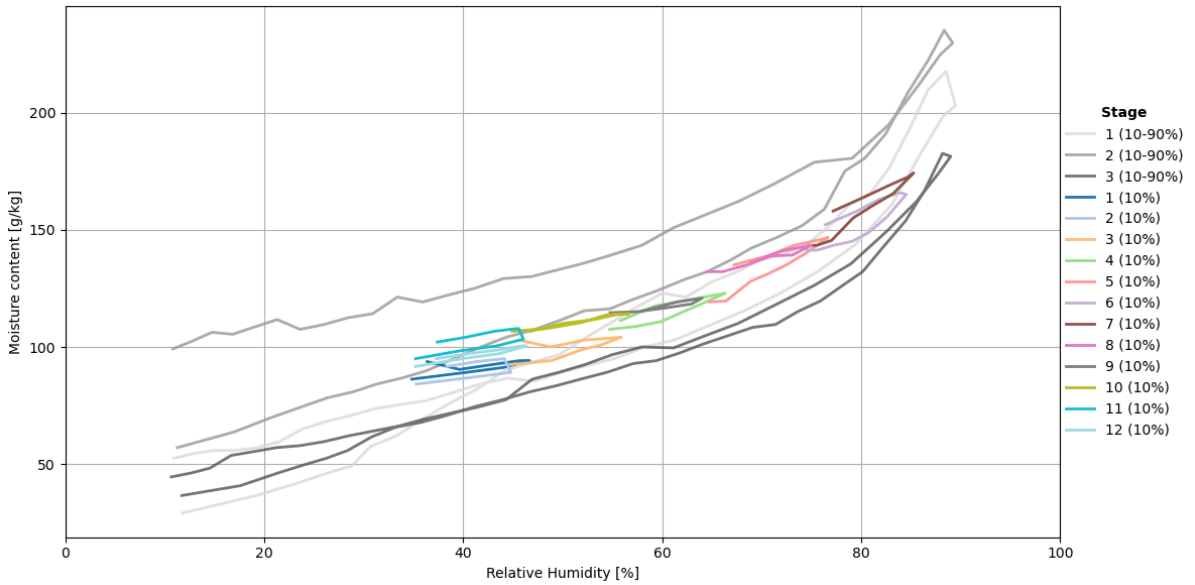

Figure 3.4. The isotherms for HFI measured in the first measurement campaign.

For HFI, it is difficult to draw definitive conclusions from the small curves, primarily because the 10–90% curves do not stabilize. As a result, it is unclear whether the small curves follow the same pattern observed for Ytong and WFI in terms of positioning. Nevertheless, the presence of two distinct bands is still evident.

3.3 Campaign 2 - Slow measurements

The smaller variations take approximately 1 hour for each stage (35%-45%-35%), but as seen in subsection 2.1.1, the timeframe of the variations in the WUFI-elements is upwards of 50 hours. Therefore, a measurement campaign with slower variations is made. For the DDI-method, the longest cycle-duration we can obtain is 6 hours. This is far from the 50 hours, but it is expected that the changes seen in an increase from 1 to 6 hours would be more significant if it were from 1 to 50 hours.

The RH stages in this measurement campaign are identical to those used in the 10% measurements, and shown in Figure 3.1. The longer duration is due to adjustments in the settings: the resolution was lowered from 0.03 to 0.003 aw, and the flow rate reduced from 100 to 10 ml/min. Because of time constraints, the slower measurements were only conducted for the 10% variation and the 10–90% variation for WFI. The isotherms can be seen on Figure 3.5.

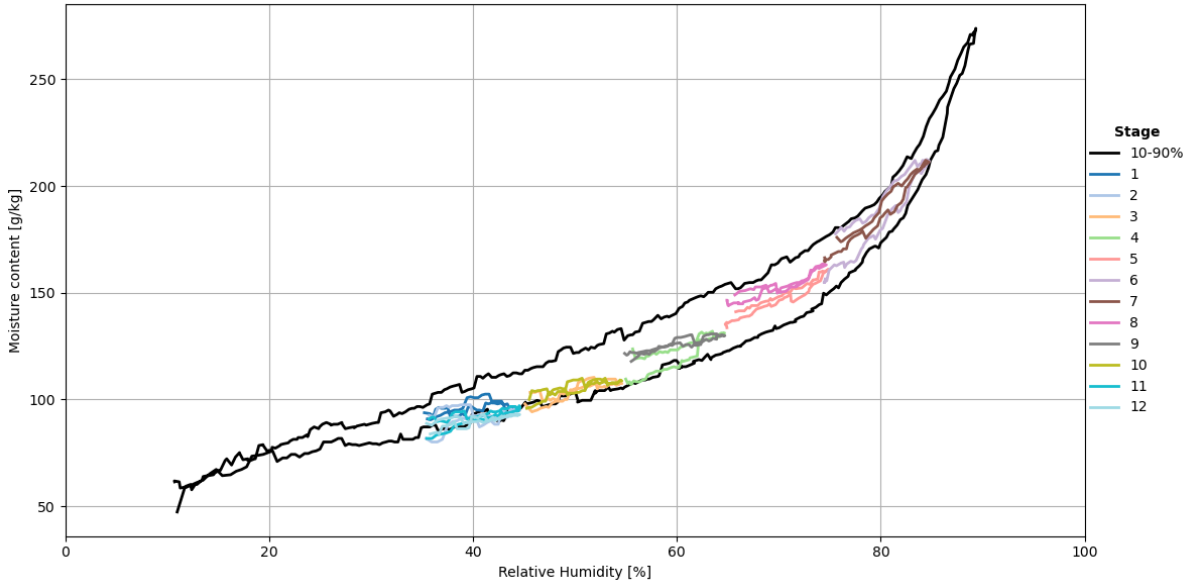

Figure 3.5. The isotherms for the slow measurements on WFI.

The slow measurements are similar to the fast, except for the small variations being closer to the center of the 10-90%.

3.3.1 Comparison of slow and fast measurements

As found in chapter 2, the duration of the RH variations is significantly longer than the 1-hour period used in measurement campaign 1. Therefore, it is essential to examine the differences between the two measurement campaigns. To facilitate this comparison, isotherms for both the 10% variation and the 10–90% variation have been plotted and are presented in Figure 3.6 and Figure 3.7, respectively.

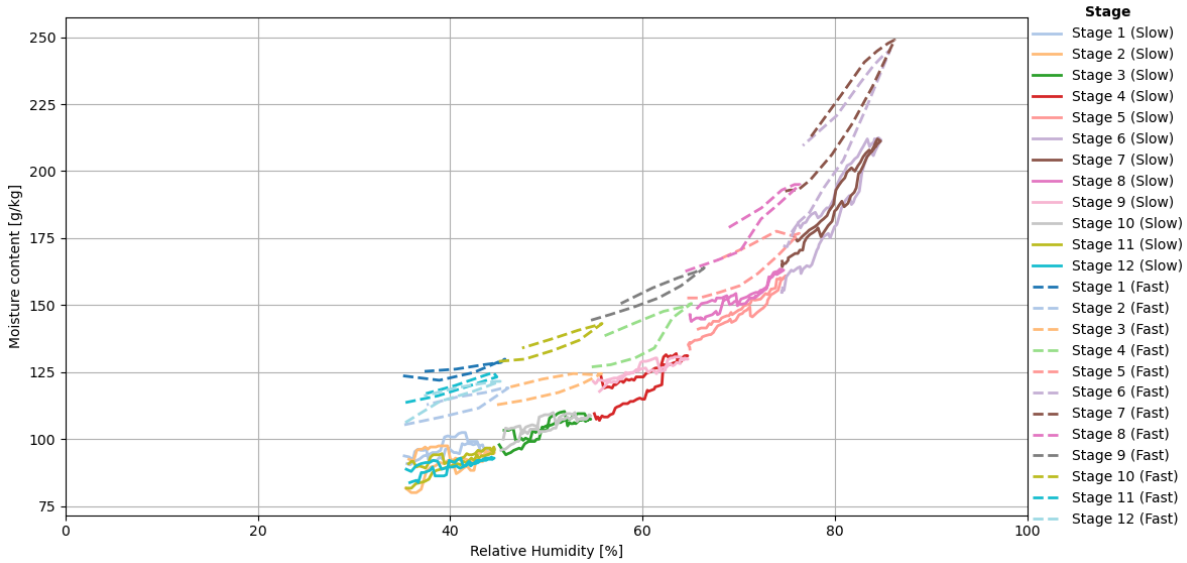

Figure 3.6. Comparison for 10% variations for the two measurement campaigns on WFI.

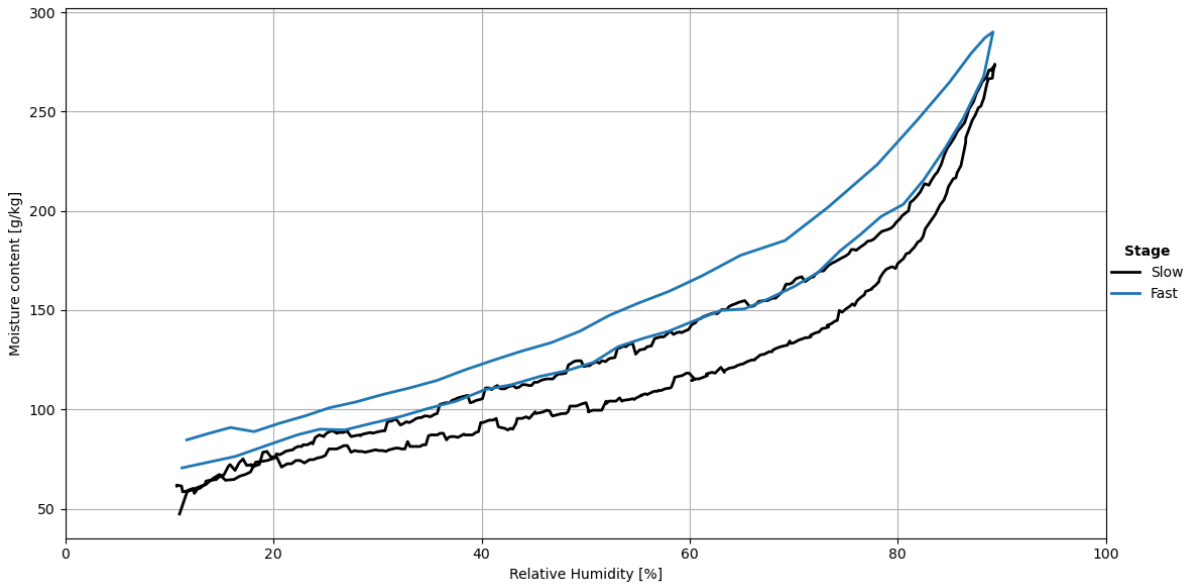

Figure 3.7. Comparison for 10-90% variations for the two measurement campaigns on WFI.

From the isotherms, it can be seen, for both measurement campaigns, that the slow variations

have a lower moisture content than the fast. This variance can be caused by the fact that we used the same sample for all measurements, as we saw a difference in weight per measurement. As all measurements per material are not done in a row, the sample has been moved, which might have changed the structure, and therefore varying starting conditions. The measurement schedule can be seen in Appendix P. In addition to the moisture content, it is also seen that on the slow variations there is more noise. This is most likely caused by the change in the resolution setting used to increase the duration of the measurement.

3.4 Analysis of Hysteresis

To quantify the hysteresis of the three materials, the commonly used GAB model was initially used. However, as illustrated in Figure 3.8, the model performs poorly on the smaller curves, likely due to the limited number of data points. It fails completely at stages 1, 3, and 12 during desorption, while the remaining fits are of low quality. Consequently, alternative fitting methods are explored.

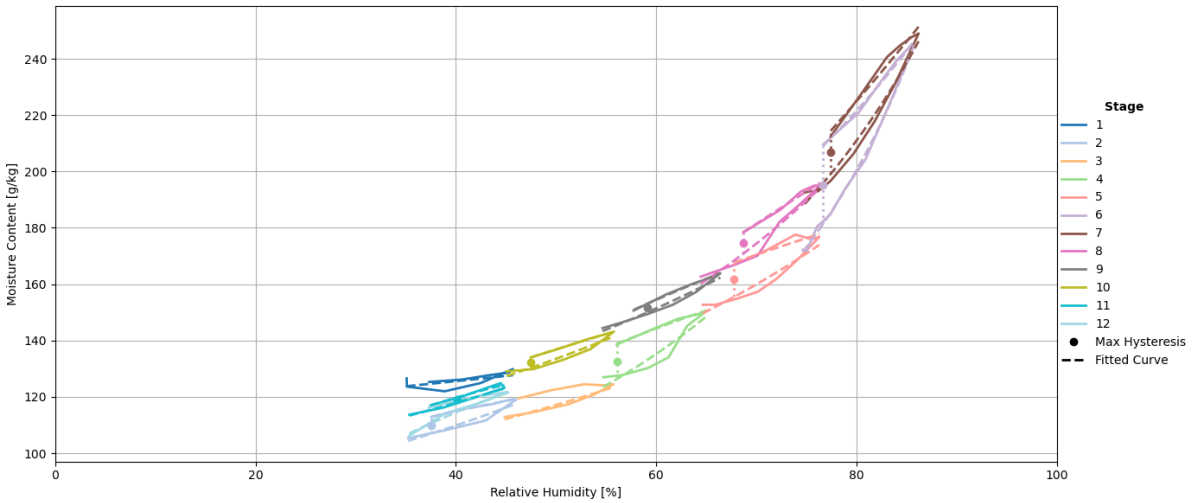

Figure 3.8. The GAB model fitted to the 10% variations for WFI.

To maintain consistency in the comparison, the same method is applied to both variations. Given the sparse data, linear interpolation is used to get the best fitting lines between the points. This method gives the best fits for both the 10% and 10-90% variations. The fitted curves are used to find the hysteresis throughout the variation. This is done by calculating the difference in moisture content for all relative humidities. As the smaller variations from the first measurement campaign are created from 8-10 points pr. stage, it is not guaranteed that the curves cover the whole RH-area. Therefore, the hysteresis is only analysed where the RH values

for adsorption and desorption overlap. The analysis for the fast WFI measurements can be seen on Figure 3.9 and 3.10. The remaining plots can be seen in Appendix Q.

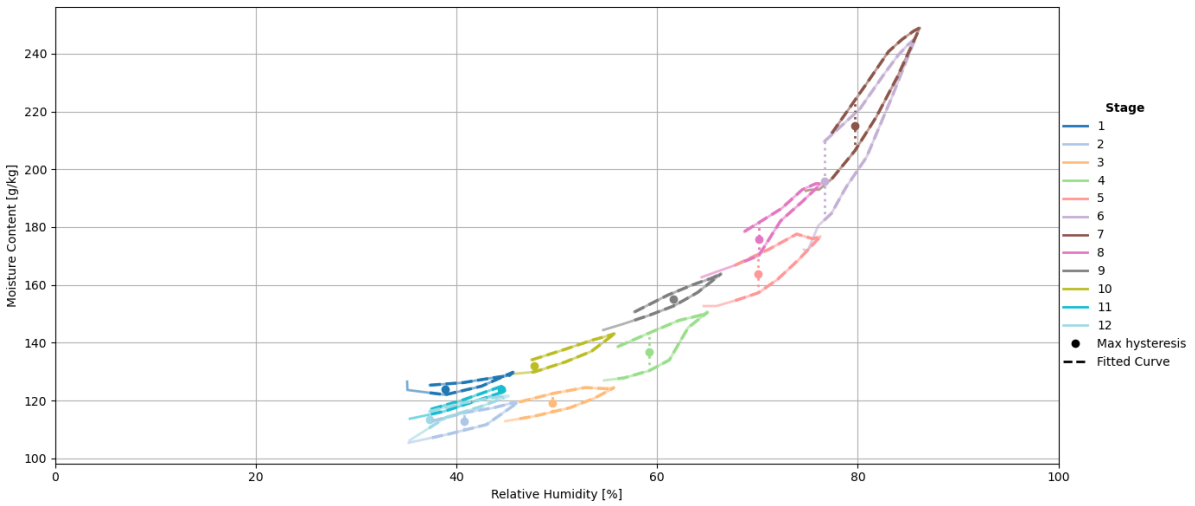

Figure 3.9. Linear interpolation used to fit to the fast 10% variations for WFI.

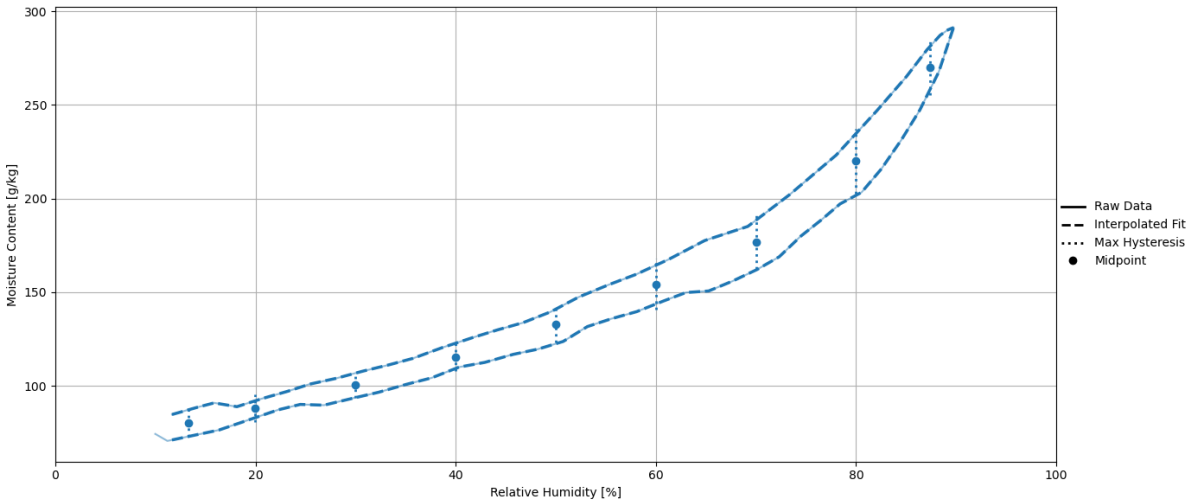

Figure 3.10. Linear interpolation used to fit to the fast 10-90% isotherms for WFI.

For each stage in the 10% variation, the maximum and average hysteresis are found, and both values can be found in Appendix Q. For the 10-90% variation, the isotherm is divided into 9 steps, each varying 10%. The found hysteresis for the 10% variations can be seen on Figure 3.11. The raw values can be seen in Appendix Q in Table Q.1 and Q.2

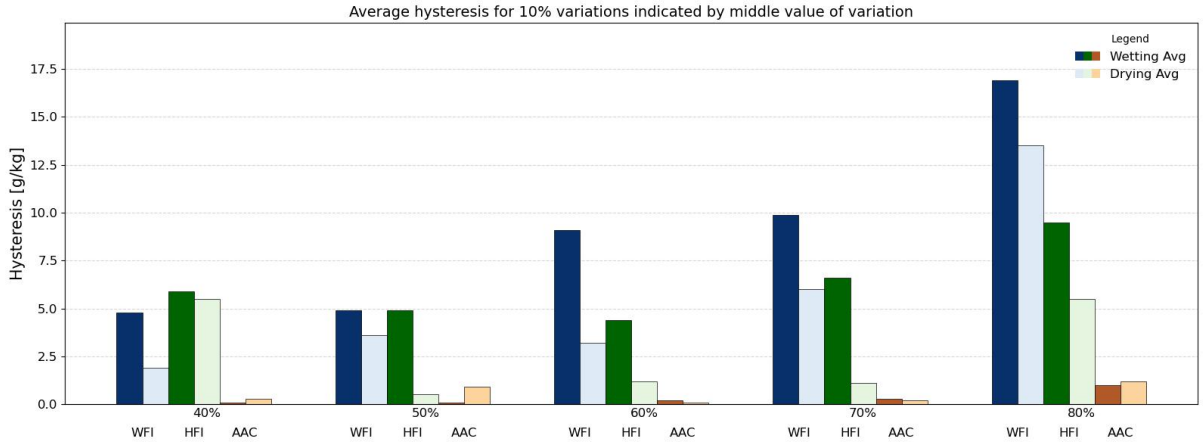

Figure 3.11. Average hysteresis of the Δ10% variations, divided into the wetting and drying cycle. WFI=Blue, HFI=Green, AAC=Orange

From the figure, it is seen that Ytong consistently shows the lowest hysteresis values across all conditions, with only a slight increase as relative humidity rises; both maximum and average values remain below 5 g/kg. HFI exhibits more hysteresis that increases steadily with relative humidity, reaching up to about 10 g/kg at higher humidity levels, with maximum values consistently exceeding average ones. WFI demonstrates the highest hysteresis values, with maximum values exceeding 30 g/kg at high humidity levels. The trend for WFI indicates a strong sensitivity to humidity changes, with both maximum and average hysteresis values rising as relative humidity increases.

Furthermore, for the 10% variations, it is seen that there is a difference in the two values in each interval - for the wetting or drying history. To identify what is causing this, would require more measurements of the same materials. This has not been done, but the difference might be caused by moisture history, uncertainties, or inconsistencies in the measurement method.

Figure 3.12 show the results of the 10-90% measurements, and for comparison the values of the Δ10% measurements. The grey lines highlight the interval for where the Δ10% measurements are done.

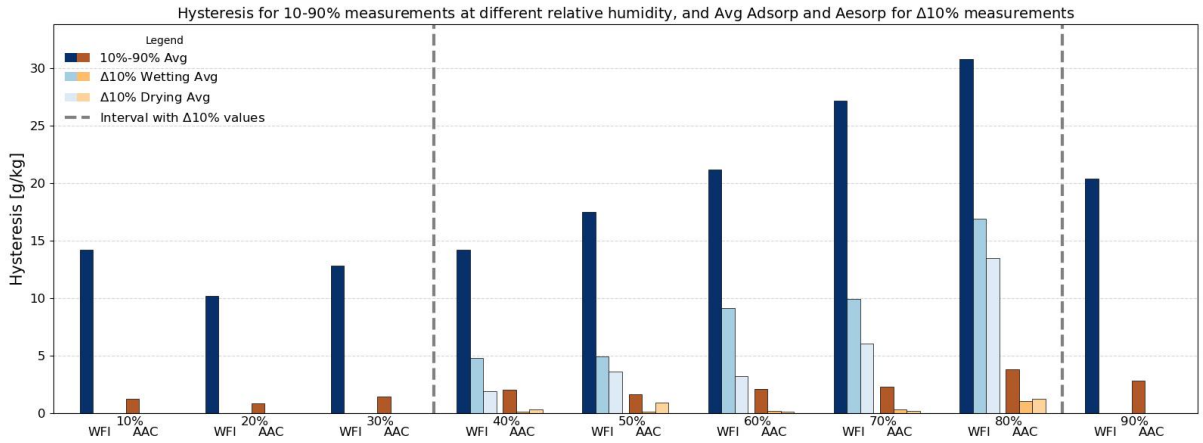

Figure 3.12. Average hysteresis of the Δ10% variations, divided into the wetting and drying cycle and 10-90% values. WFI=Blue, HFI=Green, AAC=Orange

From this, it can be concluded that using the 10-90% hysteresis might overestimate the actual hysteresis. The extent of this overestimation varies by material; while it has minimal impact for Ytong, it is more pronounced for WFI. Therefore, depending on the material, using the 10-90% isotherm could result in inaccurate assessments.

Chapter 4

Climatic chamber design and measurement setup

The use of biobased materials in building components makes it essential to employ numerical simulations that account for their strong moisture properties and dynamic behaviour to accurately evaluate the moisture robustness of a component. Simulations are a cost-effective tool that can evaluate components over a long period to predict potential risks of moisture build-up or mould growth. Even though the governing transport equations describing heat and moisture transfer are well-established, simplifications in modelling and assumptions create a model–reality discrepancy. Therefore, it is crucial to verify numerical simulations with experimental measurements.

A major part of this thesis involves designing and creating a measurement setup that supports an exploratory approach, enabling the testing of various wall assemblies — featuring, for example, different assembly principles, biobased insulation materials, and vapour or wind barriers. The climatic chamber is a measurement setup, where wall constructions can be tested under controlled indoor conditions and actual outdoor weather conditions. Additionally, the container is placed on a raised column foundation, so an investigation of the conditions in the crawl space underneath can be made. This secondary setup is briefly explained in Appendix A.

The setup is designed for wall testing, given that walls represent a major part of the building envelope, especially in multi-story buildings. This setup is made in order to obtain hygrothermal measurements from biobased wall elements under dynamic outdoor conditions to investigate the influence of hysteresis in the biobased insulation. The wall elements tested in the measurement

setup are described in section 4.2.

The climatic chamber is built inside an insulated 20-foot high-cube standard ISO container. It is placed at a test site at the Department of the Built Environment, BUILD, at Aalborg University in Aalborg, Denmark (57.013968°N, 9.972095°E). The climatic chamber setup is shown from the outside on Figure 4.1, and on the inside without wall elements on Figure 4.2.

Figure 4.1. Outside view of the facade facing north, with the rain screen for the wall elements.

Figure 4.2. Interior view of the ventilated facade, without any wall elements.

The primary work has revolved around the HVAC systems and their control, so a controlled indoor environment can be maintained. The process of designing and creating the HVAC setup was prolonged, which required adaptations to the original plan to ensure the inclusion of measurement data in this thesis. The consequences of this and the process of creating the climatic chamber are outlined in Appendix A and Appendix B.

4.1 Climatic chamber design

The insulated container measures 6.1 × 2.4 × 2.9 m (L × W × H), and one side of the container has been cut open to build the measurement setup. The container is insulated with 70 mm mineral insulation in the walls and ceiling with a U-value of $\approx 0.5 \frac{W}{m^2 \cdot K}$. The floor is insulated with 200 mm of thermoset polyisocyanurate (PIR) insulation, resulting in a U-value of $\approx 0.1 \frac{W}{m^2 \cdot K}$. The floor has a lower U-value in order to get a realistic heat loss to the crawlspace, which is further explained in section A.4. The measurement setup is facing north because this is deemed the most critical orientation with regards to moisture risk. This is because the north facade has

the lowest solar gain and lowest temperatures. Figure 4.3 shows the floor plan of the climatic chamber and the facade where the measurement setup for walls is built.

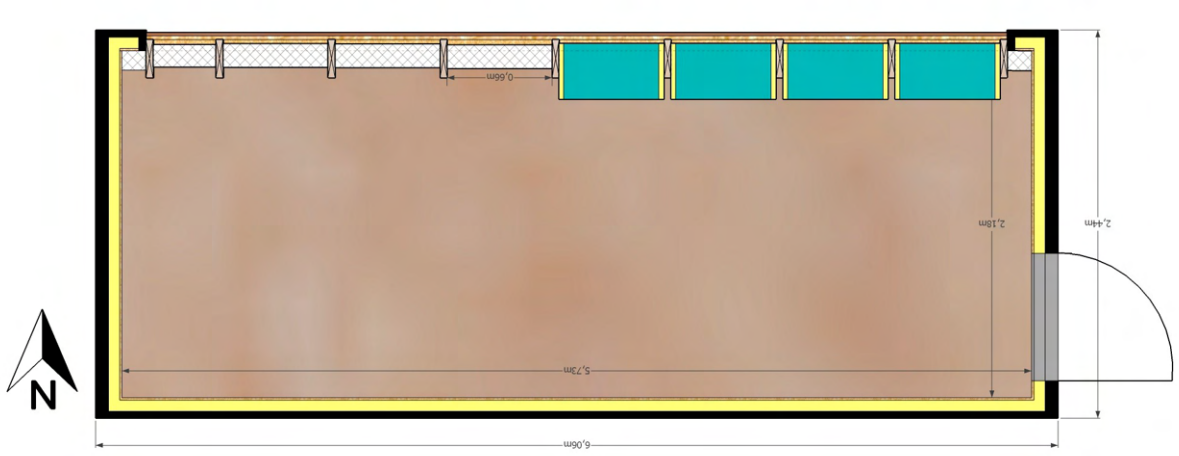

Figure 4.3. Floor plan and dimensions of the climatic chamber.

It is important that the setup is flexible and it is possible to continuously change wall elements. This is achieved by using a shared, ventilated facade to close the opening. This allows the wall elements to be constructed with only a wind barrier and to be swapped from the inside. The facade is mounted on timber studs that are spaced 660 mm apart, which aligns with current constructed wall elements. The inside of the facade is shown on Figure 4.2. The wall elements are further described in section 4.2 and Appendix C. The stud spacing can be adjusted to fit differently sized wall elements.

HVAC system specification and control

The HVAC systems are dimensioned after maintaining moisture class 3 inside the climatic chamber. Moisture class 3 is considered unlikely to occur in typical housing and is therefore used to stress-test the wall elements [6]. The aim is to design the systems to maintain a specific constant indoor air temperature and relative humidity. We have specified an accuracy goal of ±0.5℃ and ±3%. An overview of the systems, control signals, and measurement points in this project is shown on Figure 4.4. The sections below explain the designed systems and their controls.

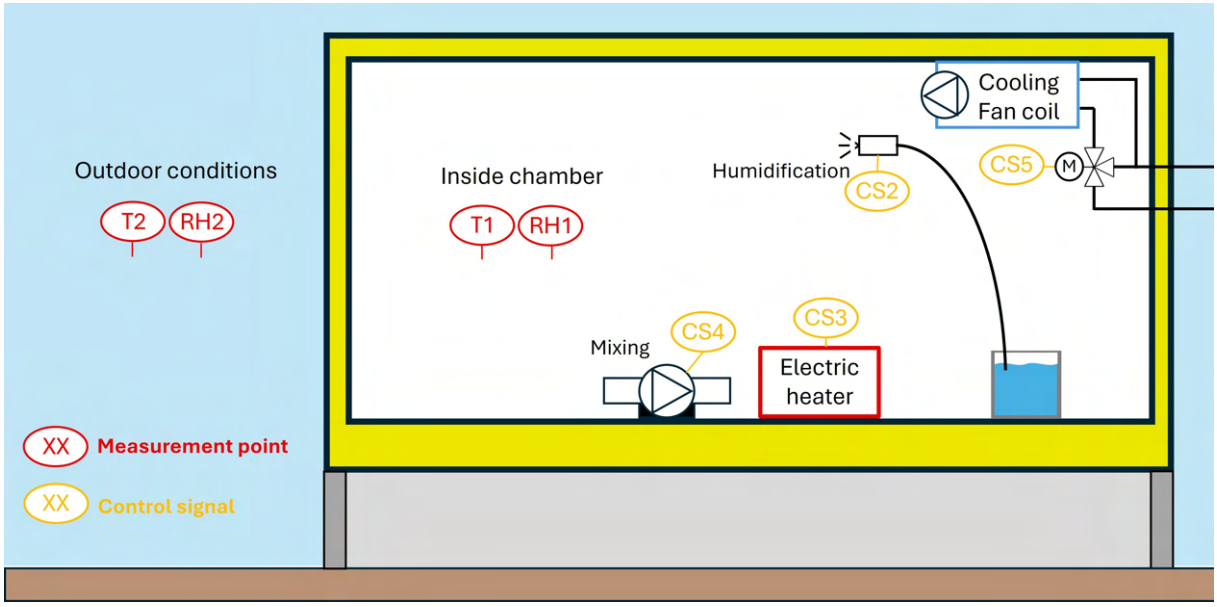

Figure 4.4. Overview of the systems used in the container setup. Only the systems used in this project are denoted.

4.1.1 Heating and cooling system and control

To determine the necessary outputs of the HVAC systems, the building simulation tool BSIM has been used, and the process is described in Appendix K. BSim is used to estimate the needed heating and cooling capacity, under the dynamic Danish weather conditions. We find that the heater must be capable of delivering at least 1350 watts, and the cooler at least 770 watts.

An electric radiator is used to compensate for the heat losses, with a maximum heat output of 3000 watts. The electric radiator allows for precise and rapid heat output regulation, allowing for accurate control. This makes it possible to stay within a narrow deadband around the setpoint. To get optimal control, a PI-controller is used and the heating output is continuously modulated. Inside of the container, next to the radiator, a fan is placed. This fan secures the mixing of the air in the room, while also making sure the radiator does not turn off due to overheating. The heating system can be seen on Figure 4.5.

Figure 4.5. Electric heater and mixing fan inside climatic chamber.

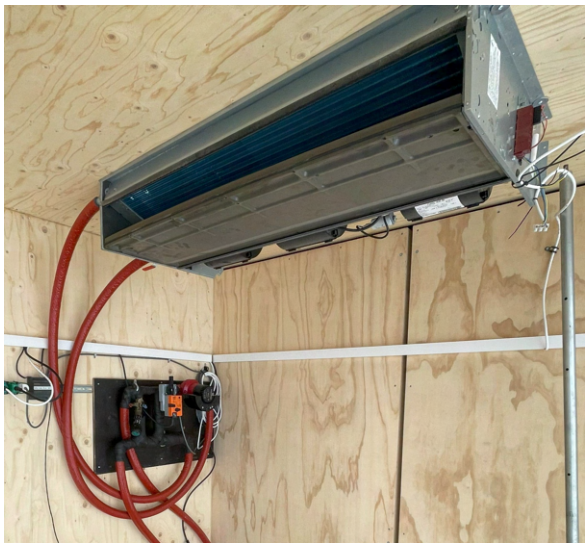

Figure 4.6. The cooling system, with the mixing loop mounted on the wall. The cooling power is adjusted with the motorized three-way valve.

For danish weather conditions, there will be some hours where the outdoor air temperature exceeds the specified indoor air temperature in the test container, and cooling is needed. The cooling system comprises three main components: an air-to-water heat pump, a three-way valve, and a fan coil unit. The heat pump, located outside the room, is set to always supply water at 15℃, and will have more than enough capacity. This chilled water feeds into a mixing loop that includes a three-way valve. The valve is controlled by a signal from the LabView program, operating within a 2–10V range. In this setup, control is applied in 1V increments to adjust the proportion of cold water directed to the fan coil. When the valve receives a 2V signal, the system recirculates water between the fan coil and the valve without introducing additional chilled water from the heat pump. The inside part of the cooling system can be seen on Figure 4.6. The fan delivers a constant airflow, regardless of the cooling output, and also ensures mixing.

The cooling output is modulated in steps in order to save energy and not have unnecessary heating. To ensure that the radiator has regulation authority, a constant cooling output is triggered when the control signal to the radiator is below 2 V. The heating control signal is then modulated so the constant temperature is maintained. If the heating output stabilises above 4 V while cooling is on, the cooling output decreases by one step. The cooling system has a cool-down period of 20 seconds, to ensure the cooling output stabilises before a change to the output is made. Therefore, no unnecessary changes are made, and it helps prevent oscillations in the control. Both of the systems are currently tuned aggressively, as this was the only tuning

where we succeeded in keeping the temperature within ±1°C. The tuning of the systems can be optimized further to decrease the energy consumption.

It was tested if a more simple combined heating and cooling setup with an air-to-air heat pump was possible. It proved not to be an option, as it was not possible to control it properly and fulfil our accuracy requirements.

4.1.2 Humidification system and control

The climatic chamber is equipped with a humidifier, which allows control of the moisture load. This system consists of a water mist nozzle, an integrated water pressure unit, and a storage tank. The nozzle is positioned to spray mist directly into the airstream exiting the fan coil. The control of the humidifier checks the relative humidity, and if the value is below the setpoint, the nozzle sprays for 5 seconds followed by a 30-second cooldown period. This allows the water mist to properly mix in the air. After the cool-down period, the humidity is reassessed, and additional mist is added if necessary. The humidification spray nozzle can be seen on Figure 4.7.

Figure 4.7. Humidification system with water mist nozzle, placed in front of the airstream from the fan coil.

A control system for dehumidification is also designed, but is currently not implemented. At the time of the measurement, there is, however, no need for dehumidification.

4.1.3 Control program and system performance

The described controls are coded into one LabView program that handles the interplay between the systems. The control system is a modification of the LabView program developed by Hicham Johra for the large guarded hot box at the Building Material Characterization Laboratory of Aalborg University [29]. The control program is configured with one DewMaster box, which has 10 Sensirion SHT-sensors that measure the process variables, temperature and relative humidity. A DewMaster box, describes an Arduino with 10 SHT-sensors and is shown on Figure 4.8.

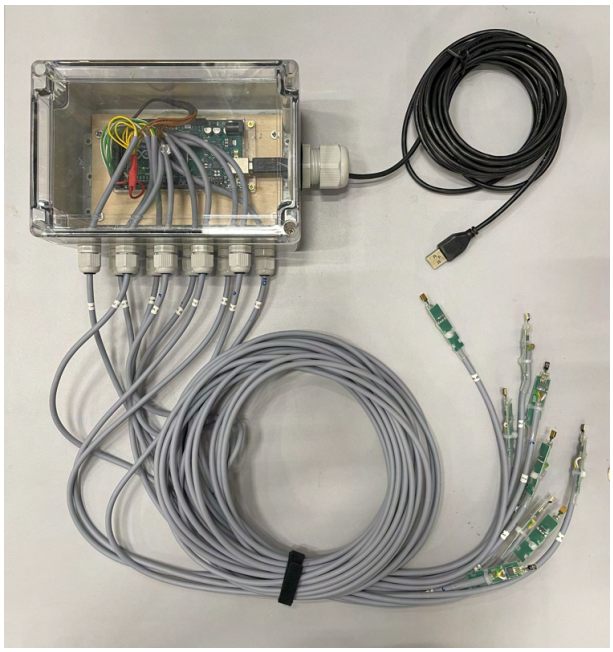

Figure 4.8. Picture of a DewMaster box, with its 10 SHT sensors, measuring temperature and relative humidity.

For the control program, the indoor conditions are the average of four sensors inside the chamber. DewMaster boxes and sensors are also used for data acquisition in the wall elements and are further described in section 4.2 and Appendix D.

The ten sensors inside the chamber, have been utilized to evaluate the mixing of air and document how well the setup maintains an evenly distributed temperature and relative humidity. Appendix A section A.5 describes the analysis, in which it is concluded that the setup achieves a well-mixed indoor environment and an even indoor boundary condition for wall elements. The indoor boundary condition is, however, not stable during the measurement period, which will be covered presented in chapter 5, and is further elaborated on Appendix F and Appendix B.

4.2 Biobased wall elements

Creating this experimental setup allows for an exploratory investigation of various bio-based wall elements, making it preferable to have many variation possibilities. For this reason, the elements are scaled to be small, so the setup can fit many elements. The wall elements used in this measurement setup measure 600mm · 600mm and are built identically, with only variations in insulation and vapor barrier. Figure 4.9 shows the composition of the wall elements. As mentioned, the wall elements share a common exterior cladding.

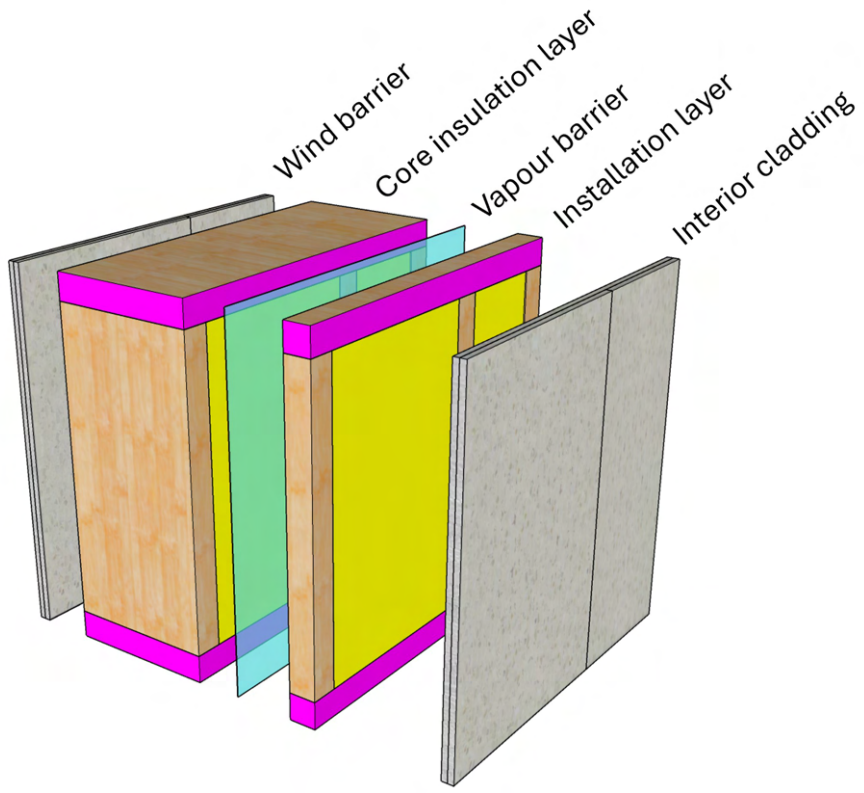

Figure 4.9. The composition of the wall elements, with its five layers.

The wall elements are built as a light-wall construction and have an included timber stud inside the wall. The insulation makes up most of a wall by volume, and we want to investigate how the hygroscopic properties of the biobased insulation influence the moisture conditions inside the wall. To evaluate this, the temperature and relative humidity are measured throughout the wall. In each element, there is one measurement column in the middle of the insulation and one along the timber stud. Figure 4.10 shows a section drawing of the elements, with the placement of the two measurement columns.

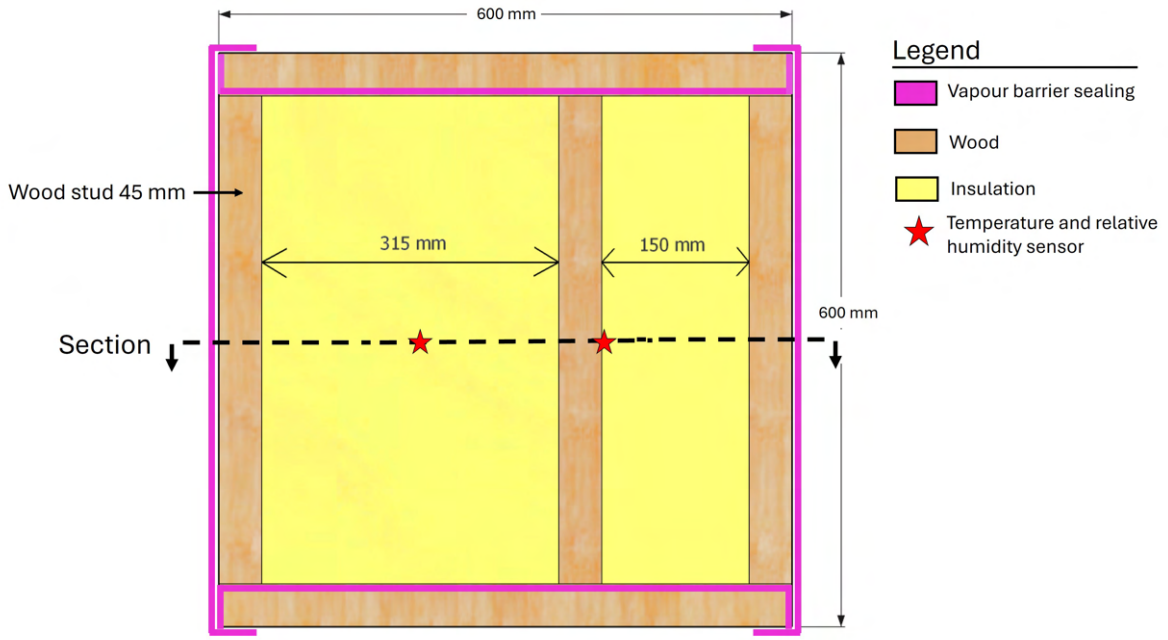

Figure 4.10. Front view drawing of core insulation in the wall elements.

For the measurements, it is important to ensure that there is one-dimensional (1D) heat and moisture transfer through the element. The goal is to measure the isolated performance of the insulation and eliminate the influence from the boundary. This is also needed in order to use the measurements for comparison with numerical 1D hygrothermal simulations done with WUFI and BSim. To balance the need to make the elements small, achieve 1D heat and moisture transfer, ensure buildability, and maintain some realism, the element dimensions have been determined to be 600 mm by 600 mm. With this dimension, the climatic chamber can hold 21 different wall elements. Using COMSOL Multiphysics, an analysis of the heat transfer in the elements is made to verify that 1D heat transfer is obtained for the two measurement columns. The model and the result can be seen in Figure 4.11.

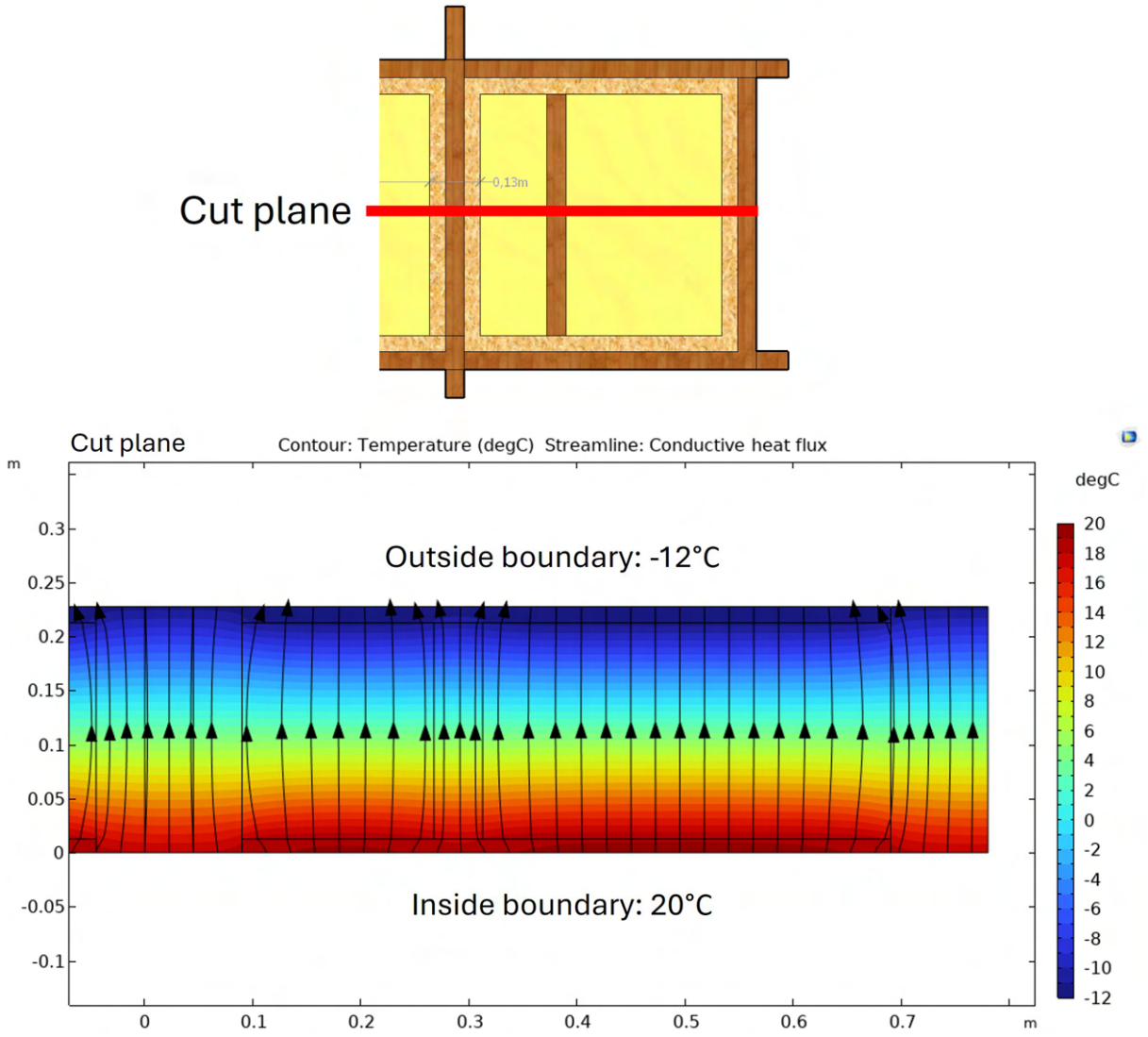

Figure 4.11. Verification of 1D heat transfer in our two measurement columns in elements sized 600 mm by 600 mm.

The streamlines for the heat flux and the temperature throughout a cut plane in the model are shown in Figure 4.11. It is seen that there is a 1-D heat flux on both sides of the timber stud and that temperature and relative humidity both in the insulation in the middle of the element and close to the vertical timber stud can be measured. Figure 4.10 shows that a high resistance vapour barrier ($Z > 400$) is mounted around the element, to avoid moisture transport through the sides of the element. This is to ensure moisture transport from the inside to the outside through the element. The vapour barrier is on the inside in the top and bottom, which yields a wood percentage around 20%. For light walls, the insulation layer is inhomogeneous with wood studs every 600 mm, by standard. Additional wood framing is added during window installation, so the wood percentage ends up being in the range of 10-20% commonly. For the sides, the placement

of the vapour barrier on the outside allows for only one penetration for the sensor cables, which needs to be sealed. This minimizes the risk of potential leaks and errors during the construction of the elements. Photographs of the construction process, sensor placement and element sealing are presented in Appendix C, section C.4 and C.5.

4.3 Measurement setup

There are 10 sensors for each element, where one is placed in front of the elements in the ventilated cavity. The sensors are digital Sensirion SHT85 humidity and temperature sensors. The sensors are known for high reliability, long-term stability and have a high precision [30]. Figure 4.12 shows the sensor placement and naming.

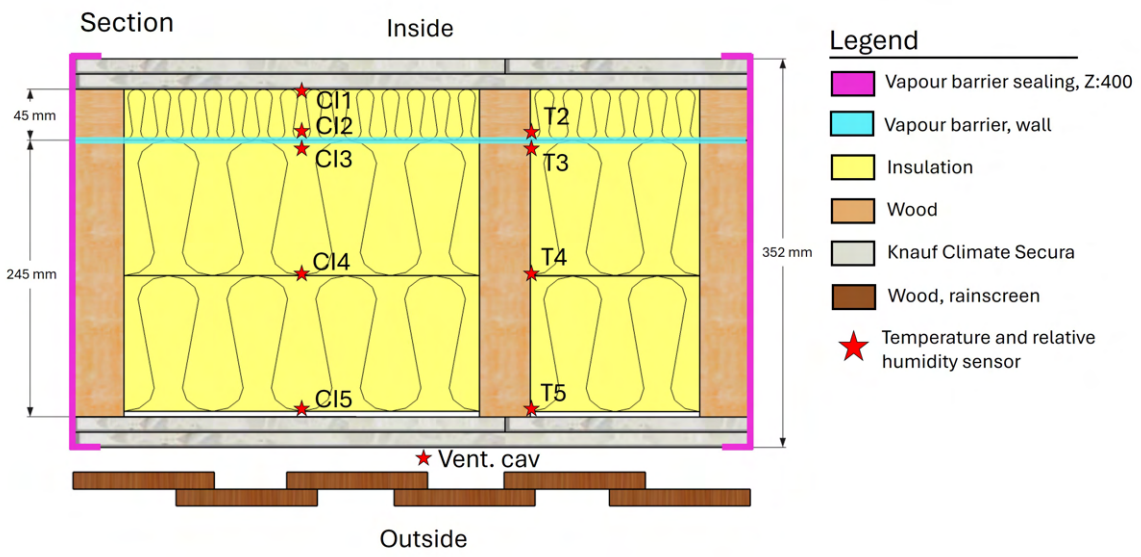

Figure 4.12. Placement of the Dewmaster sensors for the elements.

The ten sensors ensure measurements at all critical points inside the wall. The sensors are wired, which allows for long-term measurements without any power issues. The SHT85 sensors are relatively small, which is important, as they do not take up significant space inside the walls. The sensor is mounted in a connector on a small circuit board and measures in total approx. L:50 mm, W:10 mm, H:5 mm. This is shown on Figure 4.14.

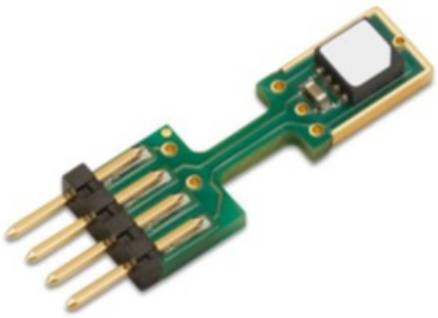

Figure 4.13. SHT85 sensor photo from datasheet. [30]

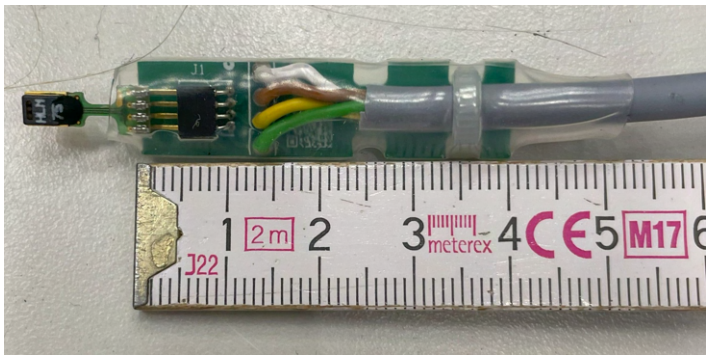

Figure 4.14. SHT85-sensor, mounted on the connector circuit board. L:50 mm, W:10 mm, H:5 mm.

The 10 sensors are connected to an Arduino, which is used for data acquisition and interface with the sensors. A box with 10 sensors and an Arduino will be referred to as a DewMaster box. 24 DewMaster boxes have been built, which allows 21 wall elements. However, at the moment, only eight of the boxes are in use — seven for the wall elements and one for HVAC control system. To further process the measurements and log them, the Arduino is connected to a computer, with LabView. For an in-depth explanation refer to Appendix D.

From the data sheets, the relevant specifications for the sensor are stated in table Table 4.1. Some of the parameters vary depending on the operating conditions, so for simplicity, the worst performance within the operating range is stated. For more details, refer to Appendix E and the data sheet. The operating range is from -15℃ to 30℃ and from 35% RH to 95% RH, which is further explained in section 2.2 and section 4.1.

Table 4.1. Specifications for temperature and humidity sensors SHT85 [30]. The typical accuracy limits are true for up to $\mu \pm 2\sigma$ of sensors in an ensemble and the maximal accuracy limits for $\mu \pm 4\sigma$. Here μ is the average and σ is the standard deviation.

Humidity specifications

Parameter	Unit	SHT85
Typ. accuracy	%RH	±1,5 @0-80%RH
Max. accuracy	%RH	±2,75 @5-95%RH
Typ. resolution	%RH	0,01
Typ. repeatability	%RH	±0,21
Hysteresis	%RH	±0,8
Operating range	%RH	$0 - 100$
Recommend normal range	%RH	$20 - 80$
Response time τ63%	s	8
Long term drift	%RH/yr	<0,25

Temperature specifications

Parameter	Unit	SHT85
Typ. accuracy	℃	±0,1 @20-50℃
Max. accuracy	℃	±0,25 @-20-40℃
Typ. resolution	℃	0,01
Typ. repeatability	℃	±0,15
Operating range	℃	$-40 - 105$
Recommend normal range	℃	$5 - 60$
Response time τ63%	s	>2
Long term drift	℃/yr	<0,03

The performance of the sensors stated in the data sheet, and potential drift have been verified. They did not comply with the stated specification and a calibration was necessary. There is a detailed description of the calibration process in Appendix E. The calibration is done using 15 measurement points to cover the expected range of temperatures and humidities. The calibration functions are found using multiple linear regression because the corrected temperature and humidity showed to be dependent both on the measured temperature and humidity. The calibration functions are found in Appendix X. The functions are directly written into the LabView program that logs the measurements. The calibration is evaluated at three calibration check points for 10 out of the 80 SHT85 sensors. The conclusion of the calibration check is that the evaluated sensors comply with an accuracy of ±0.2℃ and ±3%RH.

4.4 Experimental setup and process

Measurements are conducted on seven different wall elements. Figure 4.15 provides an overview of elements, stating the insulation type, vapor barrier type, and abbreviation used for the element.

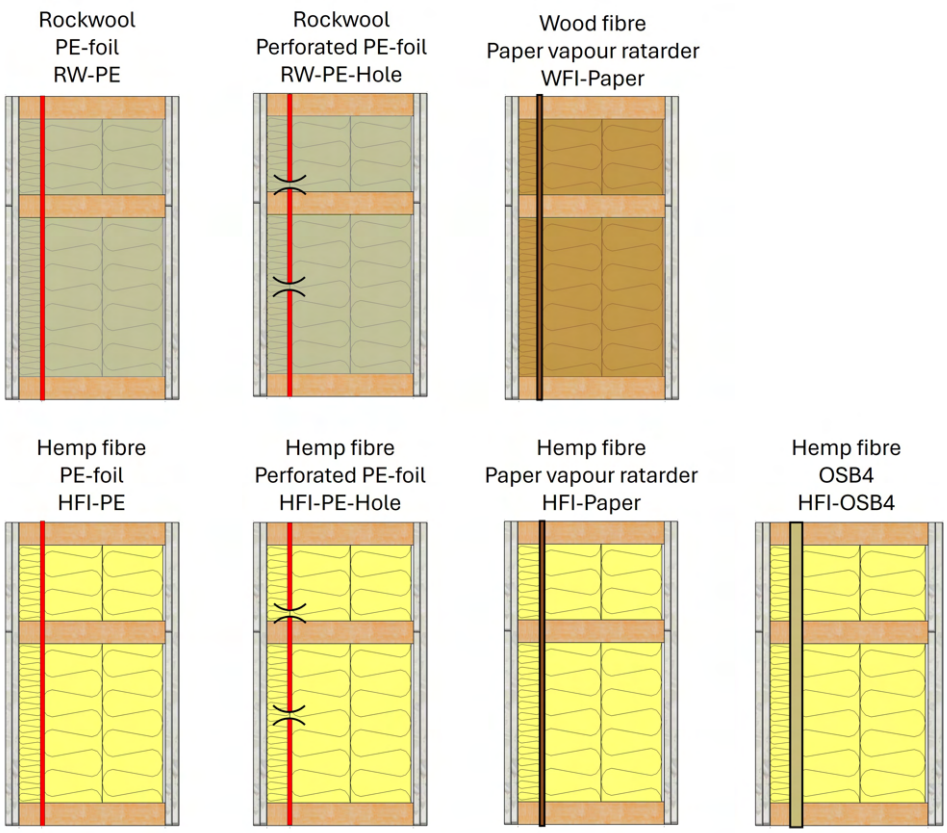

Figure 4.15. The seven wall elements, with their differences in insulation and vapour barrier. The elements are seen top-down.

The element with RockWool is used as a baseline reference. Several measurements are done on Rockwool, and it is known that mineral wool has little hygroscopic properties [31]. This element enables comparison and evaluation of the impact of using hygroscopic biobased insulation. This element can be compared to the element with hemp fiber insulation and also a PE vapour barrier. Both of these elements are also made in a variation, where the PE-foil is perforated. The vapour barrier is perforated with two one-centimetre holes, and this is done to investigate the consequences of a degraded water vapour barrier and how a wall with mineral- and biobased insulation responds.

Two elements feature a paper vapor barrier with respectively wood fiber and hemp fiber insulation. The permeability of the paper vapor barrier is a lot higher than the PE-foil, and allows more moisture diffusion. This setup is used to investigate how the biobased insulation responds in a more permeable construction. Lastly, another wall element is made with hemp fiber insulation, but an OSB4 board as a vapor barrier, which is even more permeable. These configurations with hemp fiber and three different vapor barriers, enables comparison and assessment of the impact

of the different vapor barriers. Figure 4.16 show the measurement setup with the wall elements in place.

Figure 4.16. Interior view of measurement setup with wall elements.

The wall elements are installed from the inside, with a distance of 25 mm to the surface of the furring strips holding the ventilated facade. This is to ensure airflow in the ventilated cavity, where the narrowest point is 25 mm, but it is generally 50 mm wide. There is an opening of 20 mm in the top and bottom of the facade cladding for ventilation. There are 75 mm EPS insulation (Sundolitt S60, $\lambda_D = 0{,}041 W/mK$) between the elements and 30 mm mineral insulation on the sides. The sides are filled with mineral insulation due to its compressibility, which makes the installation possible. This also makes it easy to draw the sensor cables along the element sides. For the current configuration, the unused space is filled with EPS insulation. In this installation, the elements are stacked on top of each other, making it challenging to change an element without affecting the others. To be able to change elements continuously and independently, a flexible mounting system is needed. This is not devised yet, but an idea is to have shelves the elements

are placed on. This idea needs further refinement, as this will impose challenges with placing the elements in the shelves and insulating the sides. The process of installing the wall elements is described in detail in subsection A.2.1.

The elements were built earlier and stored before the experiment was started. At the time of construction, samples of the used materials were taken and stored together with the wall elements. At the moment the experiment was started, the material samples were weighed and hereafter dried in order to determine their moisture content. This is to determine the initial water content in the materials, so the correct initial conditions can be used in the numerical models. Due to delays in the project, the experiment was started before all of the designed systems were in place and tuned. The indoor conditions have not been kept stable for most of the measurement period and not corresponding to moisture class three. The storage history and key events during the experiment are described in Appendix B.

4.4.1 Material properties

Table 4.2 provides a brief description of the materials used in the wall elements.

Interiour cladding and wind barrier	**Short name**	**Description**
Knauf Clima Secura board	Gypsum	Fibreglass reinforced windproof fire protection board. Used as a windproof and vapour permeable wind barrier. A2-s1, d0 (B1). $K_1$10.
Insulation types	**Short name**	**Description**
Rockwool A-batts 37	RW	Traditional mineral based insulation, with low to no moisture dynamics. Used as a reference.
Hunton Woodfiber Nativo	WFI	Widely used biobased insulation.
Ekolution Hempfiber	HFI	Fast growing plant, that can be an alternative to wood fiber insulation.
Vapour barrier types	**Short name**	**Description**
PE-foil Raw PRO Standard	PE	Standard very tight vapour barrier
Økønatur paper vapour retarder	Paper	Barrier that allow more moisture diffusion.
NPI Egger OSB-4 Top Tg-4	OSB4	Board based vapour barrier, that is even more open to water vapour diffusion.

Table 4.2. Description of materials used in wall elements

Table 4.3 and Table 4.4 present the material properties found in the data sheets of the wall components. We are using the Knauf Clima Secura board on the inside and outside due to its

high fire classification, which is needed because of the low fire classification of biobased insulation.

Table 4.3. Table with material characteristics of the insulation from manufacturer data sheets.

	Unit	RW [32]	HFI [33]	WFI [34]
Thickness's	[mm]	45, 95, 145	45, 120	45, 120
Density	$[kg/m^3]$	30	35±5	50 (44,2-59,8)
Thermal conductivity, λ	$[W/(m \cdot K)]$	0.037	0.04	0.038
Specific heat capacity, C_p	$[J/(kg \cdot K)]$	1030[1]	2300	2100[2]
Reaction to fire	[-]	A1	D-s1, d0	E
Water Vapour resistance factor, μ	[-]	-	2.3 (dry)	5/3 (dry/wet)

[1] This is from [35]
[2] This is from [36]

Table 4.4. Table with material characteristics for vapour barriers and wind barrier from the manufacturer data sheets.

	Unit	Gypsum [37]	PE [38]	Paper [39]	OSBB4 [40]
Thickness	[mm]	15.5	0.2	0.25	15
Density	$[kg/m^3]$	774	920	700	>620
Thermal conductivity, λ	$[W/(m \cdot K)]$	0.25	-	-	-
Specific heat capacity, C_p	$[J/(kg \cdot K)]$	-	-	-	-
Reaction to fire	[-]	A2-s1,d0 (B1)	F	E	D-S2,d0
Water Vapour resistance, Z-value	$(GPa \cdot m^2 \cdot s)/kg$	0.48	>400	32.25	15 (wet)

With the different material properties and wall variations, Table 4.5 provides an overview of the U-values and Z-value ratios for the elements.

Table 4.5. Overview of general element characteristics and differences. *Z-value ratio without perforation.

Element	Thickness [mm]	U-value $[W/(m^2 \cdot K)]$	Wind barrier / Vapour barrier Z-value ratio
RW-PE	352	0.123	1/416
RW-PE-Hole	352	0.123	1/416*
HFI-PE	352	0.133	1/416
HFI-PE-Hole	352	0.133	1/416*
HFI-Paper	352	0.133	1/33
HFI-OSB4	367	0.130	1/15
WFI-Paper	352	0.126	1/15

Chapter 5

Analysis of experiment results

The moisture transfer is influenced by the prior exposure of the elements, making it essential to consider the full measurement period, as illustrated in Figure 5.1.

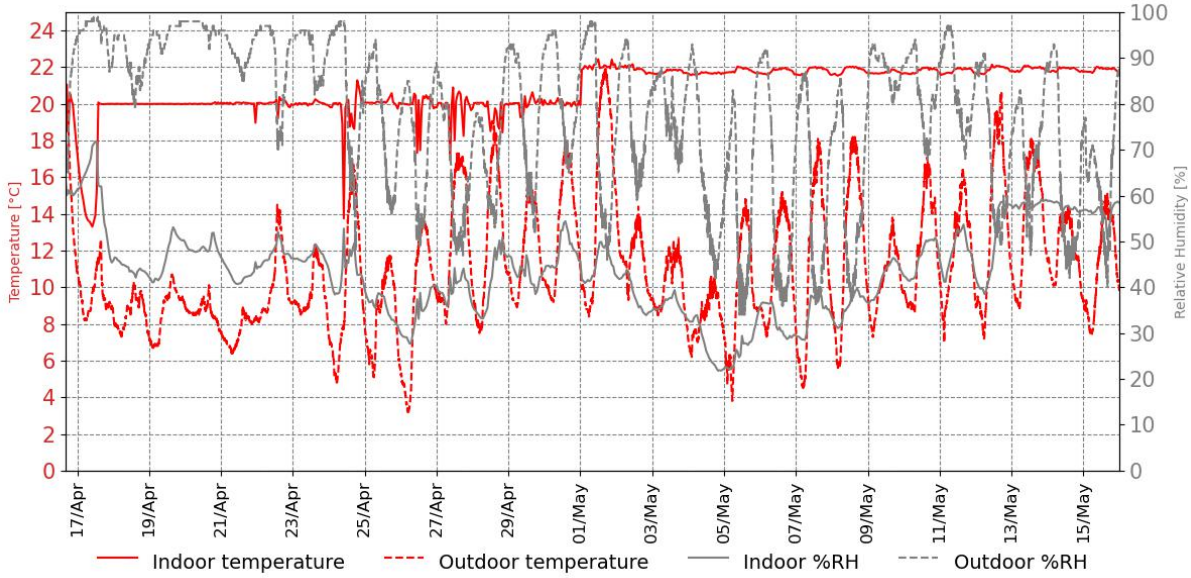

Figure 5.1. The indoor and outdoor conditions for the measurement period.

As mentioned in Appendix F, the indoor conditions have not been stable during the measurement period. This results in two distinct measurement phases. One where the humidifier is not integrated, and one after. The first part can be used to see the elements' reaction to temperature, while the second is used to see the impact of a constant moisture load. This is further described in Appendix G. Due to moisture transfer being slow, and the humidifier being integrated late in the measurement period, it is not expected to see significant differences in the elements.

5.1 Analysis of the elements

The vapor pressure throughout the elements is examined for two different timestamps. The first is before the humidifier was integrated into the setup. The profile can be seen on Figure 5.2.

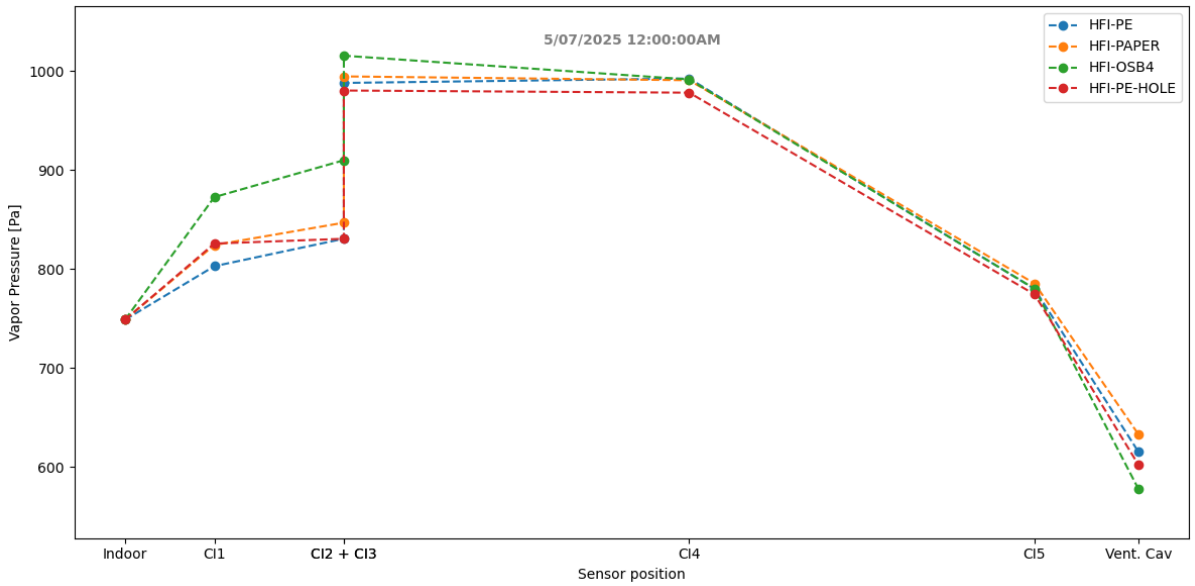

Figure 5.2. Vapor pressure profile for May 7th.

From the vapor pressure, it is observed that the moisture flows from the vapor barrier and outwards. The graph shows the four different elements with HFI and different vapor barriers. The most noticeable difference is the OSB4 element which, on the warm side of the barrier, has a higher vapor pressure. This is due to the OSB4 being the most permeable vapor barrier in this measurement setup. The difference in the ventilated cavity is caused by the position of the element, which is addressed in section F.1.

The measurements are supposed to be made with moisture class three inside of the chamber. Therefore, the vapor pressure after these conditions are upheld is examined on Figure 5.3.

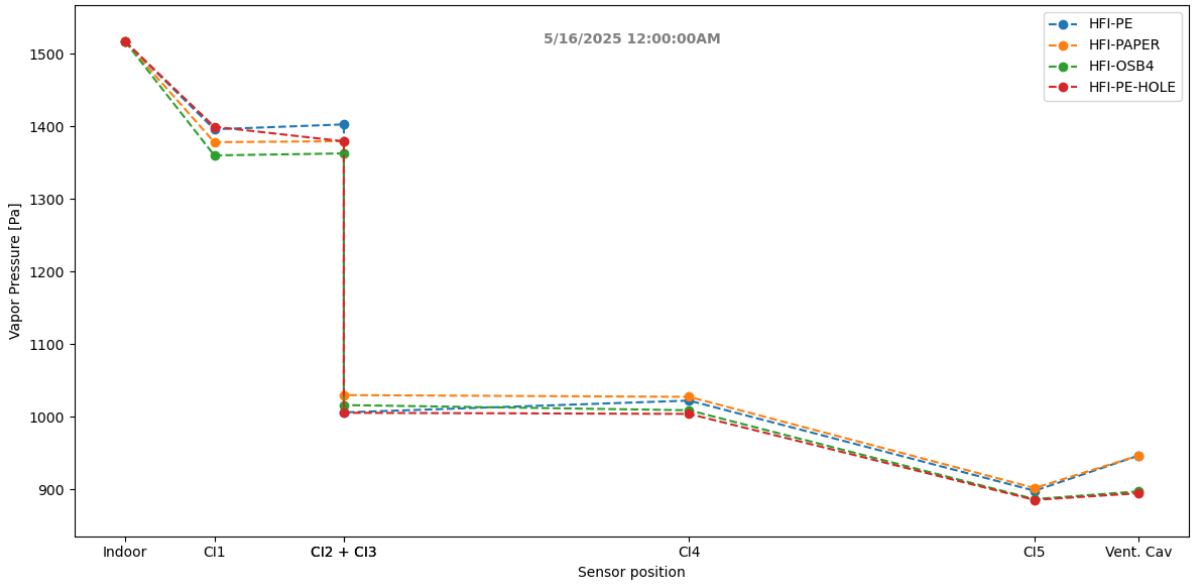

Figure 5.3. Vapor pressure profile for May 16th.

It can clearly be seen that the stabilized indoor conditions result in a moisture transfer from indoors to outdoors. This is due to a higher vapor pressure on the warm side of the vapor barrier, as the pressure on the cold side does not change. Interestingly, while the vapor pressure changes over the vapor barrier, the difference between the elements is not significant as before the humidifier. This indicates that under consistent indoor RH, the barrier type is less influential or that the elements have not had enough time to show the influence.

Additionally, the three different insulation materials are examined on Figure 5.4.

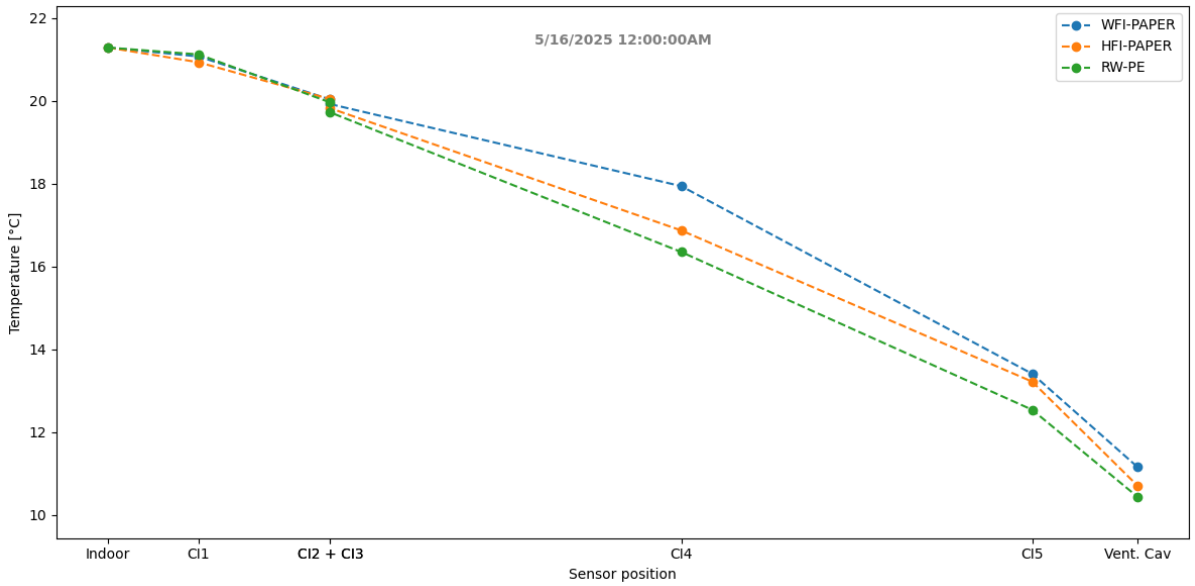

Figure 5.4. Temperature profile for May 16th.

The temperature profiles vary from the expected. Although RW has the lowest thermal conductivity, the profile shows the lowest temperatures. This result is likely influenced by the dynamic conditions in the setup. WFI and HFI possess a higher heat capacity and, being biobased, a higher moisture buffering ability, which dampens the temperature changes. From section 3.1, it is seen that WFI has a larger moisture capacity than HFI, while RW , being hydrophobic, has an even smaller moisture capacity. These observations confirm that the thermal conductivity is not enough to describe the temperature profiles for the elements.

5.2 Comparison of measurements with WUFI

With numerical simulation, we can apply our short period of measurement data and assess the future development of the conditions in the walls. As established, it is difficult to determine differences between the wall elements in our short time frame. We have however only modelled the WFI element, with the paper vapour barrier, and made simulations using WUFI [31]. Hereby we can compare our measurements with the simulations and estimate the time before the conditions should stabilise in the element. Details about the simulation are found in Appendix H and Appendix J. The model conditions will however be described briefly.

5.2.1 Model conditions

To ensure comparability between our measurements and the simulation, it is crucial that the same boundary conditions are used. We have obtained the same boundary conditions by directly applying the measurements of the indoor environment and in the ventilated cavity in WUFI. Figure 5.5 shows the full model geometry of our wall element, but this is modified to be as shown on Figure 5.6 We have removed the ventilated cavity, to apply the boundary condition of the measurements in the ventilated cavity.

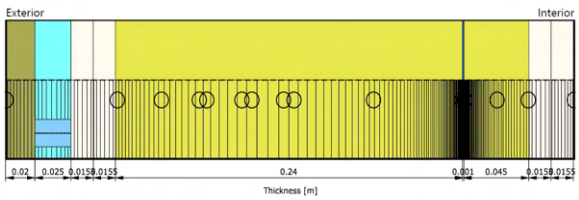

Figure 5.5. WUFI model geometry for woodfiber wall element construction. Outside to the left and inside to the right.

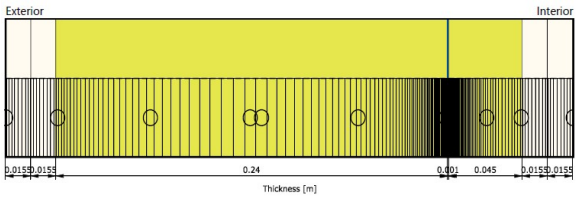

Figure 5.6. WUFI model geometry, used for comparison of model and measurements. Outside to the left and inside to the right.

Because the boundary is the ventilated cavity, weather factors can be neglected, as they should

be reflected in the temperature and humidity in the ventilated cavity. For the timestamps after the measurements, the indoor conditions are set to moisture class three, as stated in [6]. For the outdoor boundary, we use simulated values for the conditions in the ventilated cavity, from simulation on the full wall assembly, with HRY-Ref2 as weather file [41]. Our measured values in the ventilated cavity and simulated values from the same period are shown in Figure 5.7 and Figure 5.7, and are in good agreement.

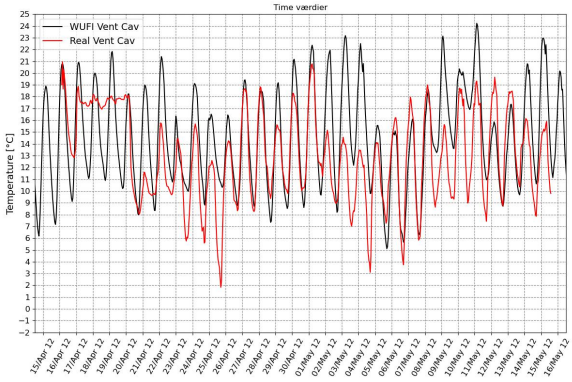

Figure 5.7. Temperature inside ventilated cavity. The red line is measured values, and the y-axis goes from -2°C to 25°C. Larger version is found in Appendix J.

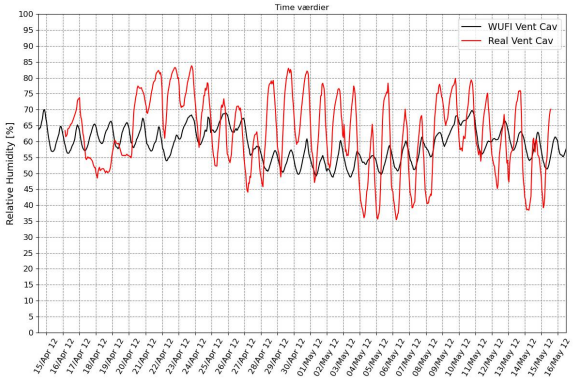

Figure 5.8. Relative humidity inside ventilated cavity. The red line is measured values, and the y-axis goes from 0% to 100%. Larger version is found in Appendix J.

As initial conditions, the measurements of moisture content in the materials have been used and matched the temperature of the materials to the measured values. Moisture content is described in Appendix R.

Besides the initial and boundary conditions, it is important that the material properties are representative. Our approach to using the best property values is described in Appendix I. We made use of our measured moisture sorption curve for WFI and naturally applied it in WUFI. WUFI does however not account for hysteresis, but uses one sorption curve. Therefore an average curve of our measurements is used. The measured absorption and desorption curve from 10 to 90% RH, and the applied average is shown on Figure 5.9.

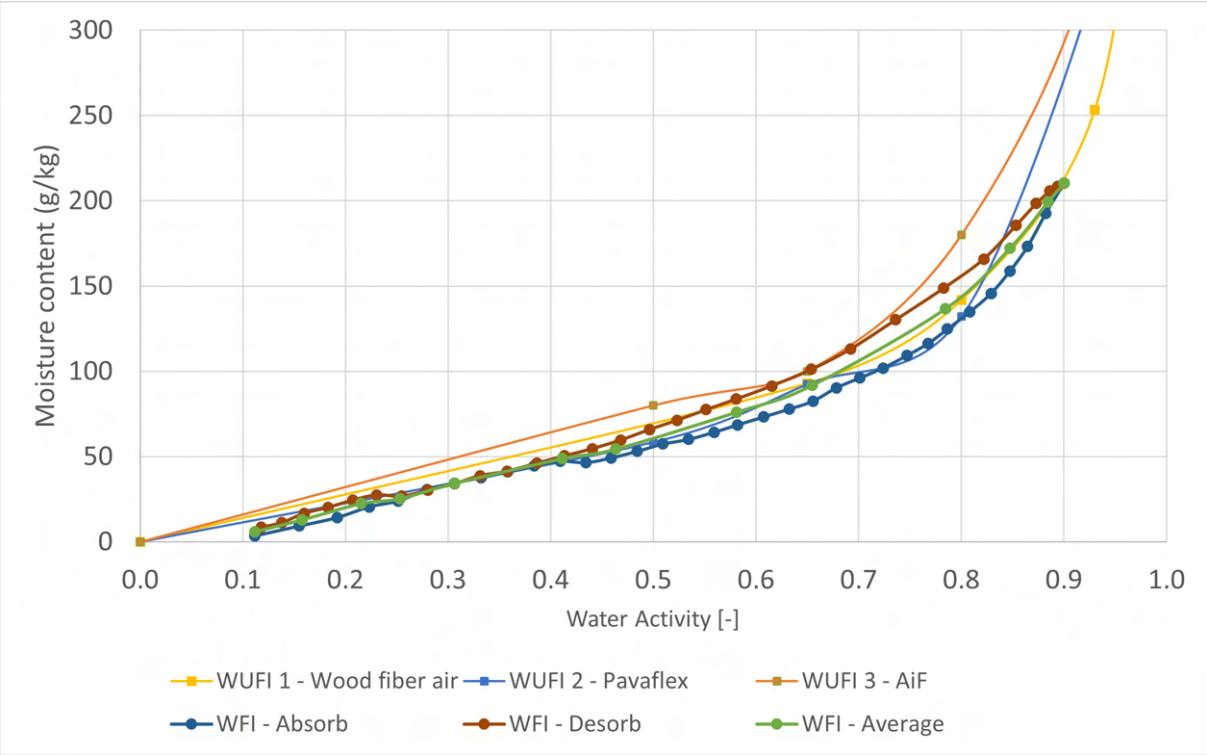

Figure 5.9. The difference in relative humidity between the first simulation year, and the second year. The difference is calculated between the measurement and simulation results, and also only between the simulation results.

Figure 5.9 show the sorption curve for three similar WFI products in WUFI, and it is clear there is a similar tendency to our measurements. Besides the measurements of moisture sorption, we did a supplementary investigation of a faster way to estimate the water vapour permeability. The water vapour permeability is a key material property to know for accurate simulations. Our investigation is covered in Appendix T.

5.2.2 Simulation results

The measurements from the WFI-PAPER element are compared with a WUFI-simulation. The comparison is made at two critical points: behind the wind barrier and on the warm side of the vapour barrier. Furthermore, the middle of the insulation is also investigated. The first critical point is seen in Figure 5.10.

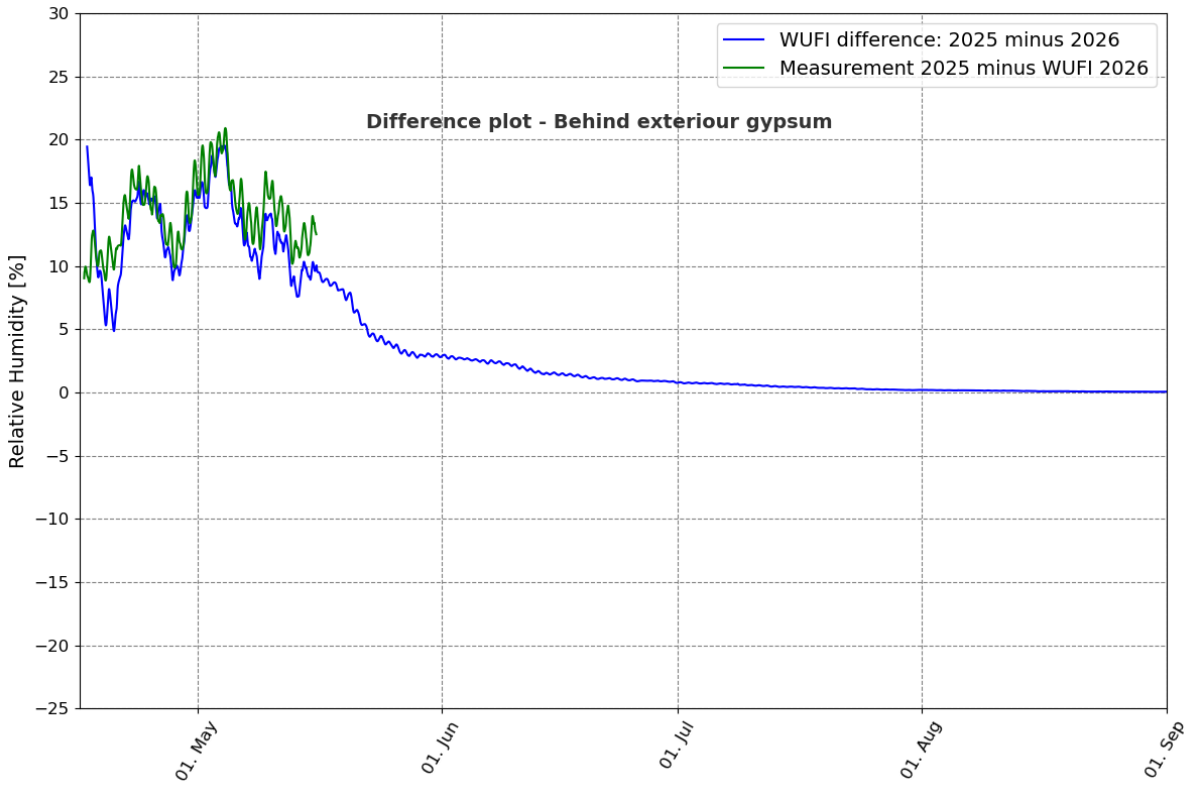

Figure 5.10. The difference in relative humidity between the first simulation year, and the second year. The difference is calculated between the measurement and simulation results, and also only between the simulation results.

Figure 5.10 show the time before the conditions stabilize inside the wall. It can be seen that the difference between the first and second year is gone after 4 months. At this time, the effects from the initial moisture content are expected to be gone.

There is a difference in the initial RH. This is due to the process of finding the RH. For the simulation, the moisture content of each material is found, and then WUFI converts it to the corresponding RH with the material's moisture isotherm. The initial temperatures are taken from the measurements. The measurements are slightly higher than the model, but they show the same tendencies in this measurement position. The same examination is made for the middle of the core insulation and seen on Figure 5.11.

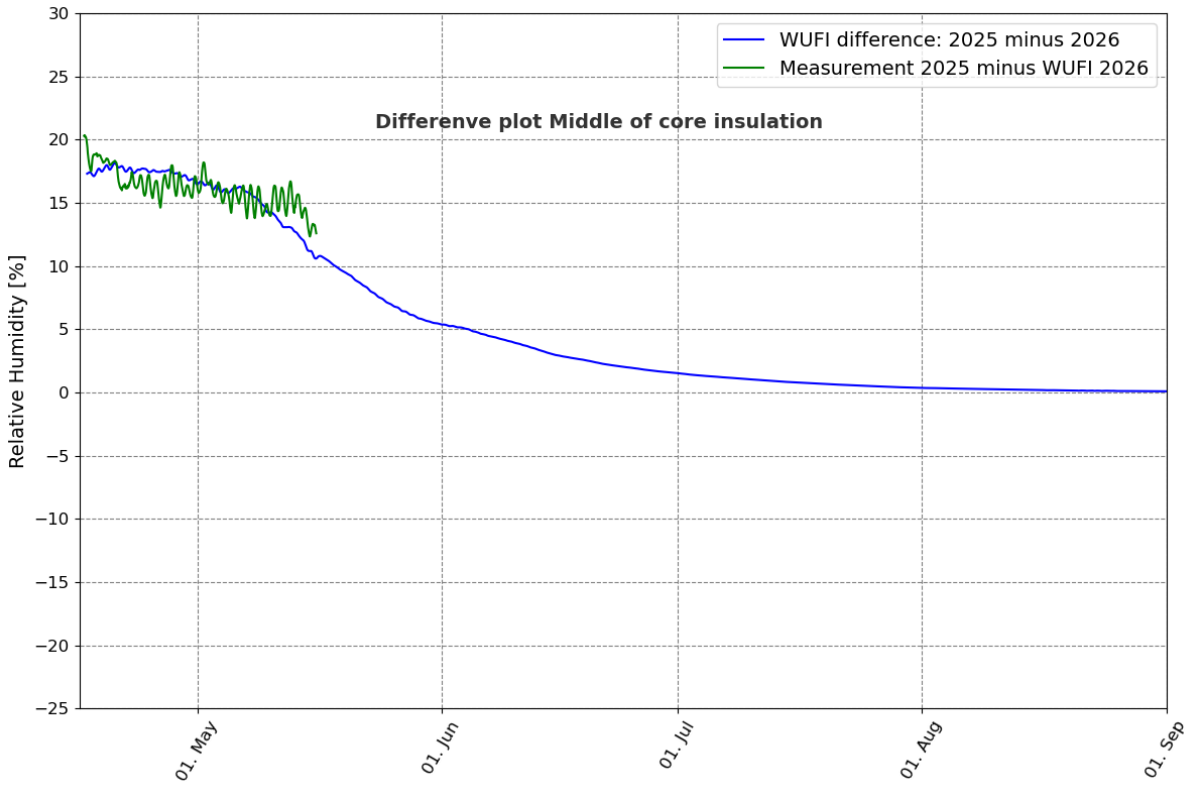

Figure 5.11. The difference in relative humidity between the first simulation year, and the second year. The difference calculated between the measurement and simulation results, and also only between the simulation results.

Similar to the position before the exterior gypsum, the model stabilises after 4 months. For the middle of the insulation, it is seen that the simulation is more stable than the measurements, however the values are comparable. The final point of interest is on the warm side of the vapor barrier, shown on Figure 5.12.

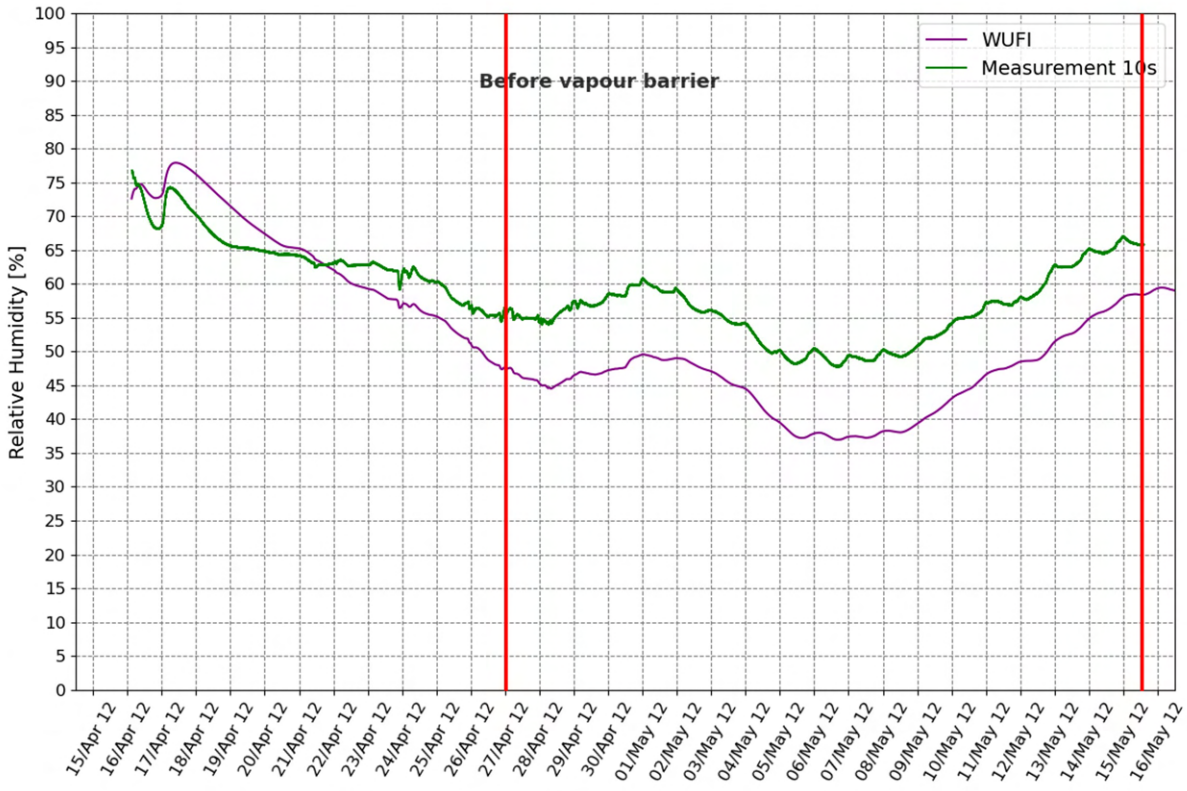

Figure 5.12. Comparison of simulated and measured values of relative humidity on the warm side of the vapour barrier. The red lines marks the time for the profiles in Figure 5.13 and Figure 5.14

On the warm side of the vapor barrier, an offset occurs after April 23rd, stabilizing at 10% RH on April 27th. Despite this offset, the simulation and measurements show the same trends.

Additionally, two profiles from the WUFI-simulation is compared to the measurements. The first profile is early in the measurement period, before the humidifier and is shown on Figure 5.13.

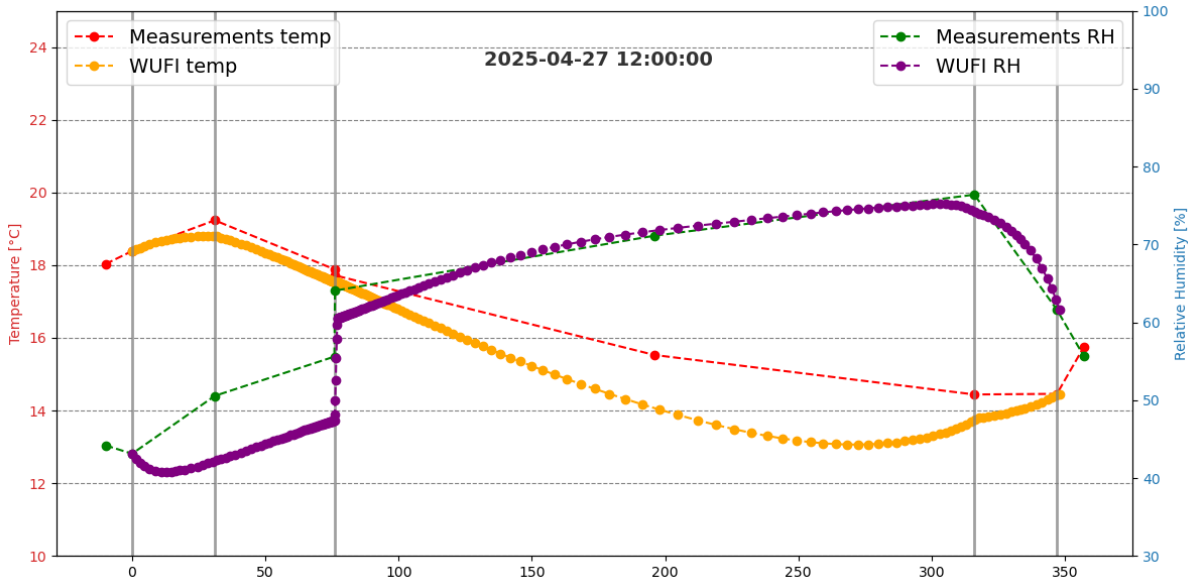

Figure 5.13. Temperature and relative humidity profile, through wall. Comparison of simulated and measured values.

The first profile shows that the WUFI-simulation and measurements do not align. Interestingly, on the warm side of the vapor barrier, the temperature matches, while the RH does not. On the cold side, it is the opposite, where the RH matches, but the temperature does not. The second profile is, after the humidifier and at the end of the measurement period. The profile is shown in Figure 5.14.

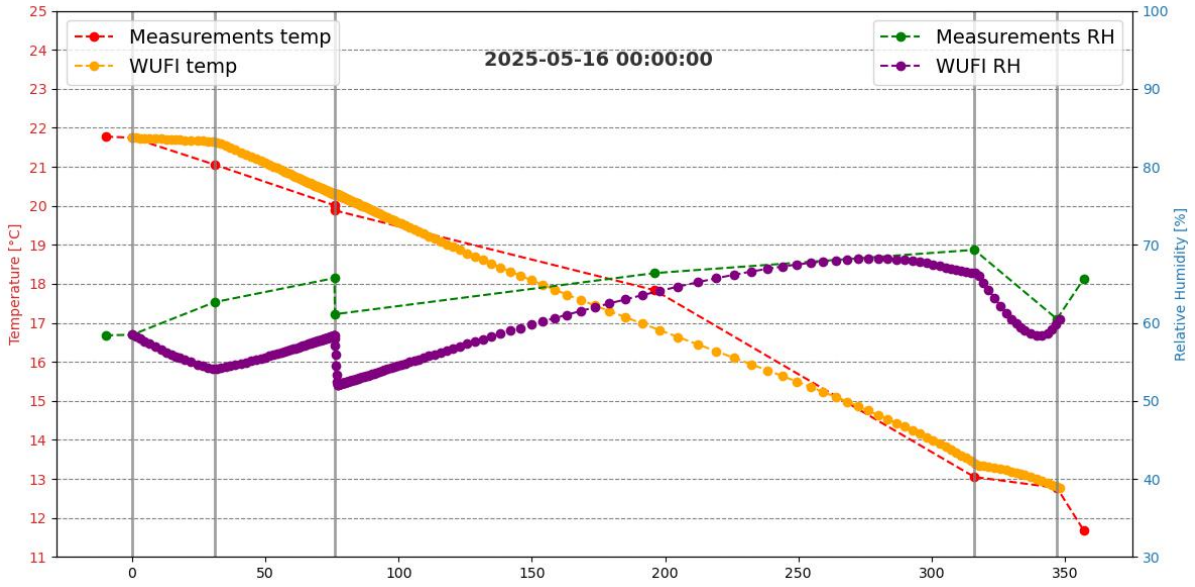

Figure 5.14. Temperature and relative humidity profile, through wall. Comparison of simulated and measured values.

From the second profile, it is seen that the temperature is more aligned throughout. On the other hand, the RH varies more than before. This might be due to the simulations being made with another sorption isotherm than presented in section 3.1. This could result in an underestimation of the RH, as described in Appendix J. The discrepancy can both be related to deviations in the actual and modelled material properties, but also in uncertainty of the measurements. The profiles plots can be skewed by our appointed sensor position and the true position of the measured values.

Chapter 6

Discussion

The report presents an investigation of the moisture performance of biobased insulation materials, focusing on hysteresis and its implications at both material and wall scales. The RH and hysteresis analysis identifies a possible flaw in current modelling practices: most material characterizations use the large RH cycles (10–90%) which are rarely encountered in real buildings. In contrast, this study finds that RH typically fluctuates within ±10% for wall constructions.

This discrepancy raises the question: Should standard sorption isotherms be re-evaluated, as they may not capture the actual behaviour of materials under real-world conditions? To address this, detailed VSA measurements - both fast and slow - were performed, uncovering pronounced hysteresis effects, especially at mid-range RH levels.

The result suggests that using the 10-90% isotherm might overestimate the actual hysteresis. The extent of this overestimation varies by material; while it has minimal impact for Ytong, it is bigger for WFI. This indicates that an accurate hysteresis model is needed for materials with large hygroscopic behaviour. This has not been done in this project, as it would require numerous additional VSA measurements. These measurements could contain both new materials and confirmation of already made measurements.

Additionally, the measurements find that the hysteresis depends on history - the same intervals produce different results depending on moisture history. This corresponds to what is found in the literature[17], but there are some differences in the found isotherms. These might be caused by uncertainties or inconsistencies in the measurement method, such as device settings or sample handling.

A climatic chamber was built to dynamically test wall assemblies, featuring biobased insulation materials and various vapour barriers. The experiment was analysed as two periods—before and after implementing a humidifier.

Despite some delays, the setup confirmed that biobased materials exhibit strong moisture-buffering effects, with differences in performance across materials. The RW showed lower buffering, while WFI and HFI displayed more stable internal conditions.

Additionally, the choice of vapour barrier affected vapour migration patterns, with unstable indoor RH conditions. OSB4, being more permeable, allowed greater moisture movement, whereas tighter barriers restricted it. However, these differences became less evident under stabilized RH, suggesting longer monitoring periods are essential for capturing the full dynamics.

Furthermore, it was found that the setup was affected by the radiant heat from the sun. This should have been prevented with a curtain, but it was noticed after the measurement period. Therefore, the measurements might have been impacted by the sun, which highlights a need for a curtain in future setups.

During the analysis, it became clear that additional elements would have been beneficial. Specifically, a RW element with a paper vapour barrier. Currently, the analysis of the insulation material is being made with elements with different vapour barriers. The temperature differences have most likely not been impacted by this, but when examining the RH and vapour pressure, the type of vapour barrier should make a difference. However, as the element with the PE-foil was RW, it might not have made a big difference, as RW shows next to no hygroscopic behaviour.

Because the WFI measurements showed big differences to HFI and RW, having an additional element with WFI insulation would have been beneficial. This would have allowed faulty DewMaster sensors or construction defects to be ruled out with more confidence, strengthening the reliability of the findings.

When comparing our measurements with WUFI, there was a good temperature agreement but clear discrepancies in RH trends. WUFI does not account for hysteresis, which can be one of the factors causing the difference. Deviation in the actual material properties will also affect the results, and the comparison suggests that the WFI acts more hygroscopic than in the model. It seems that WUFI underestimates the moisture storage and will underestimate the time for built in moisture to stabilise. This underlines the model uncertainty and reality–model gap, which

could be bigger when using new cadidates for biobased insulation.

While the findings of this thesis provide valuable insights, it opens up several areas for further investigation. Firstly, the climatic chamber should be finished and optimally tuned. This would enable the systems to maintain the indoor conditions within a narrower deadband. Stable indoor conditions would increase the reliability of later measurements. Furthermore, completing the climatic chamber allows for an investigation of the conditions in the crawl space underneath the container.

Secondly, an analysis of the elements after stabilisation would confirm if the initial trends found in this study hold over time. This is to capture the slow moisture movement and to evaluate the long-term reliability of vapour barriers and insulation types with constant indoor conditions and varying outdoor conditions.

With our measurements of moisture sorption at smaller realistic variations in relative humidity, it is now possible to evaluate and assess the performance of existing hysteresis models. How do available models reflect reality and replicate our found hysteresis scanning curves? Additionally, should the accuracy gap for existing models be further investigated to determine the significance of potential improvement of hysteresis modelling.

It has not been notably addressed, but as a supplementary analysis, we explored the potential of estimating the water vapour permeability from measurements of air permeability. Our preliminary investigation indicated some possible correlation and which supports the need and motivation for further investigation. Reducing the needed resources for measurements of water vapour permeability is an important contribution as this material parameter is key for numerical simulations.

Chapter 7

Conclusion

This thesis investigated the moisture performance of biobased insulation materials, with a focus on hysteresis under realistic dynamic conditions. Through a combination of material-scale sorption measurements, full-scale wall element testing, and numerical simulations, the study aimed to improve the understanding of how biobased insulation behaves in real-world conditions.

The results showed that relative humidity in wall constructions typically fluctuates within ±10%—a narrower range than the 10–90% used in standard material characterization. VSA measurements confirmed that hysteresis occurs within these smaller ranges, especially for wood fiber insulation and hemp fiber insulation, while AAC-Ytong exhibited minimal hysteresis. This suggests that modelling approaches, which often neglect hysteresis or simplify it using a single average isotherm, may over- or underestimate moisture storage and buffering capacity depending on the material.

The experimental setup demonstrated differences in moisture and temperature behaviour across various insulation materials and vapour barriers. The biobased materials exhibited stronger moisture buffering than mineral wool. However, the experimental measurements could only be used to find initial trends because of the short measurement period. Comparisons between measured data and WUFI simulations revealed reasonable alignment in temperature but notable deviations in RH, underlining the importance of accurate initial conditions and appropriate material modelling.

Overall, this study reinforces the potential of biobased insulation materials in moisture-sensitive constructions, while emphasizing the importance of realistic testing methods and enhanced simulation capabilities. Future work should aim to refine the experimental setup, develop dedicated hysteresis models, and extend testing durations to validate long-term trends.

Bibliography

[1] Yale Center for Ecosystems + Architecture United Nations Environment Programme. *Building Materials and the Climate: Constructing a New Future*. 2023. URL: https://wedocs.unep.org/20.500.11822/43293.

[2] Torben V. Rasmussen et al. *Biogene materialers anvendelse i byggeriet*. 2022:09, Institut for Byggeri, By og Miljø (BUILD), Aalborg Universitet, 2022.

[3] Henriette Fischer, Martin Aichholzer, and Azra Korjenic. "Ecological Potential of Building Components in Multi-Storey Residential Construction: A Comparative Case Study between an Existing Concrete and a Timber Building in Austria". In: *Sustainability* 15.8 (2023). ISSN: 2071-1050. DOI: 10.3390/su15086349. URL: https://www.mdpi.com/2071-1050/15/8/6349.

[4] Henriette Fischer and Azra Korjenic. "Hygrothermal Performance of Bio-Based Exterior Wall Constructions and Their Resilience under Air Leakage and Moisture Load". In: *Buildings* 13.10 (2023), p. 2650. ISSN: 2075-5309. DOI: 10.3390/buildings13102650. URL: https://www.mdpi.com/2075-5309/13/10/2650.

[5] Ernst J. d. P. Hansen et al. *Varmeisoleringsmaterialer og deres anvendelse*. Ed. by Lise Jacobsen. 1st ed. SBi-anvisning 280. A.C. Meyers Vænge 15, 2450 København SV: Institut for Byggeri, By og Miljø (BUILD), Aalborg Universitet, 2024. URL: https://www.anvisninger.dk.

[6] Erik Brandt et al. *Fugt i bygninger: Teori, beregning og undersøgelse*. Ed. by Lise Jacobsen. 1. udgave. SBi-anvisning 277. A.C. Meyers Vænge 15, 2450 København SV: BUILD, Aalborg Universitet, 2023. URL: https://www.build.aau.dk.

[7] VIA University College et al. *Fra Marken til Byggeri*. 2024. URL: https://realdania.dk/publikationer/faglige-publikationer/fra-marken-til-byggeri.

[8] Oskar Ranefjärd, Paulien B. Strandberg-De Bruijn, and Lars Wadsö. *Hygrothermal Properties and Performance of Bio-Based Insulation Materials Locally Sourced in Sweden.* 2024. DOI: 10.3390/ma17092021.

[9] Ulf Thrane et al. *Skimmelsvampe i bygninger – undersøgelse og vurdering.* Ed. by Lise L. B. Raunkjær and Dorte Gram. 1. udgave. SBi-anvisning 274. A.C. Meyers Vænge 15, 2450 København SV: BUILD, Aalborg Universitet, 2020, p. 169. ISBN: 978-87-563-1962-1. URL: https://www.build.aau.dk.

[10] Klaus Sedlbauer. "Prediction of Mould Fungus Formation on the Surface of and Inside Building Components". In: (2001).

[11] Birgitte Andersen and Torben V. Rasmussen. "Biobased building materials: Moisture characteristics and fungal susceptibility." In: *Building and Environment* 275 (2025). ID: 271434, p. 112720. ISSN: 0360-1323. DOI: 10.1016/j.buildenv.2025.112720. URL: https://www.sciencedirect.com/science/article/pii/S0360132325002021.

[12] Erik Brandt et al. *Fugt i bygninger: Bygningsdele.* Ed. by Lise Jacobsen. 1st ed. SBi-anvisning 279. A.C. Meyers Vænge 15, 2450 København SV: BUILD, Aalborg Universitet, 2023. ISBN: 978-87-563-2091-7. URL: https://www.build.aau.dk.

[13] Dansk Standard. *Byggekomponenter og -elementers hygrotermiske ydeevne – Indvendig overfladetemperatur for at undgå kritisk overfladefugtighed og kondensdannelse i hulrum – Beregningsmetoder.*

[14] Søren S. Hansen et al. "Requirements of the Vapour Barrier in Wood-Frame Walls". In: *Buildings* 14.10 (2024), p. 3186. ISSN: 2075-5309. DOI: 10.3390/buildings14103186. URL: https://www.mdpi.com/2075-5309/14/10/3186.

[15] MUDP rapport. *Det Åndbare Hus - Afsluttende rapport.* Ed. by Egen Vinding og Datter. Miljøstyrelsen, 2019. ISBN: 978-87-7038-100-0.

[16] Anna E. Leszmann, Martin Morelli, and Torben V. Rasmussen. "Moisture Performance Requirements for Insulation in Exterior Wood-Frame Walls without a Vapour Barrier". In: vol. 2654. 13th Nordic Symposium on Building Physics, NSB 2023, NSB 2023 ; Conference date: 12-06-2023 Through 14-06-2023. IOP Publishing, 2023. Chap. 1. DOI: 10.1088/1742-6596/2654/1/012115. URL: https://www.en.build.aau.dk/web/nsb2023,.

[17] Carsten R. Pedersen. "Koblet fugt- og varmetransport i bygningskonstruktioner: Fugtfysik". In: (1989). Publisher's PDF, also known as Version of record. Link back to DTU Orbit.

URL: https://orbit.dtu.dk/en/publications/koblet-fugt-og-varmetransport-i-bygningskonstruktioner-fugtfysik.

[18] Gregor A. Scheffler. "Validation of hygrothermal material modelling under consideration of the hysteresis of moisture storage". 2008. URL: https://orbit.dtu.dk/en/publications/validation-of-hygrothermal-material-modelling-under-consideration.

[19] Michele Libralato et al. "Damage risk assessment of building materials with moisture hysteresis". In: *Journal of Physics: Conference Series* 2069.1 (2021). ISSN: 1742-6588. DOI: 10.1088/1742-6596/2069/1/012043.

[20] Zijian Zhu et al. "Hygric properties of porous building materials (IX): Experimental evaluation of two hysteresis models". In: *Building and Environment* 272 (2025). ID: 271434, p. 112695. ISSN: 0360-1323. DOI: 10.1016/j.buildenv.2025.112695. URL: https://www.sciencedirect.com/science/article/pii/S0360132325001775.

[21] Thomas Busser et al. "Experimental validation of hygrothermal models for building materials and walls: an analysis of recent trends". working paper or preprint. 2018. URL: https://hal.science/hal-01678857.

[22] Romain Rémond, Giana Almeida, and Patrick Perré. "The gripped-box model: A simple and robust formulation of sorption hysteresis for lignocellulosic materials". In: *Construction and Building Materials* 170 (2018). ID: 271475, pp. 716–724. ISSN: 0950-0618. DOI: 10.1016/j.conbuildmat.2018.02.116. URL: https://www.sciencedirect.com/science/article/pii/S0950061818303659.

[23] Dominique Derome. "The Impact of Sorption History and Hysteresis on Moisture Pattern in a Wood-Framed Building Envelope". In: *Thermal Performance of the Exterior Envelopes of Buildings VIII*. Clearwater Beach, Florida: ASHRAE, 2001. URL: https://store.accuristech.com/standards/the-impact-of-sorption-history-and-hysteresis-on-moisture-pattern-in-a-wood-framed-building-envelope?product_id=1711589.

[24] Oskar Ranefjärd. "Investigating Bio-Based Insulation: Hygrothermal Performance: from Material Properties to the Building Envelope". Defence details Date: 2024-06-11 Time: 10:00 Place: Lecture Hall V:A, building V, John Ericssons v
g 1, Faculty of Engineering LTH, Lund University, Lund. External reviewer(s) Name: Nore, Kristine Title: Dr Affiliation: OmTre, Norway. —; Doctoral Thesis (compilation), 2024.

[25] Marie E. Ø Jensen and Amalie S. Flou. "Hygrotermiske egenskaber og deres indvirknings på skimmelvækst i ydervægge". ID: alma9921966247405762. 2025.

[26] Decagon. *Vapor Sorption Analyzer*. 2016.

[27] Emmanuel Arthur et al. "Evaluation of a Fully Automated Analyzer for Rapid Measurement of Water Vapor Sorption Isotherms for Applications in Soil Science". In: *Soil Science Society of America journal*. 78.3 (2014). ID: ctx10758689320005762, pp. 754–760. ISSN: 0361-5995. DOI: 10.2136/sssaj2013.11.0481n.

[28] Kirstine M. Frandsen. "Non-Equilibrium of Water Vapor Sorption in Building Materials". URL: https://vbn.aau.dk/en/projects/non-equilibrium-of-water-vapor-sorption-in-building-materials.

[29] Martin Veit and Hicham Johra. *Experimental Investigations of a Full-Scale Wall Element in a Large Guarded Hot Box Setup: Methodology Description*. 304. Department of the Built Environment, Aalborg University, 2022. DOI: 10.54337/aau488363266.

[30] Sensirion. *Datasheet SHT85*. 2021.

[31] The Fraunhofer Institute for Building Physics (IBP). *What is WUFI®? | WUFI (en)*. 2025. URL: https://wufi.de/en/software/what-is-wufi/.

[32] Rockwool. *YDEEVNEDEKLARATION NR. DOP-000396-02*. 2023.

[33] Ekolution. *EKOLUTION® HAMPAFIBERISOLERING*. 2015.

[34] SINTEF. *SINTEF Teknisk Godkjenning TG20440*. 2021.

[35] DS/EN ISO. *DS/EN ISO 10456 Byggematerialer og -produkter -Hygrotermiske egenskaber -Tabeldesignvaerdier og procedurer til bestemmelse af termiske deklarerede vaerdier og termiske designværdier*. 2008.

[36] Hicham Johra. "Thermal properties of building materials - Review and database". In: (2021). DOI: 10.54337/aau456230861.

[37] Knauf. *YDEEVNEDEKLARATION Nr. 0087 Clima Secura Board 15 EF*. 2017.

[38] RAW. *Data sheet Raw Pro Standard*. 2024.

[39] ISOCELL. *Technical Data sheet ÖKO NATUR Vapour Retarder fabric-reinforced*. 2025.

[40] npi. *Datablad Egger OSB-4 Top Tg-4*. 2023.

[41] Nickolaj F. Jensen et al. "Climate data for moisture simulations: Producing a Danish moisture reference year and comparison with previously used reference year locations". In: vol. 2654. 13th Nordic Symposium on Building Physics, NSB 2023, NSB 2023 ; Conference date: 12-06-2023 Through 14-06-2023. IOP Publishing, 2023. Chap. 1. DOI: 10.1088/1742-6596/2654/1/012029. URL: https://www.en.build.aau.dk/web/nsb2023,.

[42] Lars Broder Lindgren, Kirstine M. Frandsen, and Steffen E. Maagaard. *Inpspirationskatalog for biobaserede konstruktioner*. 2024. URL: https://realdania.dk/publikationer/faglige-publikationer/inspirationskatalog-for-biobaserede-konstruktioner.

[43] Sensirion. *Datasheet SHT7x*. 2011.

[44] Sensirion. *Sensor Specification Statement and Testing Guide*. 2021.

[45] Bjørn Kjærsgaard Nielsen. *Kalibreringscertifikat*. 2025.

[46] DinGeo. *DinGeo Sol*. (Accessed: 28.05.2025). URL: https://www.dingeo.dk/adresse/9220-aalborg-%C3%B8st/thomas-manns-vej-20/sol/.

[47] Mikael Salonvaara et al. "Validation of Hygrothermal Simulations with Wall Performance Experiments in an Environmental Chamber". In: *E3S Web of Conferences* 172 (2020), p. 04010. DOI: 10.1051/e3sconf/202017204010. URL: https://www.researchgate.net/publication/342576240_Validation_of_Hygrothermal_Simulations_with_Wall_Performance_Experiments_in_an_Environmental_Chamber.

[48] Statens Byggeforskningsinstitut. *BSim*. URL: https://www.build.aau.dk/til-byggebranchen/software/bsim.

[49] Kim Bjarne Wittchen, Kjeld Johnsen, and Karl Grau Sørensen. *BSim User's Guide*. 2005.

[50] Victor Ø Nyborg, Asbjørn K. Mikkelsen, and Lotte L. Pedersen. "Investigation of material properties and their effect on mold growth". 2024.

[51] WUFI Fraunhofer-IBP. *WUFI - AiF Flexible Wood-Fiber Insulation WF - Generic data*. 2016.

[52] WUFI Fraunhofer-IBP. *WUFi - Woodfiber AIR IBP laboratory report HoFM-047/2020 (F409)*. 2020.

[53] WUFI Fraunhofer-IBP. *WUFI - PavaFlex IBP laboratory test F043*. 2011.

[54] nbsp Kumaran and Mavinkal K. *WUFI - Southern Yellow Pine ASHRAE 1018-RP*. 2002.

[55] Fraunhofer-IBP. *WUFI - Rigips Glasroc X IBP laboratory report HoFM-039/2020 (F399 A)*. 2020.

[56] Danish Standards. *Beregning af bygningers varmetab*. (Accessed: 11.04.2024). 2011.

[57] *Byggematerialers hygrotermiske ydeevne - Bestemmelse af fugtindhold ved tørring ved forhøjet temperatur = Hygrothermal performance of building materials and products - Determination of moisture content by drying at elevated temperature*. ID: alma9920597630205762. 2000.

[58] Kirstine M. Frandsen et al. "Experimental investigation of water vapor diffusivity in bio-based building materials by a novel measurement method". In: *Proceedings of the Resilient Materials 4 Life 2020 (RM4L2020) International Conference*. Trans. by Anonymous. Resilient Materials 4 Life (RM4L) 2020 ; Conference date: 20-09-2021 Through 22-09-2021, Cardiff University, 2021.

[59] Per Schjønning and Michael Koppelgaard. "The Forchheimer Approach for Soil Air Permeability Measurement". In: *Soil Science Society of America Journal* 81.5 (2017). ISSN: 0361-5995. DOI: 10.2136/sssaj2017.02.0056.

[60] Per Schjønning. "Jordens permeabilitet for luft og vand i relation til jordtype samt nedmuldning og afbrænding af halm". In: *Planteavl 90, 227-239* (1986).

[61] Patrick Hundevad and Tonje Luckenwald. "Investigating the Correlation between Water Vapor Permeability and Pure Diffusion in Building Materials". 2023.

[62] Kirstine M. Frandsen et al. "Water vapor sorption dynamics in different compressions of eelgrass insulation". In: *E3S Web of Conferences* 172 (2020). DOI: 10.1051/e3sconf/202017217005.

[63] YTONG. *YTONG Massivblokke - Teknisk data*.

[64] Skamol Group et al. *Skamowall board*.

[65] IEA International Energy Agency. *IEA EBC Project Annex 14 - Catalogue of Material Properties*. 1991.

Part I

Appendices for experimental setup

Appendix A

Climatic chamber setup for dynamic testing of wall elements

This appendix will describe the climatic chamber setup and its HVAC control systems. It will cover the design plans, implementation process, and documentation for the setup. At the time of project delivery, the setup is not complete in accordance with the design plans, and more work, specifically the implementation and testing of control systems, is needed.

The purpose of the climatic chamber is to have a measurement setup, where wall constructions can be tested under controlled indoor conditions and actual outdoor weather conditions. Additionally, the container is placed on a raised column foundation, so an investigation of the conditions in the crawl space underneath can be made. The climatic chamber is built inside an insulated 20-foot high-cube standard ISO container, which was delivered to Aalborg University. The climatic chamber can easily be moved to another location, which is the plan eventually. The primary work has revolved around the HVAC systems and their control, so a controlled indoor environment can be maintained. This involves the following:

- Climatic chamber and HVAC system specification
- HVAC system control
- Installation of HVAC systems
- Evaluation and tuning of HVAC control

A.1 Insulated container dimensions

The climatic chamber is constructed within a container, with one long side cut open to allow us to build our measurement setup. The container has 70 mm mineral insulation in the walls and ceiling with a U-value of $\approx 0.5\frac{W}{m^2 \cdot K}$. The amount is a compromise due to the limited size of the container, but the insulation will greatly lower heat losses and gains, so it is easier to maintain a constant indoor temperature. In the floor, there is 200 mm of thermoset polyisocyanurate (PIR) insulation, so it has a U-value of $\approx 0.1\frac{W}{m^2 \cdot K}$. The floor has a lower U-value in order to get a realistic heat loss to the crawlspace, which makes it possible to get representative measurements of the temperature and humidity conditions inside it. A U-value of $\approx 0.1\frac{W}{m^2 \cdot K}$ is commonly needed in a floor to comply with Danish energy requirements in BR18.

Figure A.1 shows a cross-section of the container, illustrating the insulation in the building envelope and its dimensions.

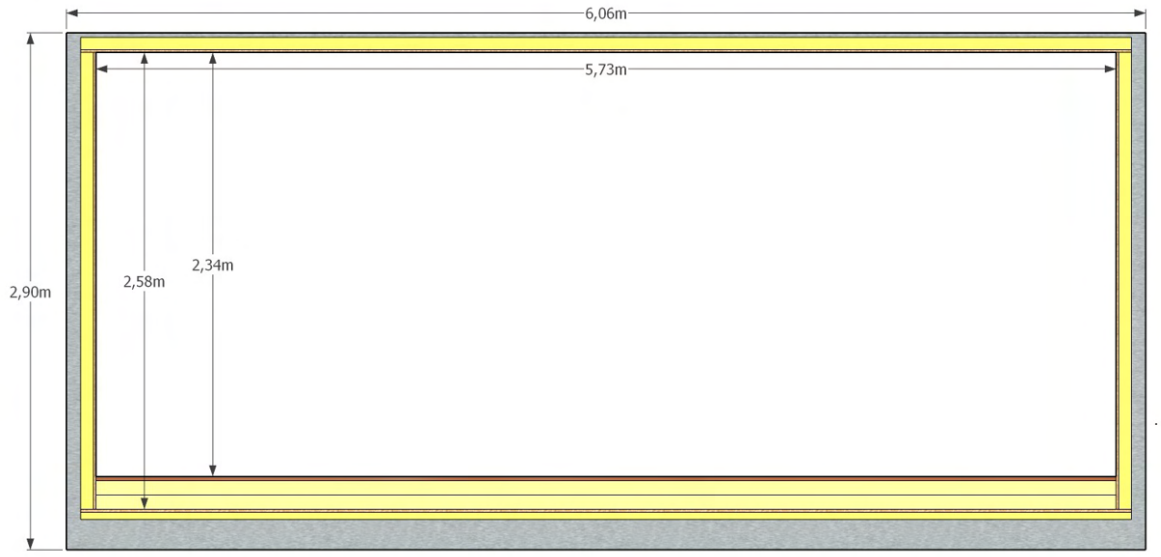

Figure A.1. Cross-section C2 of the climatic chamber, as shown in Figure A.2.

The container is placed so its opening, where our measurement setup will be, is facing north. This is shown on the floor plan on Figure A.2.

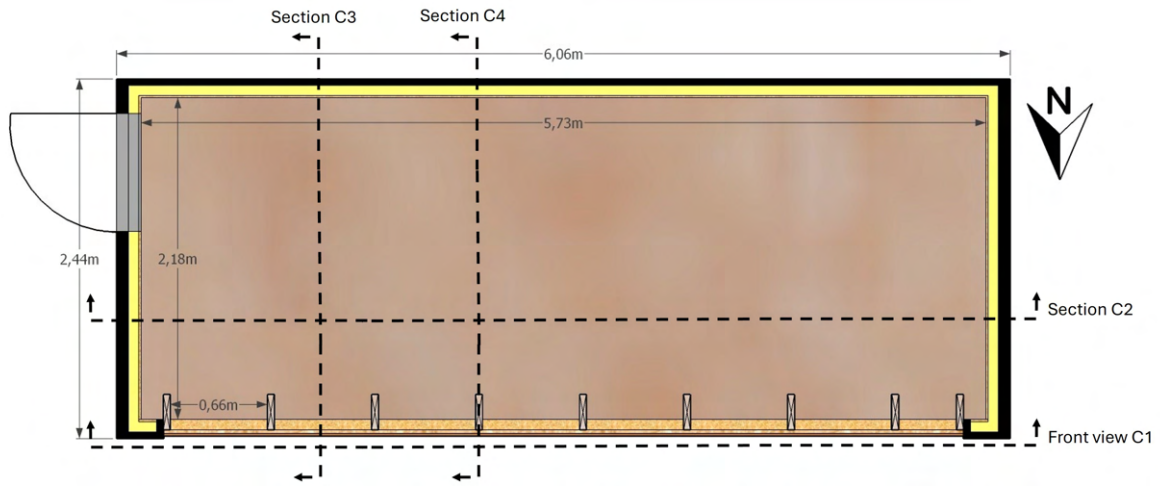

Figure A.2. Floor plan and dimensions of the climatic chamber

The floor plan shows the vertical timber studs supporting the ventilated facade cladding used in the measurement setup. The measurement setup is further explained in section A.2. The measurement setup is facing the north, because this is deemed the most critical orientation with regards to moisture risk. This is because the north facade has the lowest solar gain and lowest temperatures. Figure A.3 shows the surroundings of the climatic chamber, and that there is a free horizon in front of the testing facade.

Figure A.3. The placement and surroundings of the climatic chamber.

A.2 Measurement setup

The long side of the container is cut open, making it possible to build a setup where different wall elements can be tested with exposure to the weather. The opening in the container is slightly smaller than the interior to allow for a proper finish around the opening. A frontal view of the opening is illustrated in Figure A.4.

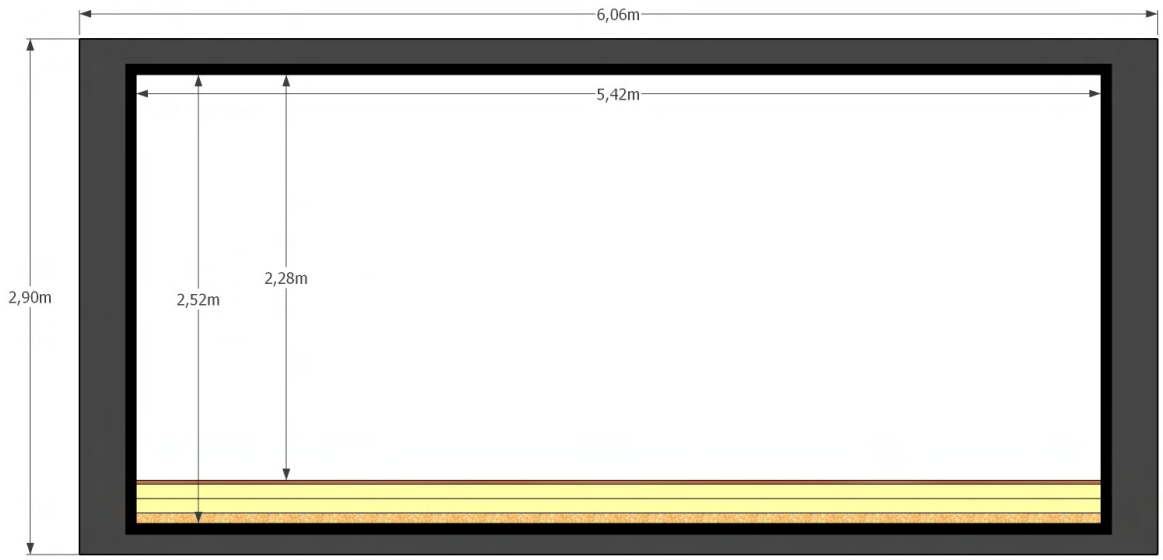

Figure A.4. Front view C1 of the container opening and opening dimensions, as shown in Figure A.2.

It is important that the setup is flexible and it is possible to continuously change wall elements. This is achieved by using a shared, ventilated facade, to close the opening. This allows the wall elements to be constructed with only a wind barrier and to be swapped from the inside. The facade is built in three sections and mounted using a hook-and-slot mounting system. This makes it possible to easily dismount the sections independently and gain outside access to the wall elements behind. The exterior facade is shown in Figure A.5 and A.6.

Figure A.5. Outside view of the facade facing the north.

Figure A.6. Interior view of the ventilated facade, without any wall elements.

The facade is mounted on timber studs that are spaced 660 mm apart, which fit the current dimensions of the wall elements. The wall elements are further described in Appendix C. The spacing can be adjusted to fit differently sized wall elements. Figure A.7 shows a cross section of the container, where the mounting of the ventilated facade is visible. Horizontal furring strips are used in order to make the facade in sections that can be dismounted.

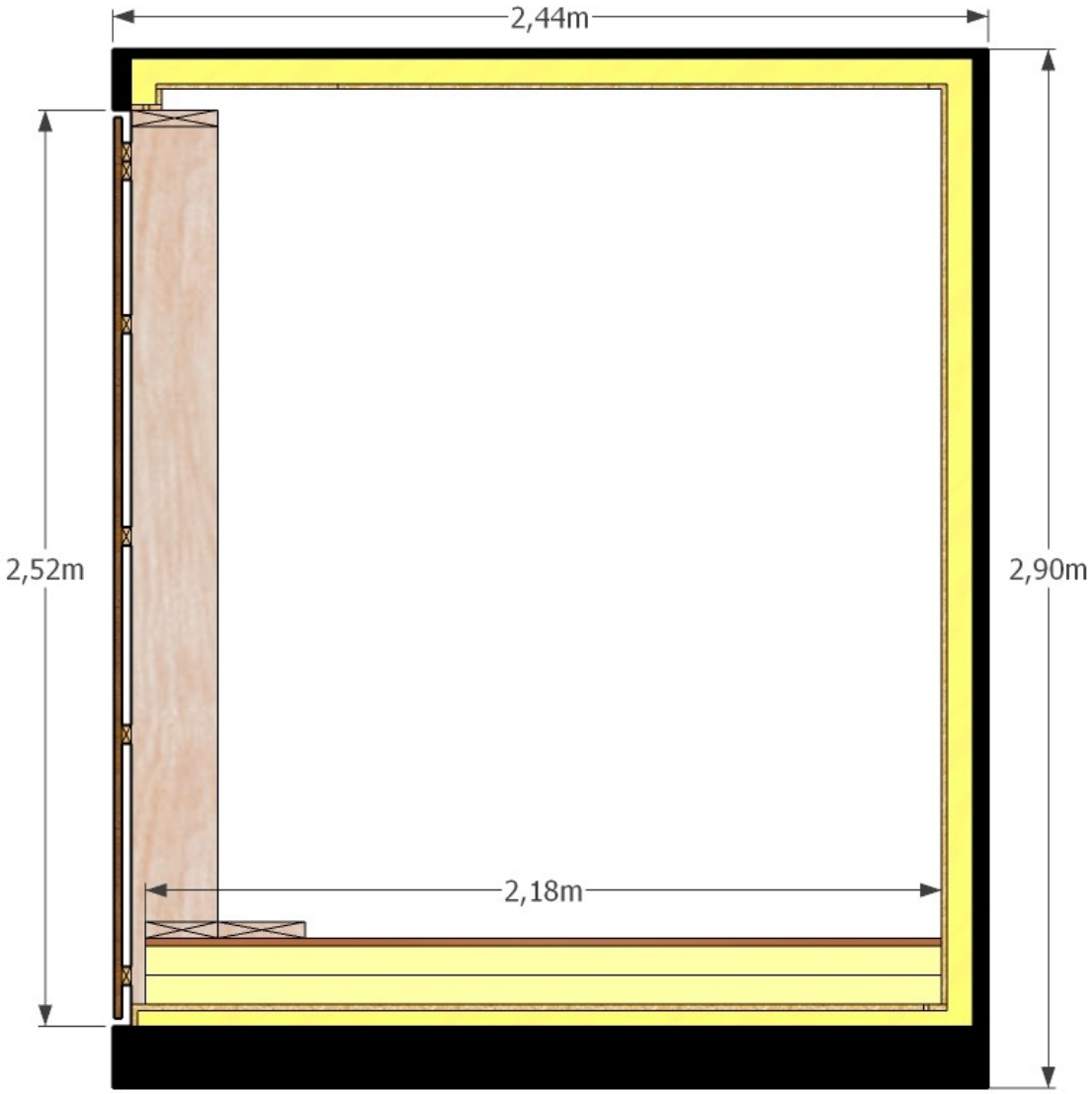

Figure A.7. Cross section C4 showing the ventilated facade, as shown in Figure A.2.

The hook-and-slot mounting system is formed by two furring strips, which are placed at the top of the facade. The facade sections hang from here and are securely fastened with screws from the outside. There is an opening of 20 mm in the top and bottom of the facade cladding for ventilation. Figure A.8 illustrates the configuration of the seven wall elements in this thesis. With an element size of $600mm \cdot 600mm$, there is space for 21 wall elements in total.

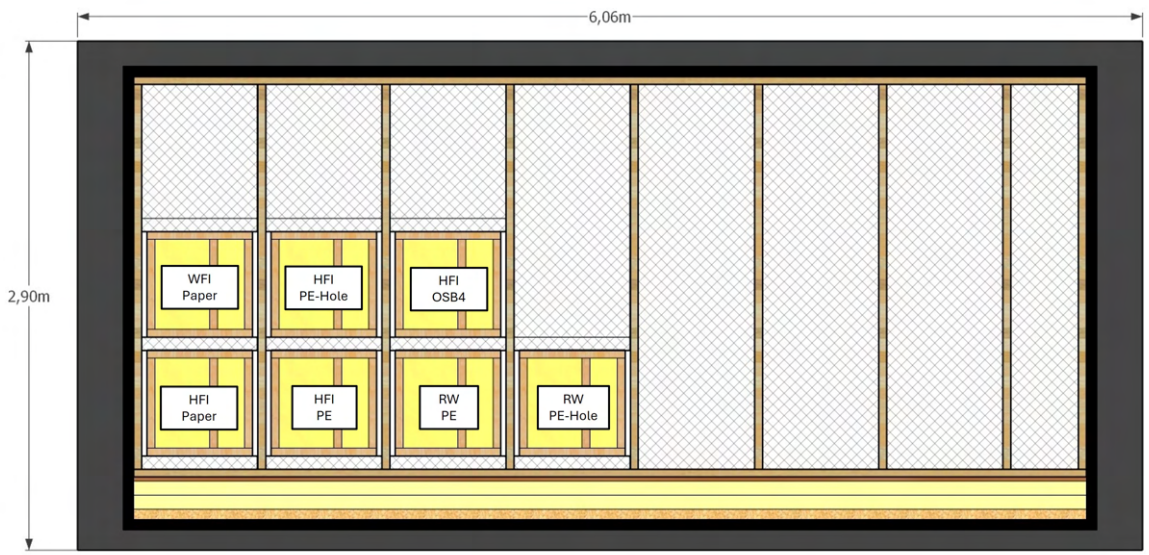

Figure A.8. Front view of the container with the tested wall elements in place.

There are 75 mm of EPS insulation (Sundolitt S60, $\lambda_D = 0{,}041 W/mK$) between the elements. The spacing between the timber studs leaves 30 mm on each side of the elements, which is filled with mineral insulation. For the current configuration, the unused space is filled with EPS insulation. Figure A.9 shows a cross section with the elements in place.

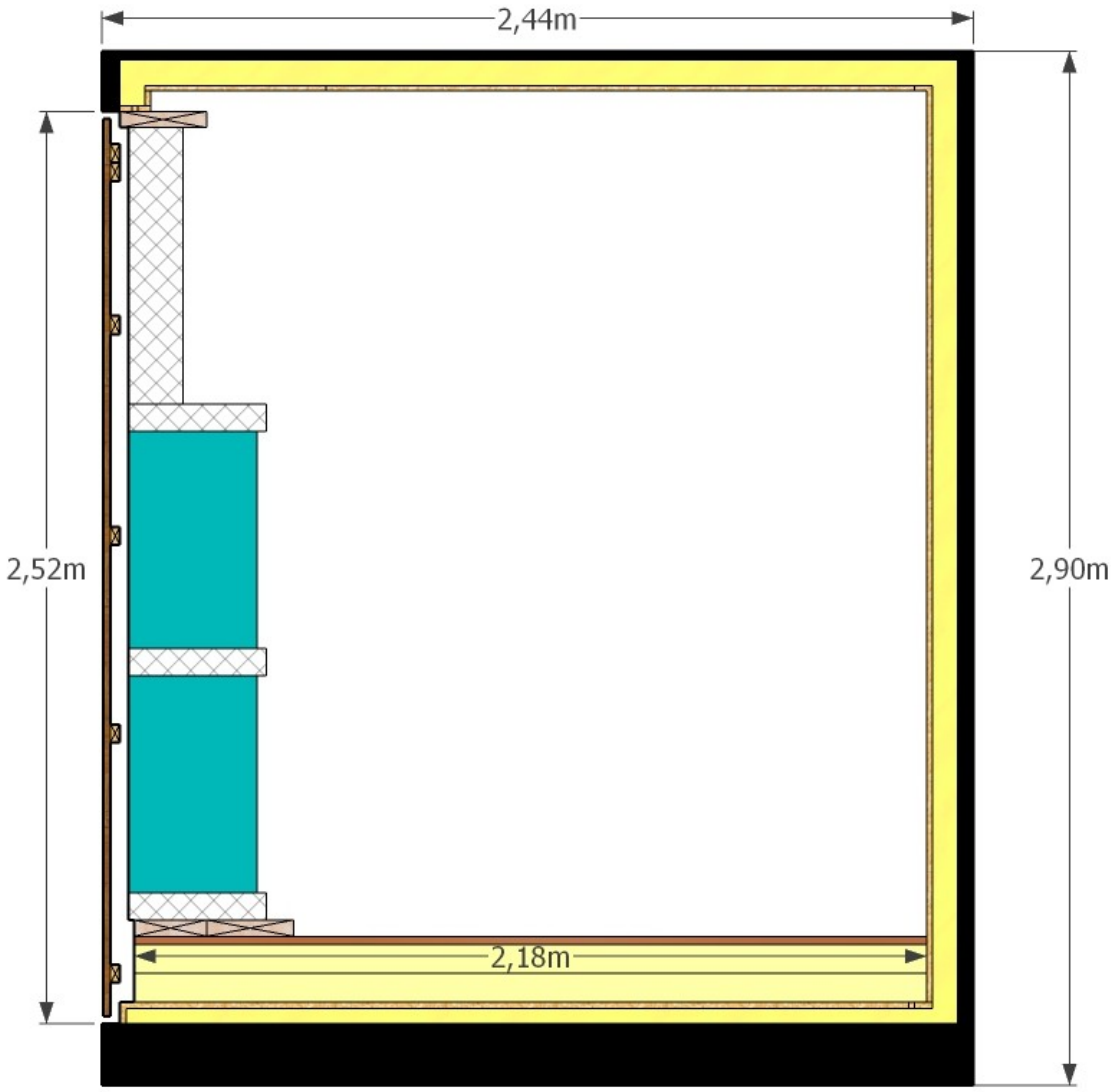

Figure A.9. Cross section C3 showing the placement of the wall elements, as shown in Figure A.2.

The wall elements are installed from the inside, with a distance of 25 mm to the surface of the furring strips. This is to ensure ventilation of the cavity, where the narrowest point will be 25 mm, but it will generally be 50 mm wide.

A.2.1 Element installation procedure

To install the elements, the first thing is to mount the sensor in front of the element in the ventilated cavity. This is shown on Figure A.10. There is 75 mm EPS insulation between the elements and 30 mm mineral insulation on the sides. The sides are filled with mineral insulation due to its compressibility, which makes the installation possible. This also makes it easy to draw

the sensor cables along the element sides. The side insulation is pre-mounted and kept in place with fishing line, as shown on Figure A.11.

Figure A.10. Installing of the sensor in the ventilated cavity.

Figure A.11. Side insulation is mounted, so a wall element can be lifted into place.

The elements are placed between the timber bracing, and Figure A.12 shows the element after it is lifted into place. When placing the element, it is very important to ensure there still is space for ventilation in the ventilated cavity.

Figure A.12. A wall element put into place in the measurement setup.

In Figure A.12, the cable for the sensor in the ventilated cavity is shown routed along the side of the element, embedded in the mineral insulation. Figure A.13 is the measurement setup with all the elements in place, and EPS insulation in the void wall space. The elements are labelled with their insulation type and vapour barrier, as described in Appendix C.

Figure A.13. Photograph of the measurement setup, with our seven wall elements in place.

This is the state of the measurement setup, for which the measurements are done. In this installation, the elements are stacked on top of each other, making it challenging to change an element without affecting the others.

To be able to change elements continuously and independently, a flexible mounting system is needed. This is not devised yet, but an idea is to have shelves the elements are placed on. This idea needs further refinement, as this will impose challenges with placing the elements on the shelves and insulating the sides.

A.3 HVAC systems

The conditions of moisture class three are maintained inside the container, with control of different HVAC systems. An overview of the systems, control signals, and measurement points is seen on Figure A.14.

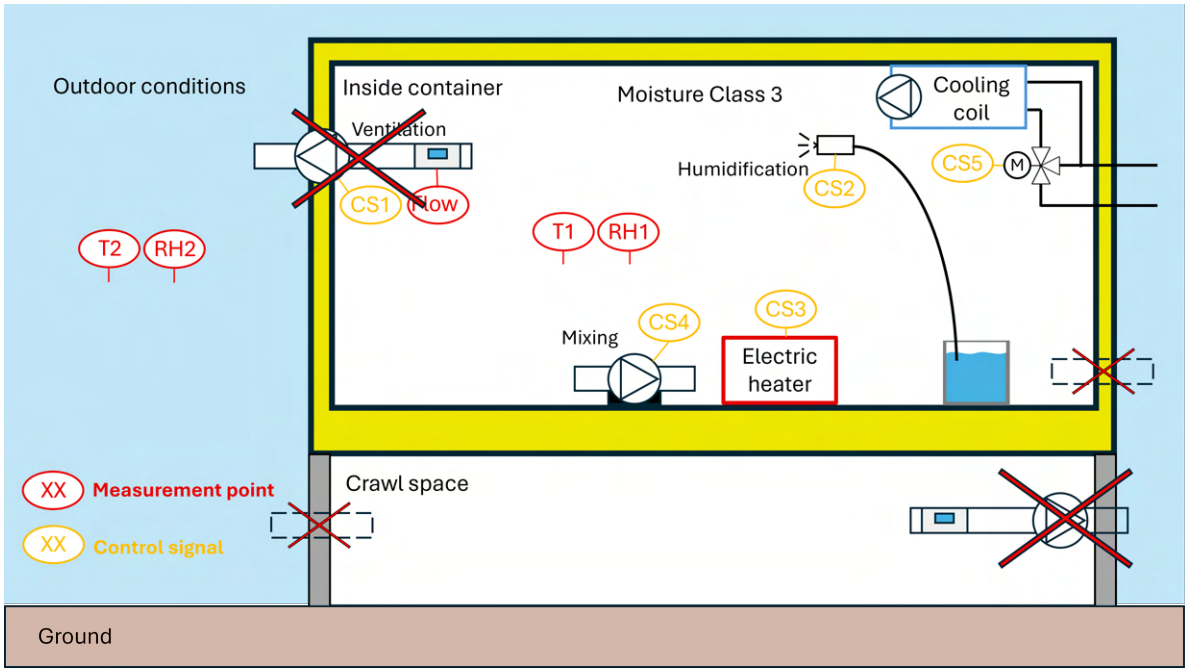

Figure A.14. Illustration of the container systems. The red crosses mark the systems that have not been implemented at this time.

In Figure 4.4, the systems that have not yet been implemented in the climatic chamber are crossed out. The process of designing and creating the HVAC setup was prolonged, which required adaptations to the original plan to ensure the inclusion of measurement data in this thesis. The consequence of this has been that the ventilation system of the climatic chamber and setup for measurements in the crawl space is not implemented. It is therefore only our design plans and considerations regarding these systems that will be described.

The aim is to maintain a specific constant indoor air temperature and relative humidity, which requires a control to manage the interplay between the different HVAC systems needed. HVAC systems are needed to counteract heat gains or losses depending on the weather. The sections below explains the designed systems and their controls.

The described controls are coded into one LabView program that handles the interplay between the systems. The program receives the control inputs, regulates the control outputs, and logs all the variables. Our control system is a modification of the LabView program developed by Hicham Johra for the large guarded hot box at the Building Material Characterization Laboratory of Aalborg University [29].

The control program is configured with DewMaster box 2, which has 10 Sensirion SHT-sensors

that can measure the process variables, temperature and relative humidity. The DewMaster boxes are further described in Appendix D. Four of the ten sensors are used to measure the indoor conditions, and their average measurement is used as control input. Of the six remaining sensors, four are planned to be placed in the crawl space, while the other two will be positioned outside to measure the local outdoor conditions. At the time being, these sensors have not been mounted yet and are instead temporarily placed inside the container. We have utilized the ten sensors inside the chamber to evaluate the mixing and document how well the setup maintains an evenly distributed temperature and relative humidity. section A.5 describes the analysis, in which we conclude that our setup achieves a well-mixed indoor environment and an even indoor boundary condition for wall elements in a measurement setup.

A.3.1 Heating and cooling system and control

To cover heat losses, there is an electric radiator. The radiator allows for precise heat output regulation, allowing for accurate control. Furthermore, the electric radiator has a fast response time, which results in better and more precise control. To get optimal control, a PI-controller is used.

For Danish weather conditions, there will be some hours where the outdoor air temperature exceeds the specified indoor air temperature in the test container. The test container is therefore equipped with a cooling system to counteract the hours with heat gains. It is not possible to accurately regulate the cooling output to maintain the indoor temperature. To work around this, a constant cooling output is triggered when the control signal to the radiator is below 2 V. The heating control signal is then modulated, so the constant temperature is maintained. The cooling output is modulated in steps in order to save energy and not have unnecessary heating. If the heating output stabilises above 4 V while cooling is on, the cooling output decreases by one step. As the cooling system has a slow response time, a 5-minute cooldown is used. This is to secure that the cooling output stabilises before a change to the output is made. Therefore, no unnecessary changes are made.

Inside of the container, next to the radiator, a fan is placed. This fan secures the mixing of the air in the room, while also making sure the radiator does not turn off due to overheating. The heating system can be seen on Figure A.15 and A.16.

Figure A.15. Heating system

Figure A.16. Heating system 2

The cooling system comprises three main components: an air-to-water heat pump, a three-way valve, and a fan coil unit. The heat pump, located outside the room, is set to supply water at 15℃. This chilled water feeds into a mixing loop that includes a three-way valve. The valve

is controlled by a signal from the LabView program, operating within a 2–10V range. In this setup, control is applied in 1V increments to adjust the proportion of cold water directed to the fan coil. When the valve receives a 2V signal, the system recirculates water between the fan coil and the valve without introducing additional chilled water from the heat pump. The cooling system can be seen on Figure A.17 and A.18.

Figure A.17. The cooling system, with the mixing loop mounted on the wall. The cooling power is adjusted with the motorized three-way valve.

Figure A.18. Air to water heat pump, that delivers the cold water continuously to the buffer tank.

As mentioned above, the cooling is dependent on the control signal to the radiator. This approach was thought of as a simple way to control the temperature in the room, but after implementation, the cooling did not have as slow a response as expected. Furthermore, the cooling output was much larger than expected. This led to a change in the control logic, where instead of having the two systems stabilize, both are tuned aggressively. This approach has a higher energy consumption, but it was the only tuning found that kept the temperature at ±1°C. The change included lowering the cooling cooldown from 5 minutes to 20 seconds, and having the PI-controller constants at $k_p = 0.4$ and $k_i = 0.005$.

A.3.2 Humidification system and control

The climatic chamber is also equipped with a humidifier. This system consists of a water mist nozzle, an integrated water pressure unit, and a storage tank. The nozzle is positioned to spray mist directly into the airstream exiting the fan coil. The control of the humidifier checks the relative humidity, and if the value is below the setpoint, the nozzle sprays for 5 seconds followed by a 30 second cooldown. This allows the water mist to properly mix in the air. After the cooldown, the humidity is reassessed and additional mist is added if necessary. The cooling system can be seen on Figure A.19.

Figure A.19. Humidification system with water mist nozzle, self-contained water pressure system and water tank.

A.3.3 Ventilation system and control

The climatic chamber is also designed with two ventilation systems. One for the chamber, and one for the crawl space underneath. Unfortunately, these two have not been implemented in the container at this time. The fan inside the room is used to create a basic air change rate of 0.5 h^-1 equalling the requirement from BR18 of 0.3 $l/s\,pr\,m^2$. This fan also serves as a dehumidifier if the RH is too high. The control of the container calculates the absolute humidity of the outside air, and checks if it is lower than the absolute humidity inside of the container. If that is the case, the fan increases the air change until the RH is at the required level. The second system is designed to keep an air change in the crawl space and the conditions can be measured at different air changes.

A.4 Conditions in crawl space

As concrete is very CO_2-intensive, there is a drive to reduce it in construction. One initiative to reduce the usage of concrete is to have a screw foundation. With a screw foundation, there will be a suspended floor, with a crawl space beneath. The crawl space will typically be closed off for aesthetics and to keep out unwanted animals. The space will have openings to ensure it is ventilated. There is a concern that there will be more critical moisture conditions in the crawl space compared to the outdoors, which then would require special measures in the floor construction.

This is due to the direct exposure to the soil, and the soil evaporation and radiative exchange. In the setup, the aim is to be able to measure the temperature and humidity in the crawl space at known ventilation rates. Hereby the necessary ventilation rate can be established in order to achieve the same conditions in the crawl space as the outdoors. There are two concerns and hypotheses:

1. The radiative exchange with the bare soil will reduce the temperature in the crawl space, and lower the surface temperature of the floor, which increases the risk of condensation.

2. There will be evaporation from the soil, which can increase the moisture load in the crawl space.

Both concerns will be dependent on the amount of ventilation the crawl space vents generate. It is essential that the combined opening area of the vents is big enough to obtain sufficient

ventilation. The actual obtained ventilation rate will be dependent on the natural driving forces. Since ventilation is the decisive factor in the conditions within the crawl space, the setup allows us to regulate the ventilation rate. This enables us to determine how high the ventilation rate needs to be for the crawl space conditions to match the outdoors.

In order to get realistic results, additional insulation is added to the floor so it has a U-value of $\sim 0.1 \frac{W}{m^2 \cdot K}$. This ensures that the heat loss to the crawl space is within a realistic range.

Figure A.20 shows the crawl space, which is about 40 cm high. The concrete tiles are supposed to be removed, so the soil is bare.

Figure A.20. Photograph of the raised foundation for the container and the inclosed crawl space.

A.5 Climatic chamber system evaluation

In this section, the conditions inside the climatic chamber are analysed to see if the conditions are homogenous. The part of the DewMaster box, originally intended for measurements in the crawl space, was repurposed to monitor indoor conditions. Since the crawl space was not ready for data collection, several sensors were left unused. These surplus sensors were instead distributed

within the climatic chamber, enabling monitoring of the indoor environment. The sensors are placed as shown on Figure A.21.

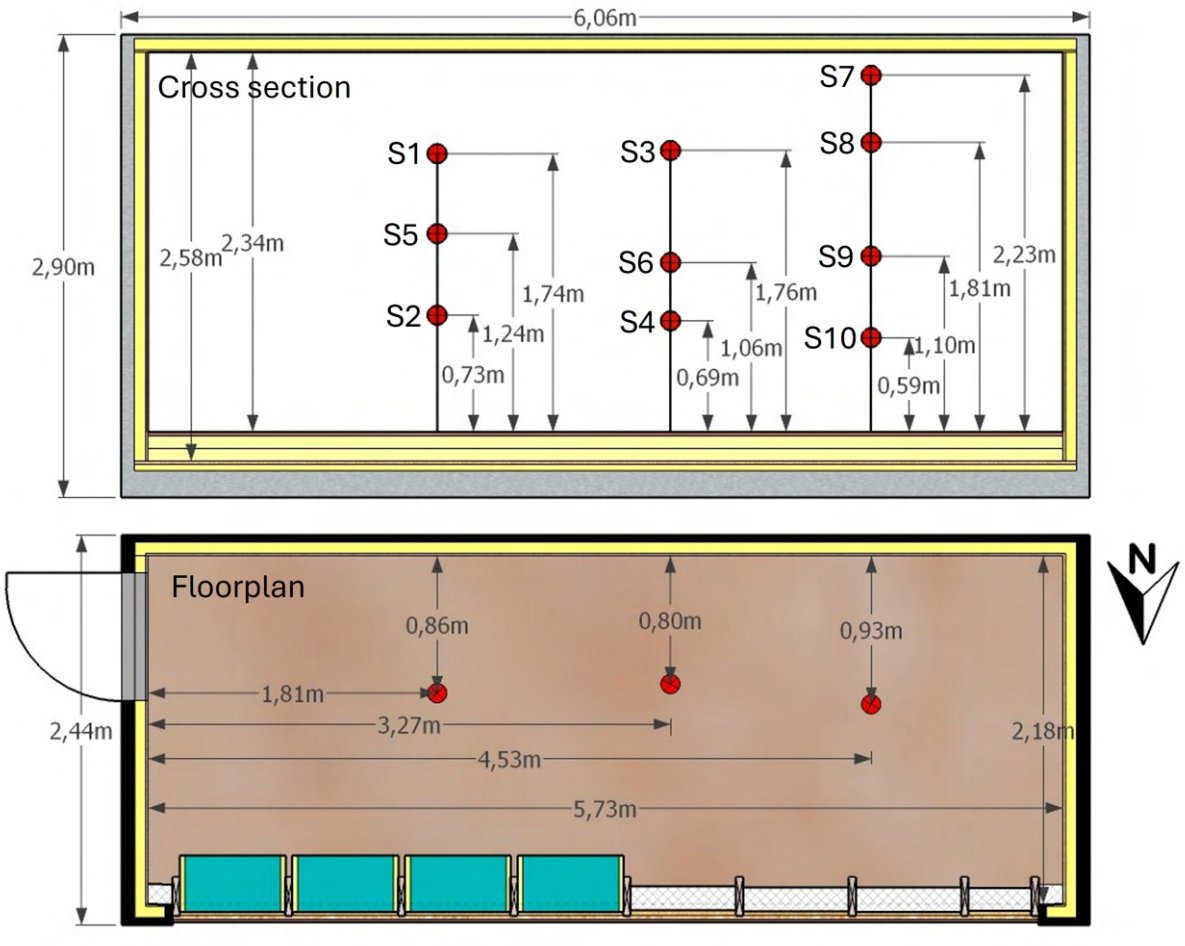

Figure A.21. Sensor placement for measurement of indoor conditions in the Climatic chamber.

Sensor 7 is positioned directly in the airstream from the fan coil, allowing it to capture the inlet air temperature. As a result, it does not accurately represent the general indoor environment and is therefore excluded from the indoor climate analysis. To evaluate the conditions inside the chamber, five full days with all systems working as intended are used, May 12th to May 17th. The first parameter examined is temperature, as shown in Figure A.22.

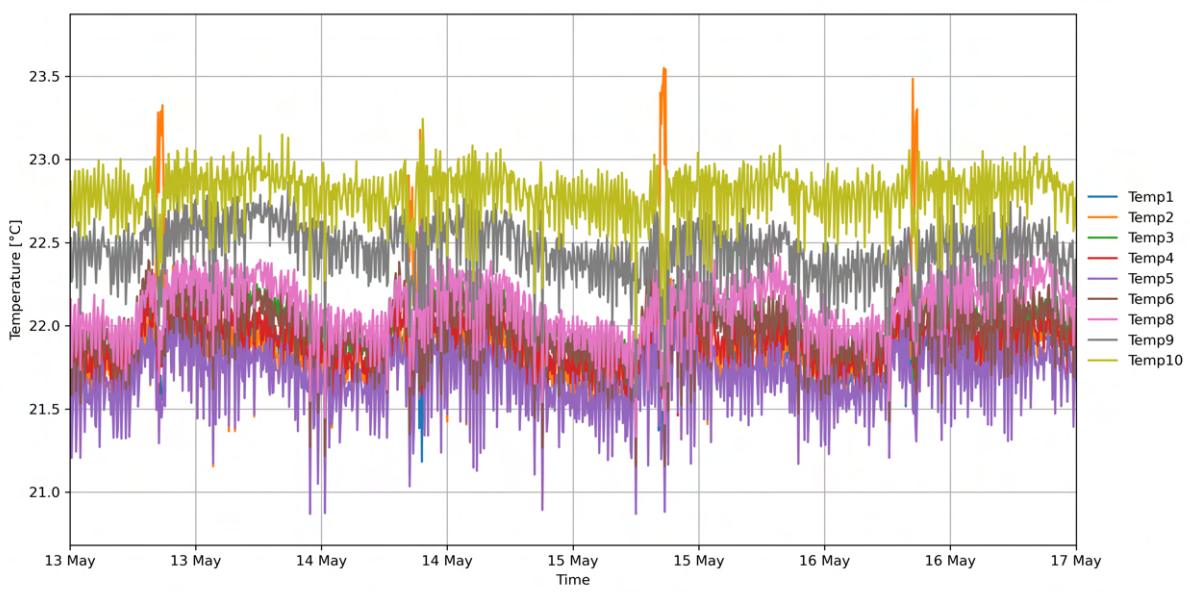

Figure A.22. The temperatures measured inside of the climatic chamber.

The temperature data shows that the sensors generally form a consistent group, indicating uniform indoor conditions. Sensor 10 consistently records slightly higher temperatures than the others, likely due to warm air from the radiator being directed toward it by the ventilation unit. Sensor 9 may also be affected by this localized airflow. The temperature shows significant fluctuations, indicating that the system tuning is not yet optimal. Although this issue is recognized, measurements were conducted under suboptimal conditions due to time constraints. Additionally, Sensor 2 exhibits occasional sharp spikes in temperature. This is attributed to its placement near the door, which includes a window. During some mornings, direct sunlight hits the sensor, causing temporary increases in its recorded temperature. The RH shows the same tendencies as the temperature. The measurements are shown on Figure A.23.

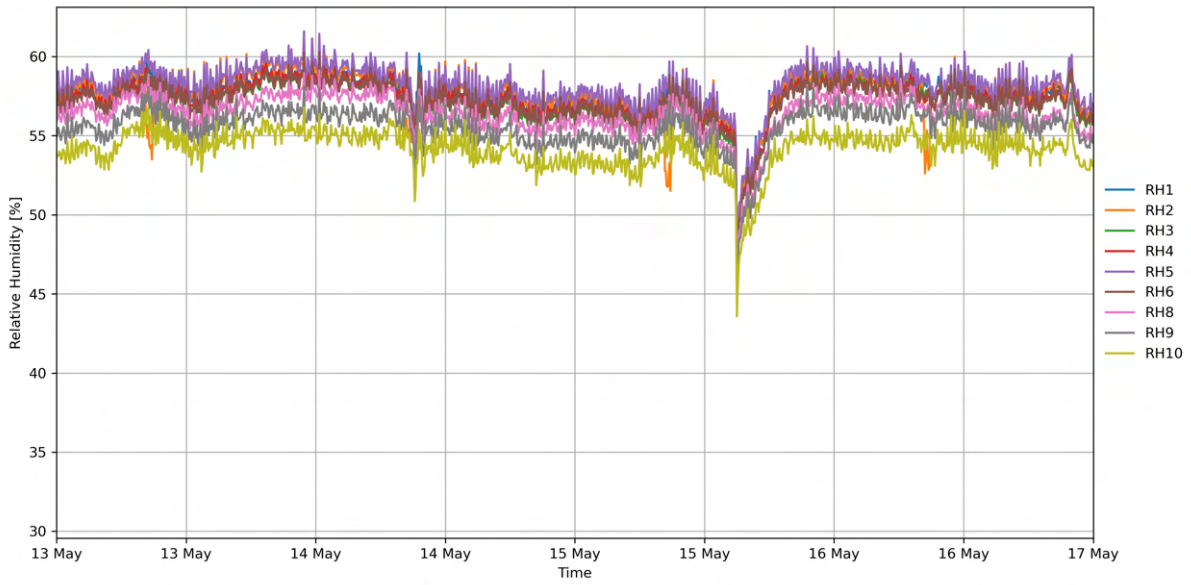

Figure A.23. The RH measured inside of the climatic chamber.

For relative humidity, Sensor 10 consistently records slightly lower values. This is expected, as relative humidity is temperature-dependent, and Sensor 10 also measures a slightly higher temperature, resulting in a lower RH reading. The same explanation likely applies to Sensor 9. Aside from these two, the remaining sensors show consistent RH values across the indoor environment. On May 15 a drop in the RH is noticed. This is most likely due to the door being opened, as the water for the humidifier had to be replenished. As with the external boundary conditions, the vapor pressure is also analysed and shown on Figure A.24.

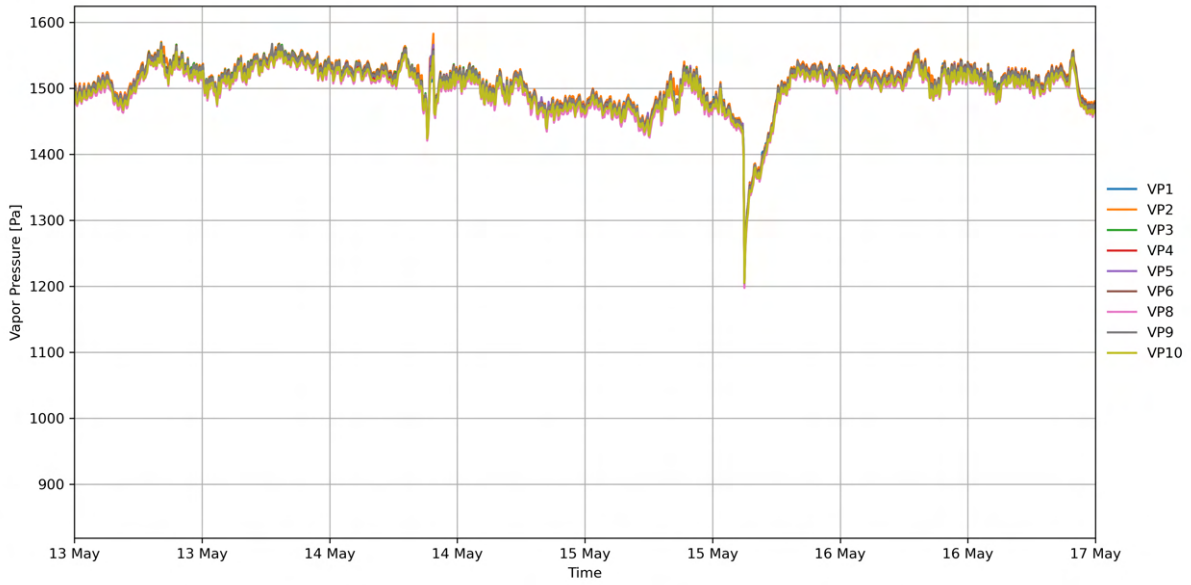

Figure A.24. The vapour pressure inside of the climatic chamber.

The vapor pressure measurements show that the slight variations in temperature and relative humidity have minimal impact, as all nine sensors display closely grouped values. This indicates a consistent level of absolute moisture content throughout the indoor environment. This confirms that the climatic chamber maintains stable indoor moisture conditions, which is important for ensuring comparable results across all test elements.

A.5.1 Mixing

In the graphs above, it is difficult to determine whether the air inside the climatic chamber is being effectively mixed, as the measured parameters show noticeable variation. To better assess the uniformity of the indoor environment, the difference between the average value of all sensors and the individual readings from each sensor was calculated. This approach helps identify localized deviations and provides a clearer indication of how well the air is mixed within the chamber. The graphs are shown on Figure A.25 to A.27.

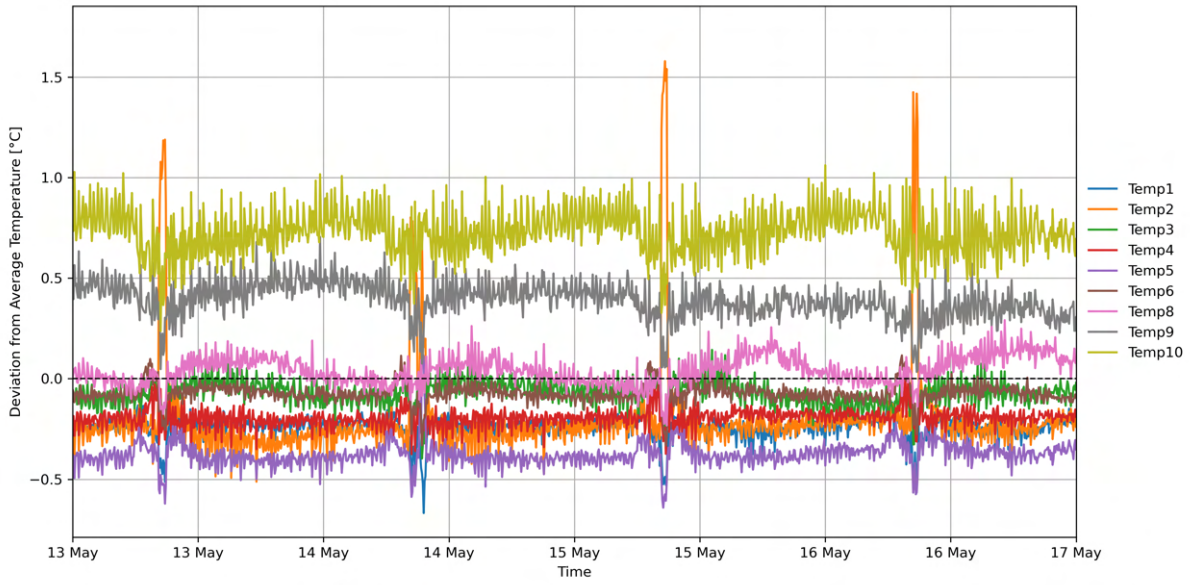

Figure A.25. The difference in temperature measured inside of the climatic chamber.

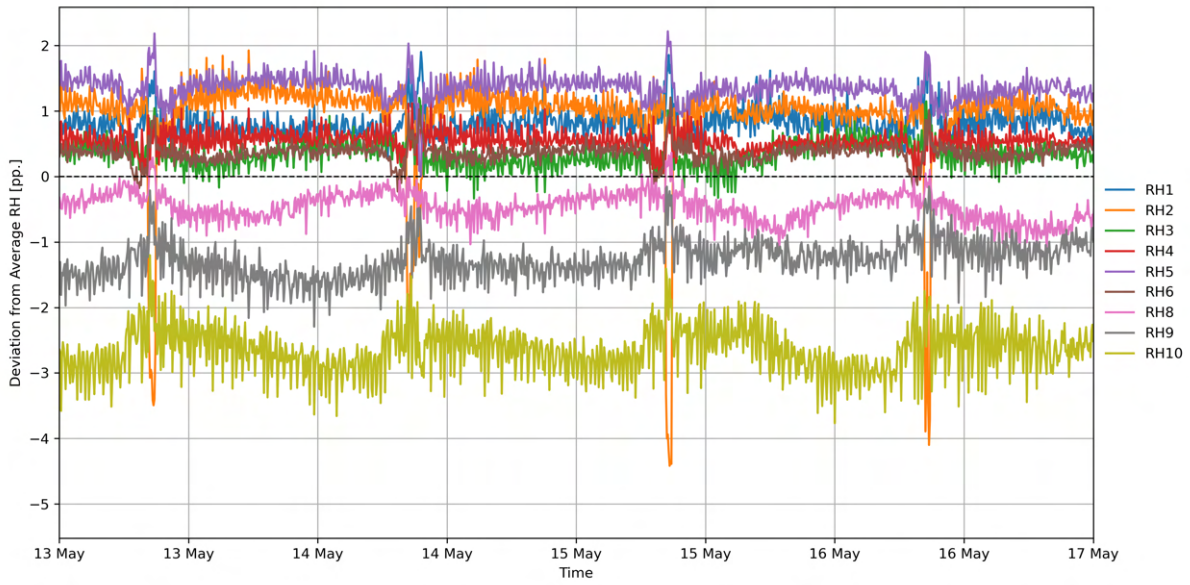

Figure A.26. The difference in RH measured inside of the climatic chamber.

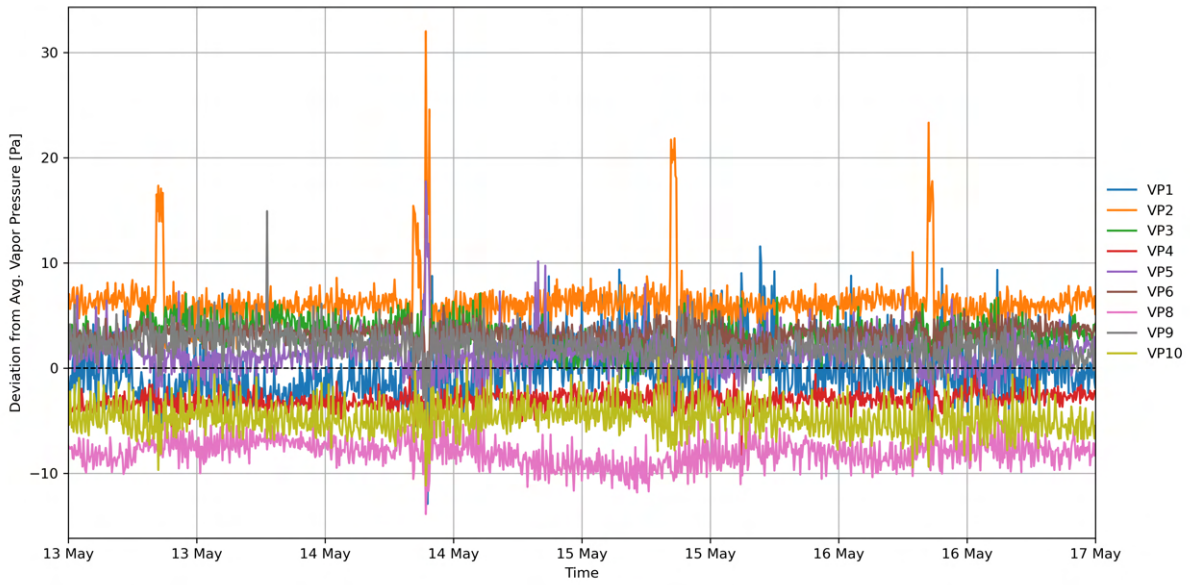

Figure A.27. The difference in vapour pressure inside of the climatic chamber.

The figures confirm the same trends observed earlier. The sensors located in the third column (Sensors 9 and 10) consistently record slightly higher temperatures compared to the rest of the room. As a result, these sensors show slightly lower relative humidity values, which is expected due to the temperature dependence of RH. However, the vapor pressure remains comparable across all nine sensors, indicating a uniform level of absolute moisture content. To support this, both the absolute maximum and average deviations for each sensor are presented in Table A.1 and A.2.

Table A.1. Absolute max variation for each sensor in the climatic chamber.

Sensor	S1	S2	S3	S4	S5	S6	S8	S9	S10
ΔT	0.7	1.7	0.4	0.4	0.6	0.3	0.4	0.7	1.1
ΔRH	1.9	5.2	1.2	1.2	2.2	1.2	1.2	2.3	3.8
ΔP	12.9	32.0	8.2	10.7	19.6	6.4	13.9	15.8	11.4

Table A.2. Absolute average variation for each sensor in the climatic chamber.

Sensor	S1	S2	S3	S4	S5	S6	S8	S9	S10
ΔT	0.2	0.2	0.1	0.2	0.4	0.1	0.1	0.3	0.7
ΔRH	0.7	1.0	0.3	0.4	1.2	0.4	0.5	1.0	2.4
ΔP	2.8	6.4	3.4	3.5	1.9	3.7	6.7	2.4	4.2

Based on these values, it can be concluded that the air within the climatic chamber is fairly well mixed, with the exception of the third column being slightly warmer due to the radiator. To achieve more uniform mixing throughout the chamber, the heat distribution from the radiator would need to be adjusted.

Appendix B

Element storage history and key events in the measurement campaign

In this project, a climatic chamber has been designed, made, and tested. In the chamber, wall elements can be tested with exposure to the weather. The climatic chamber is made as part of another project, where the aim is to test a variety of wall elements, with different biobased insulation and assemblies. The goal is to strengthen the knowledge about biobased wall constructions in order to accelerate sustainable construction and also validate numerical calculations with measurements.

It was initially the aim to install 21 different biobased wall elements, with varying insulation and construction. Originally the plan was to get 2-3 months of measurements to do an investigation of the impact of biobased insulation and construction principles. The process of designing and making the climatic chamber was more prolonged than expected, which imposed necessary adaptations and changes to the original plan to get some measurements before our thesis deadline.

Because of the delay, seven wall elements have been preliminarily installed, to do an initial investigation. This has gained valuable insights and experience with the element construction, sensor mounting, and element installation procedure, that can be applied going forward.

Due to the delay of the project, the measurement campaign started before all of the designed systems were in place and tuned. This was a necessary compromise if we wanted to be able to get some measurements from the walls before our thesis deadline. Table B.1 outlies the timeline for the wall elements and measurements, with the different key events. The measurements started with only the heating and cooling system working, but still not tuned. The consequences

of this are, however, not crucial for our initial investigation of the wall elements, because the indoor and outdoor boundary conditions have been measured. During the measurements, the humidification was set up and enabled. The ongoing process of tuning the systems and later enabling of humidification has meant that the indoor conditions have been varying.

Date	Passed time [weeks]	Description
5. Mar	0	The wall elements is assembled in an unheated workshop space at JDH-byg in Aarhus. They have stored the materials in the workshop prior to assembly. After assembly the elements are transported to Aalborg Univeristy. Samles of the used materials are taken, so initial water content can be determined.
6. Mar	0	The elements are stored in the unheated container with the material samples, with its temporal tarpaulin closure of the open front. This is shown on Figure B.2.
9. Apr.	5	The cooling coil is mounted and is turned on for 1 day.
15. Apr	6	The shared facade is finished.
17. Apr	6	The wall elements are in place and heating and cooling are enabled in the container, and measurements are started. There is ongoing tuning of the systems and adjustments, resulting in a varied indoor temperature. The facade wall is not fully insulated yet.
20. Apr	7	The facade wall is almost fully insulated, however not air tight.
2. May	9	The humidification system is enabled. The indoor humidity is however not regulated properly due to the facade not being air tight.
12. May	10	The facade wall is fully insulated and humidification is increased, so the relative humidity inside the chamber is increased and setpoint is maintained.
16. May	10	There was a breakdown in the computer logging the measurements inside the wall elements. This was first discovered the 25th of May. Therefore, there is a gap in our measurement data between these two dates.
17. May	10	The humidification systems malfunctions, and humidity drops.
19. May	11	The humidification is re-established and humidity levels are increased accroding to the setpoint.
25. May	11	Measurements is again logged for the wall elements.

Table B.1. Timeline for element storage and measurement campaign events.

The container was delivered as shown on Figure B.1. As seen on Figure B.1, the north-facing side of the container is temporarily closed with a tarpaulin, until the shared rain screen was built. The wall elements was stored here, while getting the setup ready, as shown in Figure B.2.

Figure B.1. The inside of the container, as it was delivered.

Figure B.2. The inside of the container with added insulation on the floor, and storage of the wall elements.

The insulated container was delivered with 40 mm of thermoset polyisocyanurate (PIR) insulation in the floor, which gives a U-value similarly, to the walls and ceiling, of $\sim 0.5 \frac{W}{m^2 \cdot K}$. In order to get representative measurements of the temperature and humidity conditions in the crawl space, 160 mm of PIR insulation is added on top of the floor. Thereby the floor has a U-value of $\sim 0.1 \frac{W}{m^2 \cdot K}$, and we get a realistic heat loss to the crawlspace. Figure B.3 shows the container with the open facade, before the shared rain screen is built.

Figure B.3. The container with the temporality tarpaulin open.

Appendix C

Design and construction documentation for wall elements.

This chapter will present and discuss the design of the wall elements to be used in the experimental climatic chamber setup. The design involves decisions on materials, construction composition, element dimensions, sensor placement, and sealing to ensure well-defined boundary conditions.

We have seven different wall elements designed so some different things can be investigated. Table C.1 provides an overview of the seven elements. The used DewMaster box for each element, which holds the temperature and relative humidity sensors, is also stated.

Element short name	Description (Insulation and vapour barrier)	DewMaster box
RW-PE	Rockwool insulation and PE-foil	Box 04
RW-PE-Hole	Rockwool insulation and perforated PE-foil	Box 01
HFI-PE	Hempfiber insulation and PE-foil	Box 13
HFI-PE-Hole	Hempfiber insulation and perforated PE-foil	Box 09
HFI-Paper	Hempfiber insulation and paper vapour retarder	Box 15
HFI-OSB4	Hempfiber insulation and OSB4 board	Box 19
WFI-Paper	Hempfiber insulation and paper vapour retarder	Box 11

Table C.1. Element short names and description. Overview of which DewMaster box is used for the element.

C.1 Wall element design drawings

Figure C.1 shows the composition of the wall elements, with its five layers. The five layers are the general composition of a wall, and what defines its hygrothermal performance.

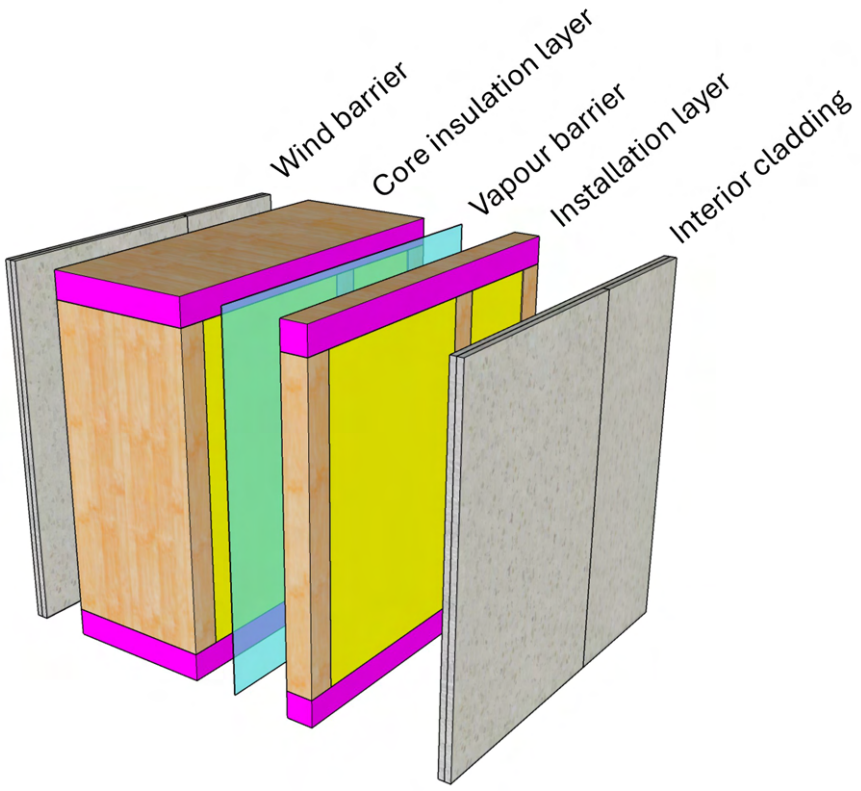

Figure C.1. The composition of the wall elements, with its five layers.

Table C.2 lists the five elements and their primary functions.

Table C.2. The layers and their function in a traditional wall construction, that define the hygrothermal performance.

1.	Interior cladding	Ensures that the wall is closed off and provides a neat finish on the inside.
2.	Installation layer	Ensures protection against perforation of the vapour barrier. With hygroscopic insulation, it potentially help regulate the indoor relative humidity.
3.	Water vapour barrier	Ensure airtightness and limit moisture transport from the indoors, and prevent condensation inside the wall.
4.	Insulation	Limit heat losses and reduce energy consumption.
5.	Wind barrier	Prevent infiltration of wind/air into the wall, to maintain effectiveness of insulation. Also limit moisture from the environment.
6.	Exterior cladding. Not shown in Figure C.1	Protect underlying layers from rain and UV, and provide external finish.

Figure C.2 illustrates the principle of moisture accumulation, and how the water vapour barrier limits moisture diffusion, shown by the profile of relative humidity through the wall.

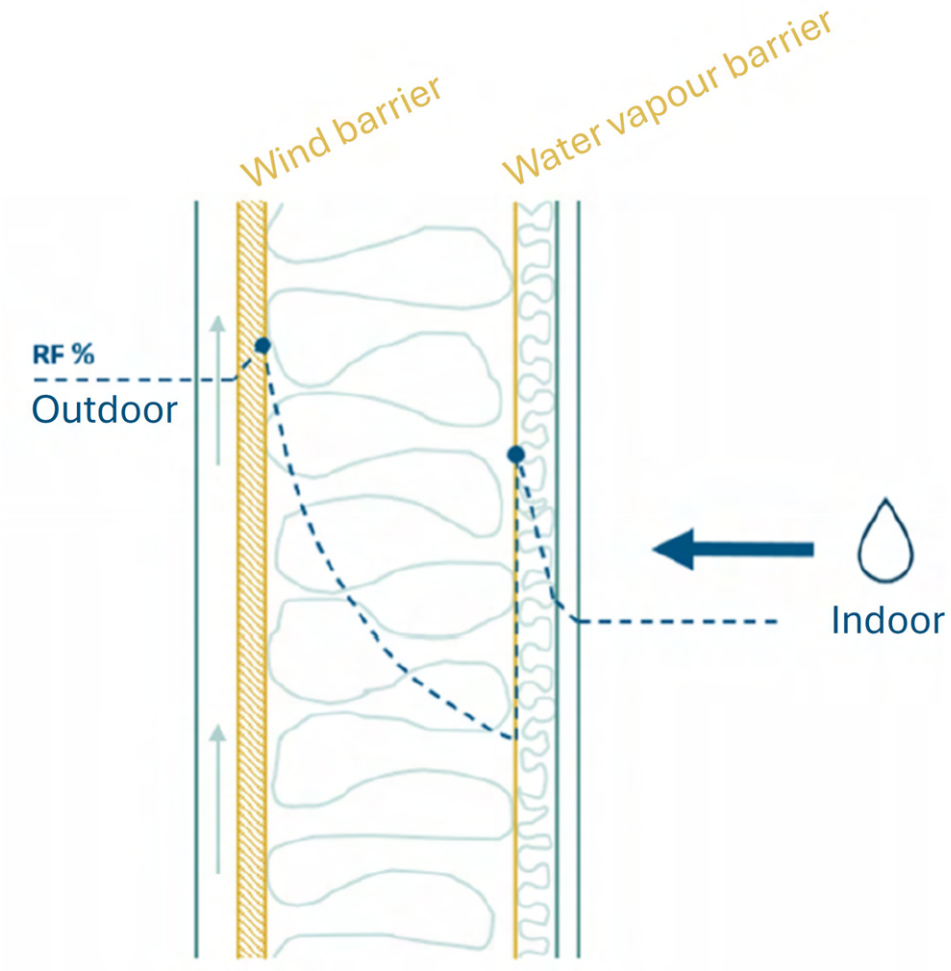

Figure C.2. Principle of moisture accumulation in front of diffusion resistant layers indicated by relative humidity. Adaptation from [42].

Information about the hygroscopic properties of materials, and how they compare. Points: Wood is very hygroscopic, biobased insulation is hygroscopic, Concrete, bricks, and mineral-based insulation are not.

C.2 Element dimensions and materials

We are creating this experimental setup to allow for an exploratory investigation of various bio-based wall elements, making it preferable to have many variation possibilities. For this reason, the elements are scaled to be small, so the setup can fit many elements. When scaling down the elements, it is important to consider if and how this will impact the physics and possibly account for it. This potential modelling uncertainty could be minimized by having the elements in true size.

The insulation makes up most of the wall by volume, and therefore it is interesting to see the impact when using biobased insulation with hygroscopic properties, opposed to mineral-based insulation. We want to investigate how the hygroscopic properties of the biobased insulation influence the moisture conditions inside the wall. To evaluate this, the temperature and relative humidity throughout the wall will be measured. For light walls, the insulation layer is inhomogeneous with wood studs every 600 mm, by standard. Additional wood framing is added during window installation, so the wood percentage ends up being in the range of 10-20% commonly. Wood is very hygroscopic, and it is therefore interesting to also investigate the humidity conditions around the wood.

For the investigation of the biobased insulation, it is important to ensure that there is a one-dimensional (1D) heat and moisture transfer through the element. We want to measure the isolated performance of the insulation and eliminate the influence from the boundary. This is also needed in order to use the measurements for comparison with numerical 1D hygrothermal simulations done with WUFI and BSim. This requirement limits how small the elements can be.

As a balance between making the elements small, obtaining 1D heat and moisture transfer, and preserving some realism, the element dimensions are determined to be 600 mm by 600 mm with varying depth. A drawing of the elements is shown on Figure C.3, with marking of the sections for the Figure C.4 and Figure C.5. To document the element design shown on Figure C.3 and Figure C.5, photographs of the construction process are taken and presented in section C.4 and section C.5.

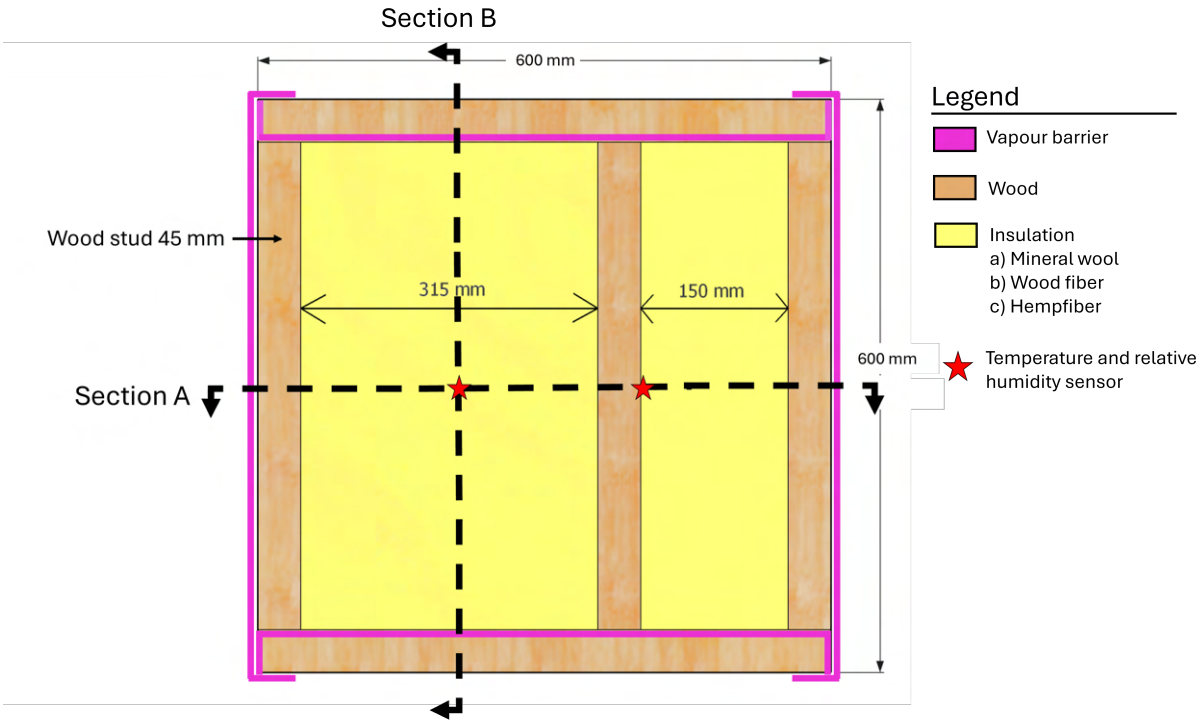

Figure C.3. As-built front view drawing of core insulation in the wall elements.

The stars show the placement of the two measurement columns through the elements. The figure shows how a vapour barrier is mounted around the element, to avoid moisture transport through the sides of the element. We want to ensure we only have moisture transport from the inside to the outside through the element. The vapour barrier is on the inside in the top and bottom, so the wood percentage is kept in the common range. On the sides, the vapour barrier is mounted on the outside, so there is only one penetration of the barrier that needs to be sealed.

On Figure C.4 a horizontal section in the middle of the element is seen. Here the stars show the placement of sensors inside the element.

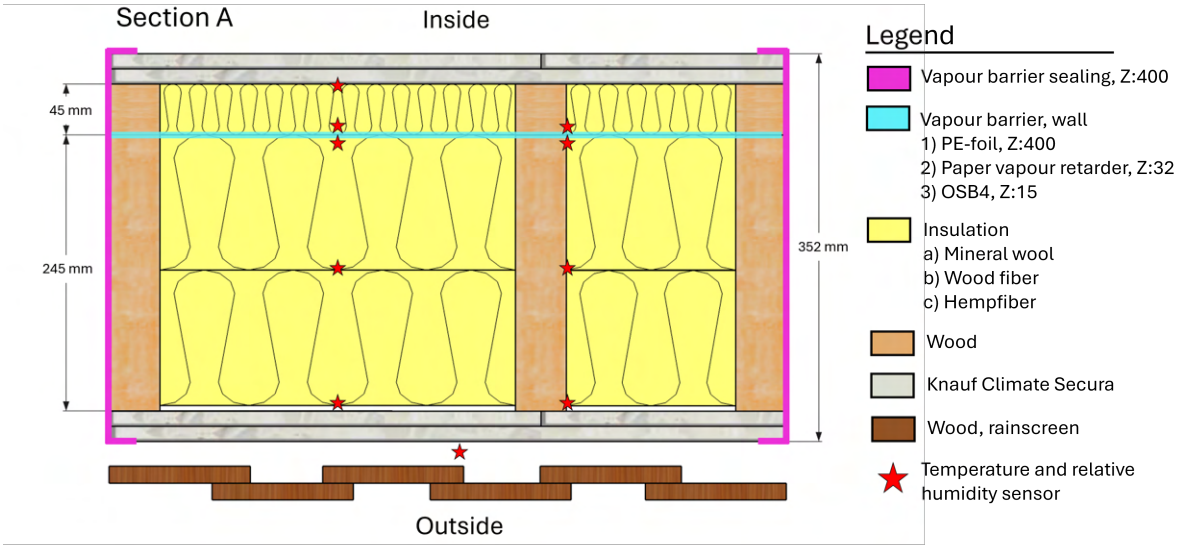

Figure C.4. Section A of element.

The sensors through the middle of the wide insulation layer are the primary measurement column.

Figure C.5 shows the vertical section of the element.

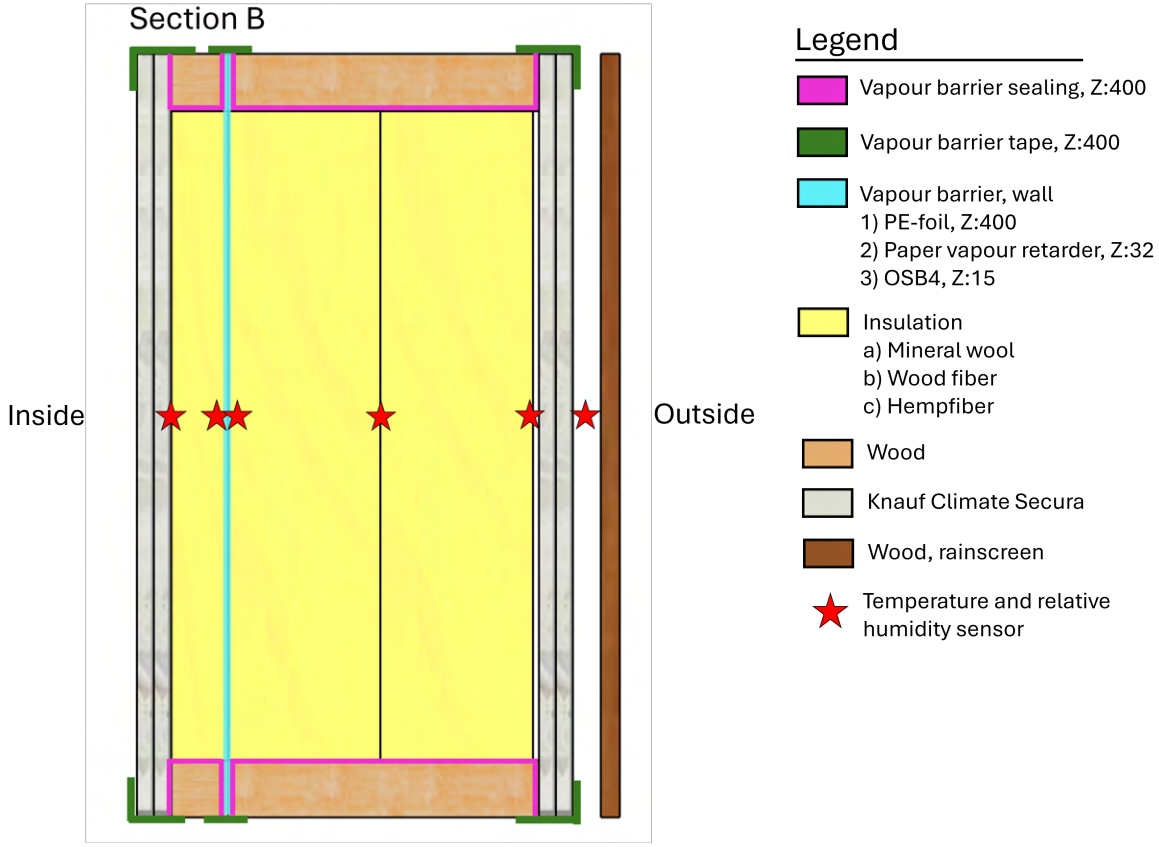

Figure C.5. Section B of element.

Here it can be seen that the vapour barrier for the top and bottom sealing is wrapped around the timber frame constituting the installation layer and core insulation layer. Then the vapour barrier for the wall element is clamped between the two timber parts. This construction principle is easy to construct and the joint is fully sealed with tape on top.

C.3 Element assembly 3D drawings

To better visualize the construction composition of the elements, the next figures are 3D drawing starting with an exploded view on Figure C.6, and then the parts are gradually joined. On Figure C.6 you can see the two layers of gypsum that are on the inside and outside of the element. To follow construction practice, one of the layers is one intact piece of gypsum, while the other layer is two pieces joined on top of the timber stud inside the element. Figure C.6 shows how the purple vapour barrier is wrapped around the timber constituting the top and bottom of the element. The purple elements at each side are the vapour barrier for the sealing of the element sides as shown on Figure C.3. The turquoise element is the vapour barrier inside the wall, which varies between the seven elements. Inside the core insulation, two batts of insulation are used to obtain the depth of 245 mm.

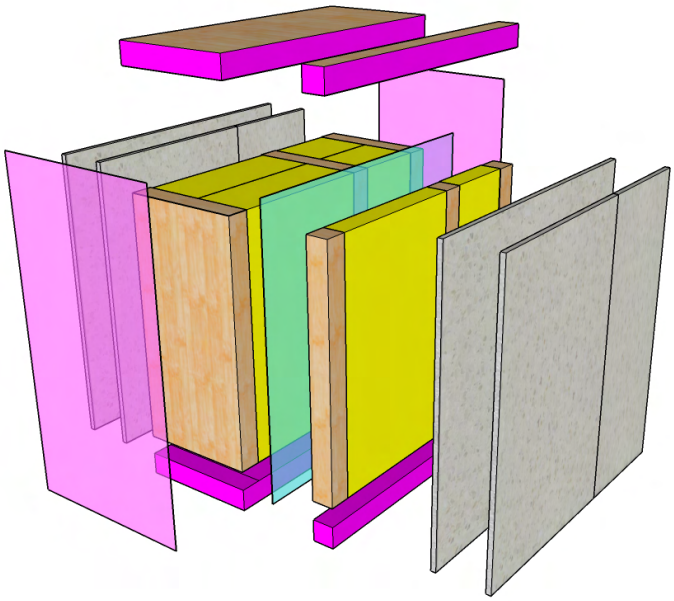

Figure C.6. Exploded view of wall element.

On Figure C.7 it is clearly visible how the vapour barrier for the wall is clamped between the

installation layer and core insulation layer.

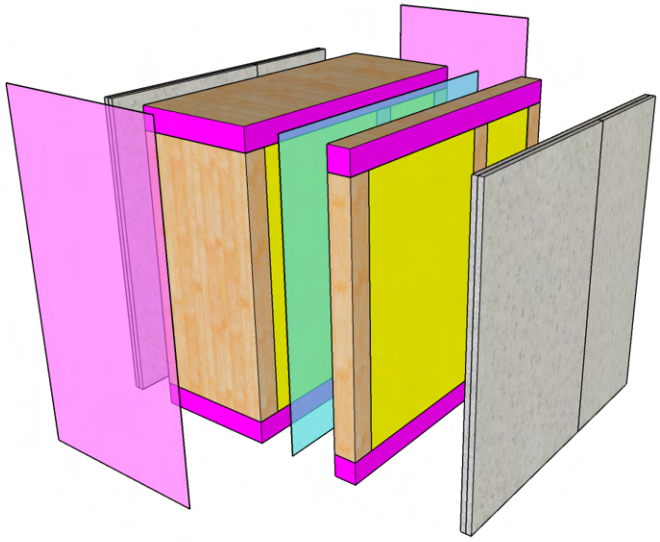

Figure C.7. Partially exploded view of wall element.

Figure C.8 show the element assembled without the gypsum front, and the insulation inside is hidden.

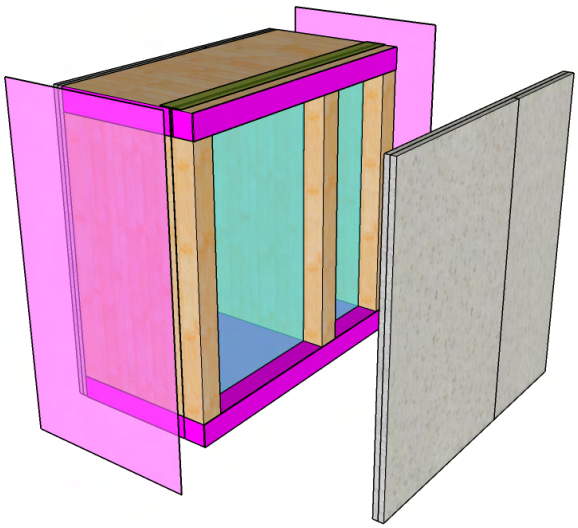

Figure C.8. Wall element without interior cladding.

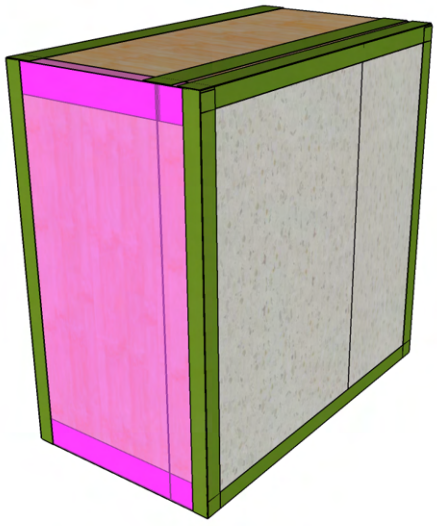

Figure C.9. Wall element without interior cladding.

Here the placement of the vapour barrier between the installation layer and core insulation is visible. On Figure C.8 the vapour barrier tape is added on top of the clamped joint of the

turquoise vapour barrier, to complete the seal. Figure C.9 shows the assembled element. Here the purple vapour barrier is mounted on the sides, and secured with more vapour barrier tape. On Figure C.9 the rain screen is not shown because the seven elements will share one common rain screen.

C.4 Sensor placement documentation

The sensors are placed according to Figure C.4, which is documented with a series of photographs. Holes are drilled in the sides of the elements in order to route the sensors into the element. This is illustrated on Figure C.10.

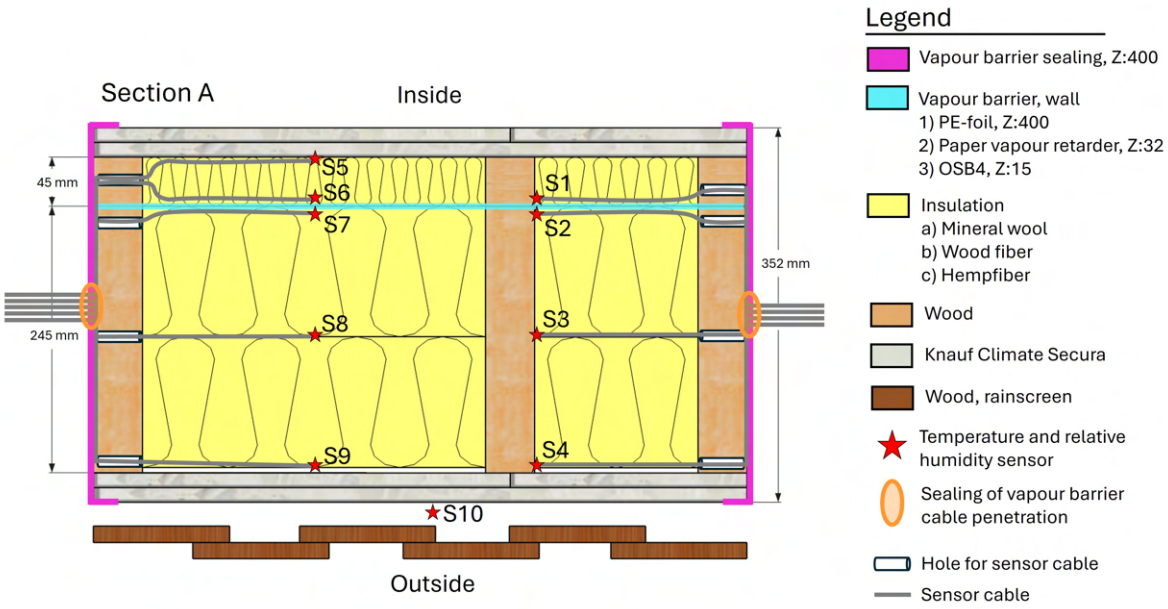

Figure C.10. Routing of sensor cables.

The sensors are numbered from 1 to 10 in the DewMaster box and log-file, and they are placed identically in all elements. The cables are bundled on the exterior to create a single penetration through the vapour barrier, which is easier to seal. This is shown in section C.5 on Figure C.23.

In the element, the sensors are fastened to their location with vapour barrier tape. This worked well and was secure when the sensors were attached to the vapour barriers (PE-foil, Paper, OSB4). But when the sensors had to be fastened on top of the insulation, it was difficult to get the tape to stick well. We managed to make it work and anticipate the sensors will stay in place, aided by the minor compression of the sensors against the materials in the closed element. Going forward, another technique is preferred so the sensors are guaranteed to stay fixated in the

correct position. A solution could be to attach a fishing line, which does not interfere with the construction, to the timber sides and use it as an anchoring point. It is crucial that the sensors stay in place so the measurements are reliable and can be used to calibrate and compare with numerical models.

The placement of sensors in the installation layer at the vapour barrier is shown on Figure C.11. On the figure the DewMaster box, where the ten sensors connect to, is visible in front of the element.

Figure C.11. Element with PE-foil and sensors placement in the installation layer.

Figure C.12 shows the element with an OSB4 board as a water vapour barrier, and the sensor mounted onto it in the installation layer. On Figure C.13 insulation is inserted, and the sensor

for the big insulation compartment just behind the interior cladding can be seen.

Figure C.12. Photo showing the sensor placed in the installation layer. in front of the OSB4 water vapour barrier.

Figure C.13. Photo showing the sensor placed in the insulation measurement column, just behind the interior cladding.Photo showing the sensor placed in the installation layer. in front of the OSB4 water vapour barrier.

Figure C.14 is a close-up of the sensors mounted on the vapour barrier, in the smaller insulation compartment. Here the sensor mounted on the other side in the core insulation layer can be seen through the PE-foil. Figure C.15 shows how the sensor is sandwiched into the insulation batt, so it is in the middle of the core insulation. For the RockWool insulation, the compartment is filled with a 145 mm batt and a 95 mm batt. A slit is cut into the 145 mm batt, so the sensor is placed in the middle of the core insulation.

Figure C.14. Photo showing the sensors placed before and after the water vapour barrier.

Figure C.15. Photo showing the sensor placed in the insulation measurement column, just behind the interior cladding.

For the wood fiber and hemp fiber insulation, two batts of 120 mm are used. One batt takes up half the space, so the middle sensor is directly mounted on top of the batt, which is seen on Figure C.16. The second batt is put in, and the sensors behind the wind barrier are mounted onto the insulation layer, seen on Figure C.17.

Figure C.16. Photo showing the sensors placed in the middle of the core insulation layer.

Figure C.17. Photo showing the sensors placed just behind the wind barrier.

During construction, the vapour barrier sealing of the element was visually inspected to ensure it is intact. Figure C.16 shows how damage at the bottom has been patched with vapour barrier tape.

The last sensor available in the DewMaster box is mounted in the ventilated cavity behind the rain screen. This is done as part of the procedure to place the wall elements into the container. Figure C.18 shows how the sensor is fixed with fishing line, so it is placed in the middle in front of the element. After the sensor is mounted in the cavity, the wall elements are lifted into place. The installation procedure of the elements and the experimental setup inside the climatic chamber is further described in Appendix A.

Figure C.18. Mounting of sensor in ventilated cavity

Figure C.19 is a photograph from above looking down into the ventilated cavity, when the wall element is placed and the sensor can be seen.

Figure C.19. Sensor placement inside ventilated cavity

C.5 Sealing of element documentation

It is important that the elements are sealed, so unintentional moisture is not leaking into the element. Figure C.20 shows how the top and bottom are wrapped with PE-foil.

Figure C.20. Element with PE-foil, showcasing how the top and bottom is wrapped with foil. Here the sensor cables are pulled through the holes into the element.

Figure C.21 is a close-up of the joint of the installation layer, the elements' water vapour barrier and core insulation layer. It shows how the two timber pieces for the top of the insulation layer and core insulation are wrapped in PE-foil. Figure C.22 shows the layers and the holes for the sensor cables that are filled with sealant after the cables have been routed.

Figure C.21. Close-up of the clamped joint between the installation layer, the walls vapour barrier and the core insulation layer.

Figure C.22. Side view of the element, with holes drilled for the sensor cables.

On Figure C.23 the cable holes are filled with sealant. To keep the cables in place and prevent misplacement, vapour barrier tape is used to attach the cables to the outside of the element. Figure C.23 shows the sealing of the sides, with vapour barrier. It shows how the cables are bundled to get one penetration that needs to be sealed. Figure C.24 shows the fully sealed side, where more sealant is used to close off the area where the cables exit the element.

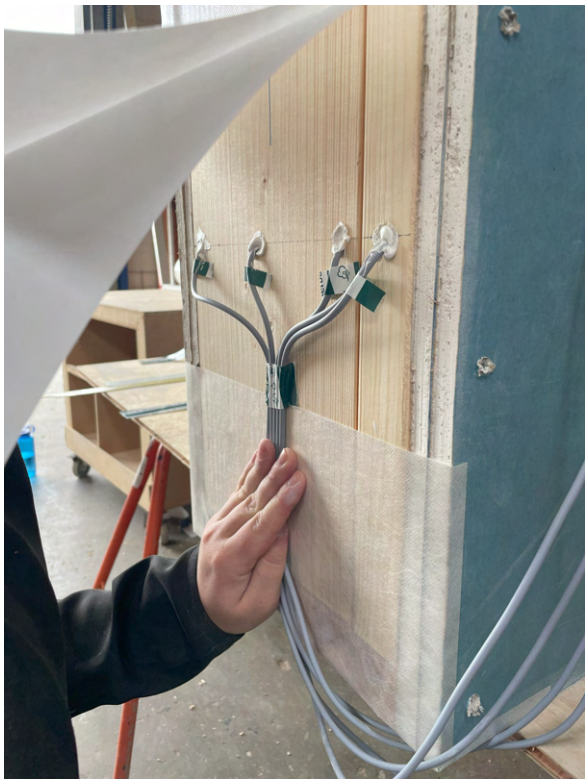

Figure C.23. Mounting of sealing tape, for the sides of the element. It shows how the cable holes is filled with sealant to make it air tight.

Figure C.24. After mounting sealing tape on the sides, additional sealant was used to close the cable penetration at the overlap between the two vapour barrier sheets.

C.6 Representation of a degraded vapour barrier documentation

In two of the seven elements, the vapour barrier is perforated with two one-centimetre holes. This is done to investigate the consequences of a degraded water vapour barrier and how a wall with mineral- and biobased insulation responds. This investigation is outside the scope of this project and will only be touched upon briefly. Two holes have been made, because we anticipate that convection of moist air poses the biggest risk. The holes are made with a 10 mm drill bit, and they are shown on Figure C.25, Figure C.25, Figure C.27 and Figure C.28.

Figure C.25. PE-foil perforation in element RW-TPE in the middle of the wide insulation layer.

Figure C.26. PE-foil perforation in element RW-TPE at the timber stud.

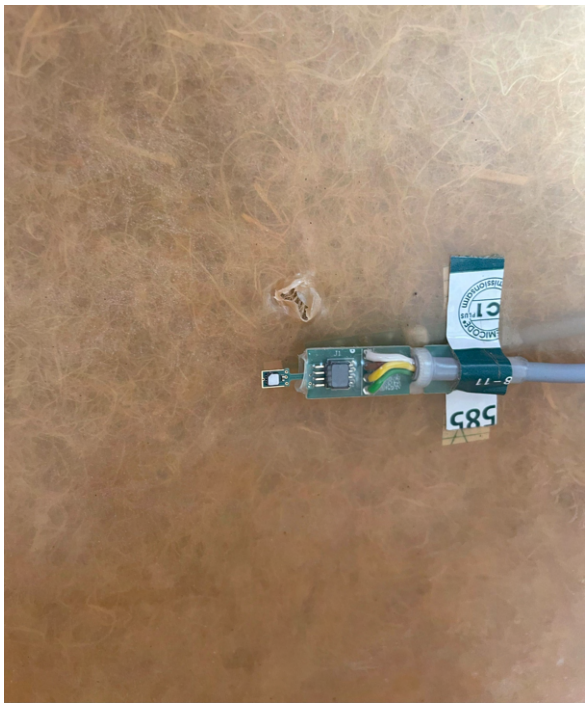

Figure C.27. PE-foil perforation in element HFI-TPE in the middle of the wide insulation layer.

Figure C.28. PE-foil perforation in element HFI-TPE at the timber stud.

The size of the perforation is chosen, so it should be equivalent to 3-4 times the expected

infiltration rate for new construction. The hole is made a little above the sensor.

The water vapour barrier is a critical component when it comes to moisture. It is very essential that it is airtight to avoid convection and the risk of condensation inside the wall. This is something that can be a challenge with conventional PE foil, which is susceptible to perforation and faulty overlap sealing. Besides installation errors and damages, there is also a time aspect of how well a vapour barrier retains its resistance during its lifetime. To address these challenges, a board-based water vapour barrier, such as OSB4, can be applied instead. The trade-off is that the OSB4 has a 20 times lower water vapour diffusion resistance, which imposes different challenges. Besides installation errors and damages, it is interesting how well a vapour barrier retains its resistance over time and how it degrades.

Appendix D

Data acquisition - DewMaster

To measure temperature and humidity, digital Sensirion SHT75 and SHT85 sensors are used. Each DewMaster box consists of one Arduino, with 10 SHT sensors connected. The Arduino handles data acquisition and sensor communication, compiling the measurements into a single formatted string containing the temperature and relative humidity data from all sensors.

The string is transferred to a computer, where it is processed and logged using LabView. In LabView, the string is parsed, so that temperature and relative humidity values can be extracted for each sensor and logged in table form.

In this Appendix, the DewMaster boxes, the Arduino codes, and the LabView code are described.

D.1 DewMaster boxes

A DewMaster box consists of an Arduino MEGA 2560 with 10 SHT sensors connected. One complete box is shown on Figure D.1.

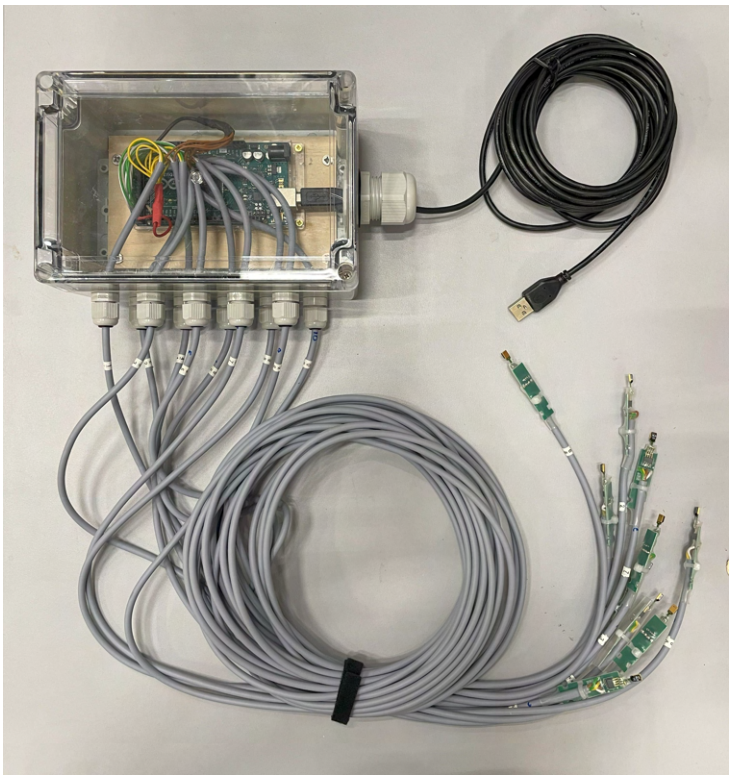

Figure D.1. Picture of a DewMaster box, with its 10 SHT sensors, measureing temperature and relative humidity.

Each sensor uses four wires: power, ground, serial clock (SCK), and serial data (DATA). The clock and data wires are individually soldered to the Arduino's digital I/O pins. Specifically, the clock lines are connected to the even-numbered pins from 24 to 42, while the data lines are connected to the corresponding odd-numbered pins from 25 to 43. The ground wire from all of the sensors is combined in a Wago connector, with one new wire connected to the Arduino's ground pin. The power wires are combined in the same way and connected to the Arduino's 5V output. A picture of the Arduino wiring and sensor connections within a DewMaster box is shown in Figure D.2.

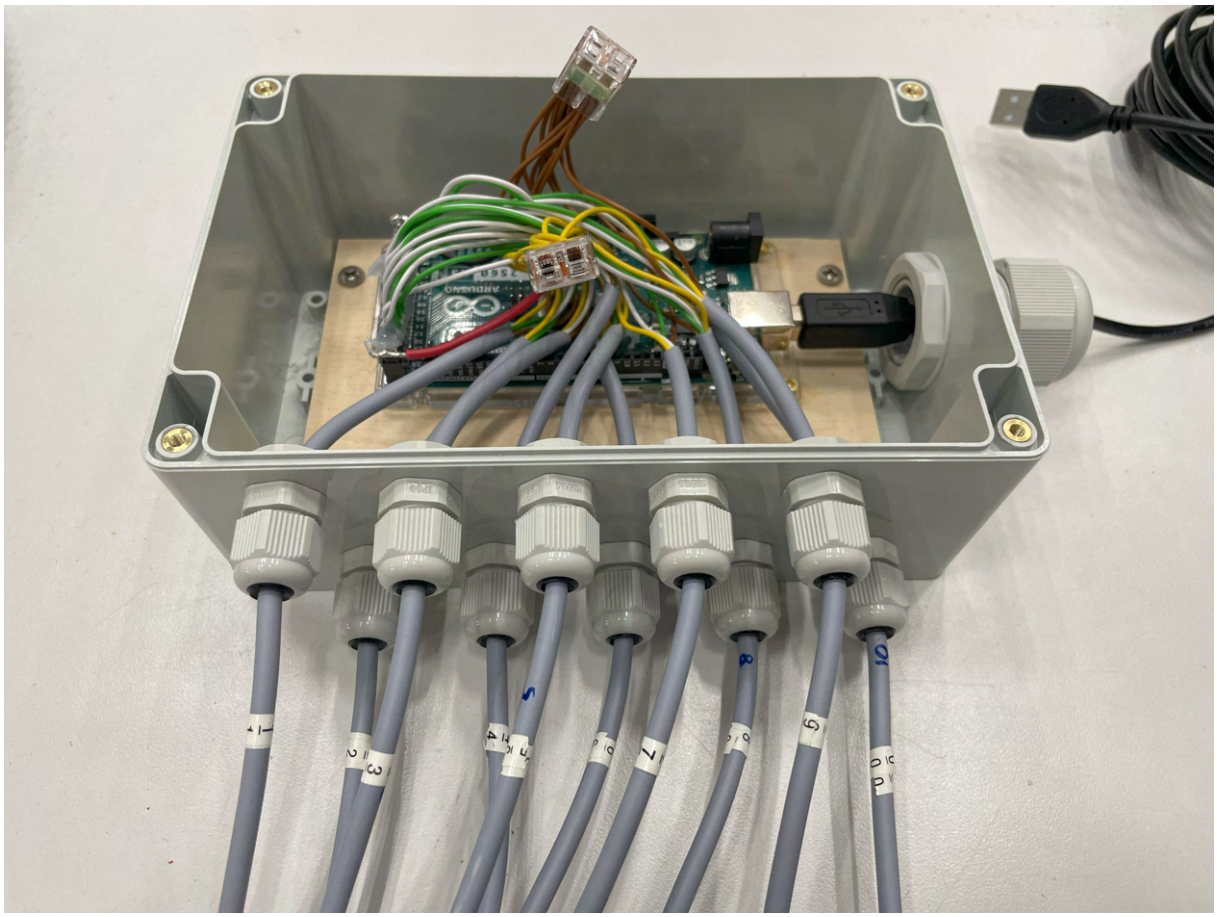

Figure D.2. Picture of a DewMaster box. The colors correspond as follows: Yellow = Power, Brown = Ground, White = Serial data, Green = Serial clock.

The figure also shows the cable numbering. Each cable is numbered on each end, so it is easy to keep track of the sensors. The number corresponds to the sensor number in the output from the Arduino. This is done identically for each box. In total, 24 DewMaster boxes are built. 13 of those are with the SHT75 sensors as we had them available and 11 are with new SHT85 sensors. The difference between the two sensors is found in Appendix E.

D.2 Arduino - Data acquisition

Two different Arduino programs have been developed for the DewMaster boxes — one for the SHT75 sensors and one for the SHT85 sensors. This distinction is necessary because the communication protocol changed from the digital SBus used by the SHT75 to I2C in the SHT85, requiring corresponding changes in the Arduino code.

Functionally, the two codes work the same. They read the digital signals and convert them to a temperature and relative humidity with the conversion formulas given in the respective

datasheets [43, 30]. The formulas for SHT85 are given in Equation D.1

$$Temperature = -45 + 175 \cdot \frac{rawTemperature}{65535} \qquad Humidity = 100 \cdot \frac{rawHumidity}{65535} \tag{D.1}$$

These values are formatted into a string as follows:

Sx:Tx:*Temperature*Hx:*Humidity*Dx:*Dewpoint*endx

In this string, x denotes the sensor number e.g. 1-10. Although dew point measurements are not currently needed, a fixed placeholder value, 10, is included to maintain compatibility with LabView, which parses the string by separating temperature and humidity based on this structure.

The code loops over all 10 of the sensors appending each sensor's string to a singular output string. If one sensor fails to return data, *ERR* replaces the temperature or humidity value, and the loop continues to the next sensor.

The primary difference in the SHT85 version is the initialization of I2C communication and assignment of I2C addresses instead of digital ports. This design allows all DewMaster boxes to be built identically. If a box originally using SHT75 sensors loses functionality, its sensors can be replaced with SHT85 models. Uploading the SHT85-specific code will restore full functionality without hardware modifications.

The two codes can be seen in Listing D.1 and D.2.

D.3 LabView - Data processing and logging

The LabView code to handle the Dewmasters consists of three parts. The first part handles the reading of the data. The second part calibrates the data, and the third part handles the logging of the data.

D.3.1 Part 1 - Reading of data

The first part of the LabView program reads the string produced by the Arduino programs. The code continuously reads an input string and searches for specific character markers that indicate temperature ('T') and humidity ('H'), and extracts the associated numeric data.

The core of the VI consists of a **While Loop** that runs continuously, with an embedded **For Loop** used to iterate through segments of the input string. The incoming string is analyzed character by character, and conditional checks are performed using a **Case Structure** to identify

when temperature or humidity data is present. When valid data is found, it is converted from a string to a numeric format.

The code retains the previous values using **Shift registers** and only updates if new valid data is detected. This prevents errors from shoving. The block diagram of the reading part from LabView is seen on Figure D.3.

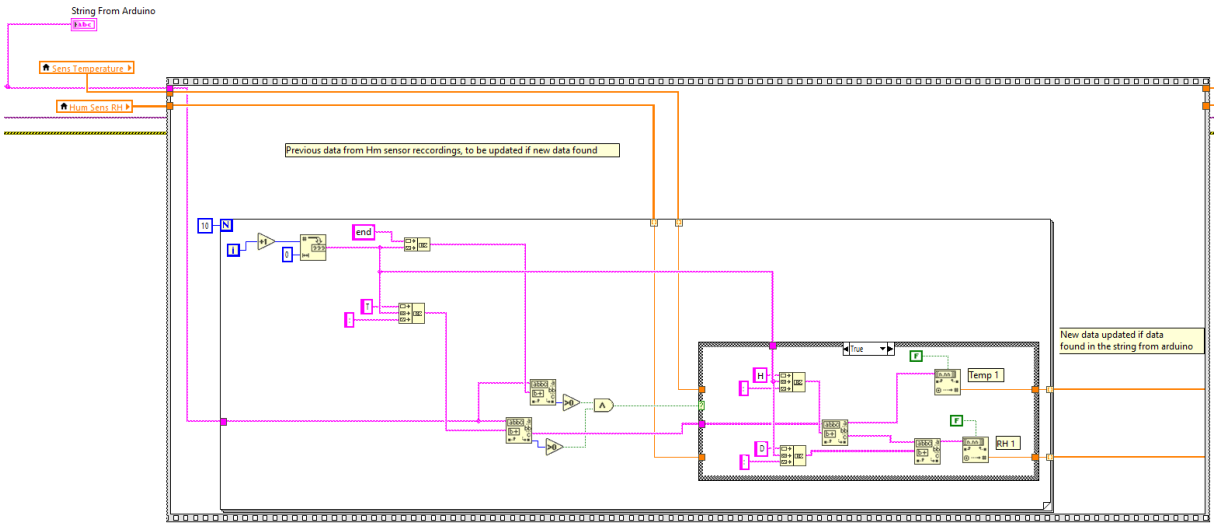

Figure D.3. The block diagram handling the reading of the Arduino.

D.3.2 Part 2 - Calibration of sensors

This part of the LabVIEW code handles the calibration and adjustment of the raw sensor data received from the Arduino. As the temperature and humidity are dependent on each other, a multiple linear regression is used. This gives two functions in the form seen in Equation D.2 and D.3. The calibration formulas can be seen in Appendix E and the block diagram for how it is implemented in LabView is shown on Figure D.4.

$$T_{corr} = \beta + \alpha_0 \cdot T + \alpha_1 \cdot RH \tag{D.2}$$

$$RH_{corr} = \beta + \alpha_0 \cdot T + \alpha_1 \cdot RH \tag{D.3}$$

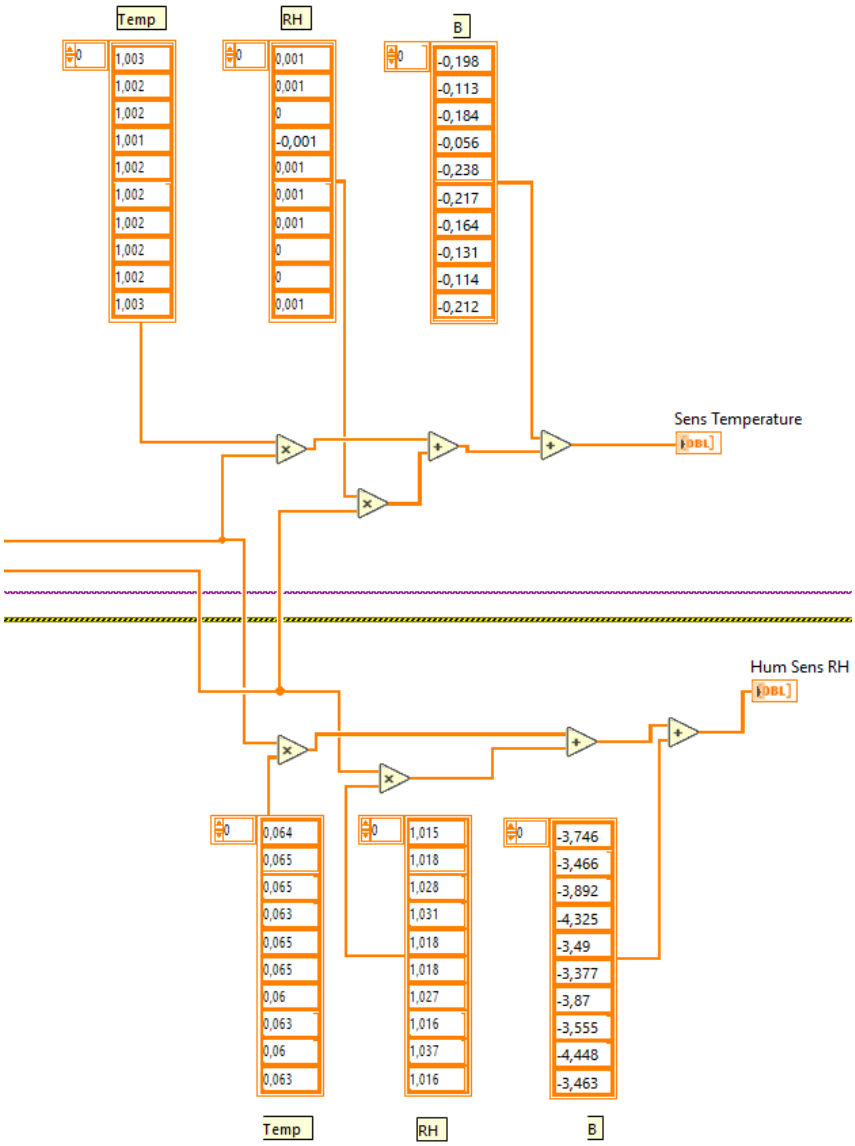

Figure D.4. The block diagram handling the calibration of the sensors.

D.3.3 Part 3 - Logging the data

The last part of the LabView handles the creation of a logfile and logging the data. First, the path of the logfile is input as a string, where the program is set to "replace or create with confirmation". Furthermore, an array with the headers of the logfile is configured. A **Flat Sequence Structure** secures that the program executes the blocks in the correct order. This order is: Create the logfile, collect timedata, write the headers and timedata in the file. After this, the *Sens temperature* and *Sens RH* from subsection D.3.2 are written into the file at the interval given in the *Time between logs*-variable. The code is seen on Figure D.5.

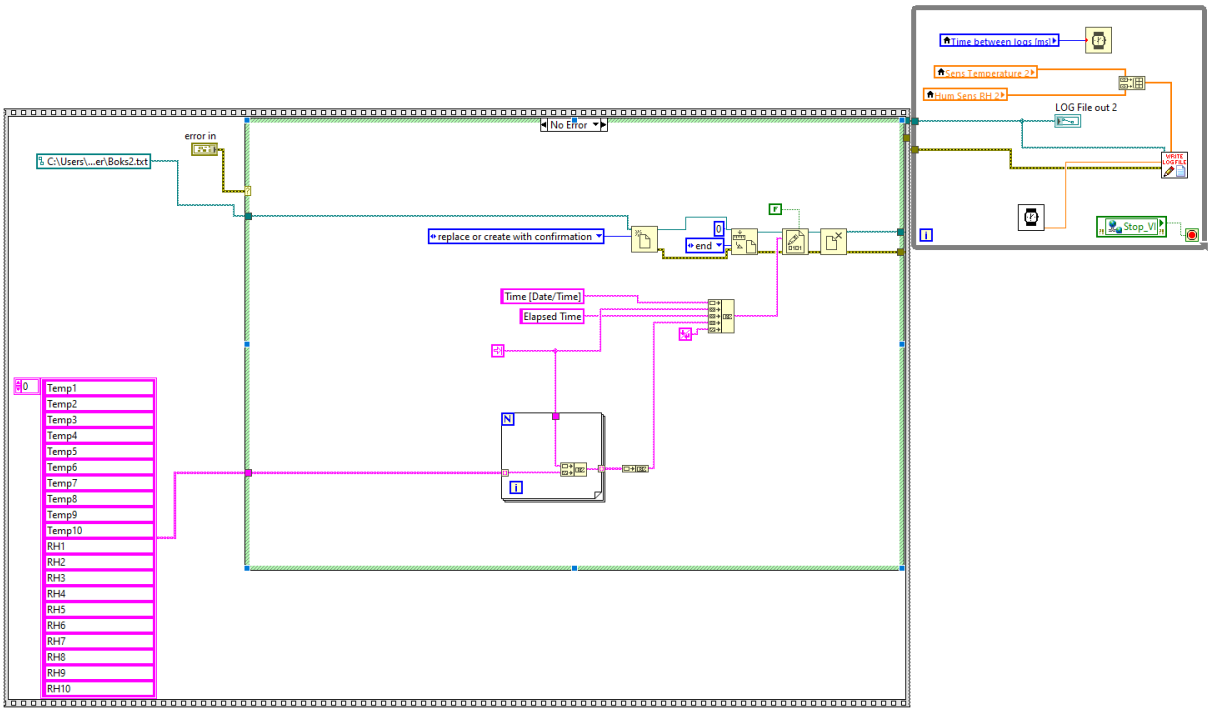

Figure D.5. The block diagram handling the logging of the data.

Listing D.1. SHT75 code

```
#include <Sensirion.h>

// Define data and clock pins for the 10 sensors
const uint8_t dataPins[] = {25, 27, 29, 31, 33, 35, 37, 39, 41, 43};
const uint8_t clockPins[] = {24, 26, 28, 30, 32, 34, 36, 38, 40, 42};

// Create an array of Sensirion objects for each sensor
Sensirion sensors[] = {
    Sensirion(dataPins[0], clockPins[0]),
    Sensirion(dataPins[1], clockPins[1]),
    Sensirion(dataPins[2], clockPins[2]),
    Sensirion(dataPins[3], clockPins[3]),
    Sensirion(dataPins[4], clockPins[4]),
    Sensirion(dataPins[5], clockPins[5]),
    Sensirion(dataPins[6], clockPins[6]),
    Sensirion(dataPins[7], clockPins[7]),
    Sensirion(dataPins[8], clockPins[8]),
    Sensirion(dataPins[9], clockPins[9]),
};

void readAllSensors() {
    String output = ""; // Initialize an empty string for the output line

    for (int i = 0; i < 10; i++) {
        uint16_t rawTemperature = 0;
```

```
26          uint16_t rawHumidity = 0;
27
28          // Initialize placeholders for temperature and humidity
29          float temperature = 0;
30          float humidity = 0;
31
32          // Read raw temperature
33          if (sensors[i].meas(TEMP, &rawTemperature, true) == 0) {
34              // Convert raw temperature to Celsius
35              temperature = -40.1 + 0.01 * rawTemperature;
36          } else {
37              output += "S" + String(i + 1) + ":T" + String(i + 1) + ":ERRH" + String(i + 1) + ":D" +
                    String(i + 1) + ":10end" + String(i + 1) + " ";
38              continue; // Skip to the next sensor if temperature read fails
39          }
40
41          // Read raw humidity
42          if (sensors[i].meas(HUMI, &rawHumidity, true) == 0) {
43              // Convert raw humidity to percentage
44              humidity = -2.0468 + 0.0367 * rawHumidity - 1.5955e-6 * rawHumidity * rawHumidity;
45          } else {
46              output += "S" + String(i + 1) + ":T" + String(i + 1) + ":" + String(temperature, 2) + "H" +
                    String(i + 1) + ":ERR:D" + String(i + 1) + ":10end" + String(i + 1) + " ";
47              continue; // Skip to the next sensor if humidity read fails
48          }
49
50          // Append the sensor data to the output string
51          output += "S" + String(i + 1) + ":T" + String(i + 1) + ":" + String(temperature, 2) + "H" +
                 String(i + 1) + ":" + String(humidity, 2) + "D" + String(i + 1) + ":10end" + String(i + 1) + "
                 ";
52      }
53
54      // Remove trailing spaces and print the output line
55      output.trim(); // Trim trailing spaces
56      Serial.println(output);
57  }
58
59  void loop() {
60      readAllSensors();
61      delay(100); // Wait before the next reading
62  }
```

Listing D.2. SHT85 code

```
1   #include <SoftwareWire.h>
2
3   const uint8_t dataPins[] = {25, 27, 29, 31, 33, 35, 37, 39, 41, 43};
4   const uint8_t clockPins[] = {24, 26, 28, 30, 32, 34, 36, 38, 40, 42};
5   const uint8_t numSensors = 10;
```

```
6  const uint8_t SHT85_ADDRESS = 0x44;
7
8  SoftwareWire* sensorWires[numSensors];
9
10 void setup() {
11     Serial.begin(9600);
12     for (uint8_t i = 0; i < numSensors; i++) {
13         sensorWires[i] = new SoftwareWire(dataPins[i], clockPins[i]);
14         sensorWires[i]->begin();
15     }
16 }
17
18 void loop() {
19     String output = "";
20     for (uint8_t i = 0; i < numSensors; i++) {
21         float temperature, humidity;
22         if (readSHT85(*sensorWires[i], temperature, humidity)) {
23             output += "S" + String(i + 1) + ":T" + String(i + 1) + ":" + String(temperature, 2) +
24                       "H" + String(i + 1) + ":" + String(humidity, 2) +
25                       "D" + String(i + 1) + ":10end" + String(i + 1) + " ";
26         } else {
27             output += "S" + String(i + 1) + ":T" + String(i + 1) + ":--.--" +
28                       "H" + String(i + 1) + ":--.--" +
29                       "D" + String(i + 1) + ":10end" + String(i + 1) + " ";
30         }
31     }
32     output.trim();
33     Serial.println(output);
34     delay(1000);
35 }
36
37 bool readSHT85(SoftwareWire &wire, float &temperature, float &humidity) {
38     wire.beginTransmission(SHT85_ADDRESS);
39     wire.write(0x24); // Command for high repeatability measurement
40     wire.write(0x00);
41     if (wire.endTransmission() != 0) {
42         return false;
43     }
44     delay(15); // Wait for the measurement to complete
45
46     uint8_t bytesReceived = wire.requestFrom((int)SHT85_ADDRESS, (int)6);
47     if (bytesReceived != 6) {
48         return false;
49     }
50
51     uint16_t rawTemperature = (wire.read() << 8) | wire.read();
52     wire.read(); // CRC byte, can be ignored
53     uint16_t rawHumidity = (wire.read() << 8) | wire.read();
```

```
54      wire.read(); // CRC byte, can be ignored
55
56      temperature = -45 + 175 * (rawTemperature / 65535.0);
57      humidity = 100 * (rawHumidity / 65535.0);
58      return true;
59  }
```

Appendix E

DewMaster SHT sensor calibration

This appendix covers the calibration of the SHT75 and SHT85 sensors, that are used in the DewMaster boxes. In order to calibrate the DewMaster SHT-sensors we have placed them inside a climatic chamber, to maintain a stable temperature and humidity and get different calibration points that cover our range.

E.1 Equipment

- Climate chamber
- Hygrodat100 - Reference humidity
- F200 - Reference temperature
- SHT75 and SHT85 sensors
- Sensor mounting device
- Computer for data collection

E.2 Sensirion sensor specifications

From the data sheets, the relevant specifications for the two sensors are stated in table Table E.2. Some of the parameters vary depending on the operating conditions, so for simplicity, we have only stated the worst performance within our operating range. Our operating range is from -15℃ to 30℃ and from 35% RH to 95% RH, which is further explained in section 2.2 and section 4.1.

Table E.1. Specifications for temperature and humidity for SHT75 and SHT85 sensors [43] [30].

Humidity specifications

Parameter	Unit	SHT75	SHT85
Typ. accuracy	%RH	±1,8 @10-90%RH	±1,5 @0-80%RH
Max. accuracy	%RH	±3 @5-95%RH	±2,75 @5-95%RH
Typ. resolution	%RH	0,05	0,01
Typ. repeatability	%RH	±0,1	±0,21
Hysteresis	%RH	±1	±0,8
Operating range	%RH	$0 - 100$	$0 - 100$
Recommend normal range	%RH	$0 - 80$	$20 - 80$
Response time τ63%	s	8	8
Long term drift	%RH/yr	<0,5	<0,25

Temperature specifications

Parameter	Unit	SHT75	SHT85
Typ. accuracy	℃	±0,4 @10-40℃	±0,1 @20-50℃
Max. accuracy	℃	±1 @-20-40℃	±0,25 @-20-40℃
Typ. resolution	℃	0,01	0,01
Typ. repeatability	℃	±0,1	±0,15
Operating range	℃	$-40 - 123{,}8$	$-40 - 105$
Recommend normal range	℃	$-20 - 60$	$5 - 60$
Response time τ63%	s	5-30	>2
Long term drift	℃/yr	<0,04	<0,03

Table E.2. Specification for temperature and humidity sensors SHT75 and SHT85 [43] [30].

Based on [44] the different specification are explained below. '@' is a common notation, meaning 'under the specified condition'.

The accuracy is dependent on the operating conditions and the accuracy limits are specified as a typical and maximal accuracy. The accuracy of a sensor is a measure of the deviation of the individual sensor readings in an equilibrium state against a reliable true reference. For an ensemble of the sensors, the measured deviations will follow a normal distribution. The typical accuracy limits are true for up to $\mu \pm 2\sigma$ of sensors in an ensemble and the maximal accuracy limits for $\mu \pm 4\sigma$. Here μ is the average and σ is the standard deviation.

Resolution is the smallest incremental change in the input that the sensors can detect and express in the output.

The stated repeatability is three times the standard deviation of multiple consecutive measurement values at constant conditions and is a measure of the noise on the physical sensor output.

The hysteresis value is the difference in measurements at a certain log point coming from a

dry environment and a humid environment, given enough dwell time. Humidity sensors carry some memory of conditions experienced in their recent past, which leads to hysteresis in their measurements. Hysteresis is dependent on the exposure range while in application. This value is additional to calibration accuracy.

Within the operating range, the sensors have the best performance within the recommended normal range. For both types of sensors, long term exposure at high humidity may temporarily offset the RH signal. The would be +3%RH after 60 hours above 80%RH. When the sensor is back within the normal range, it will slowly return to the calibration state by itself.

Response time is given by the time constant $\tau 63\%$. With an abrupt step change, this is the time it takes the sensor to reach 63% of the step height.
Sensor ageing may lead to a drift in the measured value, and the long term drift values stated are the maximal limit for drift per year.

E.3 Calibration setup

Figure E.1 shows the calibration setup, where the DewMaster boxes are on the table outside the climatic chamber, and the cables for each of the 240 sensors have been drawn into the chamber, through an opening in the side. During calibration the remaining gap in the opening, was filled with a paper towel, to limit convection and ensure the climate chamber could obtain stable conditions.

Figure E.1. Calibration setup with sensors and climatic chamber.

To manage the sensors and have some spacing around them, they are placed on a mount inside the climatic chamber. Figure E.2 shows a close-up of the sensors in the mount, where the F200 thermometer and Hygrodat100 probe, are placed in the middle of the stack. These instruments are used as the reference temperature and humidity at each calibration point. The F200 has been professionally calibrated on the 20th of January 2025, and the certificate is attached in Appendix W [45]. We have calibrated the Hygrodat100, which is explained in Appendix V.

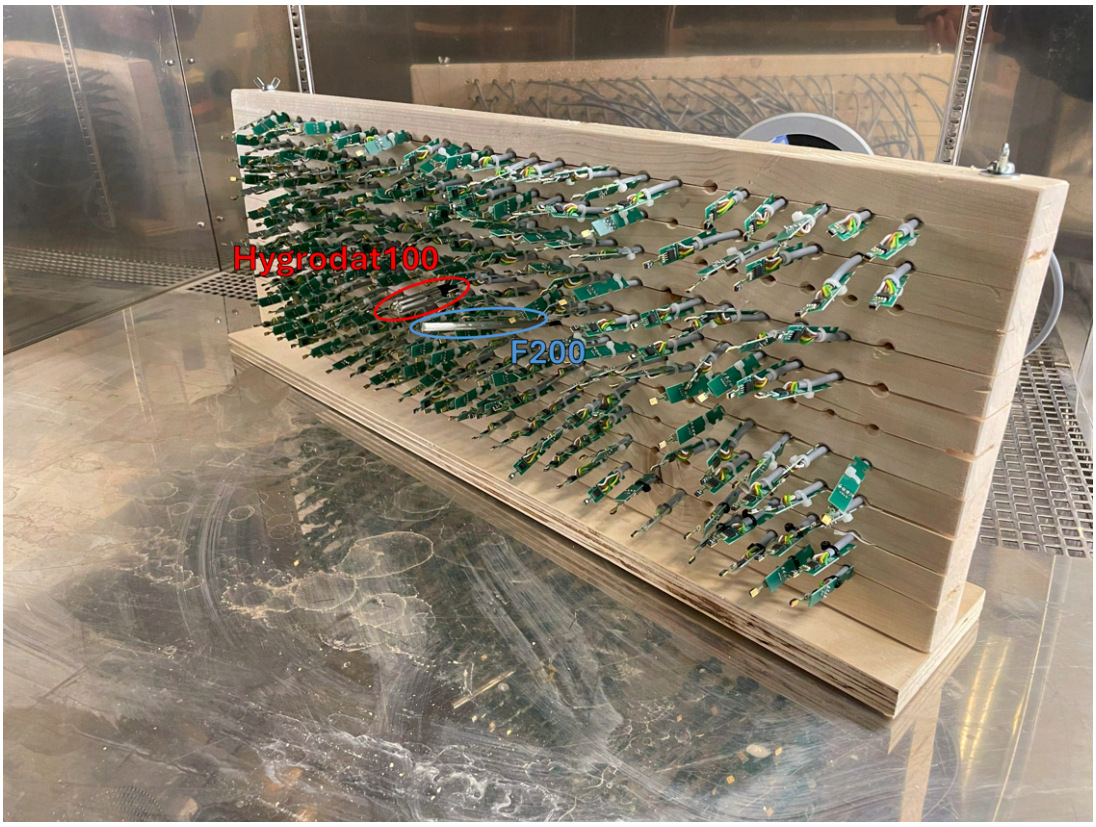

Figure E.2. Sensor mount inside climatic chamber

The sensors are placed grouped by which box they belong to. The area where the sensors for each box are placed in the mount is shown on Figure E.3.

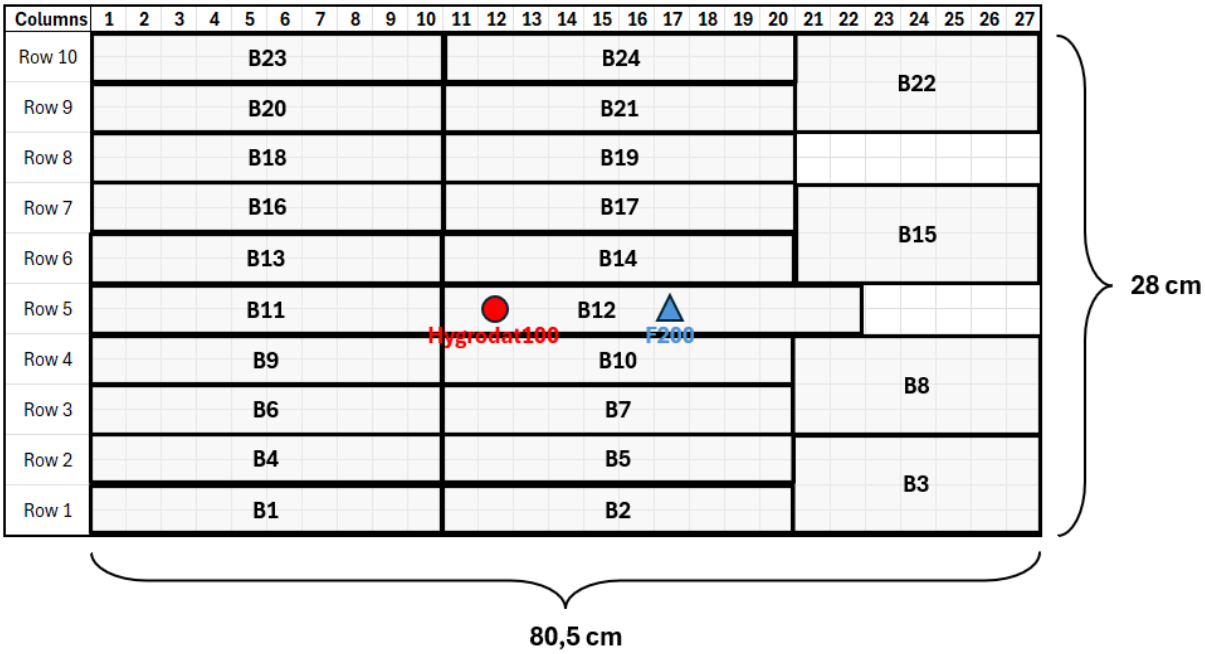

Figure E.3. Sensor placement in mount. Sensors are grouped by the box.

E.4 Calibration procedure

To calibrate the sensors, measurements are done at 15 different states, with reference measurements with the Hygrodat100 and F200 Thermometer. The calibration points we have done are shown on Figure E.4. These are chosen to cover the expected temperature range from -15℃ to 30℃ and humidity range from 35%RH to 95%RH. The figure also shows the three states used to verify the calibration functions.

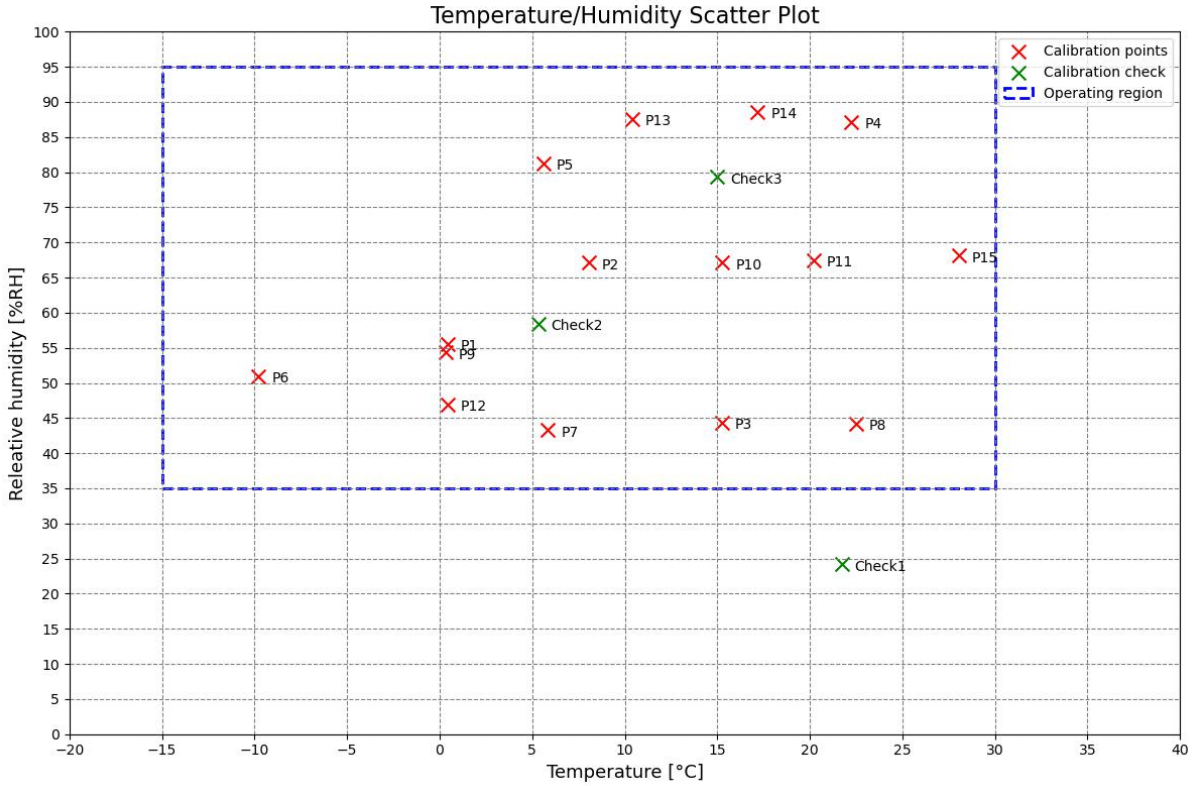

Figure E.4. Sensor calibration points, operating boundary and calibration check points

We are missing some calibration points at low temperatures and high humidities within the expected range for the sensors. It was not possible to do these, because the chamber is not able to control the humidity outside the temperature range of 2℃ to 94℃. This is, however, not considered critical, due to the few hours conditions will be in that area, and it will mostly be relevant for the sensors directly exposed to the environment.

For each point, we adjusted the setpoint for the climatic chamber, and then waited for the chamber and sensors to stabilize. The chamber is only quasi-stationary, and has some oscillation around the setpoint. The reference equipment was monitored in order to verify that the conditions had stabilized, before continuing with the next point. In general, a stabilization time

of around three hours, between each point, was needed. The Hygrodat100 humidity measurement was the slowest to stabilize, and the main reason three hours was necessary.

The measurements from the SHT-sensors are logged every three seconds and the reference equipment every 5 seconds. For each calibration point, the same 10-minute stabilized period is selected for all sensors and used to calculate the average, in order to compensate for the small fluctuations inside the climatic chamber. Figure E.5 and Figure E.7 show the time series of temperature and relative humidity measured by the reference equipment under the conditions of calibration points P6 through P15.

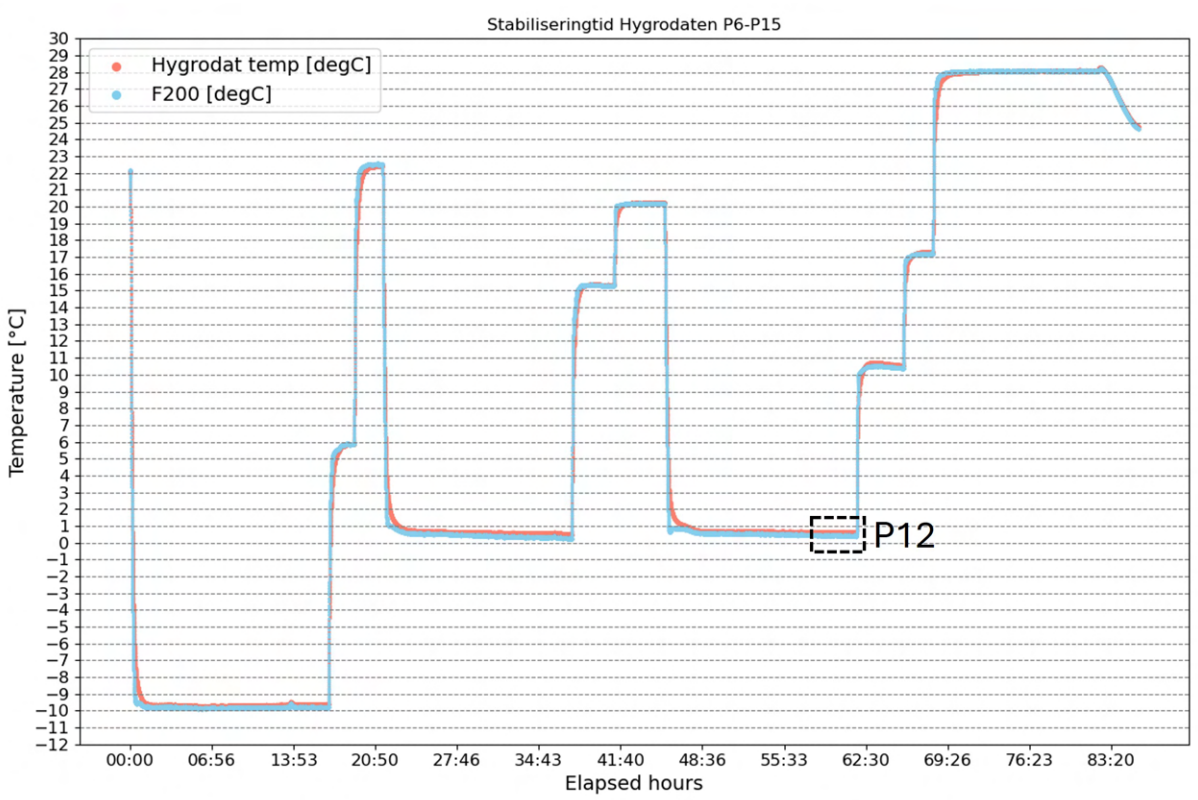

Figure E.5. Temperature time series of conditions inside climate chamber at calibration point P6 through P15. Shows the placement of graph zoom on Figure E.6

On Figure E.5 the different temperature settings and their stabilized period are very clear. Some of the periods seem short, but this is due to some very large periods of the same climate chamber setting overnight. From Figure E.6 it can be seen that the temperature is kept very stable inside the chamber, with a fluctuation for calibration point 12 of around 0.05 °C

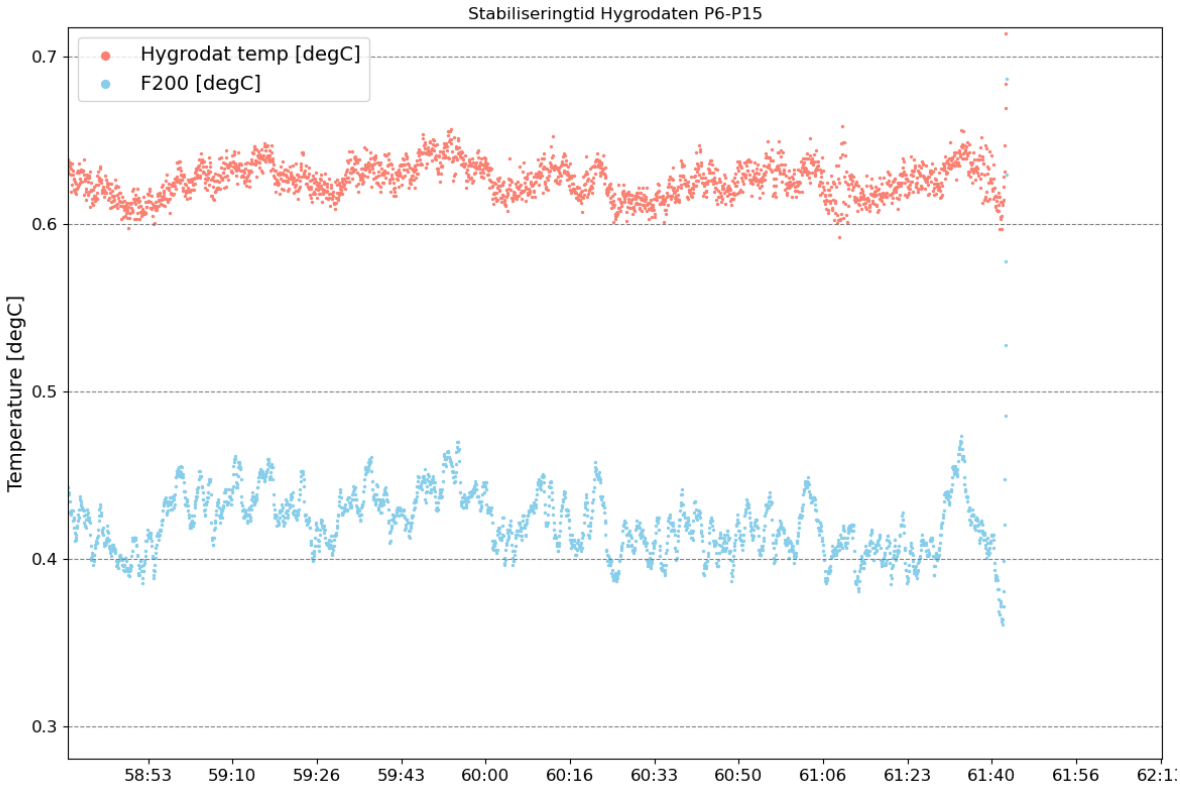

Figure E.6. Fluctuation of temperature in climate chamber at calibration point 12. See Figure E.5 for placement in time series.

The humidity is more fluctuating, which is also expected from the specifications of the climate chamber. There was great variation in how much time was needed for the relative humidity to stabilize. Figure E.7 show that the relative humidity keeps getting lower over a period of more than 10 hours, before point 12. Even if the humidity is not fully stabilized at some of the points and has a small slope, it will not have a big influence when comparing the SHT-sensors and reference equipment for the small 10-minute period.

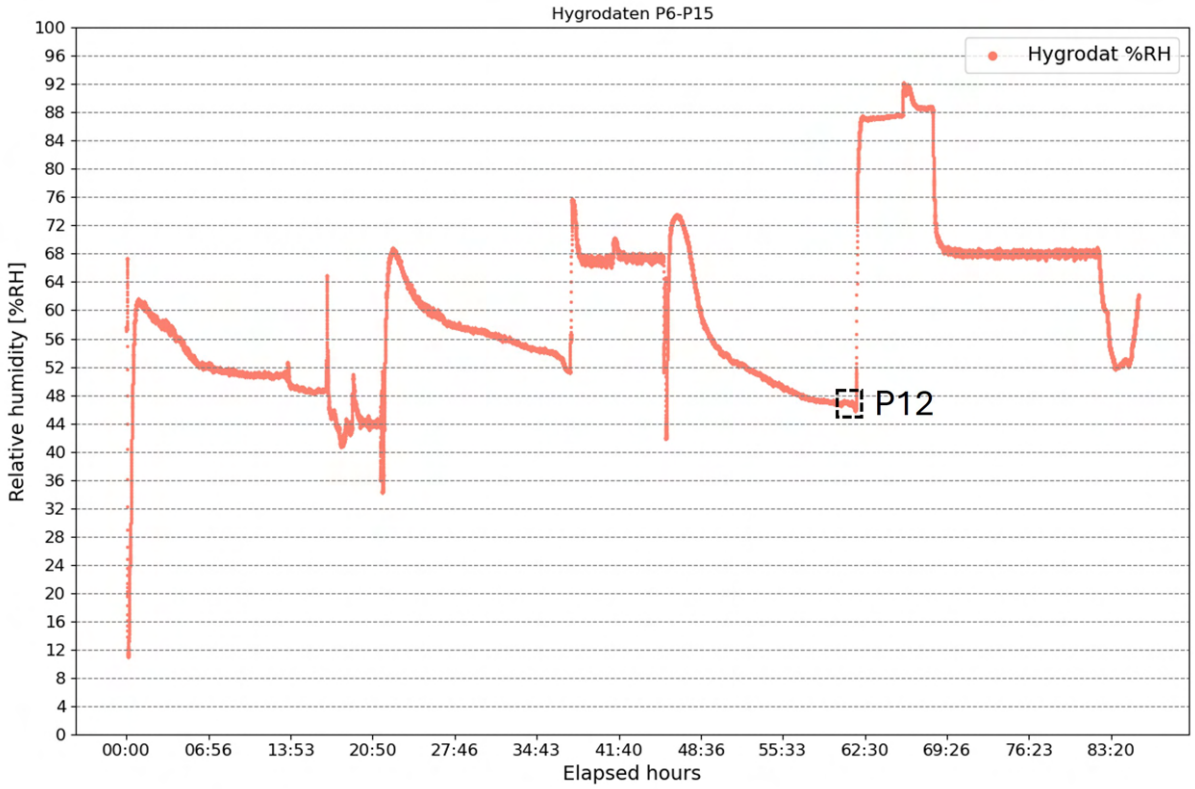

Figure E.7. Relative humidity time series of conditions inside climate chamber at calibration point P6 through P15. Shows the placement of graph zoom on Figure E.8

Figure E.6 shows the fluctuation in relative humidity at point 12. It can be observed that a 10-minute period can be isolated with a fluctuation of around 0.5 $\%RH$. The figure illustrates the chamber's regulation deadband, and when it reaches the lower boundary around elapsed hour 60:30 it reacts, and the relative humidity spikes. The drop in relative humidity in the last part of Figure E.8 is due to change of settings.

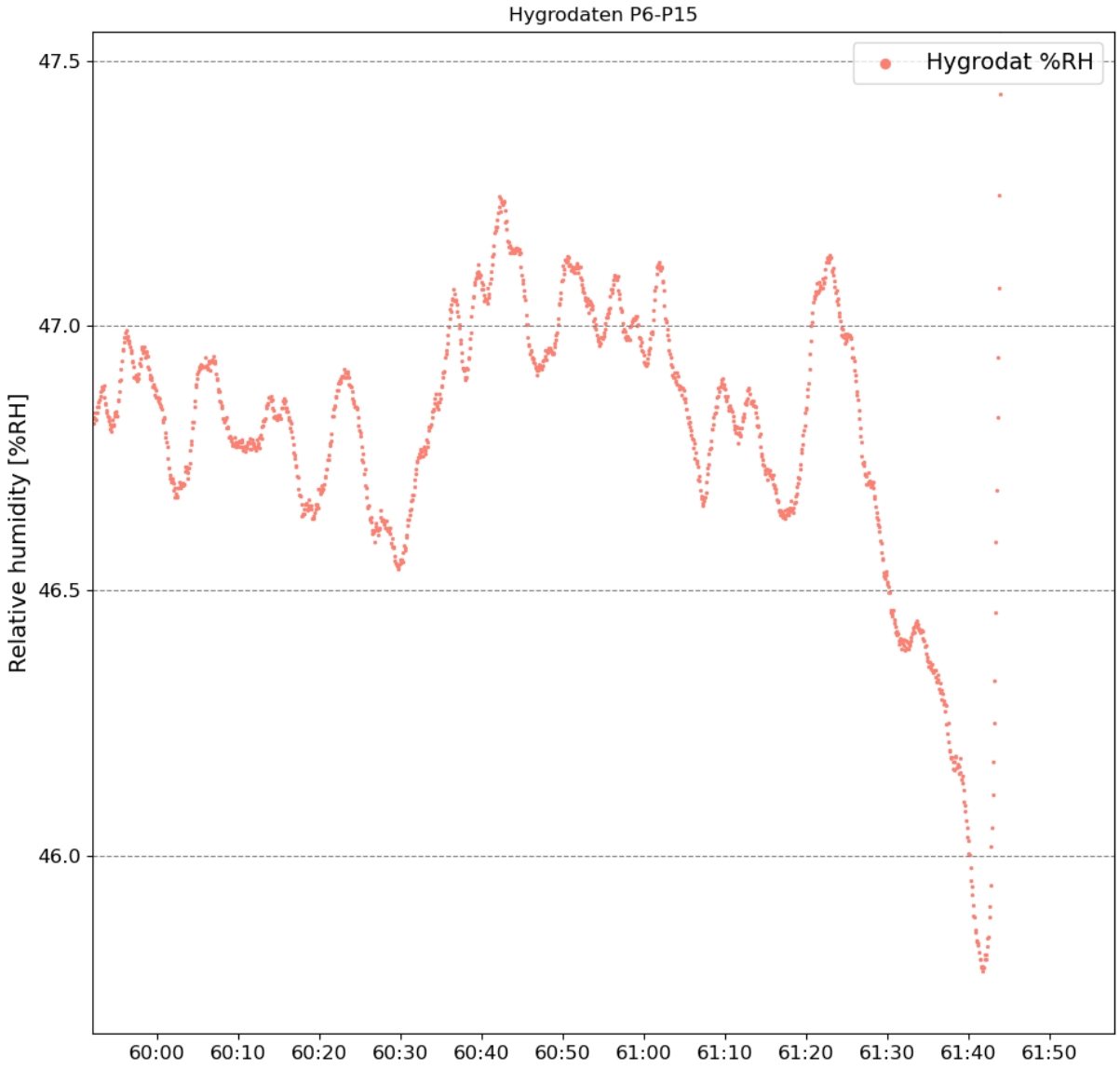

Figure E.8. Fluctuation of relative humidity in climate chamber at calibration point 12. See Figure E.7 for placement in time series.

E.4.1 Data treatment and calibration function

For each calibration point, we have calculated the reference temperature and relative humidity and the values for each sensor, as an average of a 10 minute period, corresponding to around 200 measurements. For the SHT-sensor, we can see it rarely produces some unrealistic outliers, where the value is off by a factor of 100. The outliers are filtered out, to avoid distorting the average.

Plotting the points for each sensor, it is clear that the SHT75 and SHT85 sensors behave differently, and that the SHT75 sensors have a bigger humidity error. This can be seen on

Figure E.9 and Figure E.10 where the average value for each sensor at calibration point P2 is plotted. On the figures the sensors are grouped by the box they are mounted in.

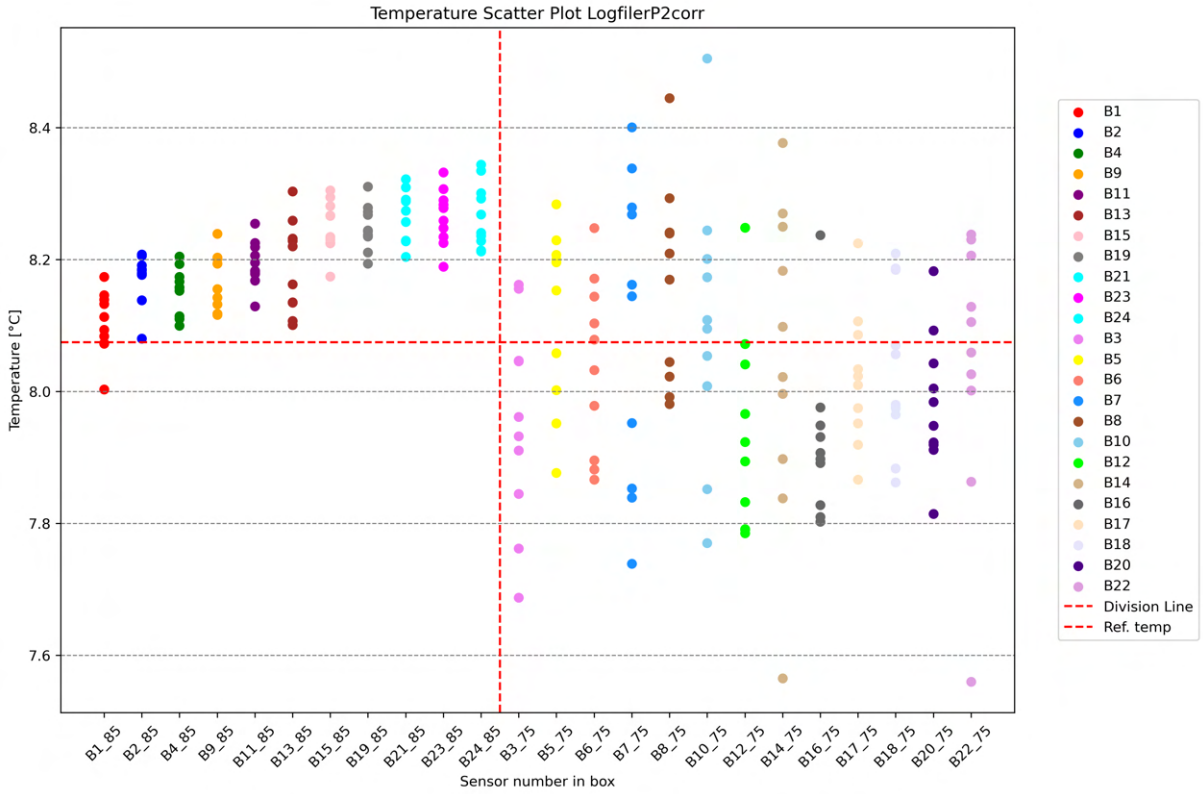

Figure E.9. Plot of the 10 minute temperature average for the 240 sensors, grouped by DewMaster box. The vertical dotted red line, seperate the SHT85 to the right and SHT75 to the left sensors.

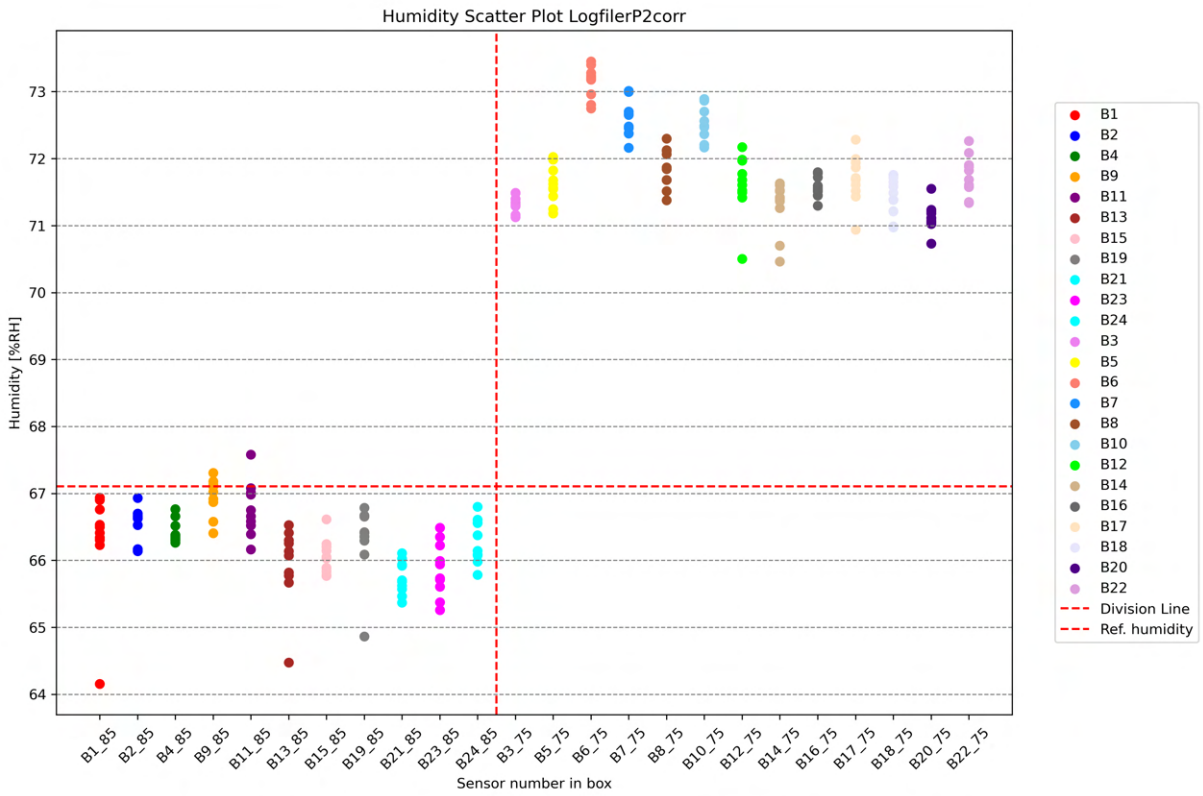

Figure E.10. Plot of the 10 minute humidity average for the 240 sensors, grouped by DewMaster box. The vertical dotted red line, seperate the SHT85 to the right and SHT75 to the left sensors.

Because of the difference between the SHT75 and SHT85 sensors, we have grouped them separately. To get a general overview of the sensor performance we have made Figure E.11 where both temperature and humidity are visible. To better visualize all the data Figure E.11 shows the average value for all of the SHT85 and SHT75 sensors at each calibration point. For each point the full range of values for all the sensors is shown with a red-dotted line and two times the standard deviation is shown by a black line. This is to indicate the spread of the sensors at each average value. The colour of each point represents the magnitude of the combined temperature and humidity error. The combined error is calculated using the euclidean distance in the x-y diagram, as shown on Figure E.12.

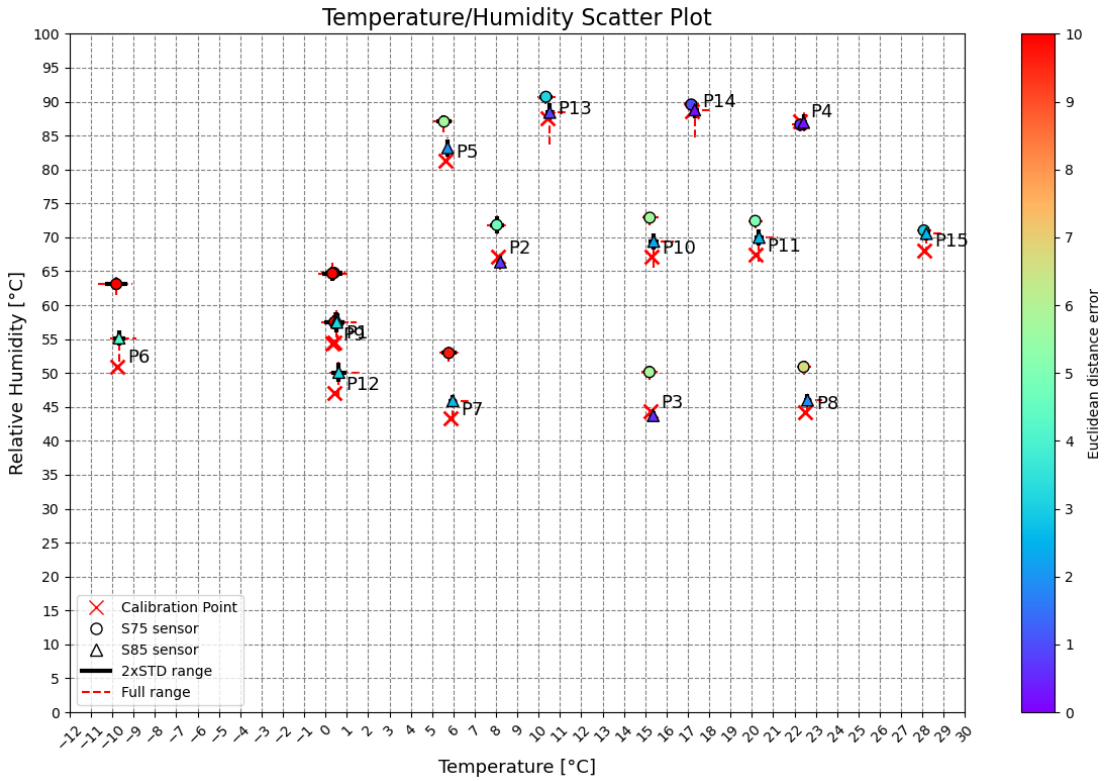

Figure E.11. Calibration data results, shown as the average value for SHT75 sensors and SHT85 sensors

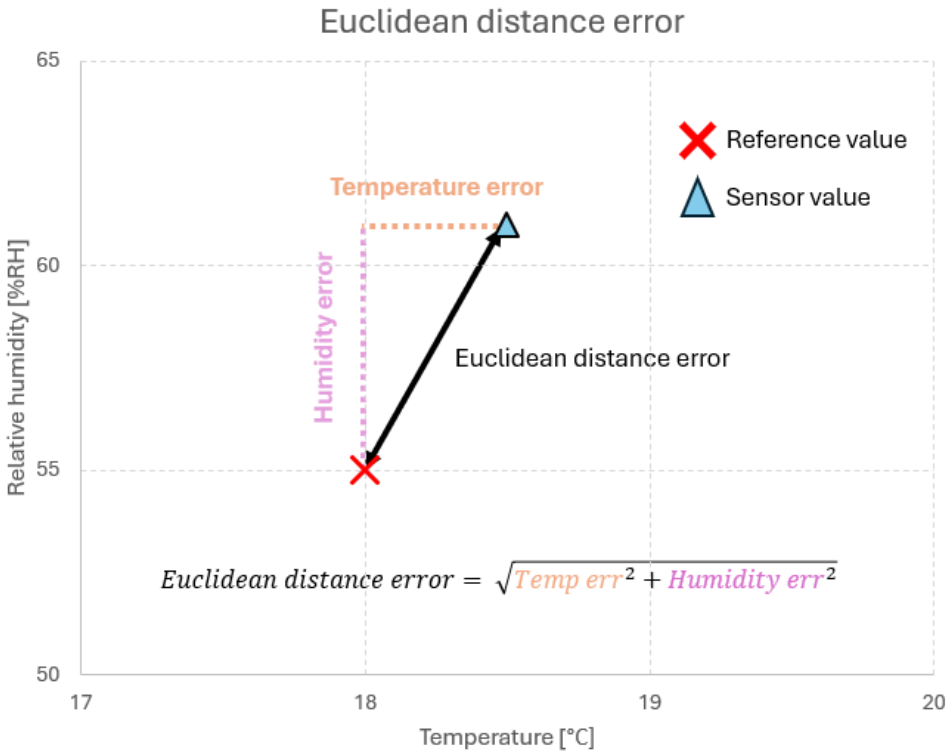

Figure E.12. Calculation of combined temperature and humidity error, using euclidean distance

Figure E.11 shows the sensor measurements are clustered together with a small range, but they have some offset from the reference. It is also clear that e.g. the humidity error changes with the temperature. For each sensor, a temperature and humidity calibration function is needed. To make the calibration functions, we use multiple linear regression because the corrected temperature and humidity are dependent both on the measured temperature and humidity. We have made the regression using the sklearn linear regression module in Python, to get two calibration functions for each sensor in the form of Equation E.1 and Equation E.2

$$T_{corr} = b + \alpha_0 \cdot T + \alpha_1 \cdot RH \tag{E.1}$$

$$RH_{corr} = b + \alpha_0 \cdot T + \alpha_1 \cdot RH \tag{E.2}$$

In Appendix X Table X.1 and X.2 show the regression outcome, with the calibration function values for each sensor and the R^2-value of the model. The model has a good fit with a R^2 of 0.99 for each sensor.

After conducting the calibration measurements, it was discovered that an error resulted in missing data from boxes 21, 22, 23, and 24 at calibration points P7 through P15. Because of the missing data, we have not calculated a calibration function for the sensors in these four boxes. A function could be made on the available calibration data.

Additionally, we see that the connection of sensor 9 in box 19, B19_S9, is unstable, with some periods where no data is received. This could be explained by a poor mounting of the sensor in the socket. For our points P1 to P5, there are connection issues with sensor 6 in box 4, B4_S6, which, however are fixed for the rest of the calibration points.

E.5 Evaluation of calibration function

In order to evaluate the calibration functions, they are evaluated on measurements at three new conditions, which are shown on Figure E.4. Check condition T1, is not inside the climatic chamber, but made at room conditions in the Indoor Climate Lab at Aalborg University. The lab is climate controlled and has quite stable room conditions.

We evaluate the calibration functions on data, which were not used in the regression to make the functions. This is only done for the sensors in DewMaster box 2 and box 16, but would ideally be done for all sensors. There are SHT85 sensors in box 2 and SHT75 sensors in box 16.

Figure E.13 compares the sensor measurement average with and without calibration applied. The comparison shows that the measurements are more closely grouped, and their spread is lowered. Table E.3 presents the statistics on the calibrated values.

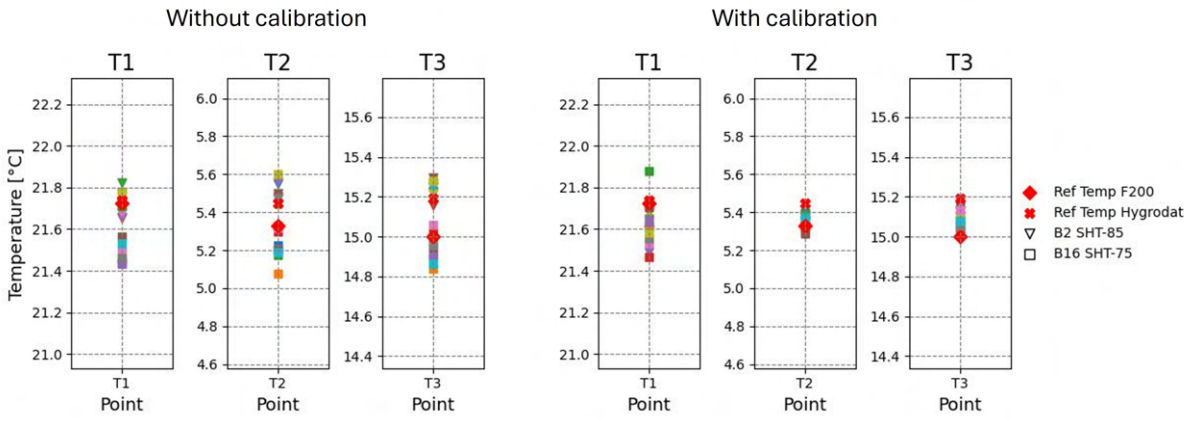

Figure E.13. Comparison of sensor temperature measurement at the three calibration conditions, with and without calibration formula applied.

Table E.3. Evaluation of sensor accuracy of temperature with calibration.

Point	T1	T2	T3
Ref Temp	21.7	5.3	15.0
B2 and B16 sensors			
Min	21.5	5.3	15.0
Max	21.9	5.4	15.2
Range	0.4	0.1	0.2
$2 \cdot std$ dev	0.2	0.1	0.1
Max diff to ref	0.3	0.1	0.2
Typ. Accuracy SHT85	±0,1 @20-50°C		

The accuracy is poorest under the check condition T1, which could be explained by it being outside the range of the calibration points. The conditions at T1 of 21.7°C and 24.2%RH, are not expected to occur during our test measurements and can be disregarded. Apart from this, the calibrated sensors are close to being within the specified accuracy limits. Disregarding T1, this evaluation concludes that the evaluated sensors comply with an accuracy of ±0.2°C for temperature. The specification is shown here only for the SHT85 sensor, but the extended specifications are found in Table 4.1.

Looking at the relative humidity on Figure E.14, there is more of a difference with and without calibration.

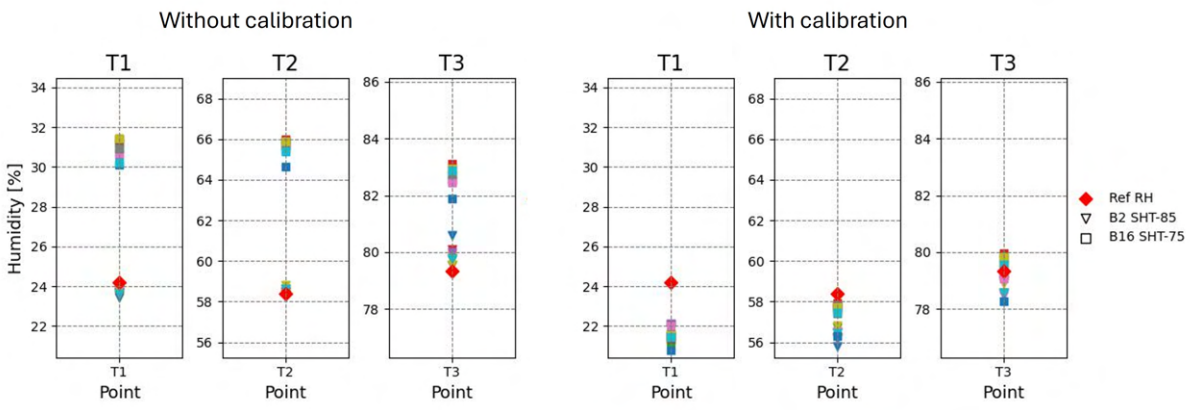

Figure E.14. Comparison of sensor relative humidity measurement at the three calibration conditions, with and without calibration formula applied.

Without calibration, the SHT75 sensors in box 16 are deviating much more than the specified accuracy. With calibration their values are corrected and are closer to the reference measurement. The case is different for the SHT85 sensors in box 2, which are closer to the reference measurement before they are calibrated. The calibration increases the error for the SHT85 sensors, at our three calibration check conditions. Looking at Table E.4 the accuracy is also poorest at check condition T1.

Table E.4. Evaluation of sensor accuracy of relative humidity with calibration.

Point	T1	T2	T3
Ref RH:	24.2	58.4	79.3
B2 and B16 sensors			
Min	20.8	55.8	78.3
Max	22.1	57.9	80.0
Spread	1.3	2.1	1.7
$2 \cdot std$ dev	0.7	1.4	1.0
Max diff to ref	3.4	2.6	1.1
Typ. Accuracy SHT85	±1,5 @0-80%RH		

For the calibrated measurements of relative humidity, there is an underestimation at the lower humidities. All the values are grouped lower than the reference and do not meet the typical accuracy. Disregarding T1, this evaluation concludes that the evaluated sensors comply with an accuracy of ±3%RH for relative humidity.

Appendix F

Analysis of full-scale boundary conditions

In this appendix, the data from the measurement in the climatic chamber is analysed. Firstly, the influence of the position of the elements is looked upon, and afterwards, the elements are compared to each other. To remove outliers and the largest fluctuations, every plot is made from 5 minute average values.

F.1 Influence of position of the wall elements

The first analysis consists of evaluating if the difference in positions impacts the measurements. This is done by analysing the measurements from the ventilated cavity and the measurements inside of the chamber.

F.1.1 External boundary conditions

Each element has a sensor installed within the ventilated cavity to monitor external boundary conditions. This setup allows for direct comparison of temperature and relative humidity across the different elements. Since the elements are arranged in two rows—four in the bottom row and three in the top—the analysis primarily focuses on the difference between these. The placement of the elements is illustrated on Figure F.1.

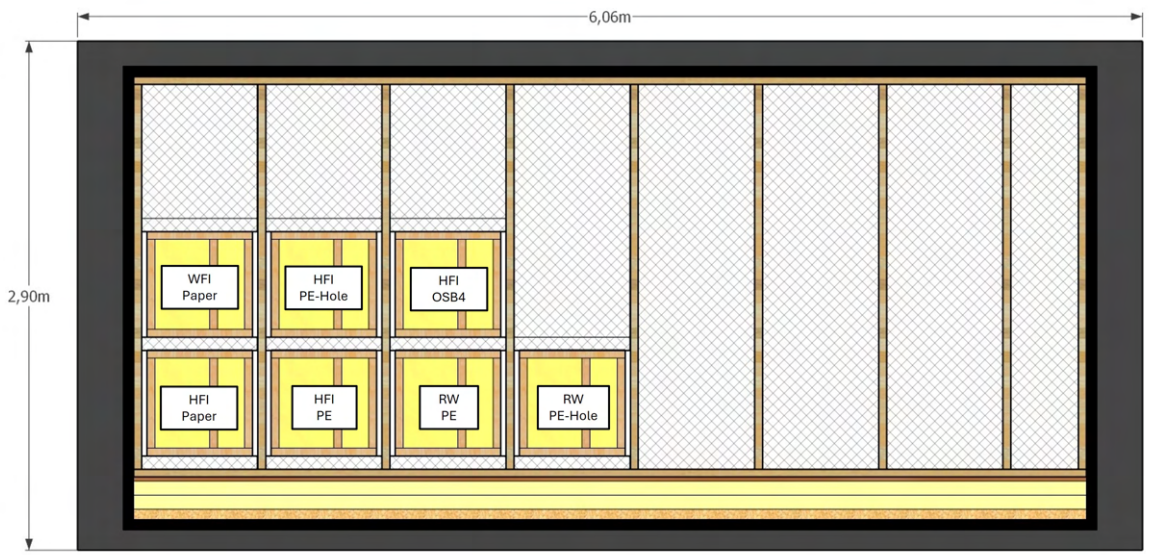

Figure F.1. The placement of the elements seen from outside of the climatic chamber.

The following analysis is made for the period April 16 to May 12. The first parameter that is looked upon is the temperature. The measurements for the aforementioned period are seen on Figure F.2.

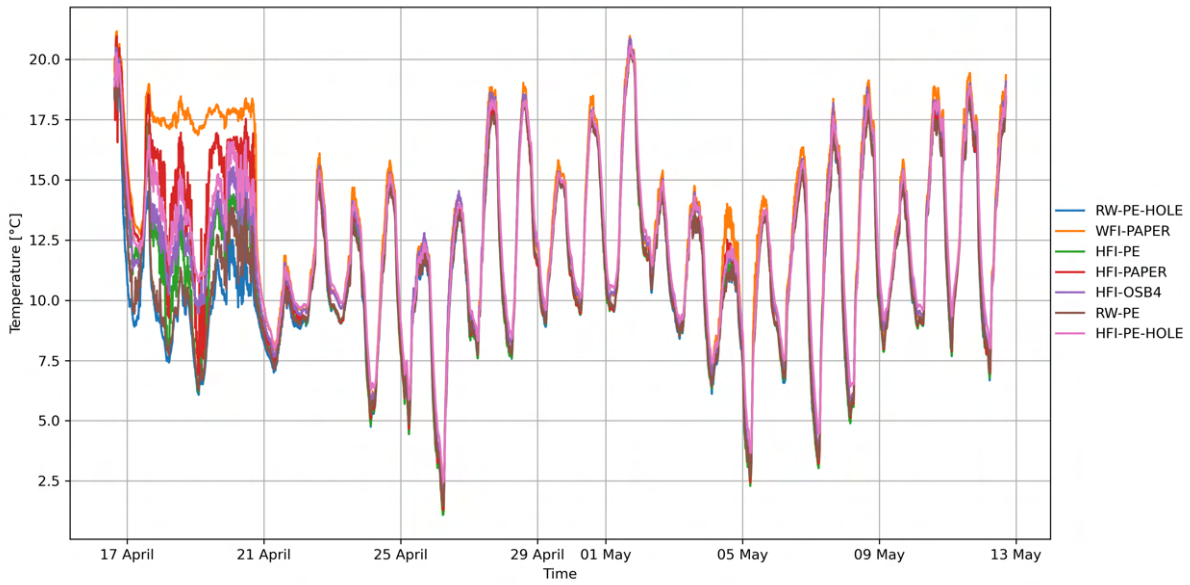

Figure F.2. The temperature in the ventilated cavity for all 7 elements.

From the temperature plot it is seen, that the different elements show no distinct variation after the wall was insulated on April 20th. Therefore the relative humidity for the same period is also analysed. The measurements are shown on Figure F.3.

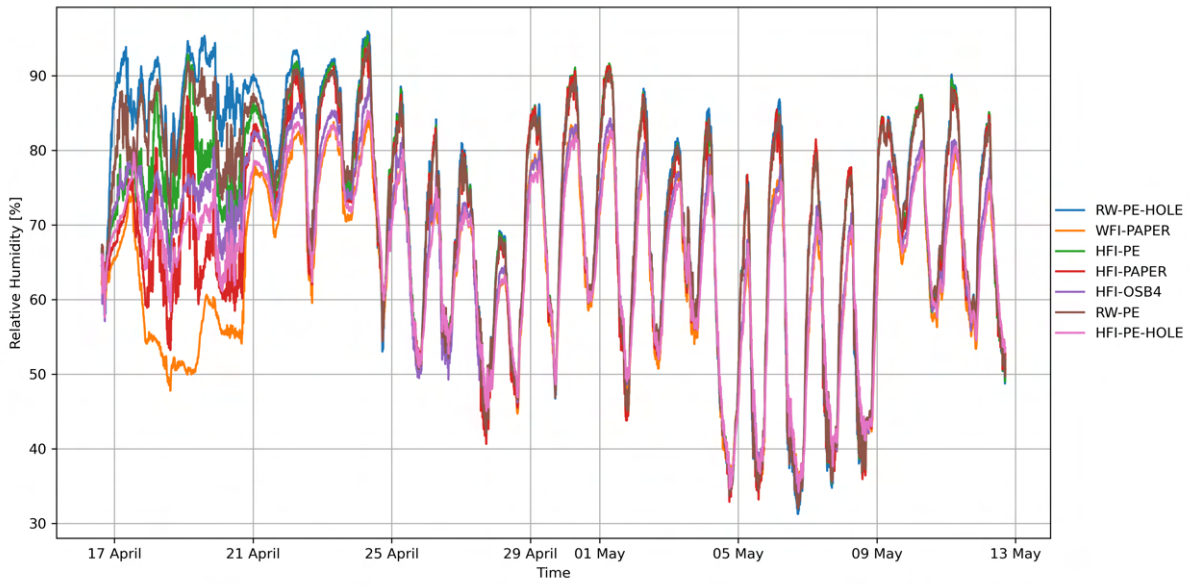

Figure F.3. The relative humidity in the ventilated cavity for all 7 elements.

The RH plot clearly shows that the measurements form two distinct bands. WFI-PAPER, HFI-PE-HOLE, and HFI-OSB4 cluster closely together and exhibit less variation compared to the other elements. As shown in Figure F.1, these elements are positioned in the second row. Being further away from the external boundaries, they are less influenced by direct external environmental fluctuations. This is because the exterior cladding is open at both the top and bottom, allowing greater exposure near the outer edges, which causes more variability in temperature and humidity for the elements in the first row.

While relative humidity provides useful information about the moisture conditions, vapor pressure offers a more direct measure of the absolute moisture content in the air. Unlike relative humidity, which depends on temperature, vapor pressure quantifies the actual partial pressure of water vapor. By examining vapor pressure alongside temperature and RH, a clearer picture emerges of the environmental conditions influencing each element. The vapor pressure is shown on Figure F.4.

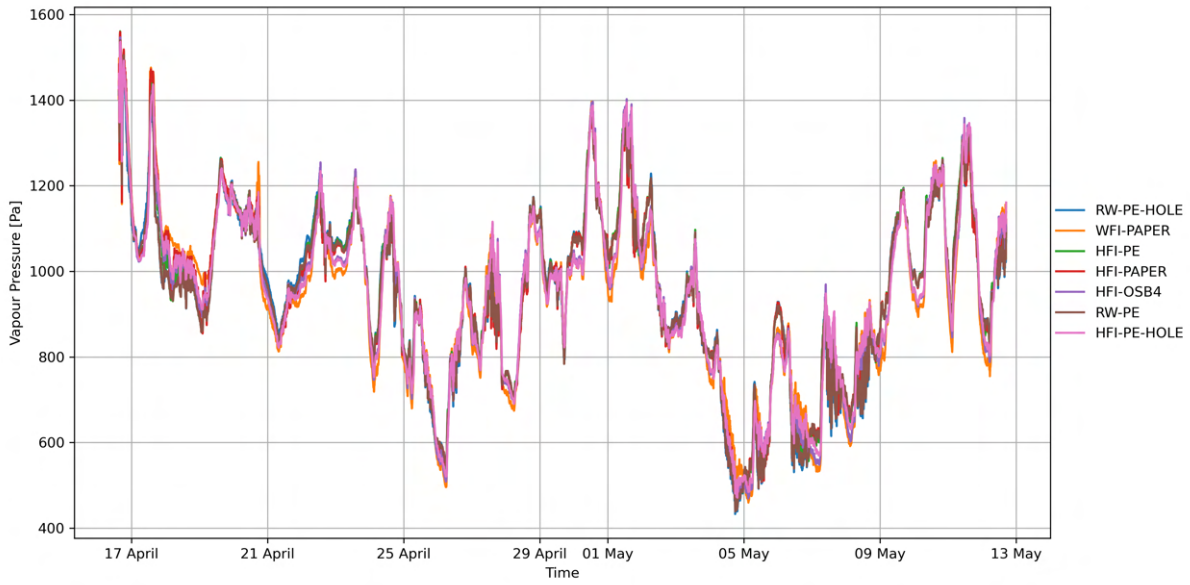

Figure F.4. The vapour pressure in the ventilated cavity for all 7 elements.

The vapor pressure shows only minor variations, which tend to occur at the same times when the two distinct RH bands appear. Overall, the differences in vapor pressure between the elements are relatively small, indicating that the absolute moisture content in the air remains fairly consistent across the measured locations.

F.2 Climatic chamber conditions

In Appendix A section A.5 it was found that the mixing of air inside the climatic chamber was acceptable. Therefore, the average of the four Dewmaster sensors used to control the indoor conditions represents the conditions. The temperature and RH for the full measurement period can be seen on Figure F.5 and F.6.

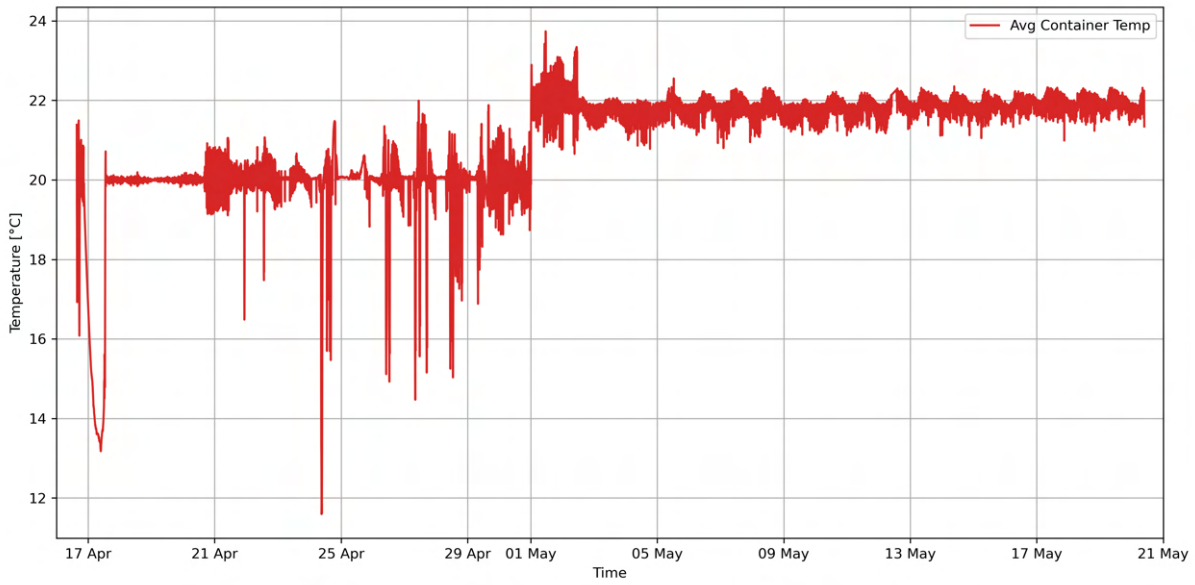

Figure F.5. The temperature measurements inside the climatic chamber for the measurement period.

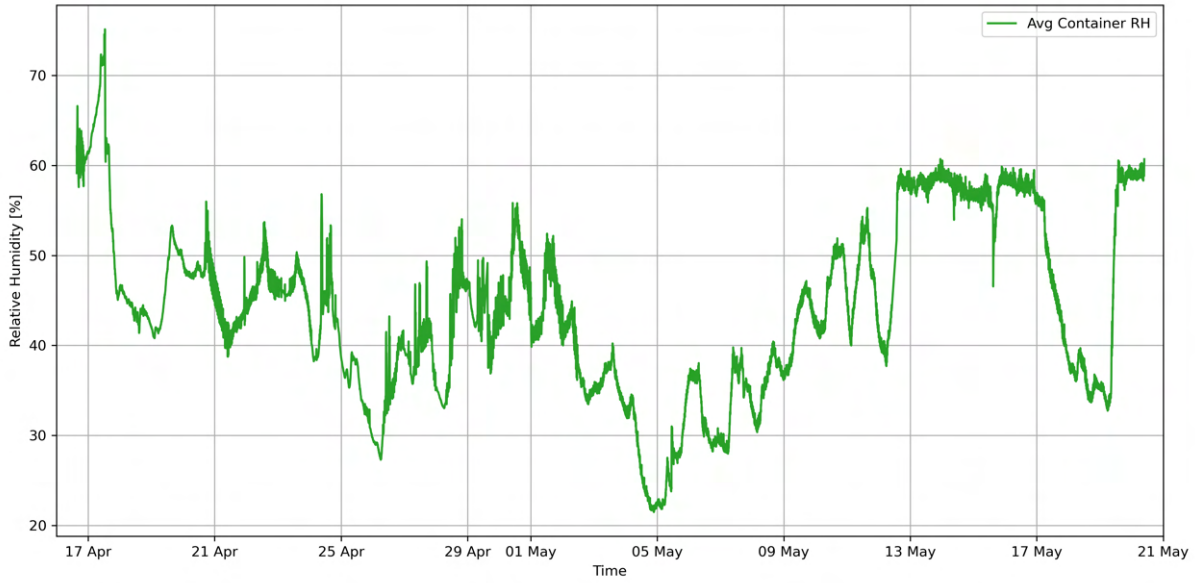

Figure F.6. The RH measurements inside the climatic chamber for the measurement period.

From the indoor conditions, it is seen that the temperature remains constant after the last tuning on May 3. On the contrary, the RH fluctuates a lot. This is because the humidifier was not working before May 12. After this, the RH remains stable, with the exception of two periods. The first small drop is caused by the door being opened to refill the water for the humidifier. The large drop is caused by a malfunction in the humidifier. The full timeline of our measurements can be seen in Table B.1 in Appendix B. As with the conditions in the ventilated cavity, the vapor pressure is also analysed, and can be seen on Figure F.7.

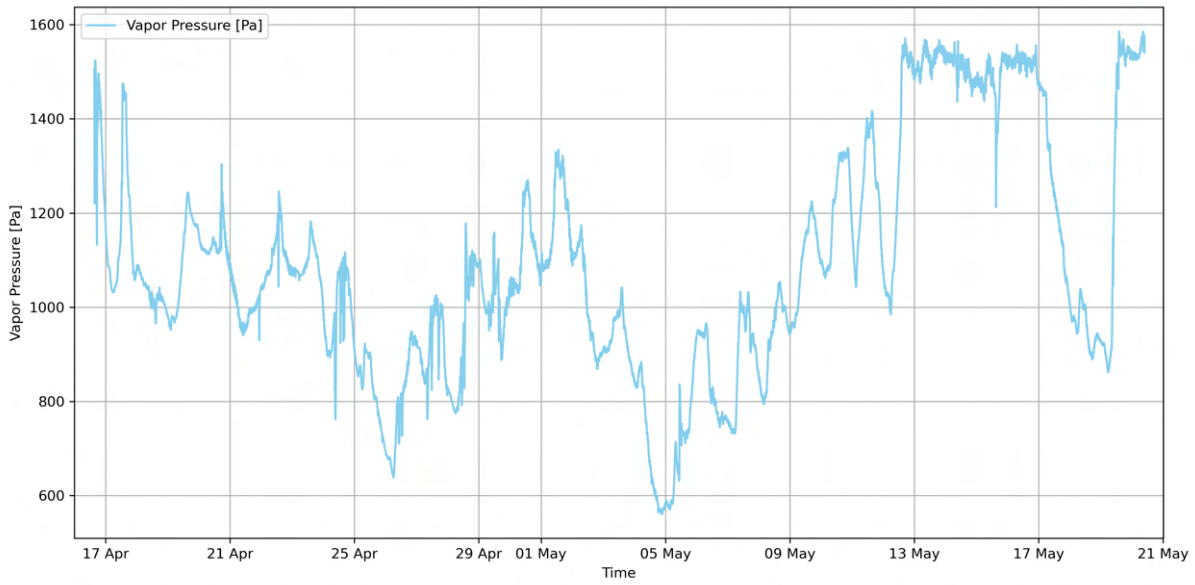

Figure F.7. The vapor pressure inside the climatic chamber for the measurement period.

Because of the temperature being stable inside of the climatic chamber, the vapor pressure follows the RH. Therefore, the pressure fluctuates a lot until May 12. where the humidifier was fully working.

Appendix G

Analysis of the wall elements

This appendix presents an analysis of the measurements from the climatic chamber. The focus is on the temperature and moisture conditions within the elements. Several factors are evaluated, such as material-specific properties like different insulation and vapor barrier performance. In addition to that, the influence of solar radiation is examined. Lastly, the two measurement columns in one element are examined to determine whether differences occur between the middle of insulation and close to the timber.

G.1 Different insulation material

In this section, the impact of different insulation materials is examined. The three elements used are with three different insulation materials: WFI, HFI, and RW. Unfortunately, as seen in chapter 4 section 4.2, we did not have three elements with the same vapor barrier in the setup. Therefore, the RW element has a PE-foil, while the other two have a paper barrier. This should be kept in mind throughout the analysis. The temperature measurements for the full measurement period can be seen on Figure G.1.

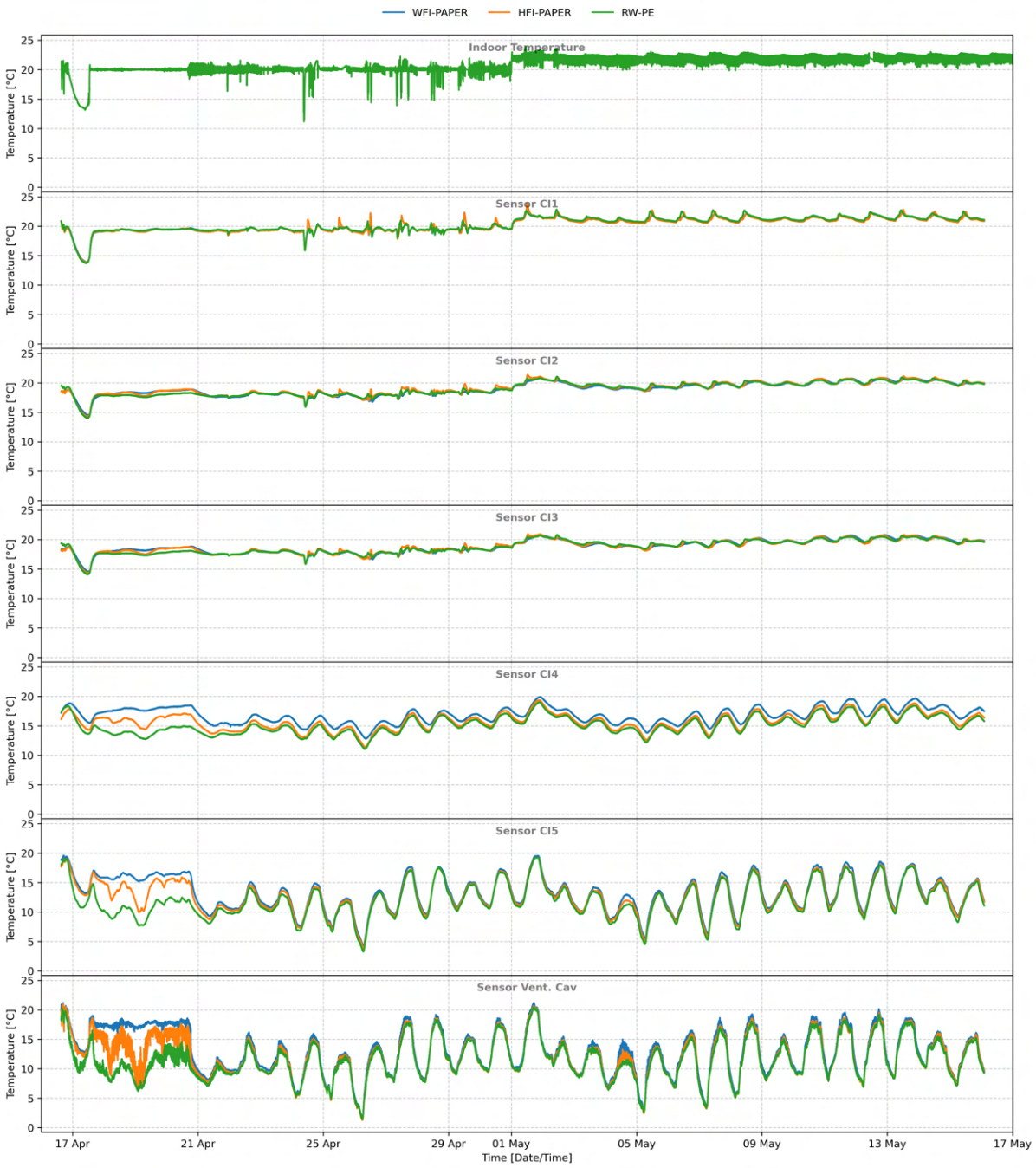

Figure G.1. The temperature for three elements with different insulation.

The internal temperatures throughout the elements are generally the same except for CI4 and minor differences in CI5. To analyze this, a profile from before the dehumidifier was integrated is examined. The profile is from May 7th at 12:00 and is shown on Figure G.2.

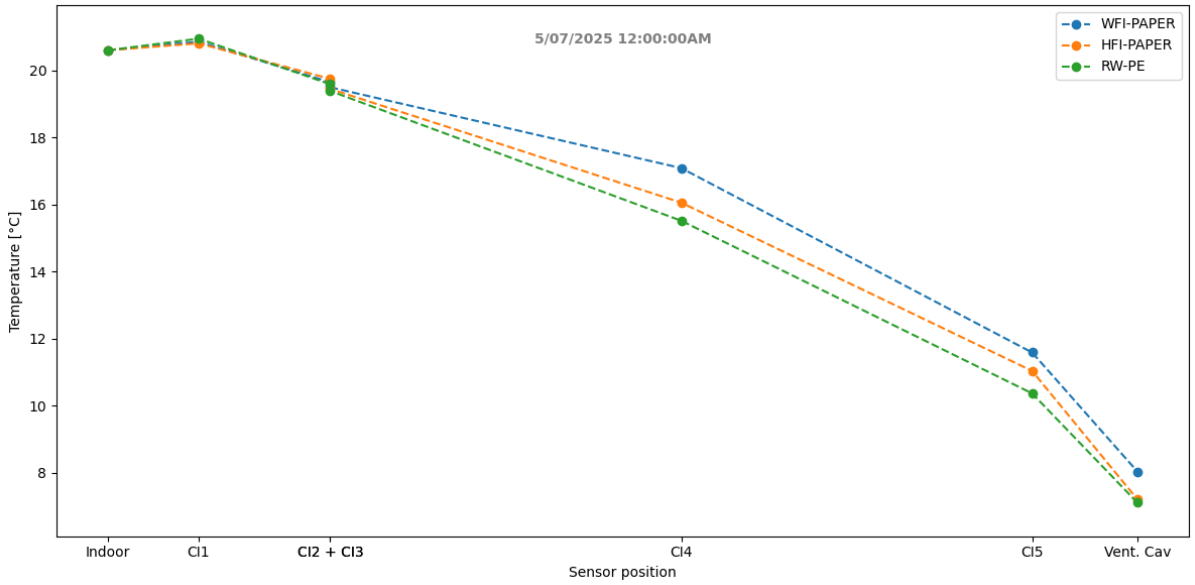

Figure G.2. Temperature-profile for the three elements.

The temperature profiles vary from the expected. Although, RW has the lowest thermal conductivity, its profile shows the lowest temperatures. This result is likely influenced by the dynamic conditions in the setup. WFI and HFI possess a higher heat capacity and, being biobased, a higher moisture buffering ability, which dampens the temperature changes. From section 3.1, it is seen that WFI has a larger moisture capacity than HFI, while RW , being hydrophobic, has an even smaller moisture capacity. These observations suggest that the thermal conductivity is not enough to describe the temperature profiles for the elements in dynamic conditions. The difference in temperature in the ventilated cavity is caused by the position of the element, which is addressed in section F.1.

To gain further insight, the RH-profiles for the same timestamp are examined in Figure G.3.

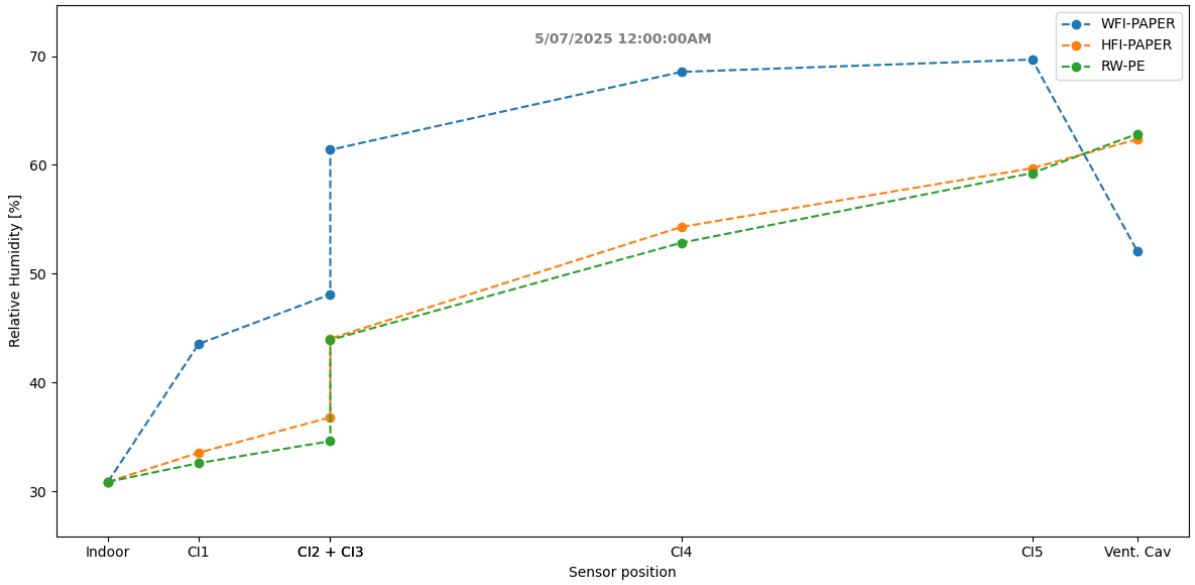

Figure G.3. RH profile for the three different elements with different insulation.

From the profiles, it is seen that WFI consistently displays higher RH throughout the wall-element. Unexpectedly, RW and HFI show nearly identical profiles. This might be due to the different moisture properties of the materials, and the short timeframe for which the measurements have been made.

To determine the moisture flow direction, the vapor pressure profile is reviewed in Figure G.4.

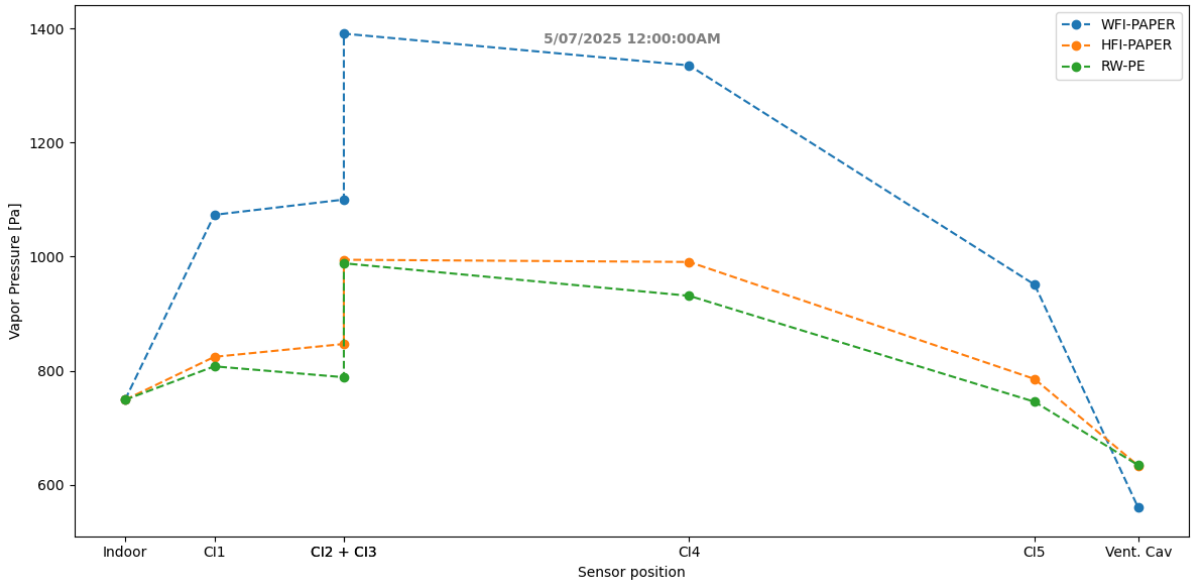

Figure G.4. Vapor pressure profile for May 7th.

From the plot, it can be seen that the moisture flows from the vapor barrier both to the outdoors

and indoors. This is especially pronounced for WFI possibly due to the initial moisture content in the material being higher than for the other elements. The initial moisture contents are found in Appendix R.

Because the profiles are from before the humidifier was integrated and working, a follow-up review is made on May 16th at 12:00. These are the latest measurements we have, and the temperature profiles can be seen on Figure G.5.

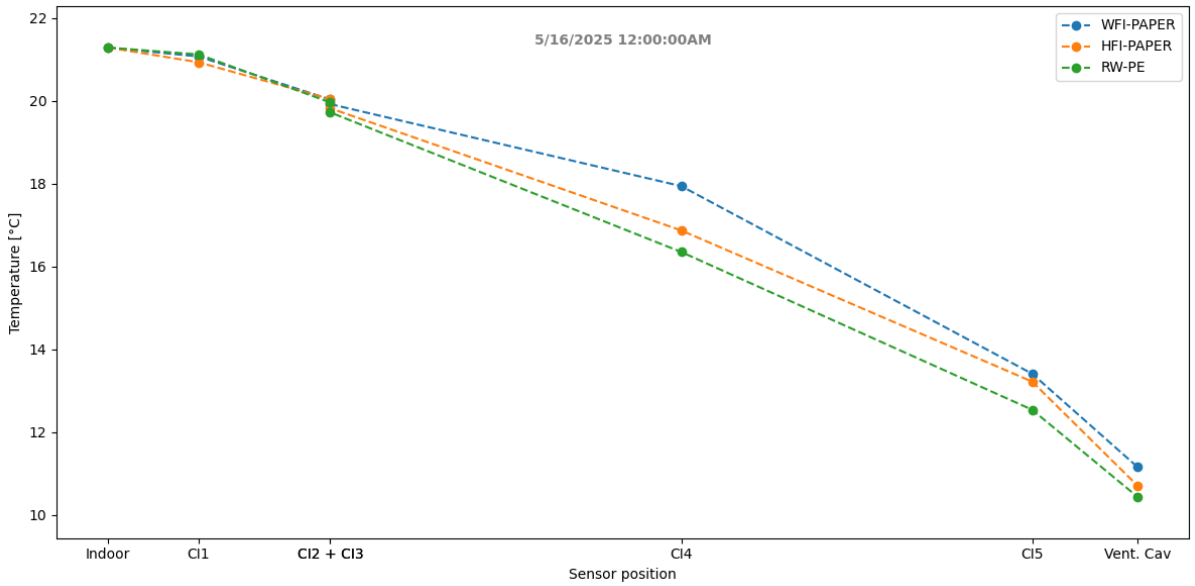

Figure G.5. Temperature profile for May 16th.

The temperature profiles before and after the humidifier remain consistent. Therefore, no further analysis is made on this, and the focus is shifted to the RH-profiles presented in Figure G.6.

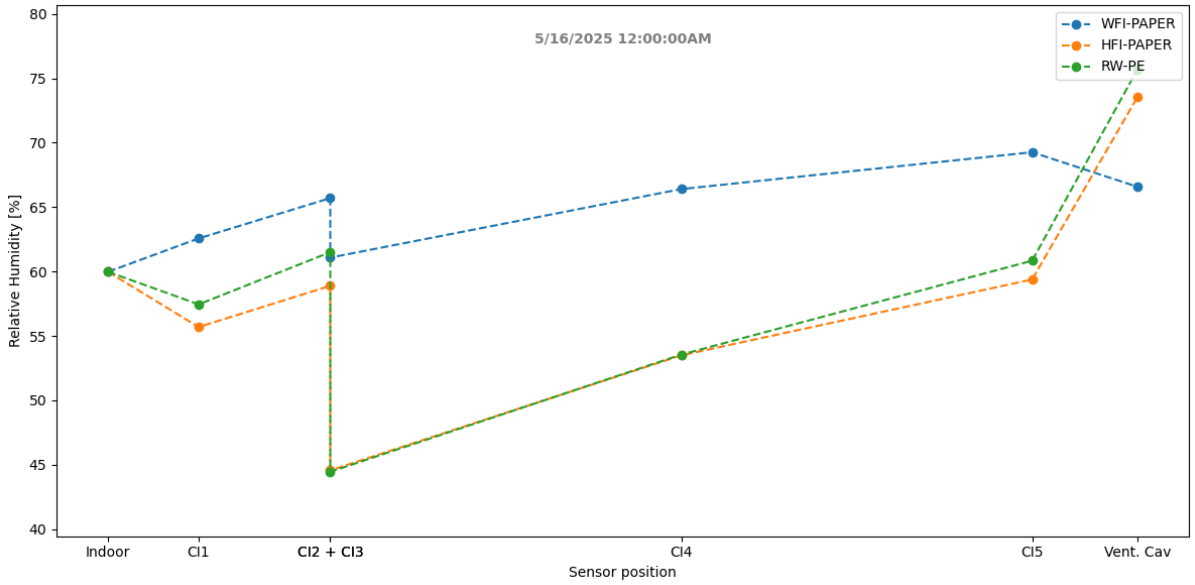

Figure G.6. RH profile for May 16th.

After the humidifier is installed, the indoor humidity is kept at a consistent level. This change impacts the profile, to where the RH on the warm side of the vapor barrier is increased. The remaining part of the element remains similar compared to before humidification. To explore the effect on moisture transfer, the vapor pressure distribution is examined in Figure G.7.

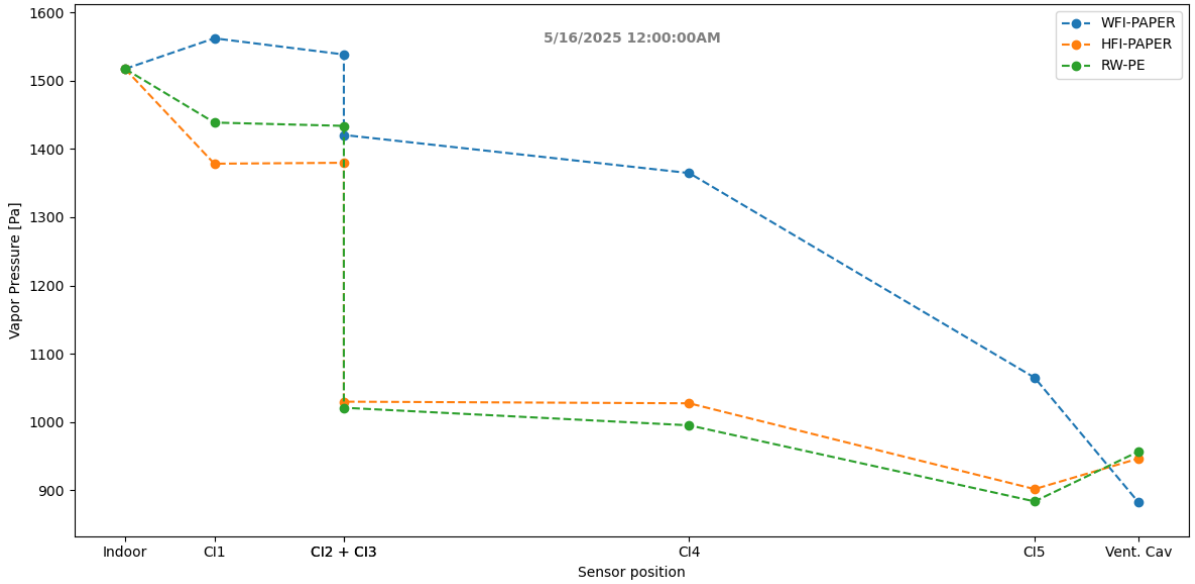

Figure G.7. Vapor pressure profile for May 16th.

Following the installation of the humidifier, the vapor pressure profile reveals a shift in moisture transfer direction. Without the humidification, the moisture was flowing outwards away from

the vapor barrier. Now the moisture flows from indoors towards outdoors.

G.2 Different vapor barriers

This section investigates how different vapor barriers influence the internal conditions on different HFI-elements. We start by looking at the temperatures Figure G.8.

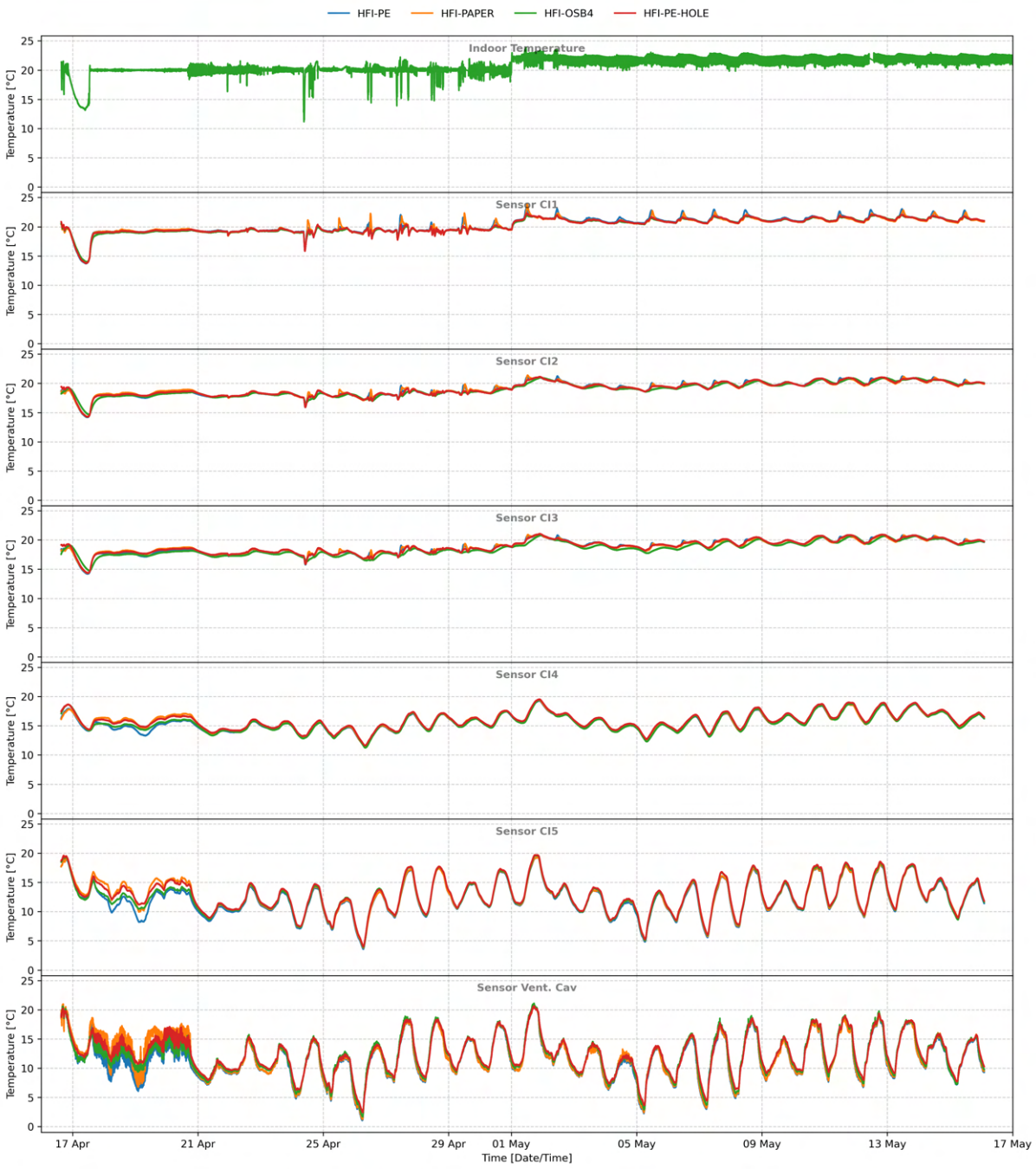

Figure G.8. Temperatures for the four elements with HFI

Across the entire measurement period, no noticeable differences in temperature can be observed. This indicates that the choice of barrier does not impact the internal temperature profiles significantly. To assess whether differences appear in moisture, the RH measurements for the whole period are shown in Figure G.9.

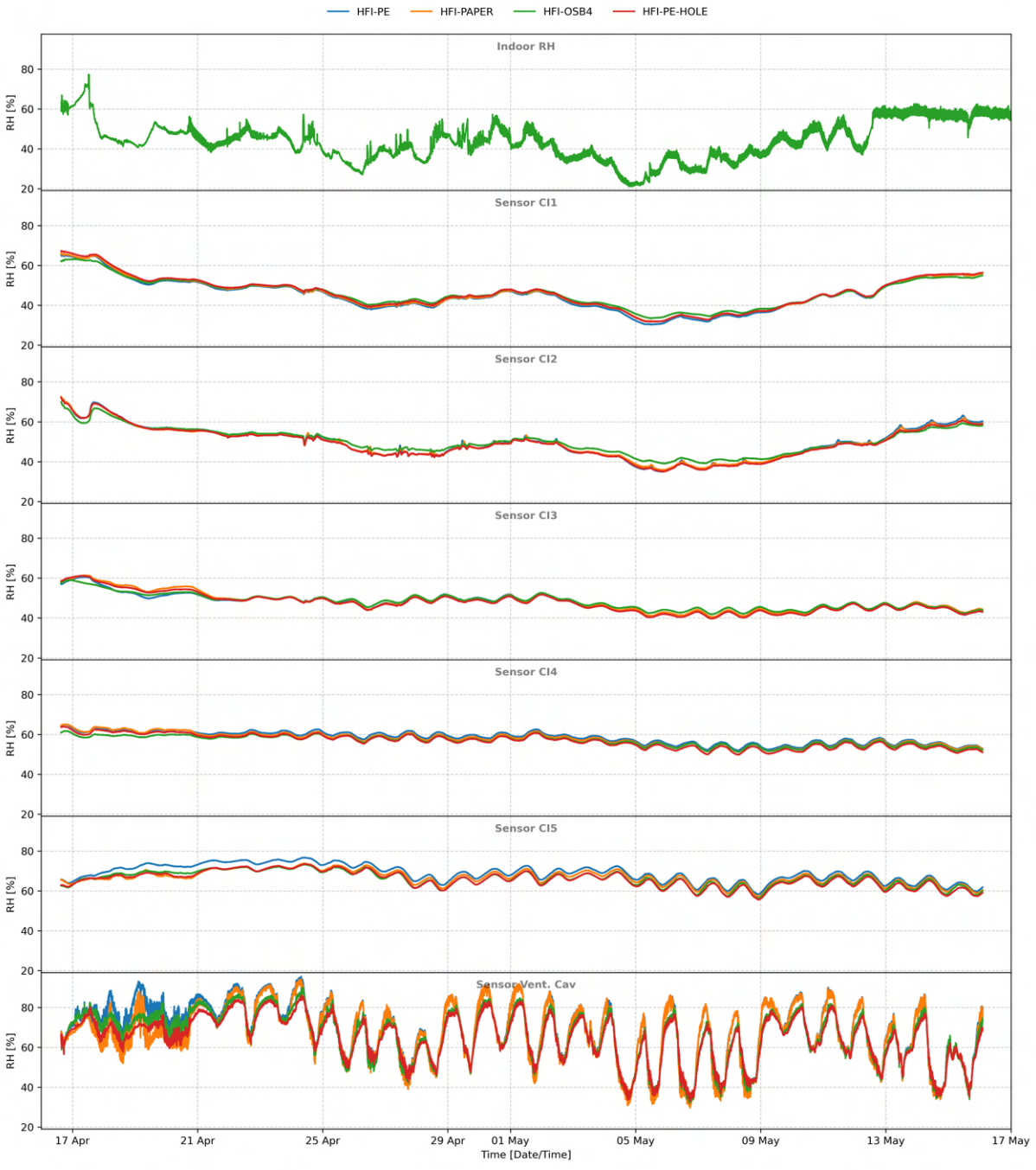

Figure G.9. RH for the four elements with HFI

While the overall RH values follow similar patterns, small differences are present across all

sensors. To explore this further, a profile, from before the humidifier was installed, is selected. The temperature profile for May 7th is presented in Figure G.10.

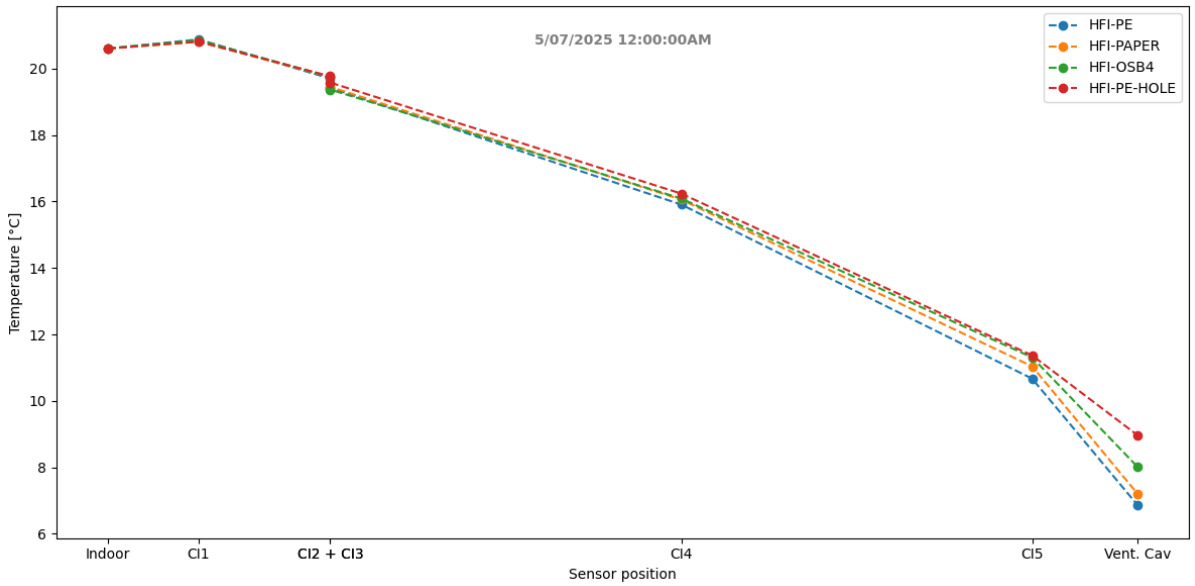

Figure G.10. Temperature profile May 7th.

The temperatures vary slightly between the elements. This is likely due to their placement in the measurement setup, and the small differences in the ventilated cavity. To gain a better understanding, the RH profile for the same timestamp is shown in Figure G.11.

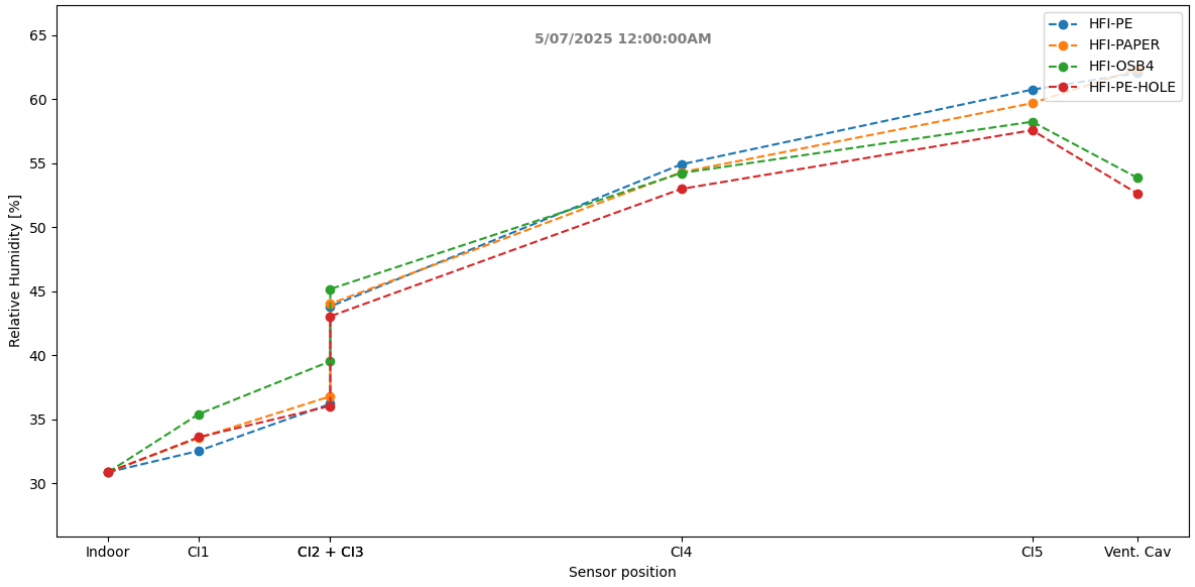

Figure G.11. RH profile for May 7th.

The RH profiles for the different vapor barriers vary slightly. The most noticeable is the OSB4

element which, on the warm side of the barrier, has a higher RH. This is most likely due to the OSB4 being the most permeable vapor barrier in this measurement setup. To confirm this, the vapor pressure is examined on Figure G.12.

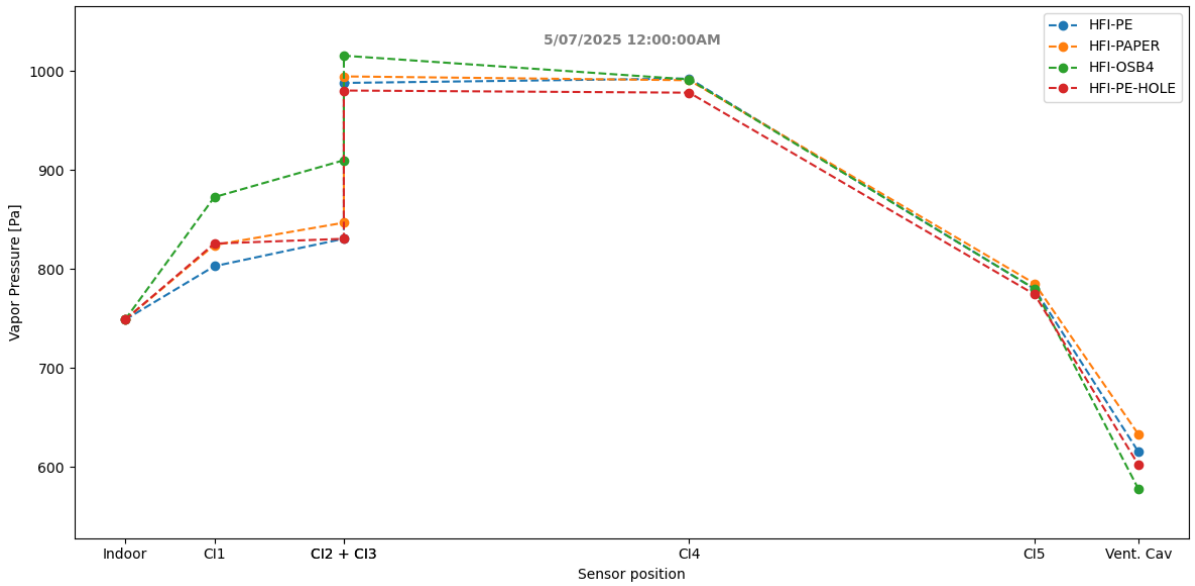

Figure G.12. Vapor pressure profile for May 7th.

As seen in the insulation study, the moisture flows from the vapor barrier and outwards. With the OSB4 being more permeable, this allows more moisture to transfer to the warm side, resulting in the higher RH. To assess the situation after the humidifier is operational, the temperature profile from May 16th is shown in Figure G.13.

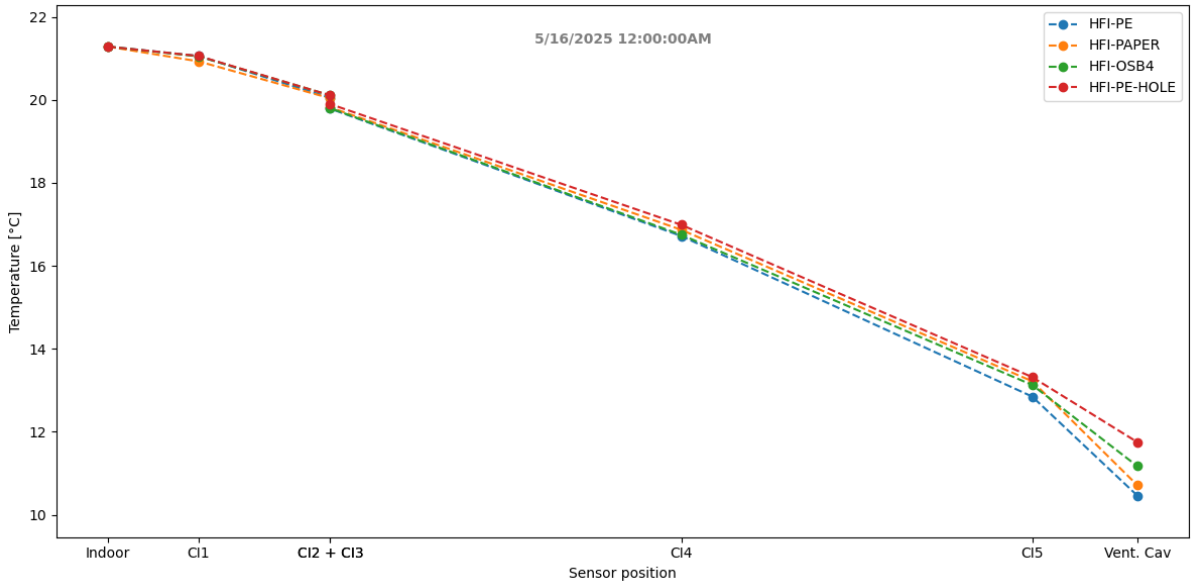

Figure G.13. Temperature profile May 16th

Consistent with the earlier findings, the addition of a humidifier does not impact the temperature profiles. Therefore, the impact of stabilized indoor RH is shown on Figure G.14.

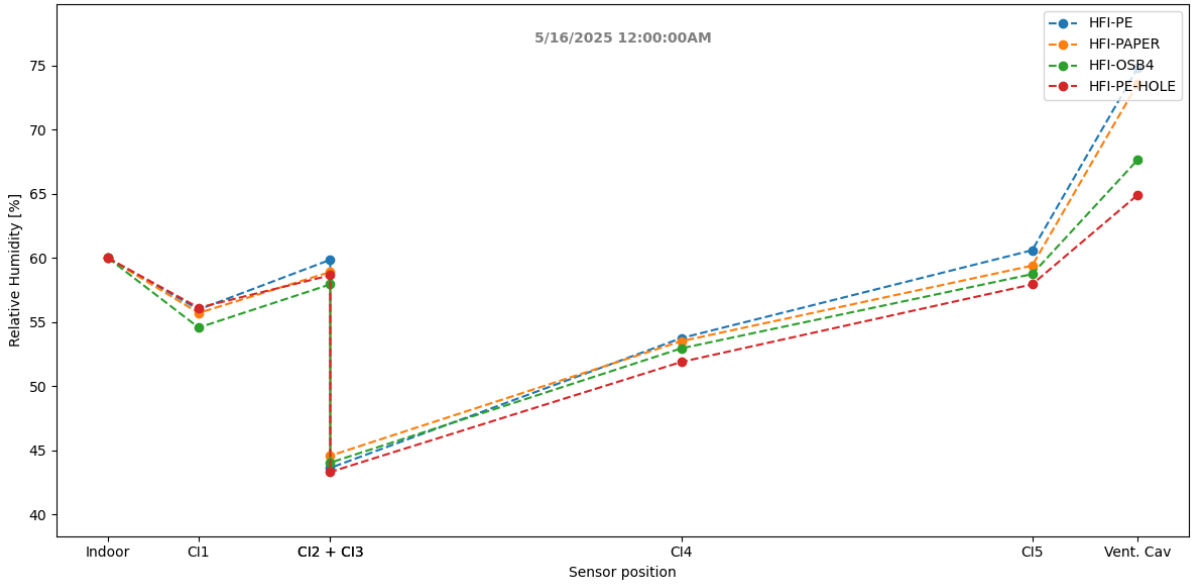

Figure G.14. RH profile May 16th.

The RH profiles are impacted by the humidifier in the same way as with the elements with different insulation. The humidity on the warm side of the vapor barrier is increased, while the cold side remains at the same values. This shows that the indoor RH primarily controls the RH before the barrier, while the cold side is influenced by the exterior conditions. Lastly, to see the flow direction, the vapor pressure is shown on Figure G.15.

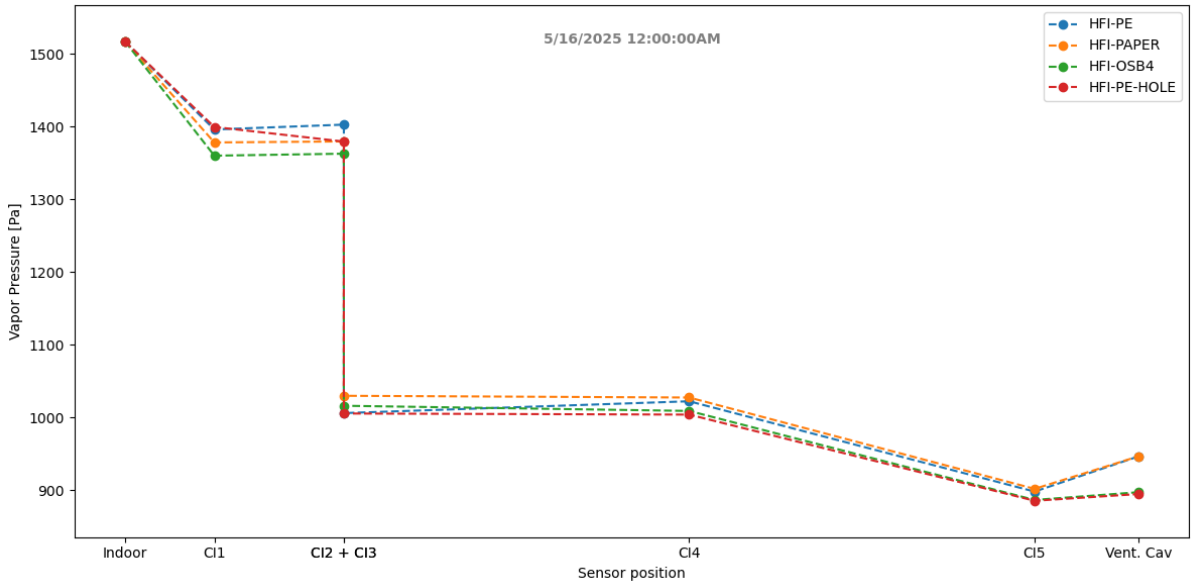

Figure G.15. Vapor pressure profile for May 16th.

From the vapor pressure, it can clearly be seen that the stabilized indoor conditions result in a moisture transfer from indoors to outside. Interestingly, while the vapor pressure changes over the vapor barrier, the difference between the elements is not significant. This indicates that under consistent indoor RH, the barrier type is less influential or that the elements have not had enough time to show the influence.

G.3 Influence of the sun

We can see some spikes in the temperature at the same time every day. One of these spikes can be seen on Figure G.16

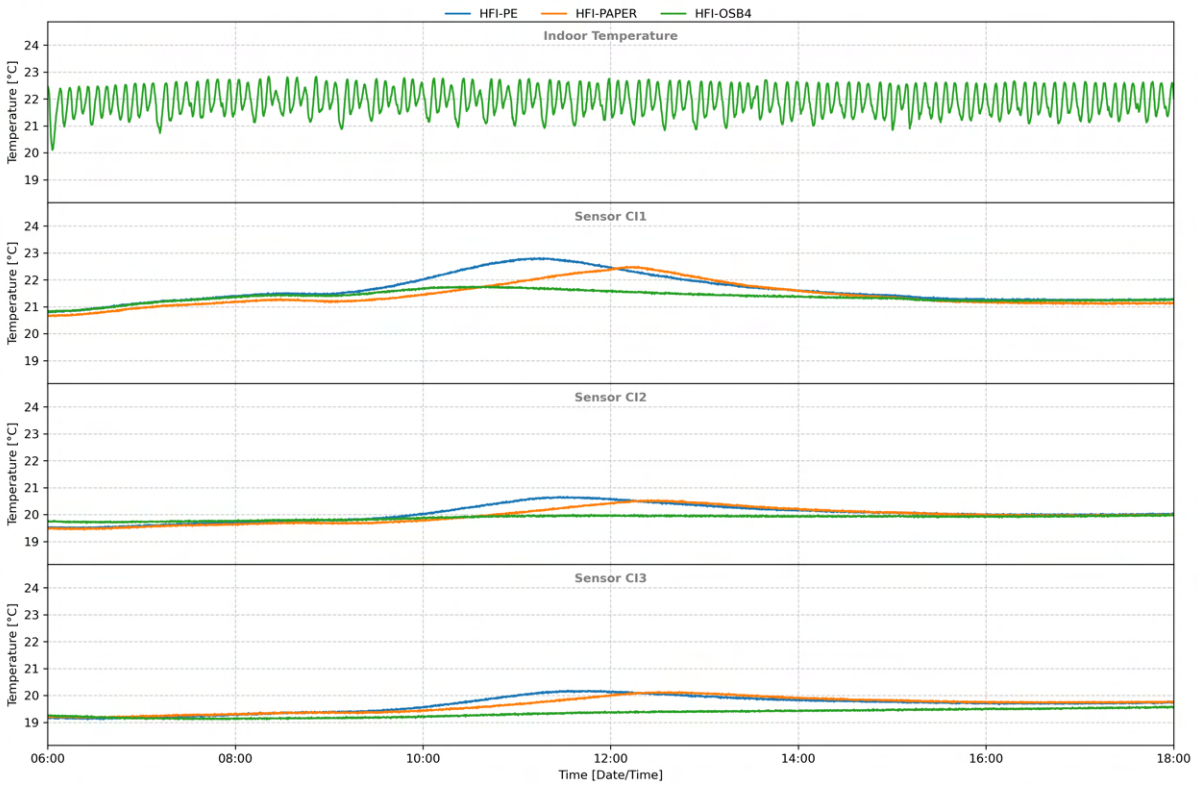

Figure G.16. Temperature during May 15th on three HFI elements.

The spike starts at around 9:00 and the temperatures stabilize at 15:00. The spike is different for each element. Since the indoor temperature is not influenced by the spikes, it is thought to be the radiant heat from the sun affecting the elements. To better understand this, the sun's position throughout the day has been analysed. The sun's position, at the beginning of the first spike and the peak of the 2nd, can be seen on Figure G.17 and G.18.

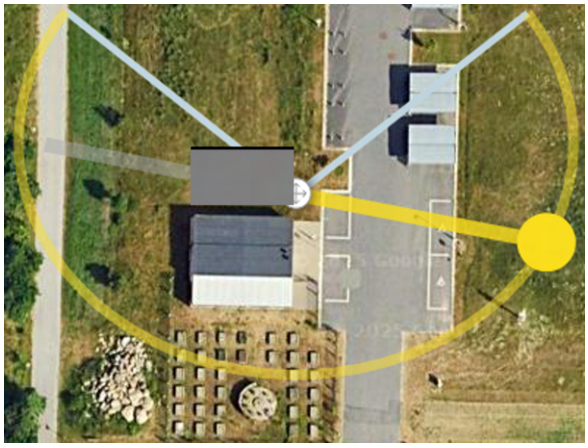

Figure G.17. The sun's position at 9:00[46]. The black line symbolizes the elements.

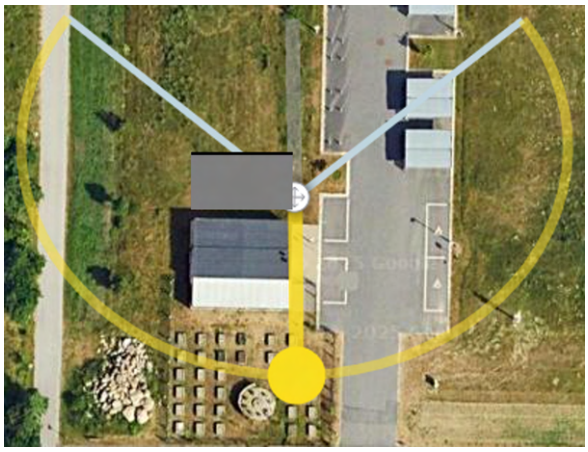

Figure G.18. The sun's position at 13:00[46]. The black line symbolizes the elements.

At 9:00 the sun is in a position to shine through the window in the door. This results in direct sunlight on some of the elements. At 13:00 the sun is parallel to the door, eliminating the possibility of further radiant heat. The differences in the spikes can be described by the placement of the element in the setup. The placement is illustrated on Figure G.19.

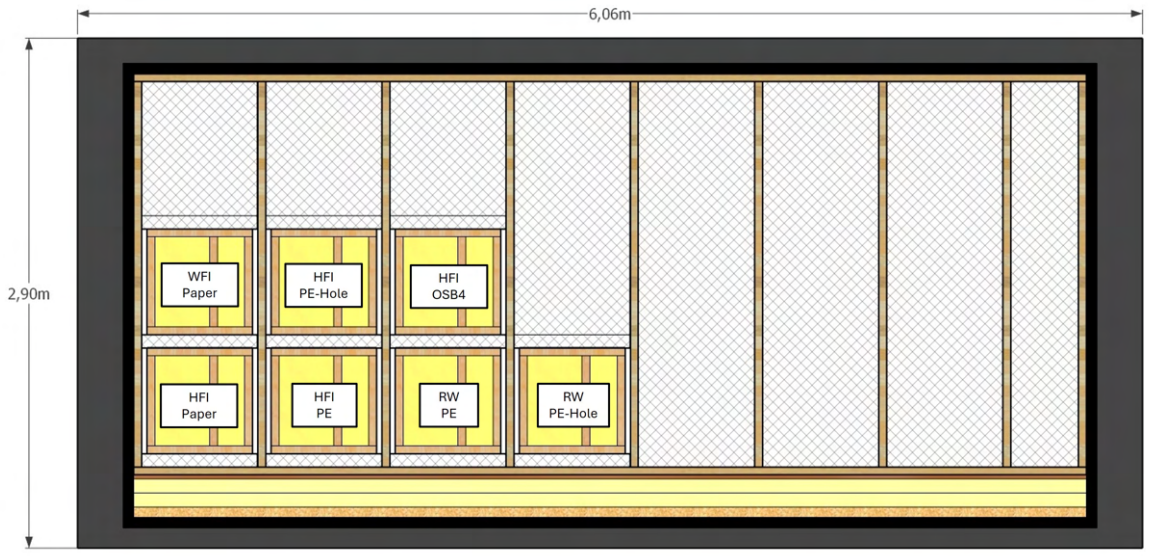

Figure G.19. Placement of the elements.

The OSB4 element is located in the top row, and therefore less exposed to the sun. In contrast, the paper element is close to the outer wall, which explains the delay, as the sun hits the element later in the day.

Furthermore, it can be observed that the sensor on the cold side of the vapor barrier is affected by the sunlight, as seen on sensor CI3 on Figure G.16. This demonstrates that the setup is sensitive to the influence of radiant heat from the sun.

G.4 Difference between CI and T sensors

To assess the consistency and reliability of the measurement setup, we compare data from two sensor columns within each wall element: the CI and T sensors. The CI sensors are embedded in the center of the insulation, while the T sensors are positioned next to a timber beam within the same cross-section. This placement allows for analysis of how the presence of timber influences thermal and moisture performance. The sensor locations are shown in Figure G.20.

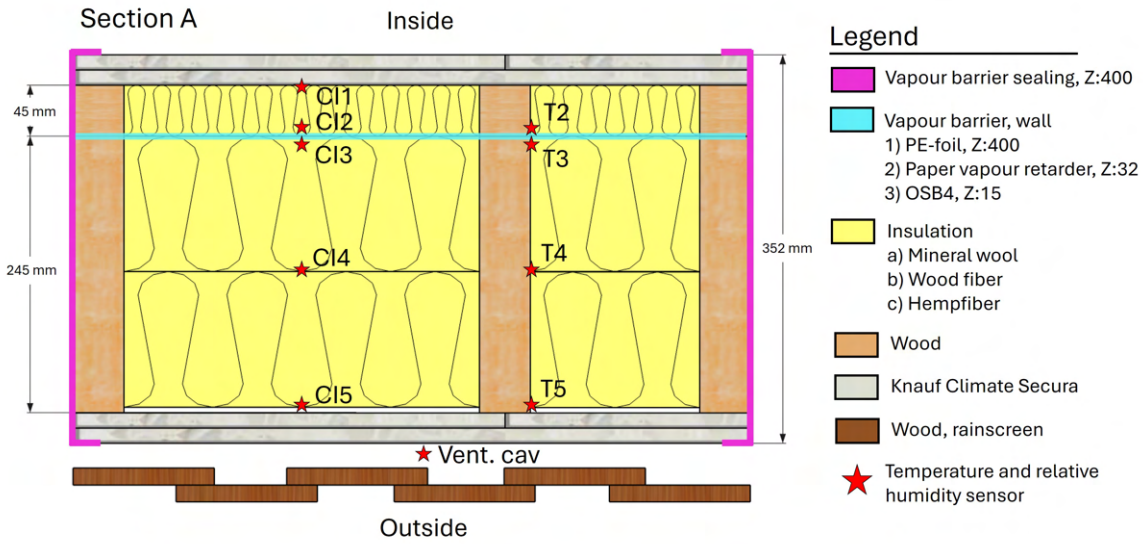

Figure G.20. Sensor placement within all elements.

We begin with comparing the temperature profiles from both sensor columns, in the WFI element on May 16th, shown in Figure G.21.

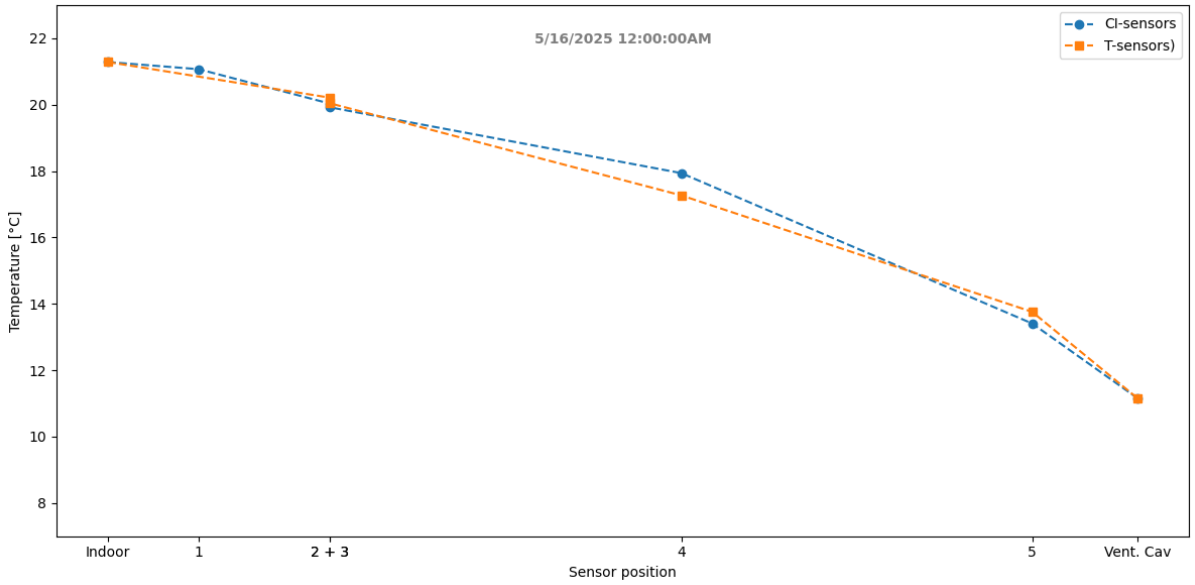

Figure G.21. Temperature profile for the two measurement columns in the WFI element.

The temperature profiles reveal almost no difference between the two columns. There is a small deviation, approximately 0.5 ℃, in sensor position 4 (the middle of the insulation). This is most likely caused by the dynamic conditions, and therefore the difference in heat conductivity, moisture buffering, and specific heat capacity. Next, we examine the RH profiles in Figure G.22.

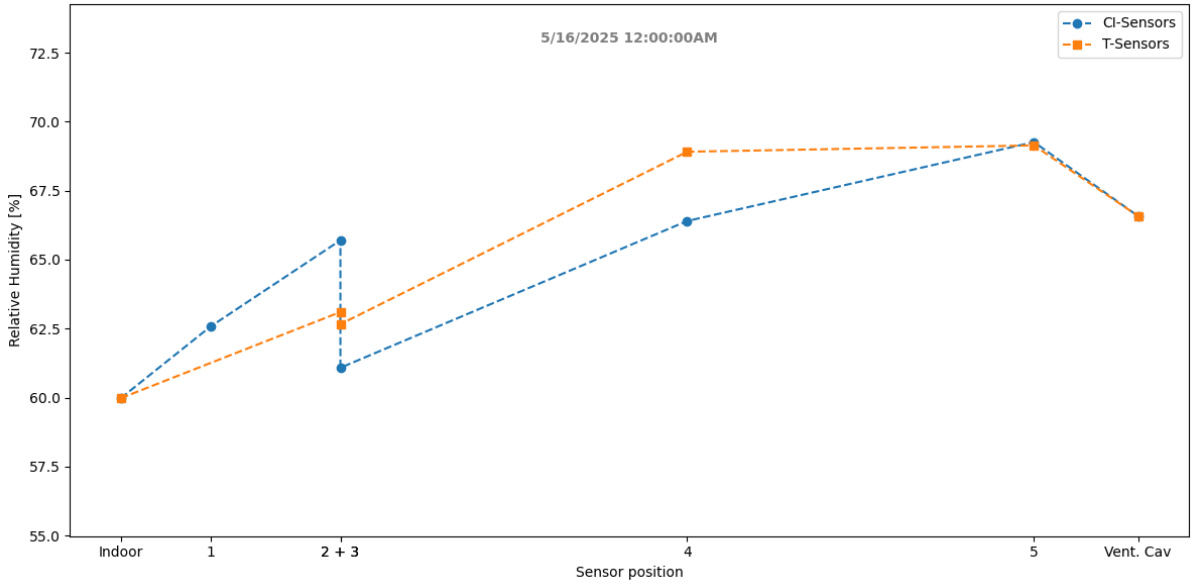

Figure G.22. Temperature profile for the two measurement columns in the WFI element.

The RH profiles indicate that the moisture content is slightly higher before the vapor barrier for the CI sensor. In addition to this, the RH also decreased more over the barrier. These differences

suggest that the timber beam may act as a moisture buffer, and therefore potentially influence the moisture distribution for the T sensors. To better understand the moisture flow, the vapor pressure profiles are presented in Figure G.23.

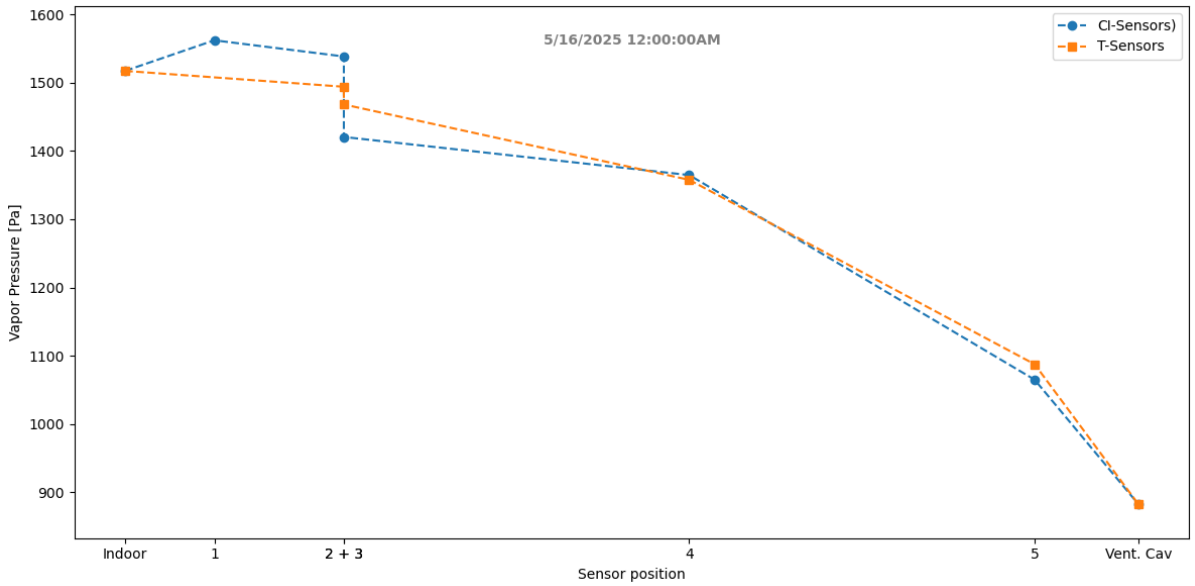

Figure G.23. Temperature profile for the two measurement columns in the WFI element.

The vapor pressure profiles confirm the general trend seen after the humidifier is installed. The moisture transfer direction is from indoors towards outdoors. The largest variation between the two sensor columns occurs around the vapor barrier, likely due to differences in material properties.

G.5 Summary

The measurements showed that radiant heat from the sun caused recurring temperature spikes, depending on the elements' placement, even affecting sensors on the cold side of the vapor barrier. Insulation materials performed differently than expected based on thermal conductivity alone, as biobased materials like WFI and HFI demonstrated significant moisture buffering effects. The vapor barrier type influenced moisture transport, especially before the indoor humidity stabilized, with more permeable barriers like OSB4 allowing greater vapor migration. Once stable conditions were established using a humidifier, moisture movement became predominantly unidirectional, from indoors to outdoors, and the differences between vapor barriers became less significant. Finally, comparing CI sensors with T sensors revealed only minor temperature and RH variations but confirmed that timber affects local hygrothermal behavior due to its different

material properties.

Overall, the test setup proved to be sensitive but reliable, capable of capturing both expected trends and more nuanced effects. However, the limited measurement period has prevented the elements from reaching moisture equilibrium, making long-term behavior less certain. Future work should allow more time for stabilization to improve the accuracy of conclusions about wall performance.

Part II

Appendices for simulations

Appendix H

Hygrothermal simulations

This appendix provides a general overview of our studies using numerical simulation tools. Moisture transport happens slowly and it takes several years before potential consequences and moisture problems become evident. This is why numerical simulations are a good tool, so different constructions can be quickly evaluated over the necessary time period. This is crucial to make informed decisions and good assessments of moisture performance for constructions. The different tools do however make different assumptions and simplifications, which can lead to a model/reality discrepancy [47] [21]. In this project, we are looking into the simulation tools WUFI and BSim.

WUFI is developed by the Department of Hygrothermics at Fraunhofer IBP, and is a state-of-the-art dynamic hygrothermal simulation tool for building components. It allows realistic calculation of the transient coupled one- and two-dimensional heat and moisture transport in walls exposed to natural weather [31]. It has a big built-in catalogue of materials with all the necessary properties defined.

BSim is developed by Statens Byggeforskningsinstitut a part of BUILD - Aalborg University, and is a dynamic hygrothermal simulation tool for buildings. It can simulate indoor climate, energy use and also moisture transport inside building components [48].

We have made models and done investigations using both BSim and WUFI. WUFI accounts for more moisture transport dynamics and is expected to be more accurate than BSim. An interesting difference is however that moisture sorption isotherms are implemented differently. WUFI does not account for hysteresis in the moisture sorption isotherm for materials, but only uses a combined absorption and desorption curve. In BSIM there is both an absorption and

desorption isotherm, and it uses a model developed by Carsten Rode to determine the hysteresis [49].

Representative material properties are essential to get accurate simulation results, and our used values across both programs are covered in a combined appendix. The general model setup and settings are described separately for each program. The aim is however to make the models as identical as possible.

Table H.1 provides an overview of the different appendices explaining the simulation investigations and the used boundary conditions.

Appendix I - Material inputs for simulations	
Appendix J - Comparison of wall measurements with WUFI simulation	
Description	**Outdoor boundary:**
We evaluate the simulation model, against our measurements. The model is used to predict the long term development of moisture in the wall in the climatic chamber	Measurement inside ventilated cavity. **Indoor boundary:** Climatic chamber indoor measurements
Appendix L - Comparison of WUFI and BSim simulations	
Description	**Outdoor boundary:**
We compare the simulation results for the same model in BSIM and WUFI. Additionally we investigate how the different physics in WUFI impact its results.	HRY-Ref2 **Indoor boundary:** Approximated moisture class 3 with BSIM.
Appendix K - Impact of hysteresis evaluated using BSim	
Description	**Outdoor boundary:**
We evaluate the simulation results, where the wood-fiber insulation only has absorption, desorption, average curve and hysteresis.	HRY-Ref2 **Indoor boundary:** Approximated moisture class 3 with BSIM.
Appendix M - Sizing of HVAC systems for climatic chamber using BSim	
Description	**Outdoor boundary:**
A general model, where the focus is the heating and cooling need at our expected operation. The constructions are not in focus.	DRY **Indoor boundary:** Approximated moisture class 3 with BSIM.

Table H.1. Overview of simulation studies, and their appendices.

H.0.1 Simulation boundary conditions

Inside WUFI it is easy to specify the indoor boundary conditions to be moisture class 3. WUFI does not do indoor climate simulation, but only do hygrothermal simulation of building components. BSim does both things, and it is not possible to specify the indoor climate. In BSim we have, by adjusting heat and moisture loads, HVAC system controls and setpoints, tried to get the simulation to achieve moisture class 3. We obtain moisture class 3 according to the interpretation made in [6], but this is however not one-to-one equal to the conditions of moisture class 3 inside WUFI. WUFI can apply moisture class 3 directly from the specification in [13], which is different from the conditions we have obtained by approximation in BSIM. The difference between our obtained conditions in BSIM and moisture class 3 from WUFI is shown on

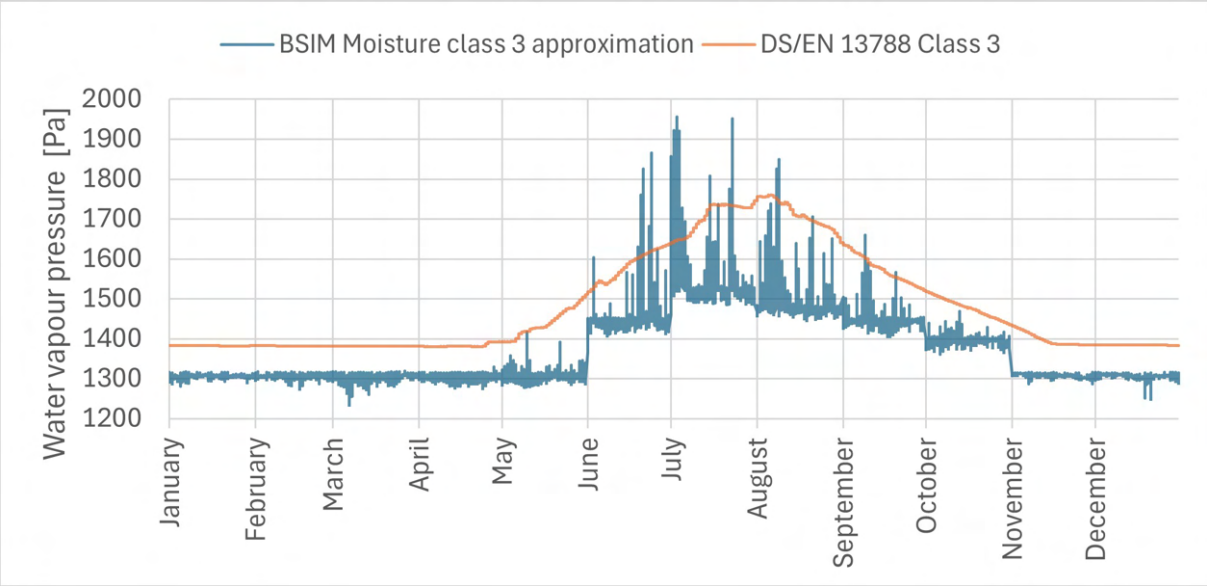

Figure H.1. Indoor vapour pressure by our BSIM aproximated moisture class 3, and WUFI moisture class 3 [13]

Initially, we accounted for this by manually adjusting the indoor conditions in WUFI to try and match what we had in BSim. It is however, possible to make an indoor "weather file" for WUFI, by which we later obtained the exact same indoor conditions in WUFI as BSIM.

For the outdoor weather it is typical to use DRY-2013 for simulation. There has however recently been established a Hygrothermal reference year in a report by Jensen et al. [41], that better accounts for moisture. They establish five reference years, but conclude that reference year 2 is a good proposal to use for hygrothermal simulations. The HRY-Ref2 is used to better asses the moisture performance in simulation tools. This reference year has been developed in .wac

format, which can be loaded into WUFI. We have also translated the weather, so we could use it in BSim. Figure H.2 and Figure H.3 show the difference between DRY and HRY-Ref2.

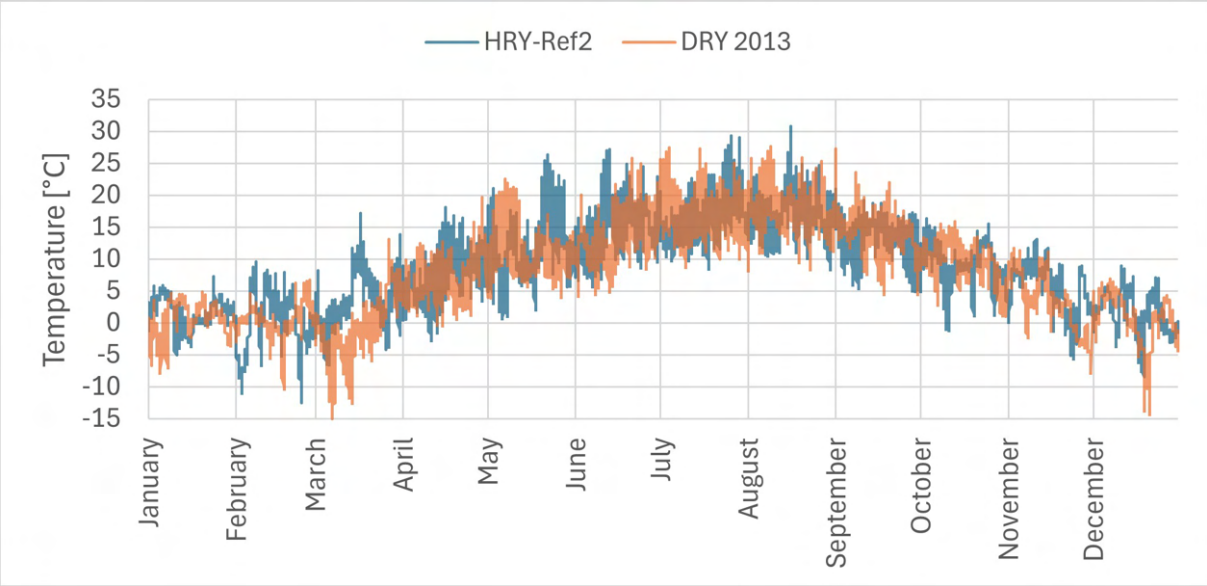

Figure H.2. Plot of temperatures in DRY and HRY-Ref2 [41]

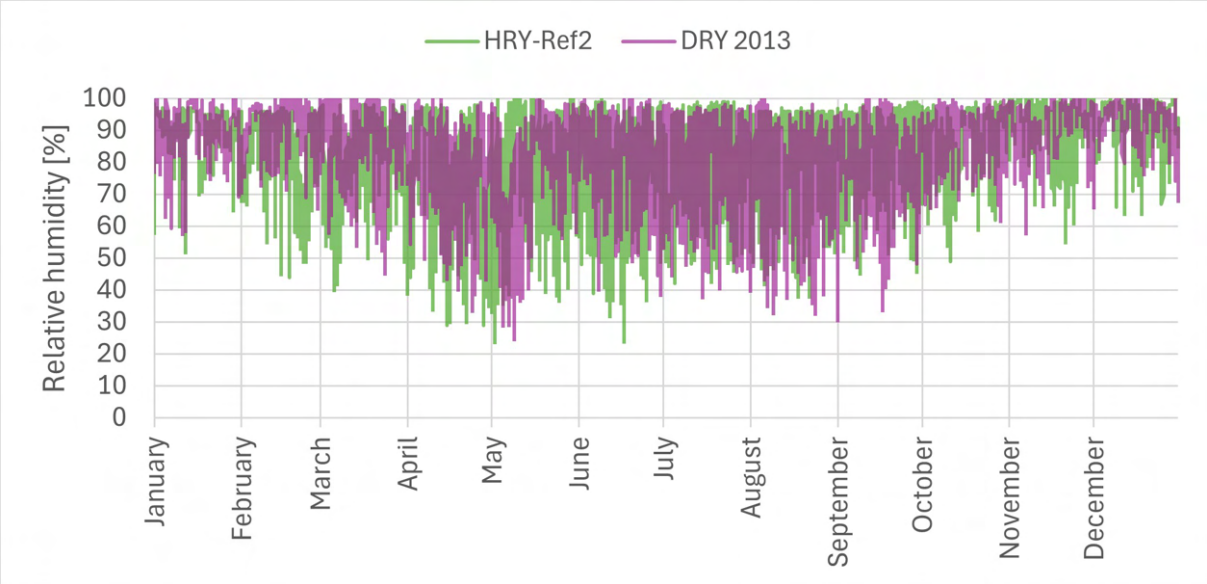

Figure H.3. Plot of relative humidities in DRY and HRY-Ref2 [41]

Appendix I

Numeric model material inputs

When setting up the numerical models, we want to match the material properties to the materials used in the wall elements in the experimental setup. This is to align our measurements with the results from the models, so they are comparable. When defining our materials, we have based them upon a similar predefined material in the database and then modified the properties to match ours. We have chosen to model the wall element with wood-fibre insulation in BSim and WUFI because woodfibre is currently more widely used in the building sector.

For our numerical models in WUFI and BSIM it has been necessary to find property values in different sources. The manufacturer data sheets lacks properties regarding moisture dynamics. WUFI accounts for several moisture physics mechanics, and we have used property values from the WUFI database to fill out missing values.

In WUFI we have found a comparable material and used its values where we are missing data. We have compared based on density, thermal conductivity, and specific heat capacity. The accuracy of the used material properties is not studied in detail, but we compare the values from different products. We follow the assumption that the available properties in WUFI in general, are representative.

For the woodfibre insulation we have used the material properties from [50]. They measured a coherent collection of properties for Hunton Woodfiber Nativo. As we are using a different batch of insulation, there will be an unknown uncertainty in the actual material properties for the insulation we have used. We assume these data to better reflect the actual material behaviour than the manufacturer's data, because they are measured on a recent specific material batch purchased in Denmark.

This section presents the specific material values we have used for the numerical simulations. Explanation for the chosen materials to copy is also provided here.

I.1 Insulation properties

This provides an overview of the different sources used to obtain the necessary material properties. The values highlighted with green, is the ones we have used. For the insulation we have used AiF Felxible Wood-Fiber insulation WF as our template. We have selected the wood-fibre insulation based on a similar density and thermal conductivity. It should be noted that we use our measured moisture sorption curve.

		Hunton Nativo Woodfiber		**AiF Felxible Wood-Fiber insulation WF**
	Data sheet [34]	Measured by [50]	Own measurement	
Density $[kg/m^3]$	50 (44,2-59,8)	53,2	-	50
Thermal conductivity, $\lambda\ [W/mK]$	0.038	[-]	Table I.4	Table I.3
Specific heat capacity, $C_p\ [J/kgK]$	2100 [36]	-	-	1400
Porosity $[m^3/m^3]$	-	0.96		0.97
Water Vapour permeability, σ_d $kg/(m \cdot s \cdot Pa)$	-	9.96E-11		-
Water Vapour resistance factor $\mu\ [-]$	5/3 (dry/wet)	2.01	-	2
Moisture sorption isotherm	-	-	Table I.6	Table I.7c
Liquid transport coefficient, suction	-	-	-	Table I.2a
Liquid transport coefficient, redistribution	-	-	-	Table I.2b
Particle density $[kg/m^3]$	-	1450		-
Active air-filled porosity $[m^3/m^3]$	-	0.66	-	-
Specific surface area $[km^2/m^3]$	-	1.5	-	-
Relative 02 diffusivity D_p/D_0, -	-	0.524	-	-

Table I.1. Overview of used materials parameters for woodfibre insulation.

Table I.2. Liquid transport coefficients for suction and redistribution from AiF Felxible Wood-Fiber insulation WF [51]. It is expressed in water mass per volume.

(a) Suction

Water content $[kg/m^3]$	**Dws** $[m^2/s]$
0	0
9	3.60×10^{-12}
300	2.93×10^{-9}

(b) Redistribution

Water content $[kg/m^3]$	**Dww** $[m^2/s]$
0	0
9	3.60×10^{-12}
300	2.93×10^{-10}

I.1.1 Thermal conductivity

This is the difference between our measure thermal conductivity and the one specified in WUFI. The values in the tables are plotted on Figure I.1.

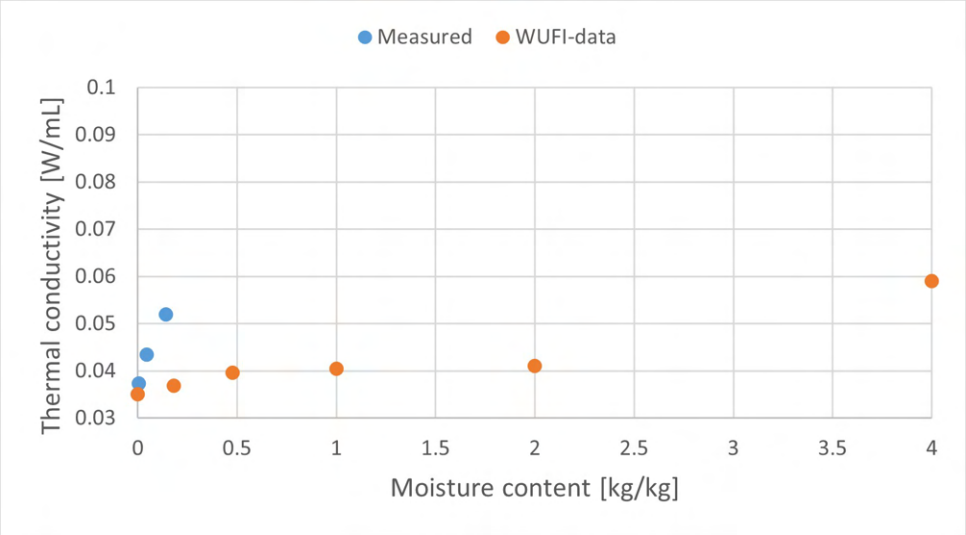

Figure I.1. Comparison of measured thermal conductivity dependent on moisture content, compared to values available in WUFI. The values are only shown for the area, close to our measure values, but their continue for the WUFI-data.

It can be seen that our measurement is quite different, where we see that the thermal conductivity increases more with a higher moisture content.

Table I.3. Thermal conductivy as function of moisture content for AiF Felxible Wood-Fiber insulation WF [51].

Water content per volume $[kg/m^3]$	**Thermal conductivity [W/mK]**
0.0	0.035
9.0	0.0368
23.8	0.0396
50.0	0.0405
100.0	0.041
200.0	0.059
300.0	0.089
400.0	0.131
500.0	0.185
600.0	0.251
700.0	0.329
800.0	0.419
900.0	0.521
910.0	0.532
920.0	0.543
930.0	0.554
940.0	0.566
950.0	0.577
960.0	0.588
970.0	0.6

Table I.4. Own measurements of thermal conductivity at different moisture contents. It is water content per. m^3 volume.

Water content		**Thermal conductivity**
[kg/kg]	$[kg/m^3]$	**[W/mK]**
0.00427	0.234	0.0373
0.0460	2.52	0.0434
0.141	7.75	0.052

I.1.2 Comparison of moisture sorption curves

We have in our simulations used the moisture isotherms we measured using the VSA, as described in section 3.1. In BSIM you can enter an absorption and desorption curve, because BSim accounts for hysteresis. WUFI however only uses on sorption curve. In WUFI we have inputted an average of our measured absorption and desorption curve. WUFI has a database with ready-to-use materials. Here we have compared our moisture isotherms, with similar wood-fibre insulation available in the WUFI-database. We have looked at three different wood-fibre insulations in WUFI, and their general characteristics are presented in Table I.5. The following section shows the tabulated values and sorption curves.

	Hunton Nativo Woodfiber	Wood fiber Air [52]	Pavaflex [53]	AiF Felxible Wood-Fiber insulation WF [51]
Density $[kg/m^3]$	50 (44,2-59,8)	43	53	50
Thermal conductivity, λ $[W/mK]$	0.038	0.0364	0.039	0.035
Specific heat capacity, C_p $[J/kgK]$	2100	1400	2100	1400
Porosity $[m^3/m^3]$	0.96	0.975	0.96	0.97
Water Vapour resistance factor μ $[s]$	2.01	1.9	1.35	2
Porosity $[m^3/m^3]$	0.96	0.975	0.96	0.97

Table I.5. Comparison of material properties for different types of woodfiber insulation available in WUFI.

Figure I.2 show the sorption curves from WUFI for the three different insulation materials and our measurements. It is important to note, that two version of our measured sorption curve is showed. The one marked, "VSA - WFI Wrong" is made based on a wrong dry weight. This curves does however fit well with the curves found in WUFI. Our actual sorption curve, "VSA -WFI" is placed higher, but its endpoint is in good agreement with the curve from AiF and Pavaflex.

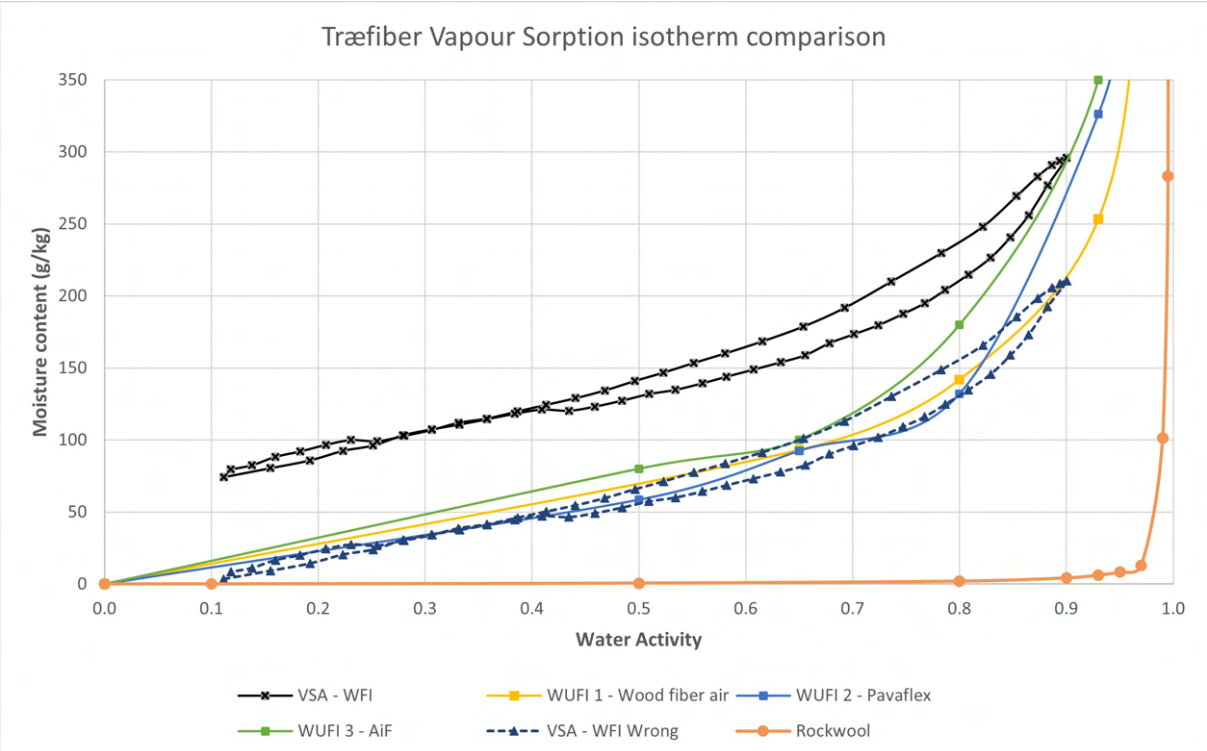

Figure I.2. Comparison of measured sorption isotherm, and available sorption curves in WUFI, not accounting for hysteresis.

For perspective is the sorption curve for a Rockwool insulation form WUFI plotted.

I.1.3 Tabulated values for moisture sorption isotherms

We have in our simulations used the wrong sorption curve, and Figure I.3 and Table I.6 shows the curves we used for the different investigations. It is not ideal that, we have not used the actual result form our VSA-measurement.

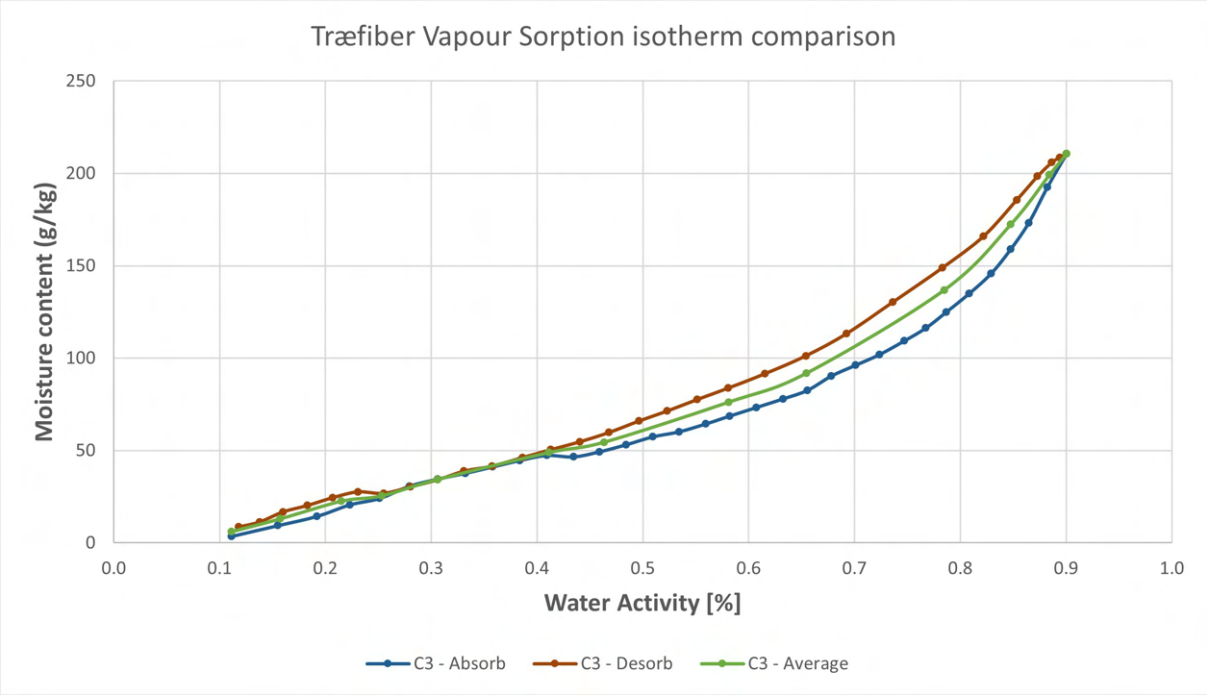

Figure I.3. Absorption, desorption and average curve used for woodfiber insulation in WUFI and BSim.

Table I.6. Tabulated values of moisture sorption isotherms from our measurement on WFI. section 3.1

RH [-]	Absorp [g/kg]
0.1115	3.49
0.2513	24.03
0.2793	30.62
0.4092	47.29
0.4345	46.51
0.4843	53.10
0.5341	60.08
0.5820	68.60
0.6325	77.91
0.6782	90.31
0.7238	101.94
0.7675	116.28
0.8083	134.88
0.8476	158.91
0.8824	192.64
0.9003	210.47

RH [-]	Desorp [g/kg]
0.1181	8.53
0.1379	11.24
0.1599	16.67
0.2306	27.52
0.2550	26.74
0.3311	38.76
0.4132	50.39
0.4681	59.69
0.5231	71.32
0.5807	83.72
0.6540	101.16
0.7361	130.23
0.8219	165.89
0.8731	198.45
0.8939	208.53
0.9003	210.47

RH	Avg.	
[-]	[g/kg]	$[kg/m^3]$
0.1115	6.01	0.32
0.1575	12.98	0.69
0.2151	22.48	1.20
0.2532	25.39	1.35
0.3061	34.30	1.82
0.4112	48.84	2.60
0.4635	54.46	2.90
0.5814	76.16	4.05
0.6548	91.86	4.89
0.7848	136.82	7.28
0.8476	172.29	9.17
0.8844	199.22	10.60
0.9003	210.47	11.20

Table I.7. Moisture storage function from WUFI for the three types of woodfibre insulation

(a) Wood fiber Air

RH [-]	Moisture storage [g/kg]
0	0.0
0.65	93.0
0.8	141.9
0.93	253.5
0.97	458.1
0.99	946.5
0.995	1523.3
0.999	4132.6
0.9995	5897.7
0.9999	10600.0
1	16255.8

(b) Pavaflex

RH [-]	Moisture storage [g/kg]
0	0.0
0.65	93.0
0.8	141.9
0.93	253.5
0.97	458.1
0.99	946.5
0.995	1523.3
0.999	4132.6
0.9995	5897.7
0.9999	10600.0
1	16255.8

(c) AiF Felxible Wood-Fiber insulation WF

RH [-]	Moisture storage [g/kg]
0	0
0.5	80
0.65	100
0.8	180
0.93	350
0.97	600
0.99	1310.6
0.995	1976
0.999	3865.8
0.9995	4563.2
0.9999	5527.6
1	6000

I.2 Wood properties

For the wood cladding, we have used "Southern Yellow Pine" from the WUFI database and "Spruce inner and outer sapwood" from the BSIM database. We have not matched the properties of the wood cladding between the two simulation programs, as the cladding is separated from the wall construction by the ventilated cavity. The two materials are quite similar in the standard material properties as shown in Table I.8. We have not inserted the moisture storage function and water vapour diffusion resistance factor for the wood but it is available in WUFI.

Table I.8. Table with general material characteristics for wood cladding used in BSim and WUFI.

	Unit	Spruce inner and outer sapwood [48]	Southern Yellow Pine [54]
Thickness	[mm]	20	20
Density	$[kg/m^3]$	470	500
Thermal conductivity, λ	$[W/(m \cdot K)]$	0.12	0.119
Specific heat capacity, C_p	$[J/(kg \cdot K)]$	1800	1880
Porosity	[-]	-	0.858

When adjusting the simulation models to match our measurements from the wall elements in the climatic chamber, we do not model the wood cladding. This is because our boundary condition is the humidity and temperature inside the ventilated cavity, which is then our outer boundary.

I.3 Gypsum properties

As template for the Kanuf Clima Secura gypsum board, we have used Rigips Glasroc X in WUFI. The two products have a similar product description and general material properties, shown in Table I.9. Rigips Glasroc X is also fibreglass reinforced and made to be used as a wind barrier.

Table I.9. Table with material characteristics for vapour barriers and wind barrier from the manufacturer data sheets. An assumed water vapour permeability for air of 2.00E-10 $kg/(m \cdot s \cdot Pa)$ is used.

	Unit	Gypum [37]	Rigips Glasroc X [55]	BSIM gypsum
Thickness	[mm]	15.5	12.5	-
Density	$[kg/m^3]$	774	879	881
Thermal conductivity, λ	$[W/(m \cdot K)]$	0.25	0.25	0.2
Porosity	[-]	-	0.63	-
Specific heat capacity, C_p	$[J/(kg \cdot K)]$	-	850	1000
Water Vapour permeability, σ_d	$kg/(m \cdot s \cdot Pa)$	3.23E-11	2.00E-11	2.00E-11
Water Vapour resistance factor, μ	[-]	6.2 (dry)	10	10

We have used the moisture sorption isotherm from WUFI inside BSim as well. The sorption curve for gypsum in BSim, is quite different from the one in WUFI. This is shown on Figure I.4. The Kanuf Clima Secura gypsum board is different from a traditional gypsum board, and we are convinced that the values from WUFI is a lot more representative.

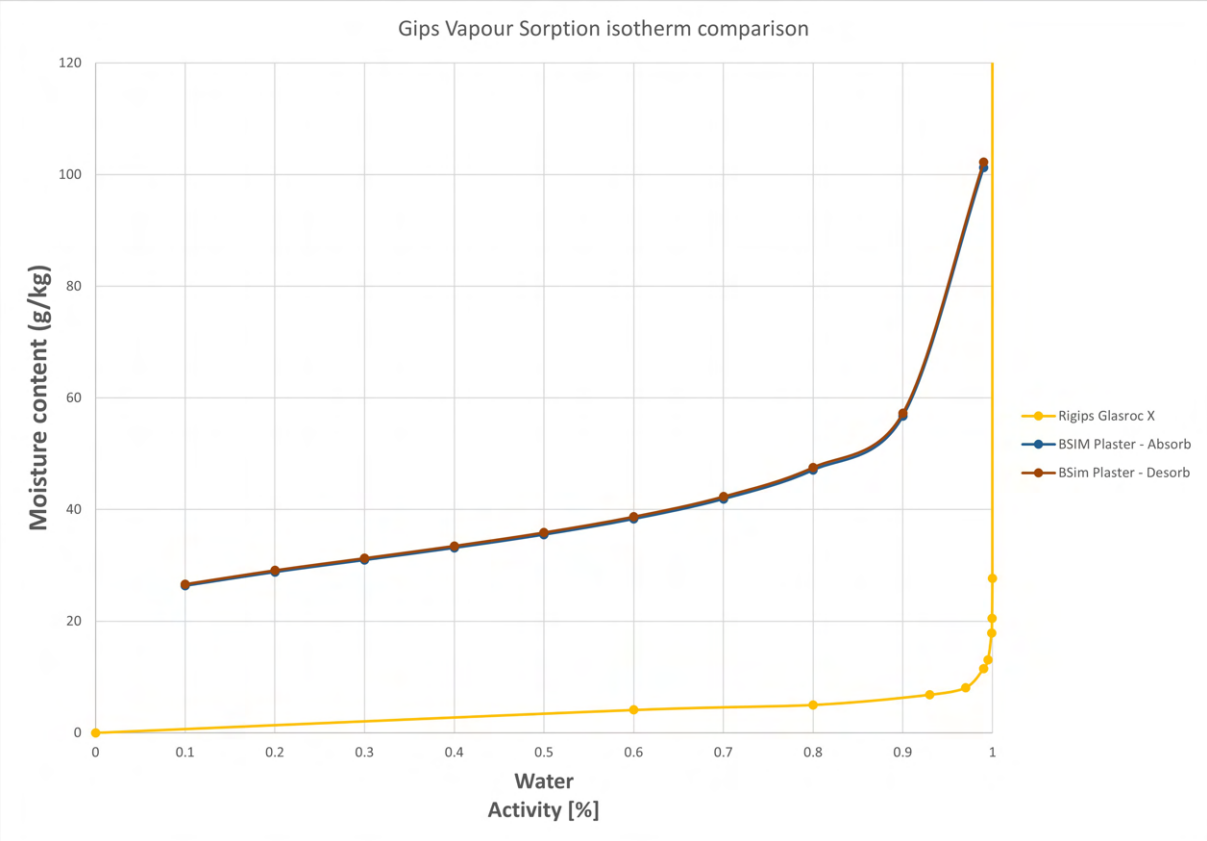

Figure I.4. Sorption curve for gypsum in BSIM and WUFI.

Table I.10. Tabulated values of moisture sorption isotherms of BSIM Gypsum and WUFI Rigips Glasroc X [55]. Water content is expressed in water mass per unit pore volume.

(a) Rigips Glasroc X

RH	Water content	
[-]	$[kg/m^3]$	[g/kg]
0	0	0
0.6	3.6	2.58
0.8	4.4	3.15
0.93	6	4.30
0.97	7.1	5.09
0.99	10.1	7.24
0.995	11.5	8.24
0.999	15.7	11.25
0.9995	18	12.90
0.9999	24.3	17.42
1	403	288.84

(b) Gypsum BSIM database

RH	Absorp	Desorp
[-]	[g/kg]	[[g/kg]
0.1	26.35	26.61
0.2	28.80	29.09
0.3	30.96	31.27
0.4	33.13	33.47
0.5	35.52	35.87
0.6	38.32	38.70
0.7	41.90	42.31
0.8	47.08	47.55
0.9	56.72	57.29
0.99	101.24	102.26

Table I.11. Liquid transport coefficients for suction and redistribution from Rigips Glasroc X [55]. It is expressed in water mass per unit pore volume.

(a) Suction

Water content $[kg/m^3]$	**Dws** $[m^2/s]$
0	0
4.4	2.04×10^{-14}
403	1.90×10^{-11}

(b) Redistribution

Water content $[kg/m^3]$	**Dww** $[m^2/s]$
0	0
4.4	2.00×10^{-10}
403	2.20×10^{-10}

Table I.12. Thermal conductivity as function of temperature and moisture for Rigips Glasroc X [55]. Water content is expressed in water mass per unit pore volume.

(a) Thermal conductivity, moisture dependent

Water content $[kg/m^3]$	**Therm cond** W/mK
0	0.25
630	1.68

(b) Thermal conductivity, temperature dependent.

Temperature ℃	**Therm cond** W/mK
-20	0.244
80	0.264

I.4 Vapour barrier properties

For the vapour barrier, we have used "Vapor retarder (sd=5m)" from Fraunhofer-IBP as our starting point in WUFI. We have modified it to match the known properties from the data sheet of our applied vapour retarder Ökonatur.

WUFI uses the vapour resistance factor (μ-value), and for comparability between vapour

membranes, a standard thickness of 1 mm is used, regardless of the actual product thickness. In BSim is the actual water vapour resistance is typed in, with the unit of $[(m^2 sPa)/kg]$.

	Unit	Paper [39]	Vapor ratarder (sd=5m) [40]
Thickness	[mm]	0.25	1
Density	$[kg/m^3]$	700	130
		Equals 175 if 1 mm thick.	
Thermal conductivity, λ	$[W/(m \cdot K)]$	-	2.3
Specific heat capacity, C_p	$[J/(kg \cdot K)]$	-	2300
Water Vapour resistance factor, μ	[-]	25800	5000
		Equals 6450 if 1 mm thick.	
Z-value	$(GPa \cdot m^2 \cdot s)/kg$	32.25	25

Table I.13. Table with material characteristics for our vapour barrier and the one used in WUFI. An assumed water vapour permeability for air of 2.00E-10 $kg/(m \cdot s \cdot Pa)$ is used.

Appendix J

WUFI model documentation

This chapter will describe general settings used for our WUFI model. Figure J.1 shows our model geometry in WUFI.

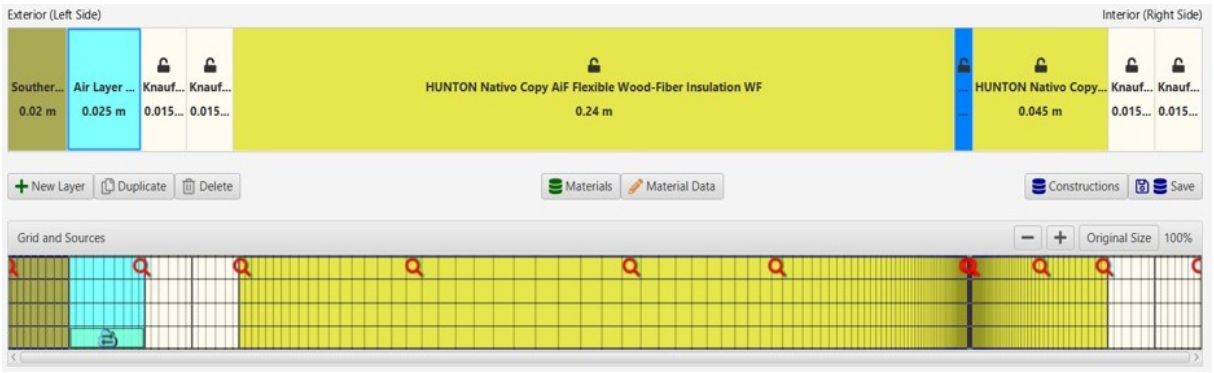

Figure J.1. Model geometry inside WUFI.

The little cloud inside the ventilated cavity, symbolises that we have applied an Air Change rate to the air layer, thus making it ventilated. We have used a value of $20h^1$, which WUFI recommends. Both in BSim and WUFI it is possible to add a finish to the exterior surface. With a finish WUFI accounts for short-wave absorptivity of sun. We have applied the wood-finish "Bankirai" which has a short-wave radiation absorptivity of 0.47 and long-wave radiation emissivity of 0.92. Similar finish is used in BSim. For surface heat transfer coefficients we have used the ones stated in [56].

It is a slow process for moisture to settle in a quasi-stationery equilibrium. That is the reason we simulate for 7 years in both WUFI and BSIM, to ensure the variations have stabilized. When comparing the results, we are looking at the seventh year. By looking at the seventh year, it reduces the impact of the initial conditions for the materials. In WUFI we also start the

simulation in October, because it by experience makes the simulation stabilize faster.

J.1 WUFI simulation for WFI-Paper element

This section elaborates on the model we have made in WUFI, that should match our measurements for the wood fiber wall element. We have measured the boundary conditions and initial conditions for the wall elements in the Climatic chamber setup. We only have 1 month of data, but can use the simulations to predict the development of moisture inside the wall elements. This also makes it possible for us to compare our measurements with the simulation results. The simulations will support the analysis of our measurements, and can show if the trends we see in our data continue when assessed over a proper time-frame.

J.1.1 Boundary conditions

For the initial conditions, we have assigned our measured moisture content to the materials, and the initial temperature is matched with the measurements.

For the indoor boundary, we have created an indoor "weather" file that directly represents the indoor conditions to which the elements have been exposed. This is important as we have had quite a variation in the indoor conditions in the beginning of the measurement period. The indoor conditions during our measurement period is described in Appendix F. When we go beyond our measurement data, we have set the indoor conditions to follow our BSIM approximated moisture class 3, which is explained in Appendix K [13].

For the outside boundary condition, we are using our measurements inside the ventilated cavity. We are simulating without the exterior cladding and ventilated cavity. This is implemented as a modified outdoor weather file, where sun, wind, and rain are equal to zero. Our measured conditions are the resulting values, where there is accounted for the sun, wind, and rain. When going beyond our measurements in the ventilated cavity, we are using the values we can export from inside the ventilated cavity from our WUFI simulation with the exterior cladding. The temperature and relative humidity are shown on Figure J.2 and Figure J.3. The documentation for this model is attached as a PDF in Appendix O.

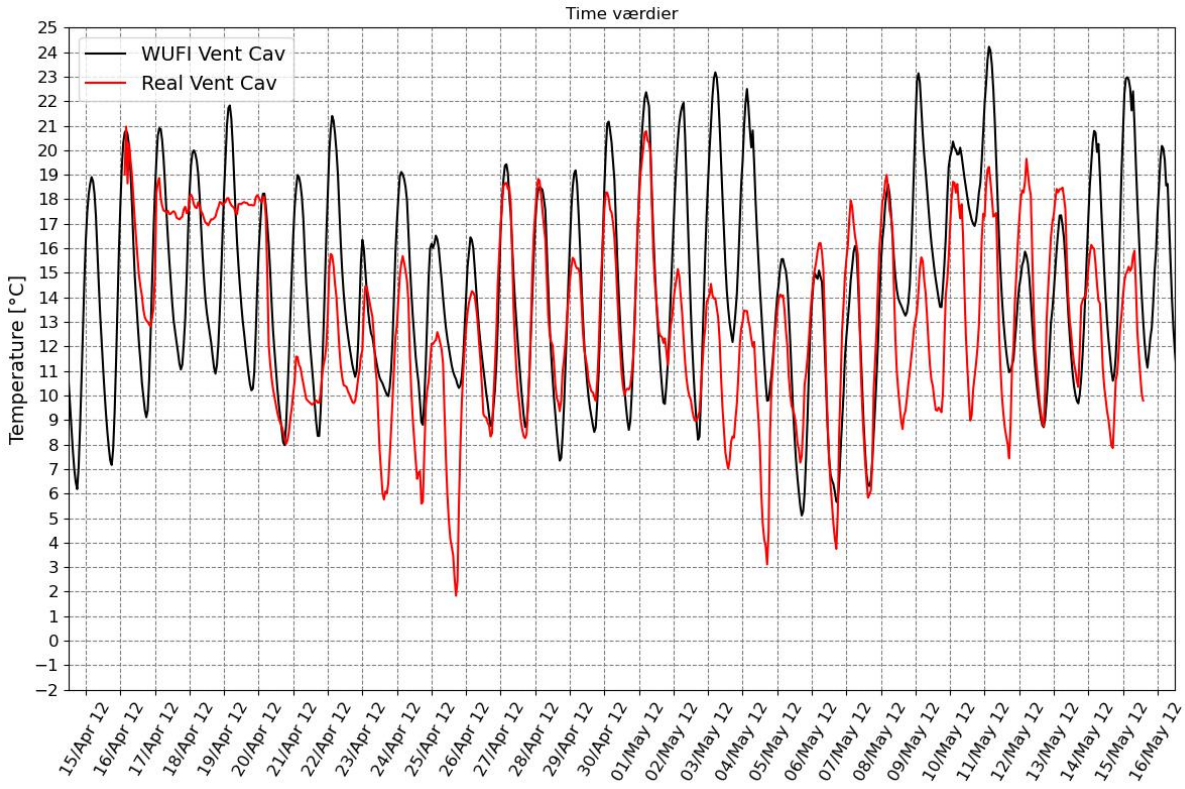

Figure J.2. Temperature inside ventilated cavity. The red line is measured values and the black is simulated.

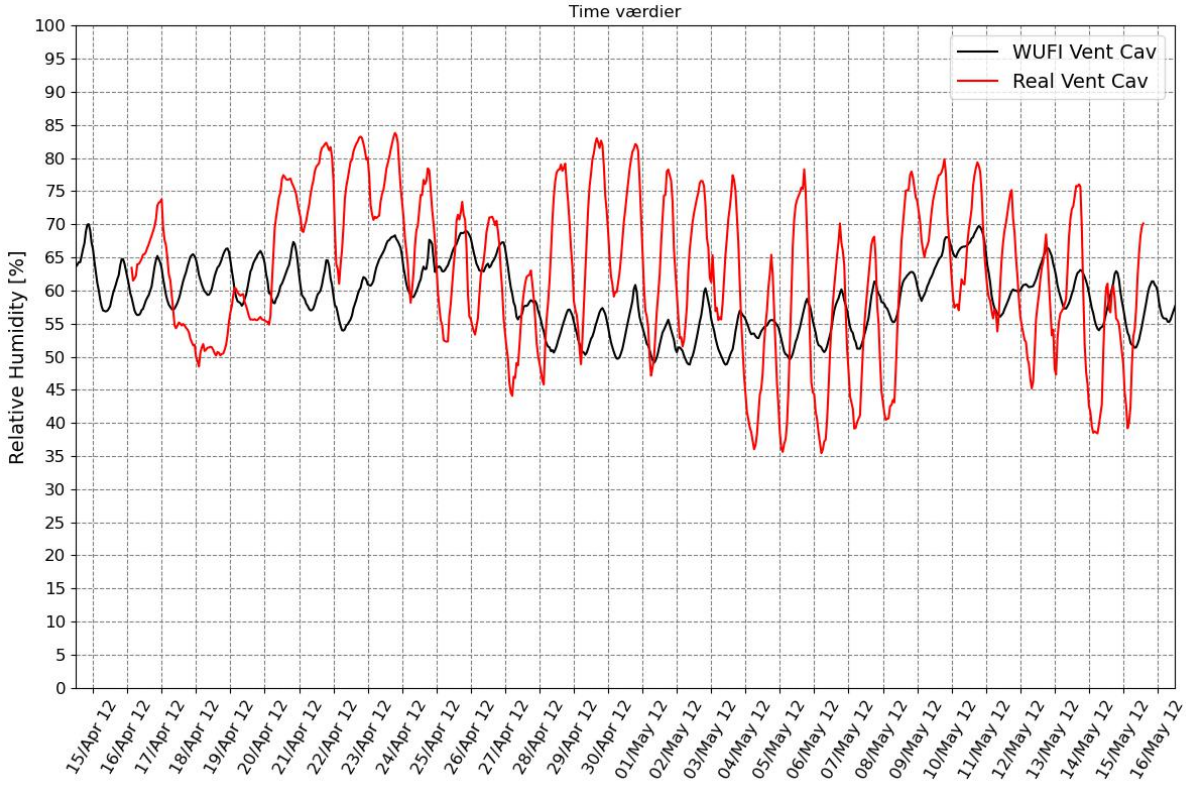

Figure J.3. Relative humidity inside ventilated cavity. The red line is measured values the black is simulated.

Appendix K

Investigation of hysteresis in BSIM and WUFI comparison

BSim accounts for hysteresis based on a model of the absorption and desorption curve. We have investigated the impact of the hysteresis effect in BSim. The BSim model was made in parallel with WUFI, and the room geometry is shown on Figure K.1, with the layers of our biobased wall. Model documentation generated by BSim is found in Appendix N.

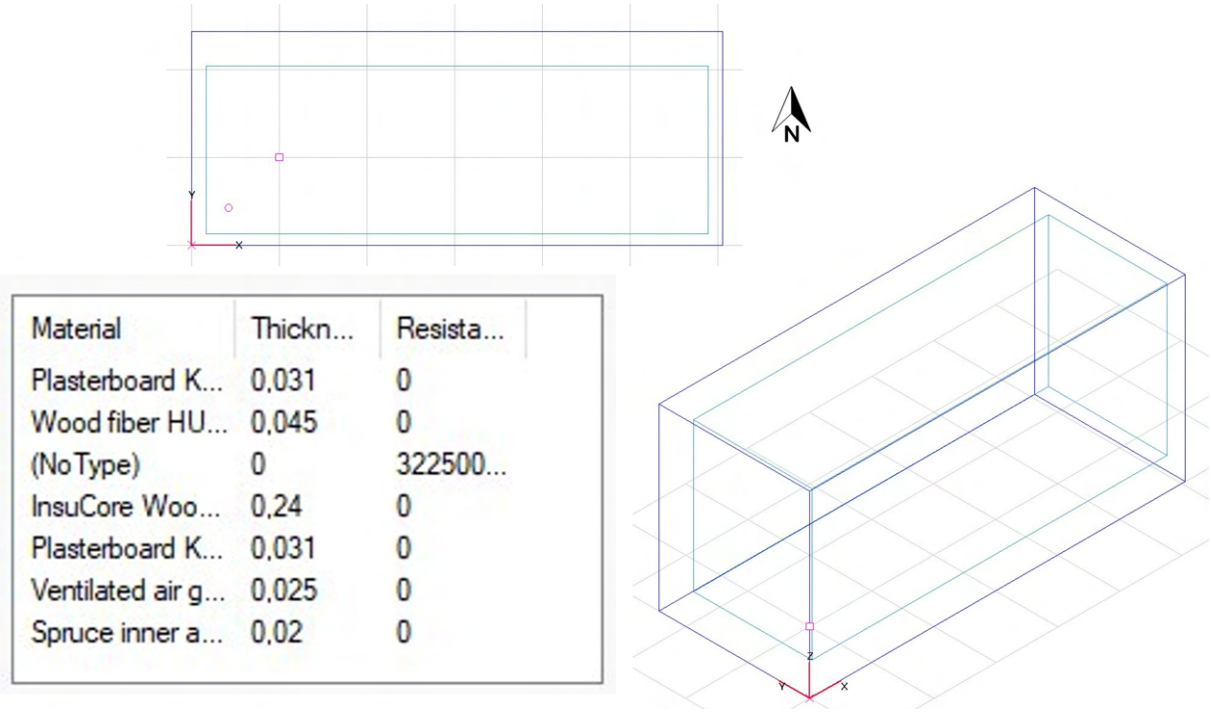

Figure K.1. BSim model geometry.

As mentioned earlier in Appendix H we have approximated the moisture class inside BSim. Our indoor temperature and relative humidity in BSim are shown on Figure K.2.

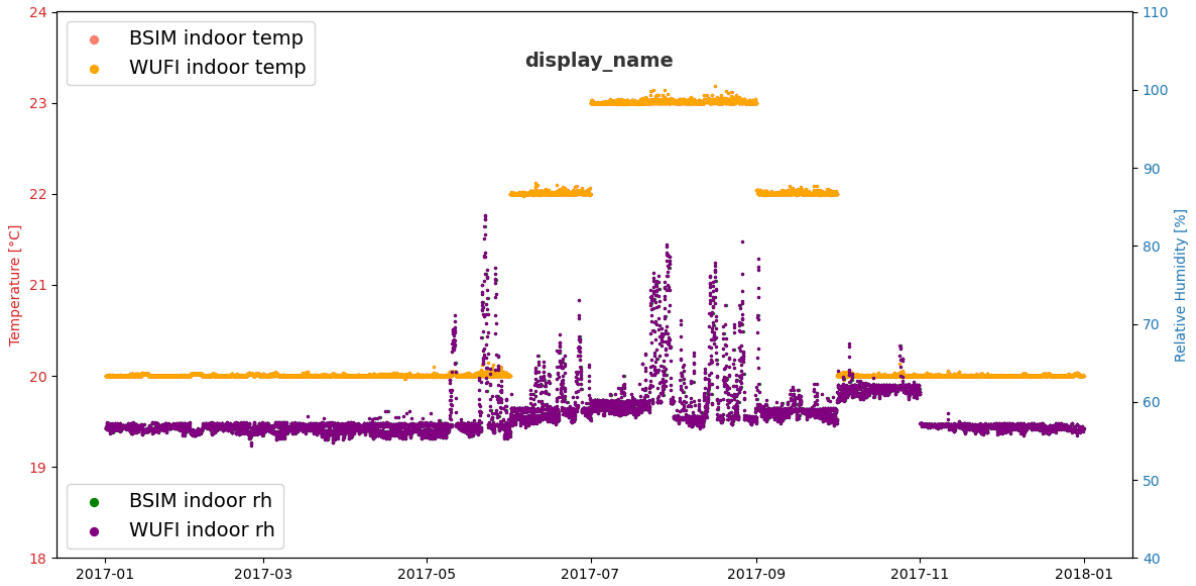

Figure K.2. Indoor weather used in BSim and WUFI, which is an approximation of moisture class 3[13]

As weather file, We use reference year 2, from the project by [41]. In the project, they produce candidates for a new and better simulation Hygrothermal reference year (HRY), which is better for simulations focussed on moisture. We have adopted their weather file into BSim, and also use the same weather file in WUFI. The outdoor weather is shown on Figure K.3.

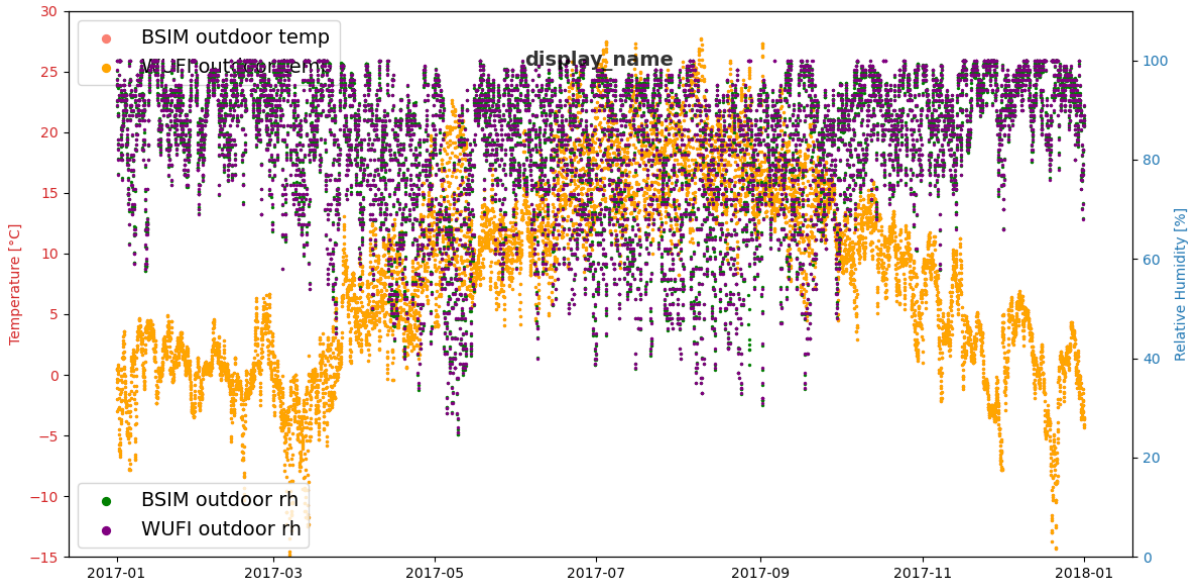

Figure K.3. Outdoor weather used in BSim and WUFI. It is the HRY-Ref2 weather file from [41].

In BSim we have applied the same finish as used in WUFI, with a short-wave radiation absorptivity of 0.47 and long-wave radiation emissivity of 0.92. We have input wind coefficients to ensure we obtain a ventilated cavity.

K.1 Monitor points in BSim

For numerical solution of the transfer equations, BSIM divides the wall into layers, with a calculation node in the middle of each layer, because the finite volume method is used. When exporting values of the conditions inside constructions, the placement is not stated. It can however, be deduced by reviewing the layer mesh, and the absolute location of the calculation nodes can be determined. This calculation is shown in Table K.1

Table K.1. BSim layer mesh and location of exported monitor points.

Inside	**Wall structure**	**Layer thickness (mm)**	**Nodes**	**Layer mesh thickness (mm)**	**Node placement (mm)**	**True wall monitor point (mm)**
	Gypsum	31	1 2 3 4	3.8 5.723 8.585 12.877	1.9 2.8 4.2 6.4	1.9 6.6 13.8 24.5
	Installation	45	5 6	18 27	9 13.5	40 62.5
	Insulation	240	7 8 9 10	60 60 60 60	30 30 30 30	106 166 226 286
	Gypsum	31	11	31	15.5	331.5
	Ventilation cavity	25	12	25	12.5	359.5
	Wood	20	13	20	10	382
Outside	**SUM:**	**392**		**392**		

K.2 Investigation of hysteresis impact in BSim

To test the impact of hysteresis, we made four models in BSIM, which are shown in section K.2.

1. Hys - Our measured absorption and desorption are used
2. Absorp - Only the absorption curve is used
3. AvgHys - An average curve between the absorption and desorption is used

4. Desorp - Only the desorption curve is used

It is the results from these models we will discuss. Additionally, we made a similar model in WUFI, and the simulation results will also be compared. WUFI uses the average sorption curve. When comparing data from BSim and WUFI, it should be noted that BSim exports data seen from the inside to the outside, and WUFI does the opposite. The monitor point location therefore needs to be inverted, to ensure measurements from the same location are compared.

It is challenging to establish a clear and consistent methodology for comparing simulation results between BSim and WUFI. There are several monitor points, and full year time series. We have chosen to compare the humidity and temperature profiles at two observation times, because a profile provides an overview of the state in the wall element. Additionally, we compare the full time series for three points of interest in the construction. They are on the inside of the vapour barrier, in the middle of the insulation and on the inside of the wind barrier. The points on the inside of the vapour barrier and of the wind barrier are chosen, because they are considered critical points when it comes to mould growth. The point in the middle of the insulation is chosen because we want to investigate the impact of hysteresis dynamics in the biobased insulation.

In general, does the BSIM models compared equally with regards to temperature, but there are however clear differences in relative humidity. Figure K.4 shows the relative humidity in the installation layer, on the inside of the vapour barrier.

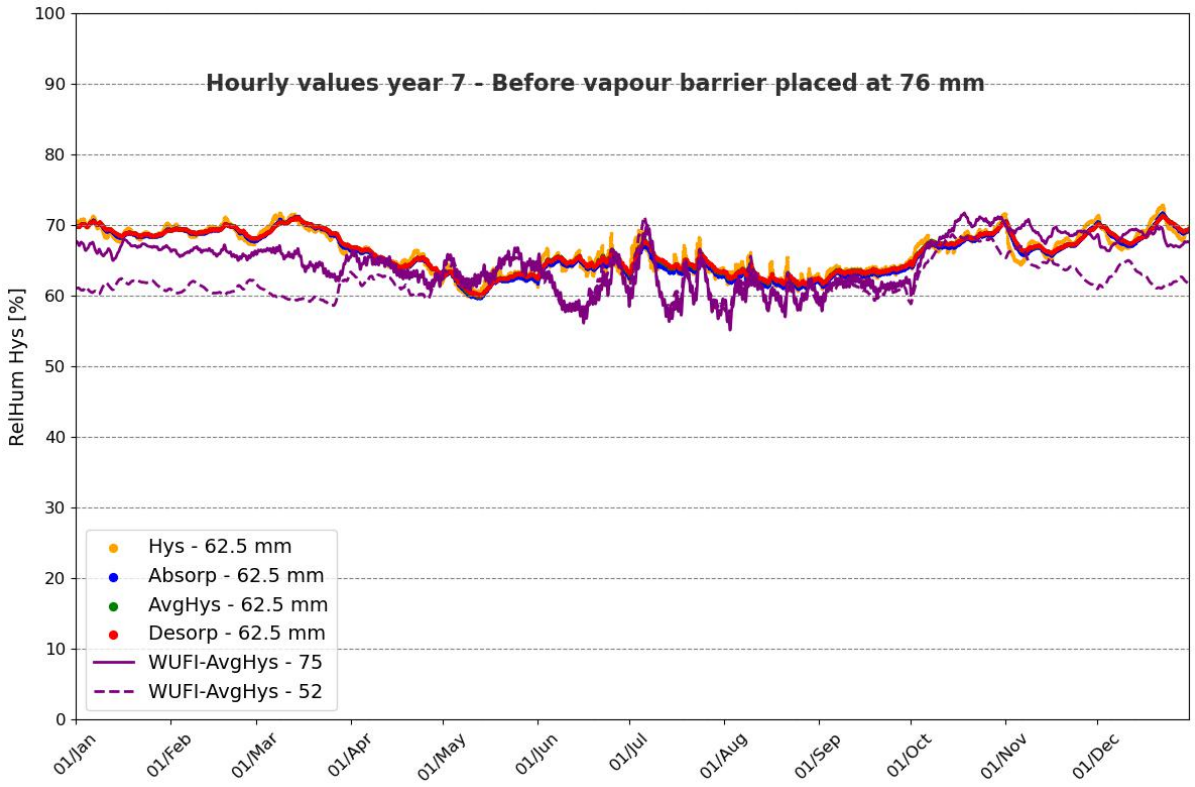

Figure K.4. Comparison of relative humidity before the vapour barrier for the different model variations.

Before the vapour barrier all the BSIM models produce the same result, and WUFI is quite similar, but a little lower. The differences between the models will increase as we progress through the construction. As mentioned, there is good agreement in the temperature, which is shown on Figure K.5 inside the core insulation layer.

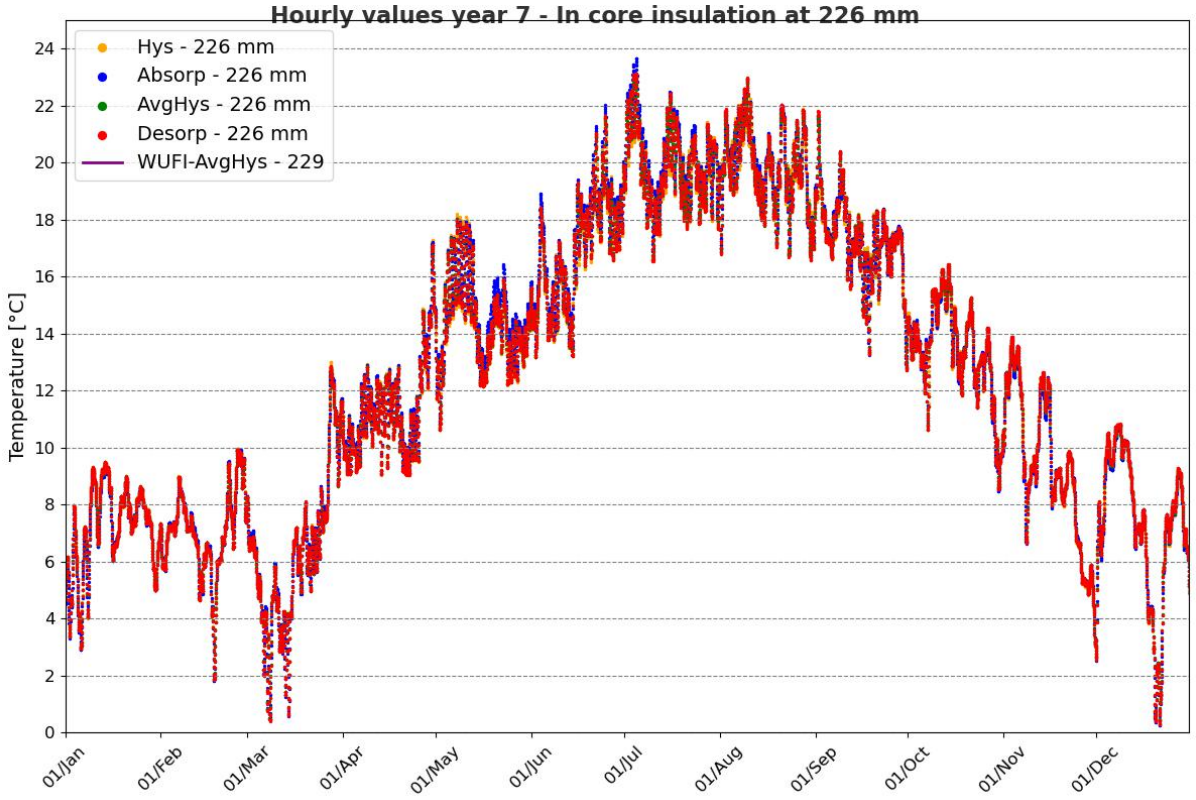

Figure K.5. Comparison of temperatures around the middle of the core insulation for the different model variations.

Figure K.6 reveal that there are differences in the relative humidity. It seems as if WUFI has much lower relative humidity values. Potential variations in initial conditions should not have any impact, when we are looking at the 7th simulation year.

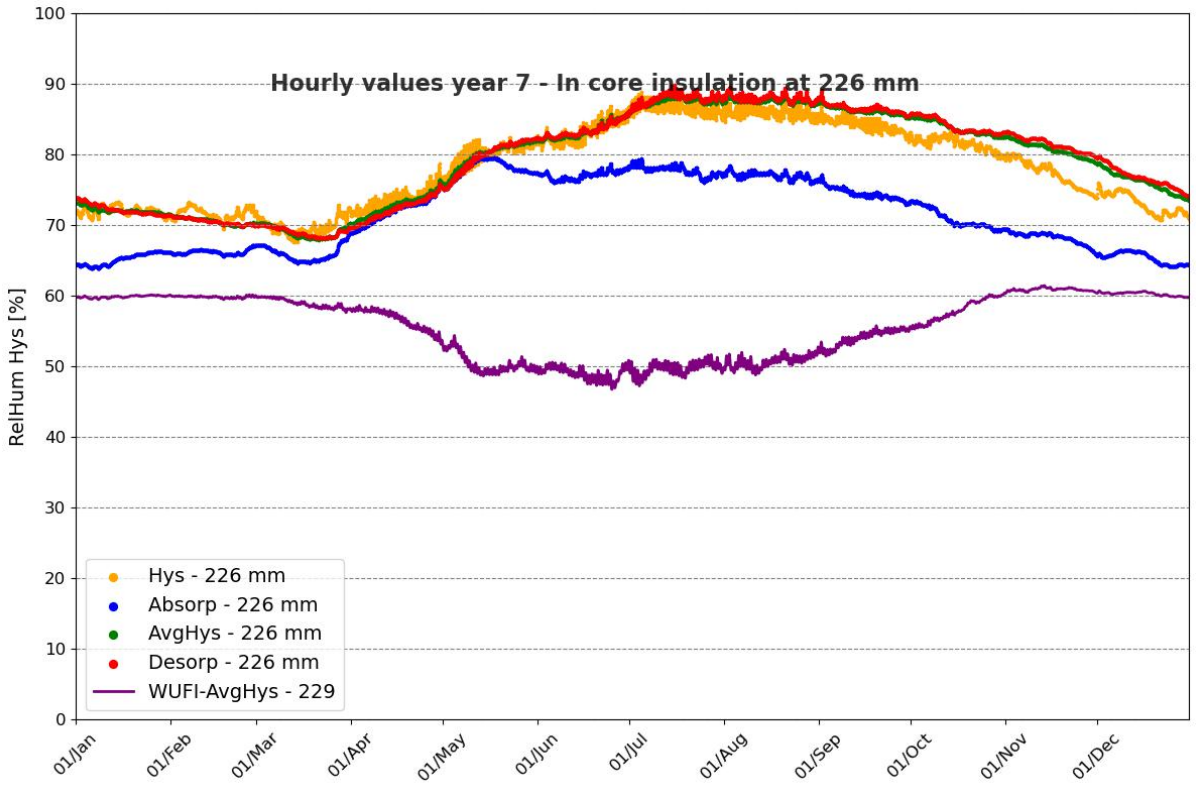

Figure K.6. Comparison of relative humidity around the middle of the core insulation for the different model variations.

We would expect differences between BSim and WUFI, due to the more advanced moisture modelling in WUFI, that accounts for more moisture physics. In a mould risk analysis, WUFI and BSim would come to radically different conclusions based on these humidity levels. When comparing our measurements with WUFI, we find WUFI to match our measurements. Because of that, we are more confident in the WUFI results to reflect reality, and that BSim do not model moisture accurately inside the walls. When isolated looking at the impact of a hysteresis model in BSim, it is clear that it has an impact. Only using the absorption curve produces generally lower relative humidities, and could indicate underestimation. The Desorb, Hys and AvgHys models are quite similar, but with the hysteresis model being lower. Figure K.7 shows the values before the wind barrier.

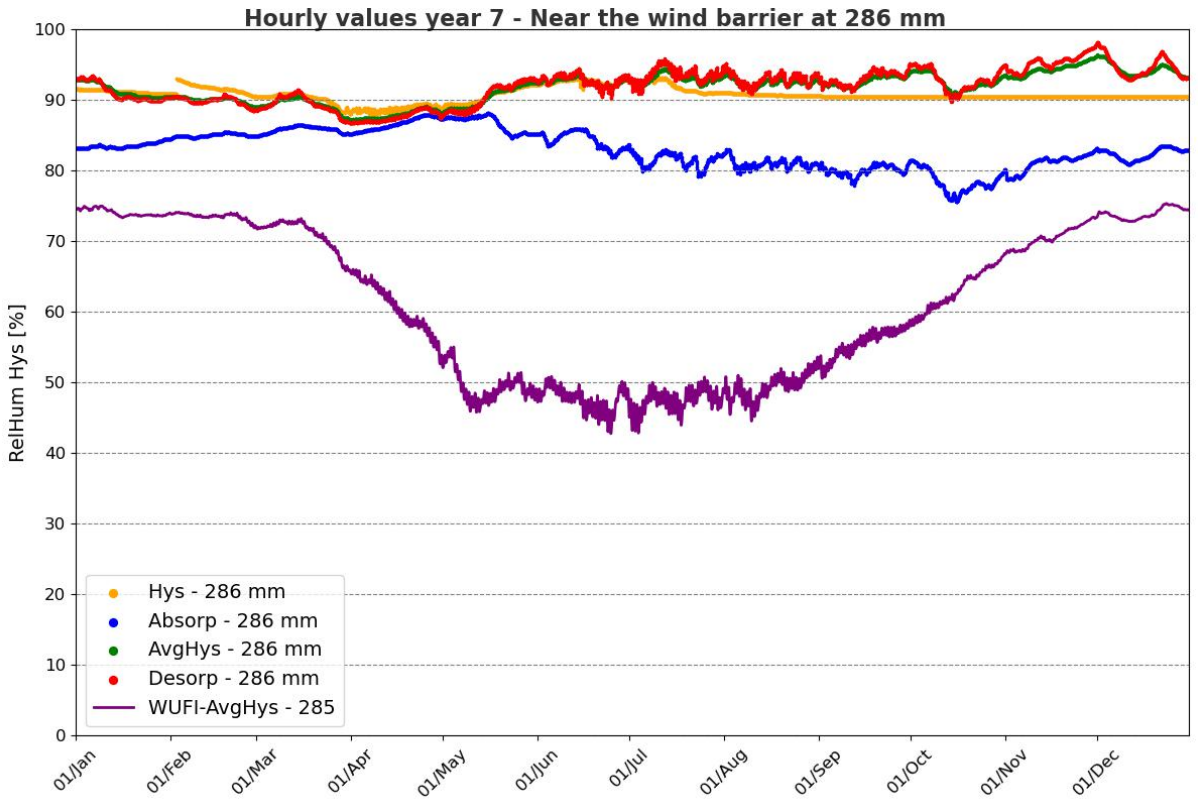

Figure K.7. Comparison of relative humidity near the wind-barrier for the different model variations.

Both Figure K.6 and Figure K.7 show lower relative humidity in WUFI in the warmer months. This drop could indicate a modelling difference between BSim and WUFI, and could be due to how sun and short wave absorptivity are handled, even though the models and weather files should be the same.

Figure K.8 and Figure K.9 show the relative humidity profiles through the wall at two times. Here the big difference in the summer in is very pronounced to see.

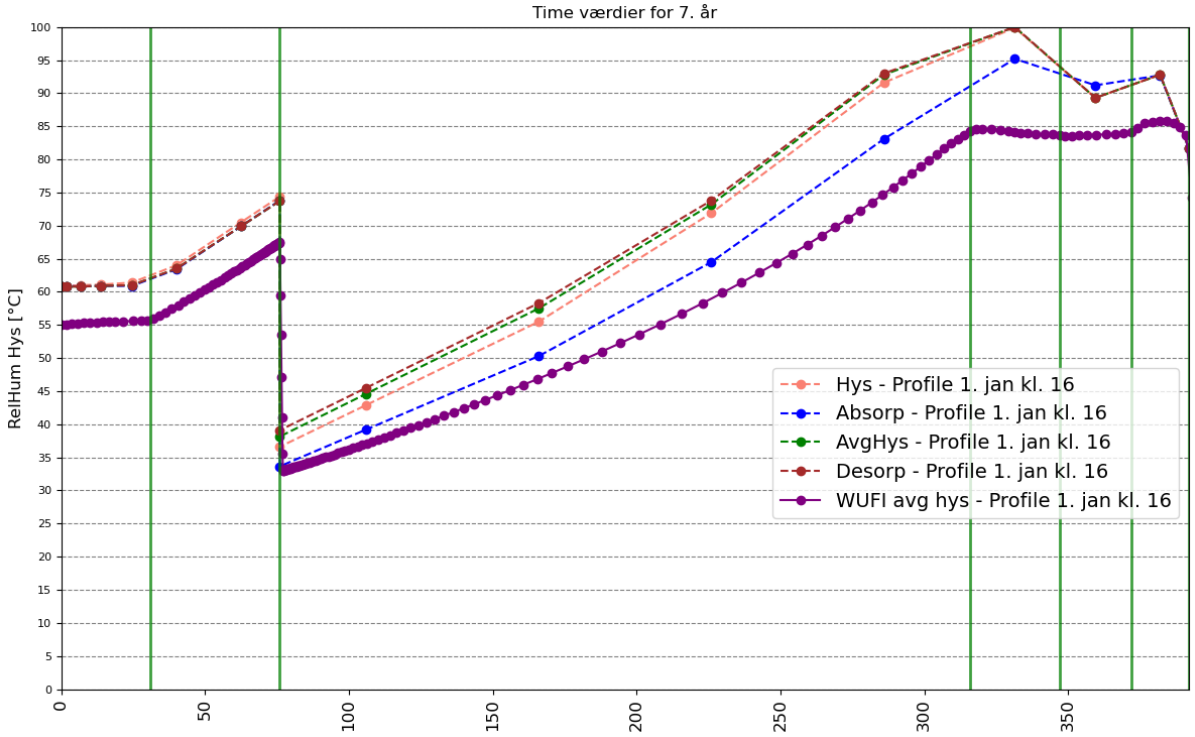

Figure K.8. Relative humidity profile at the 1st of January 16:00.

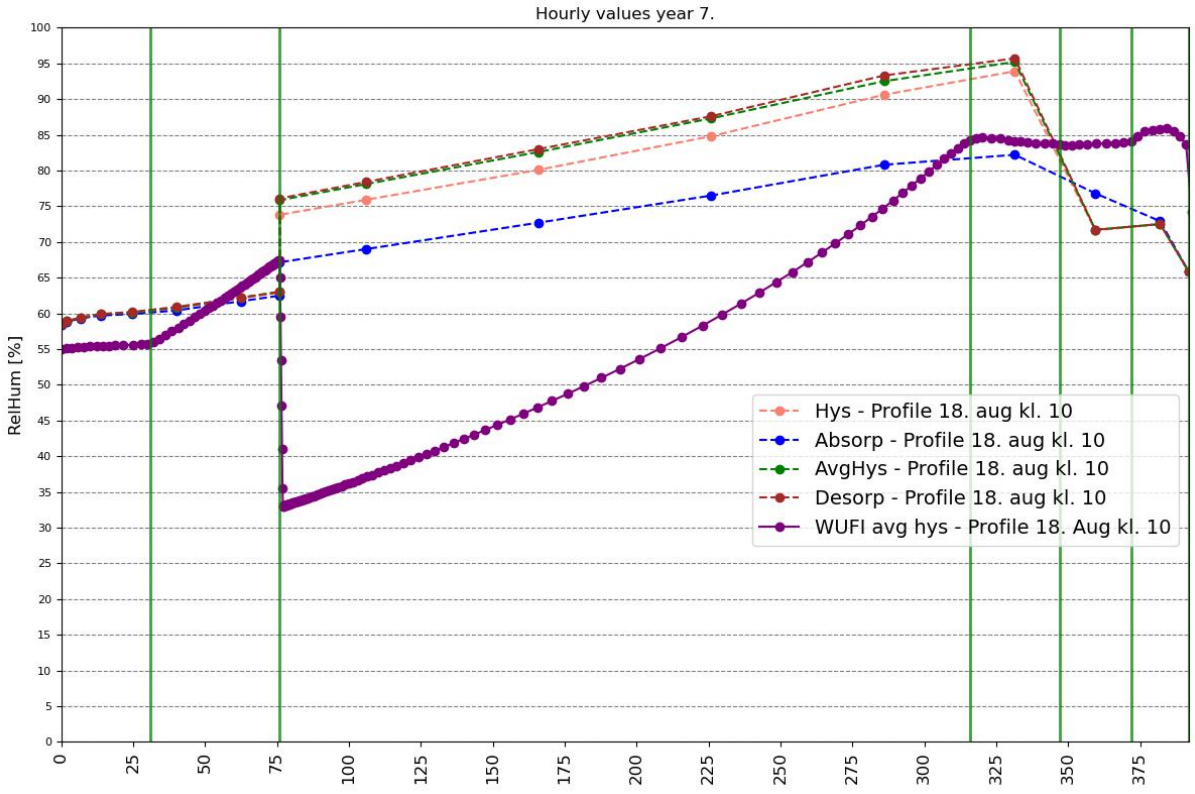

Figure K.9. Relative humidity profile at the 8th of August 10:00.

The two profiles clearly show, how WUFI in general is lower.

Figure K.10 and Figure K.11 show the temperature profiles through the wall at two times. Here it is clear that something is different at the boundary in WUFI, because there are greatly higher surface temperatures in that model.

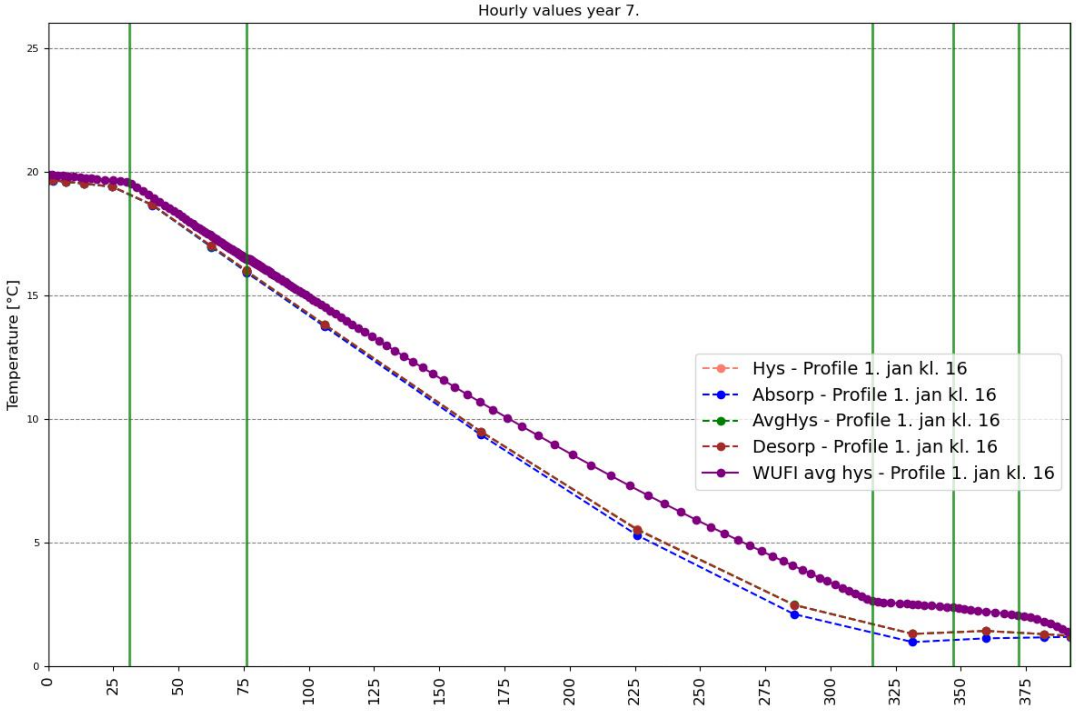

Figure K.10. Temperature profile at the 1st of January 16:00.

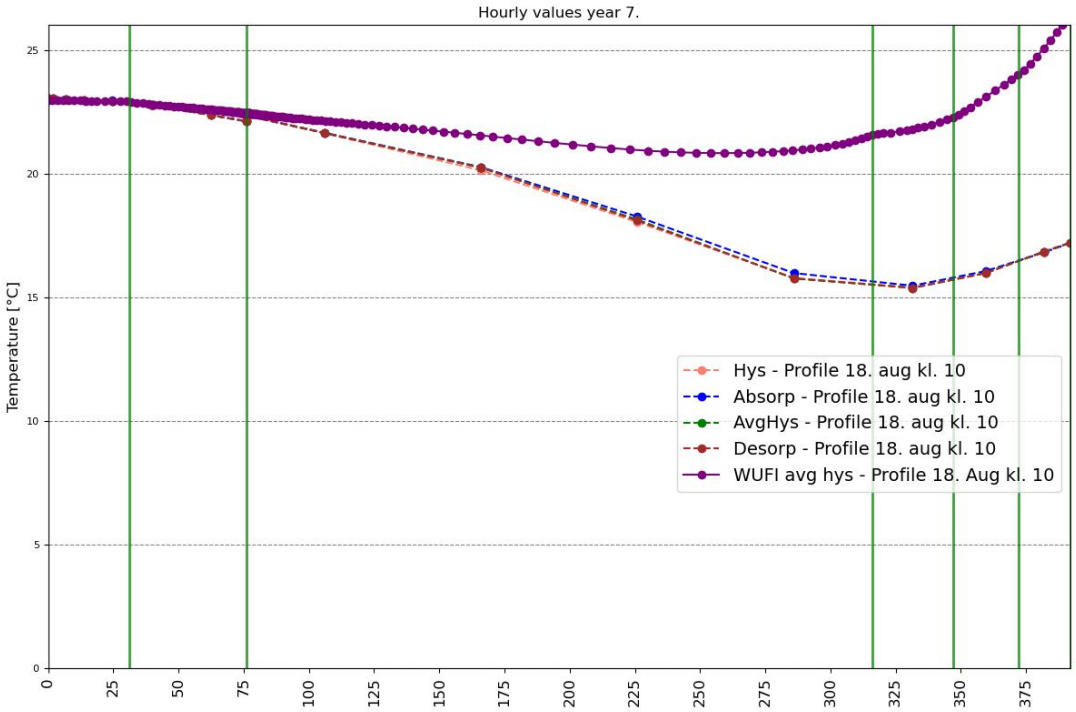

Figure K.11. Temperature profile at the 18th of August 10:00

Appendix L

Comparison of WUFI and BSim

In Appendix K we compared simulation results form WUFI and BSim, and found WUFI is quite different from BSim. This could be due to several factors, among which the different modelling physics.

For the simulation settings in WUFI, it is possible to exclude different physics dynamics. We therefore did a little manual parameter variation to test the impact in the results, when excluding different physics. The aim was to get the WUFI simulation results, closer to the BSim results and maybe be able to pinpoint the physic dynamic with most impact.

Table L.1 show the different setting options, and we have names the S1 to S5. S1 to S5 will be used as a model prefix to indicate which physics are excluded in the visualised data.

Setting	Option
S1	Excluding Capillary Conduction
S2	Excluding Latent Heat of Evaporation
S3	Excluding Temperature Dependency in Latent Heat of Evaporation
S4	Excluding Latent Heat of Fusion
S5	Use Design Values for Thermal Conductivities, if known

Table L.1. Description of settings and their corresponding options.

The general conclusion from the small investigation is that we unfortunately do not see any significant impact when excluding different physics in the solver. This is quite peculiar, and further questions the discrepancy of the simulations between BSim and WUFI. Figure L.1 show the results near the wind barrier.

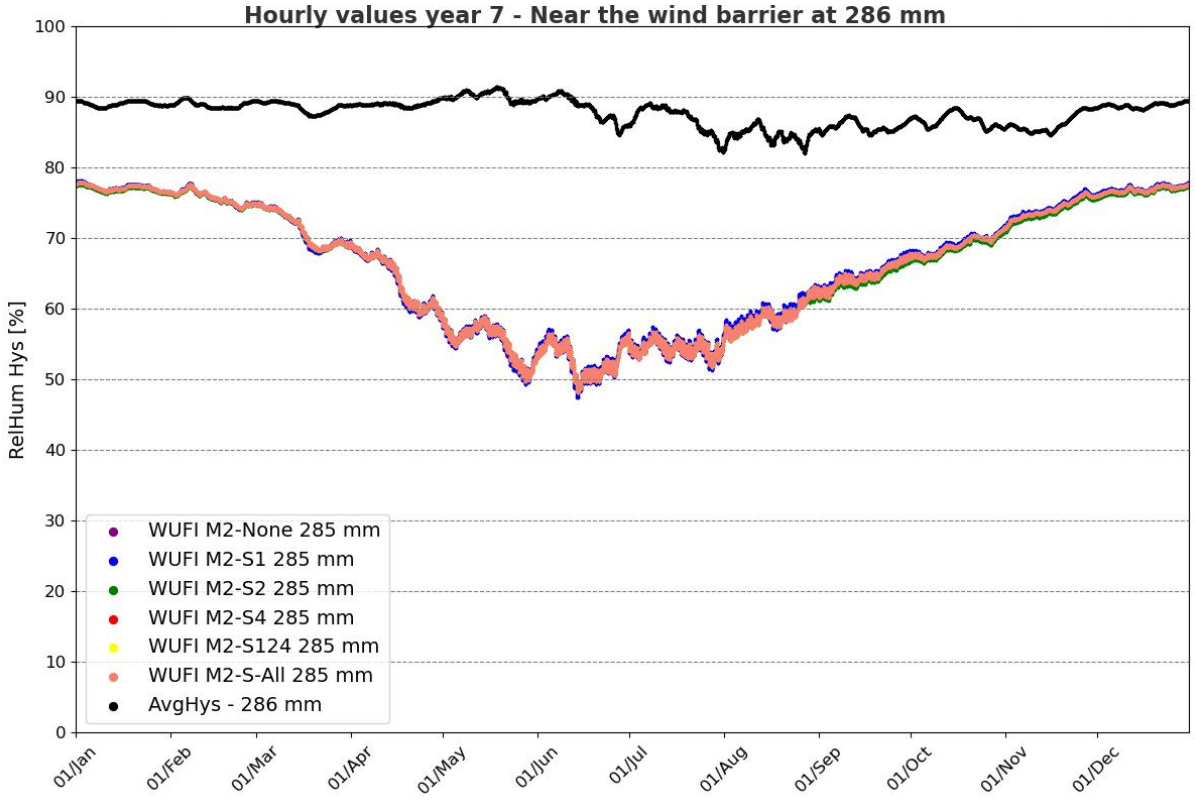

Figure L.1. WUFI simulation results of relative humidity near the wind barrier, for models with different physics excluded. BSIm AvgHys model results is also shown.

In Figure L.1, M2-S1 is the model where the S1-effect is excluded, and so on. M2-None includes all the effects and is the general setting we have used, where M2-S-All excludes all the effects shown in Table L.1. AvgHys is the data with our BSim simulation results. From the figure, it is clear that all the models give similar results, and the excluding different physics do not seem to have an impact.

Appendix M

Sizing of HVAC systems using BSIM

This appendix describes our usage of BSim to estimate the needed power of the HVAC systems. The goal of these simulations is to find the needed heating and cooling capacity in the climatic chamber in order to maintain a stable temperature of 20℃, except 21℃ in June and September and 23℃ in July and August.

Additionally we evaluate if we have tuned the system in BSim, so we achieve moisture class in the simulations. BSim simulates the indoor climate, and do not allow to set a fixed moisture generation as described in [13]. The target is to be in moisture class 3, which is considered very rare for residential housing, and is therefore critical.

We did some different model variation. Models with and without fresh air intake and where the test-wall has a U-value of 0,1 or 0,2. In here we only present the results for the model with ventilation and the higher U-value, as this model outlines the needed upper limit of power for the HVAC systems. Our found power requirements are shown in Table M.1.

Table M.1. Building Simulation Summary

Parameter	**Value**	**Unit**
Airchange rate	2.5	h^{-1}
U-value wall	0.2	$W/m^2 \cdot K$
Cool max power	-0.763	kW
Cool sum	-315.6	kWh/yr
Heat max power	1.337	kW
Heat sum	3350.1	kWh/yr

We have planned to have an air change rate in the climate chamber between 0.5-1h $^{-1}$, as an air change rate of 0,5 h^{-}1 equals the requirement from BR18 (Danish building regulation) of

0,3 l/s pr m^2. For the shown powers, we have used an air change rate of 2.5^{-1}, which is greatly above what we plan to have. With the BSim simulation we also estimate the upper range of yearly power consumption.

M.1 Approximation of moisture class 3

As mentioned in Appendix H we have to approximate moisture class 3 in BSim. Figure M.1 shows our obtained indoor conditions.

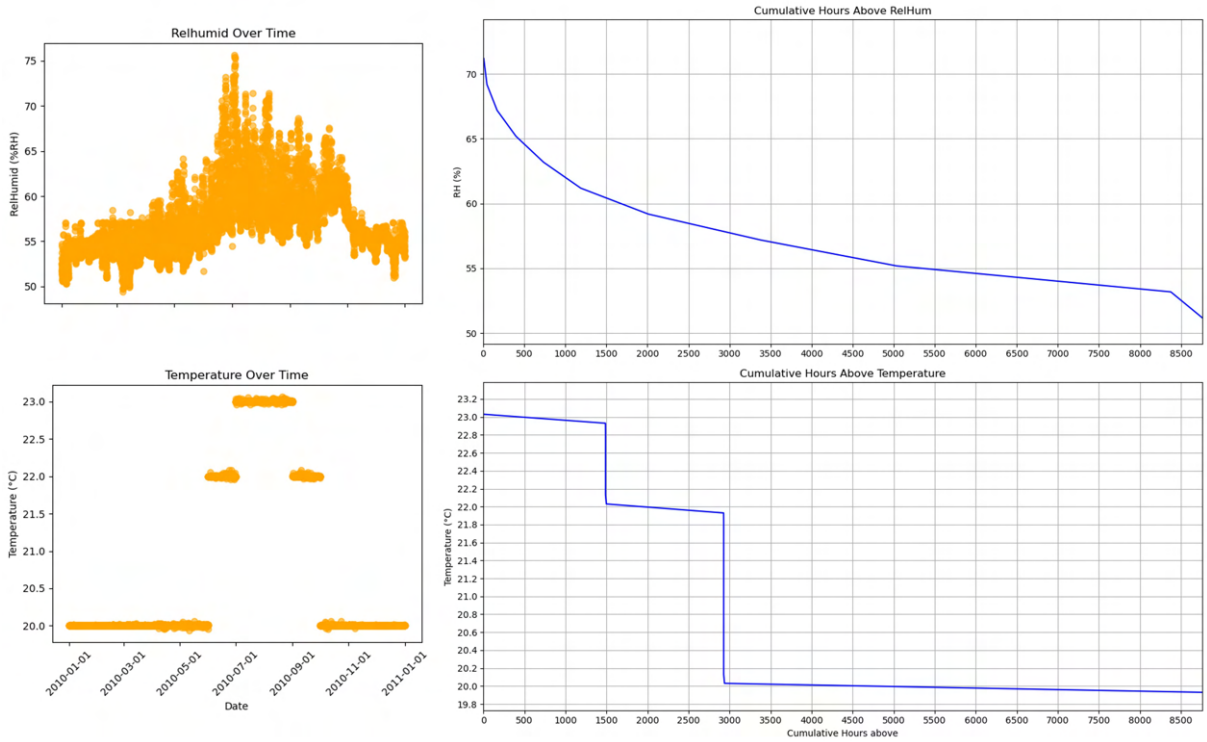

Figure M.1. Model specifications

Figure M.2 show our evaluation of what moisture class we achieve. The table show the monthly average for the DRY-weather file and our indoor conditions. In can be seen that we fall within class 3, for all months.

Måned	ExtTmp °C	RelHumid Outdoor%	TopMean °C	RelHumid %	Moist Class	RF Class 1	RF Class 2	RF Class 3	RF Class 4
Januar	0,7	89,2	20,0	53,9	RF Class 3	36	47	58	69
Februar	0,4	91,1	20,0	54,3	RF Class 3	36	47	59	70
Marts	-0,7	86,7	20,0	54,1	RF Class 3	33	44	56	68
April	7,1	76,2	20,0	55,2	RF Class 3	42	49	57	64
Maj	11,5	75,5	20,0	56,1	RF Class 3	51	56	61	66
Juni	14,2	79,9	22,0	59,3	RF Class 3	55	58	61	63
Juli	17,8	76,8	23,0	61,7	RF Class 3	60	61	62	63
August	17,9	73,7	23,0	59,8	RF Class 3	58	59	60	61
September	14,5	78,2	22,0	59,1	RF Class 3	55	57	60	63
Oktober	9,8	87,7	20,0	60,5	RF Class 3	53	59	65	71
November	3,4	90,9	20,0	55,6	RF Class 3	41	50	60	69
December	0,7	92,7	20,0	55,0	RF Class 3	37	48	59	70

Figure M.2. Calculated outdoor and indoor monthly averages of temperature and relative humidity to verify we fall within moisture class 3.

We are however not at the upper boundary, but in between the upper boundary for class 2 and 3. This could explain why we have less water vapour pressure than moisture class 3 in WUFI, as shown in Appendix H.

From the simulation, we can also get the amount of added moisture, which is shown on Figure M.3.

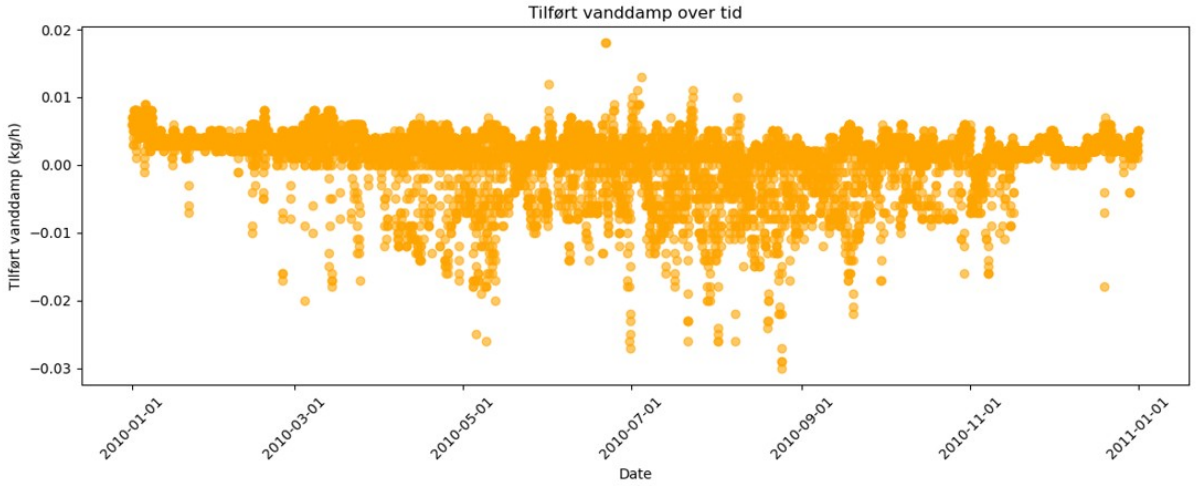

Figure M.3. Amount of added moisture (kg/hr) to obtain specified humidity levels. Negative values is removed moisture.

Figure M.3 clearly shows the need for humidification in order to obtain the relative humidity levels. The indicated dehumidification should not be considered valid for the actual setup, as these values occur to the control mechanics in BSim, which is not working as intended.

Appendix N

Attached BSIM model documentation

Building	Design Heat Loss, W	Rotation, deg	Net - Gross Volume, m³	
Container	935,211	0	26,336	42,7722
Site	**Weather File**	**Ground**	**Terrain Type**	
Site377	DRY_2001-2010 v3.dry	Ground380	Urban	

Thermal Zone	Design Heat Loss, W	Net - Gross Floor Area, m²		Net - Gross Volume, m³	
ThermalZone376	935,211	10,9825	14,7694	26,336	42,7722
Container	935,211	10,9825	14,7694	26,336	42,7722
Enclosing Elements	**Building Element**	**Thick, m - U, W/m² K**		**Net - Gross Area, m²**	
Constructions	Con gulv Con side Con ende BioVæg-Papir-Hys-u0,1 Con ende Con loft	0,388 0,128 0,166 0,392 0,166 0,11	0,123978 0,509771 0,509771 0,119981 0,509771 0,517688	10,9825 13,7309 4,59936 13,7309 4,59936 10,9825	14,7694 17,544 7,06045 17,544 7,06045 14,7694
Systems	**Component**	**Control**		**Time**	
Equipment	Udstyr	Altid		Altid	
Heating	Opvarmning	HeatCtrl20deg HeatCtrl22deg HeatCtrl23deg		Jan->Maj+Okt->Dec Juni + sep Juli + August	
Cooling	Cooling618	CoolCtrl20 CoolCtrl22 CoolCtrl23		Jan->Maj+Okt->Dec Juni + sep Juli + August	
Ventilation	Vent_heat_cool_humdi	Vent-humid60 Vent-humid62 Vent-humid57 Vent-humid58 Vent-humid59		July Okt Jan->Maj+Okt->Dec Aug Juni + sep	
MoistureLoad	MoistureLoad480	Altid		Altid	

Figure N.1. Model specifications

Appendix O

WUFI model documentation for measurement comparison

WUFI®

WUFI Pro 7.0

Component

Case name: #3 Uden ventlag

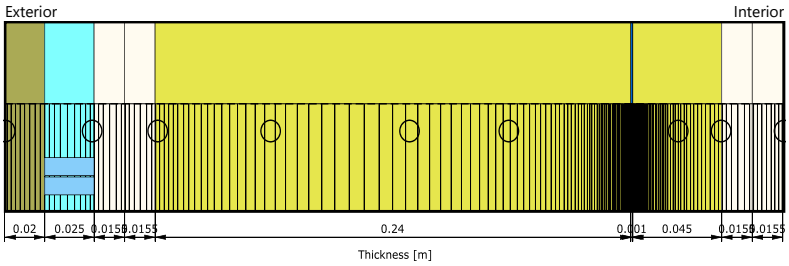

— Monitors

— Sources, Sinks

Material Data

— Southern Yellow Pine	0.02 m
— Air Layer 25 mm	0.025 m
— *Knauf - Copy Rigips Glasroc X	0.0155 m
— *Knauf - Copy Rigips Glasroc X	0.0155 m
— *HUNTON Nativo Copy AiF Flexible Wood-Fiber Insulation WF	0.24 m
— *Öko natur copy vapor retarder (sd=5m) 1mm	0.001 m
— *HUNTON Nativo Copy AiF Flexible Wood-Fiber Insulation WF	0.045 m
— *Knauf - Copy Rigips Glasroc X	0.0155 m
— *Knauf - Copy Rigips Glasroc X	0.0155 m

Total Thickness	0.393 m
R-Value (dry)	8.08 m²K/W
U-Value (dry)	0.12 W/m²K

WUFI® **WUFI Pro 7.0**

Material: Southern Yellow Pine

Property	Unit	Value
Bulk density	kg/m³	500
Porosity	m³/m³	0.858
Water Vapor Diffusion Resistance Factor	-	1734
Spec. Heat Capacity	J/kgK	1880
Thermal Conductivity	W/mK	0.119
Thermal Conductivity Supplement	%/M.-%	-
Thermal Conductivity Supplement	W/mK²	0.0002

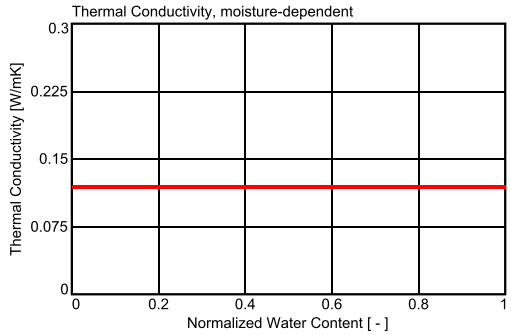

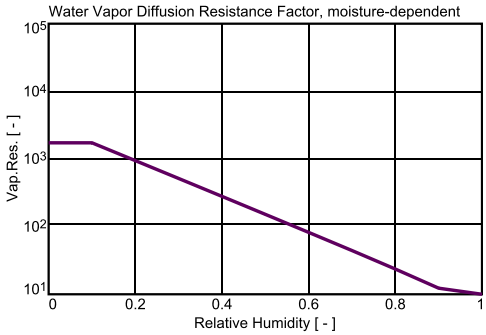

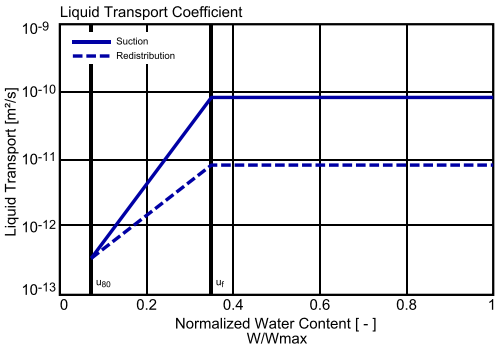

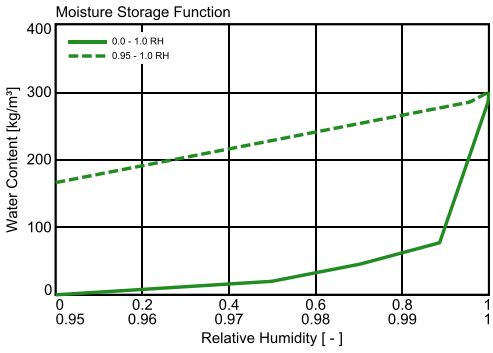

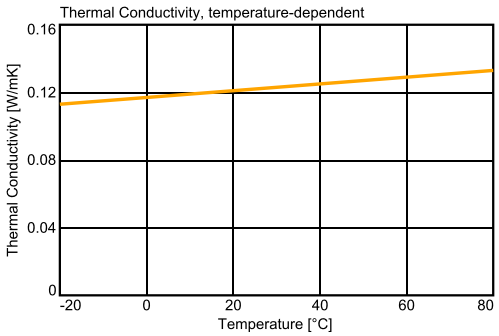

WUFI Pro 7.0

Material: Air Layer 25 mm

Property	Unit	Value
Bulk density	kg/m³	1.3
Porosity	m³/m³	0.999
Water Vapor Diffusion Resistance Factor	-	0.51
Spec. Heat Capacity	J/kgK	1000
Thermal Conductivity	W/mK	0.155
Thermal Conductivity Supplement	%/M.-%	-
Thermal Conductivity Supplement	W/mK²	-

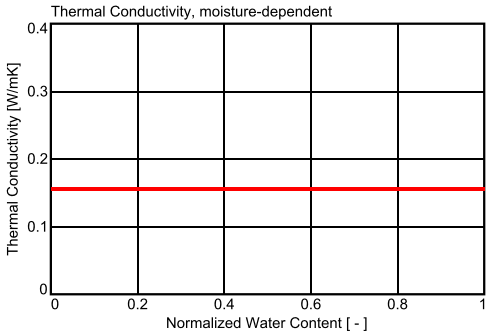

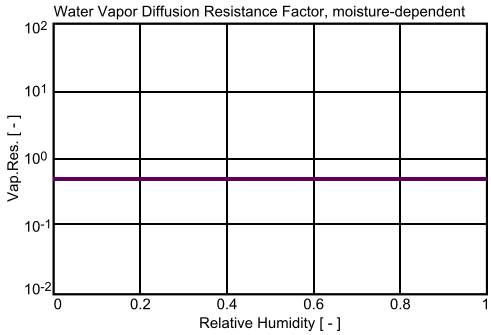

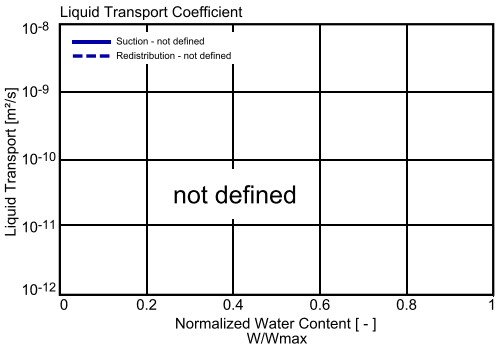

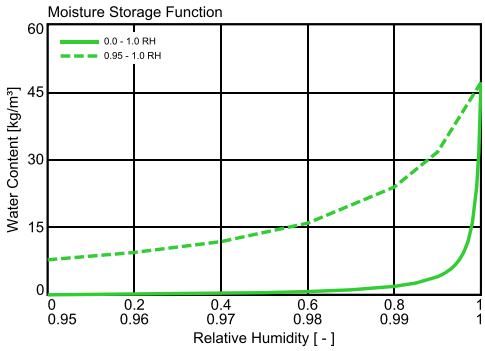

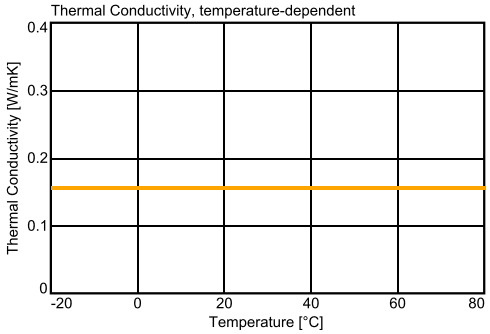

Material: *Knauf - Copy Rigips Glasroc X

Property	Unit	Value
Bulk density	kg/m³	774
Porosity	m³/m³	0.63
Water Vapor Diffusion Resistance Factor	-	6.2
Spec. Heat Capacity	J/kgK	850
Thermal Conductivity	W/mK	0.25
Thermal Conductivity Supplement	%/M.-%	8
Thermal Conductivity Supplement	W/mK²	0.0002

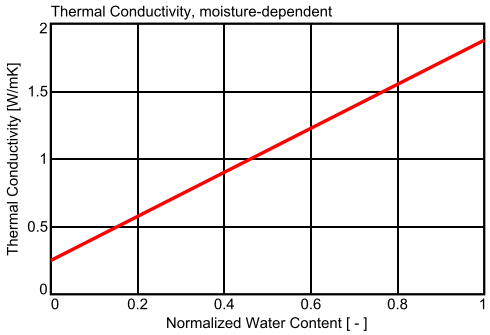

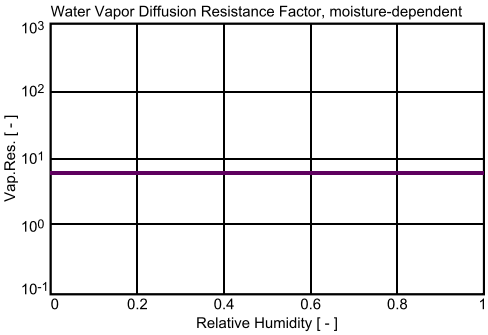

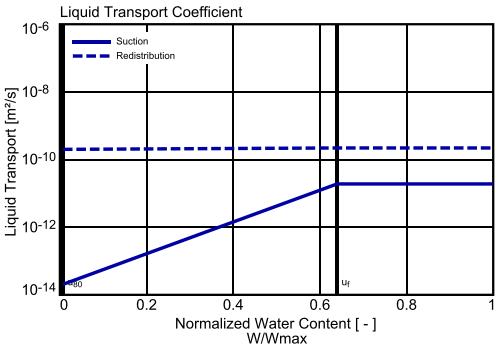

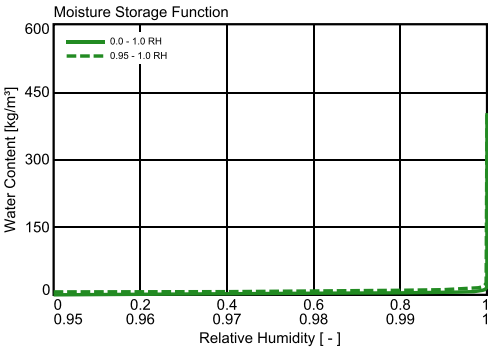

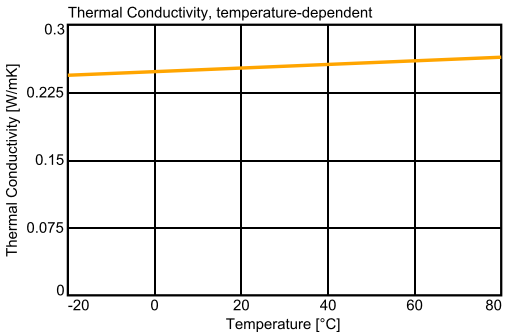

Material: *Knauf - Copy Rigips Glasroc X

Property	Unit	Value
Bulk density	kg/m³	774
Porosity	m³/m³	0.63
Water Vapor Diffusion Resistance Factor	-	6.2
Spec. Heat Capacity	J/kgK	850
Thermal Conductivity	W/mK	0.25
Thermal Conductivity Supplement	%/M.-%	8
Thermal Conductivity Supplement	W/mK²	0.0002

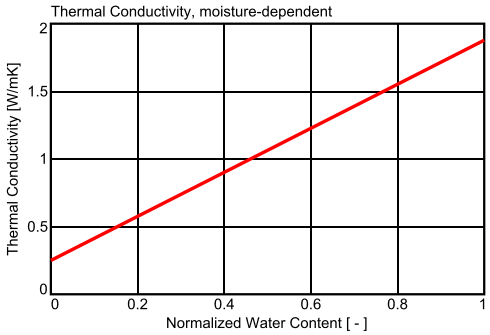

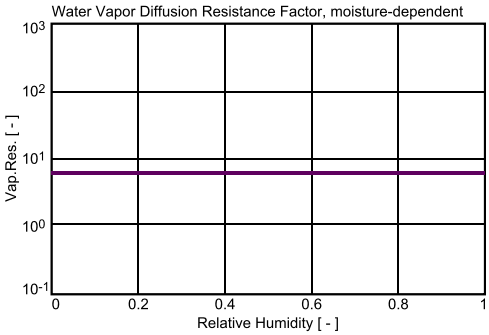

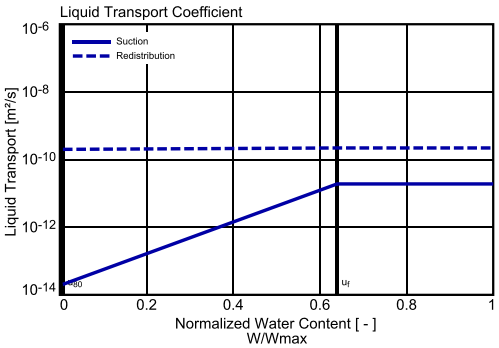

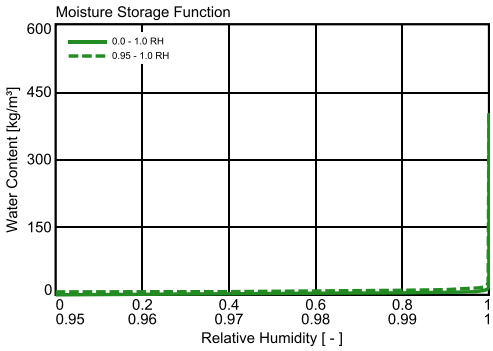

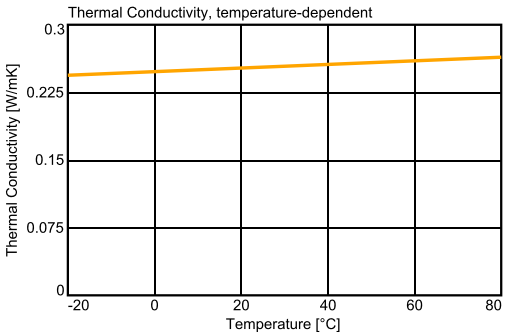

Material: *HUNTON Nativo Copy AiF Flexible Wood-Fiber Insulation WF

Property	Unit	Value
Bulk density	kg/m³	53.2
Porosity	m³/m³	0.97
Water Vapor Diffusion Resistance Factor	-	2
Spec. Heat Capacity	J/kgK	2100
Thermal Conductivity	W/mK	0.038
Thermal Conductivity Supplement	%/M.-%	-
Thermal Conductivity Supplement	W/mK²	-

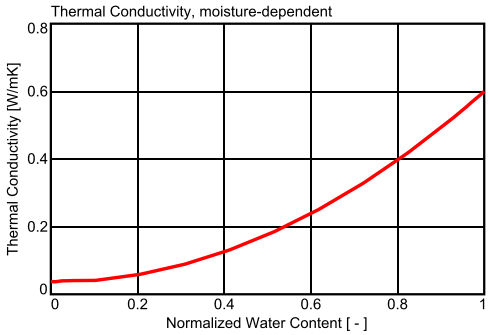

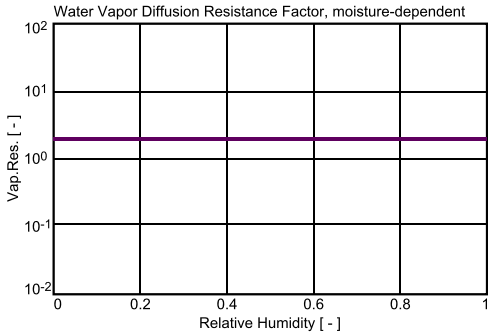

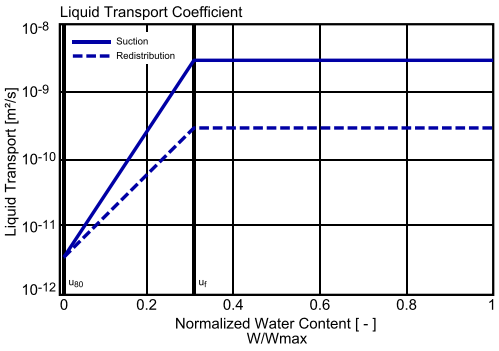

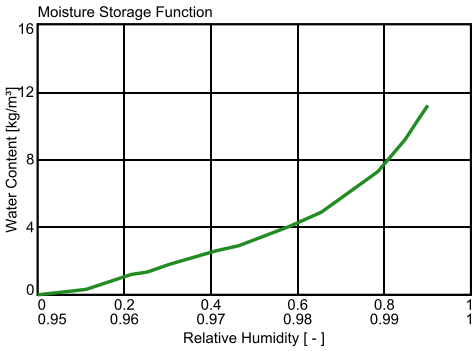

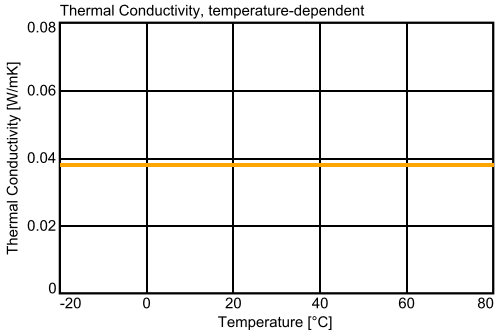

Material: *Öko natur copy vapor retarder (sd=5m) 1mm

Property	Unit	Value
Bulk density	kg/m³	175
Porosity	m³/m³	0.001
Water Vapor Diffusion Resistance Factor	-	6450
Spec. Heat Capacity	J/kgK	2300
Thermal Conductivity	W/mK	2.3
Thermal Conductivity Supplement	%/M.-%	-
Thermal Conductivity Supplement	W/mK²	0.0002

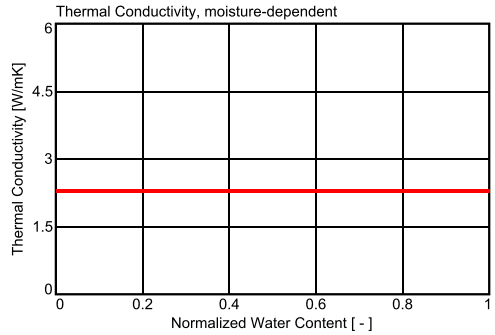

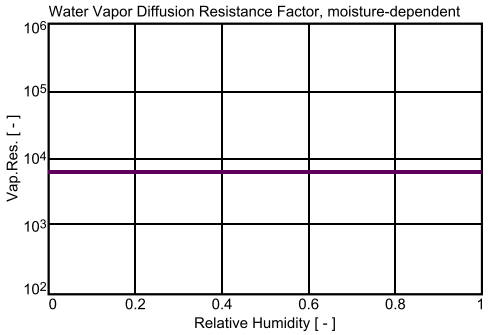

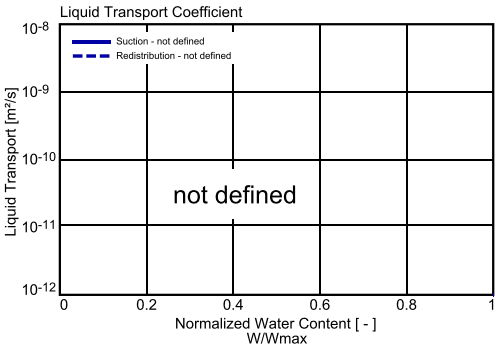

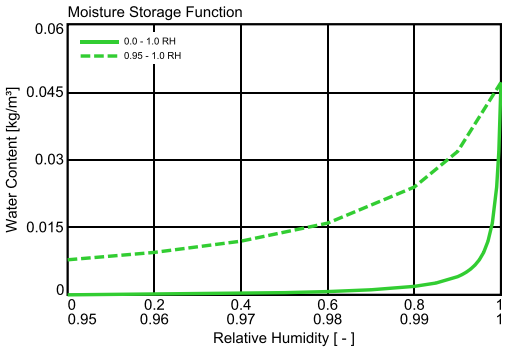

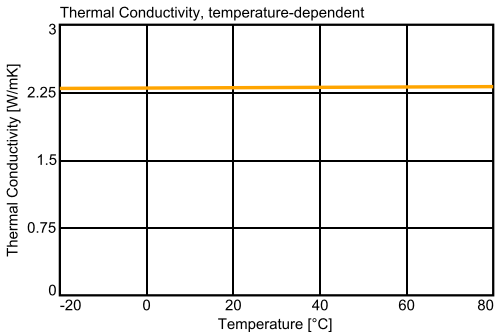

Material: *HUNTON Nativo Copy AiF Flexible Wood-Fiber Insulation WF

Property	Unit	Value
Bulk density	kg/m³	53.2
Porosity	m³/m³	0.97
Water Vapor Diffusion Resistance Factor	-	2
Spec. Heat Capacity	J/kgK	2100
Thermal Conductivity	W/mK	0.038
Thermal Conductivity Supplement	%/M.-%	-
Thermal Conductivity Supplement	W/mK²	-

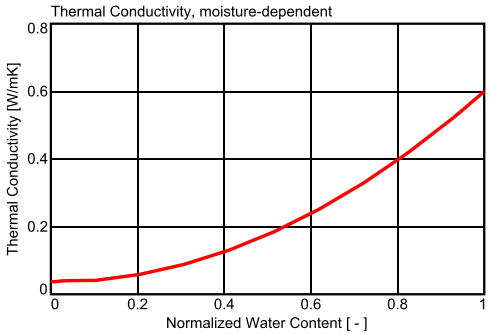

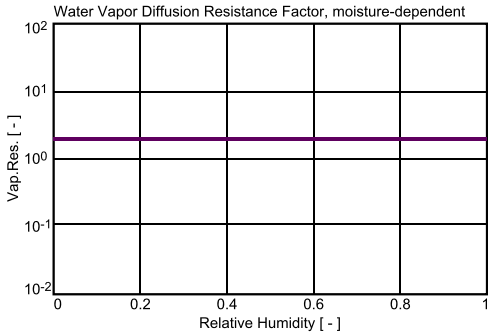

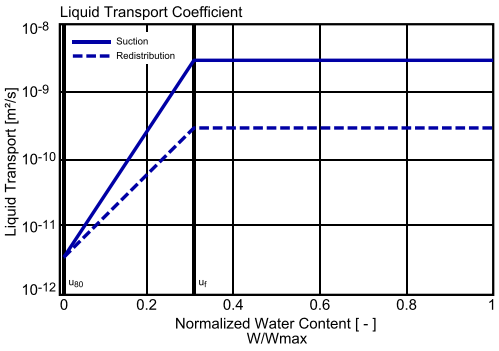

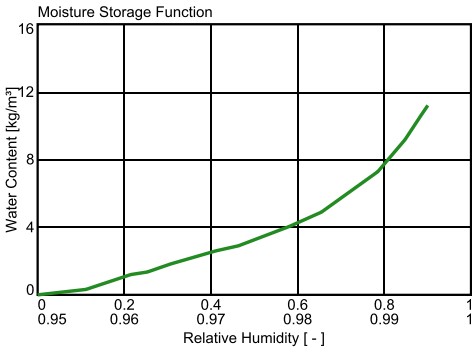

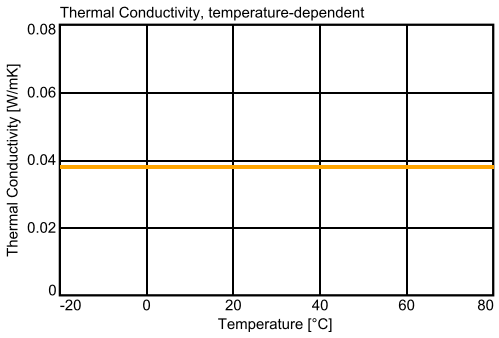

Material: *Knauf - Copy Rigips Glasroc X

Property	Unit	Value
Bulk density	kg/m³	774
Porosity	m³/m³	0.63
Water Vapor Diffusion Resistance Factor	-	6.2
Spec. Heat Capacity	J/kgK	850
Thermal Conductivity	W/mK	0.25
Thermal Conductivity Supplement	%/M.-%	8
Thermal Conductivity Supplement	W/mK²	0.0002

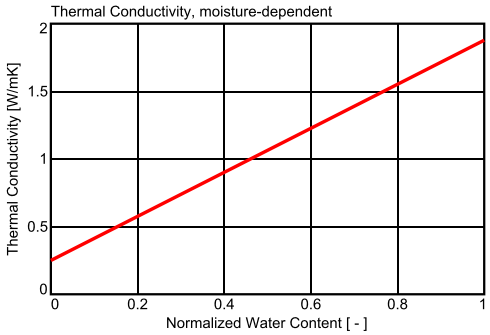

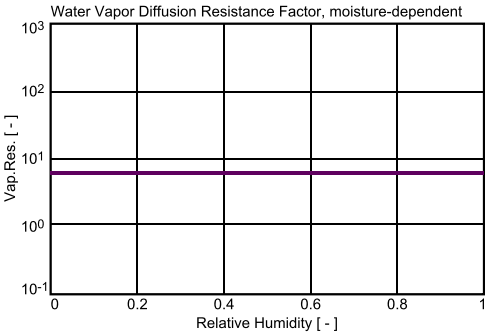

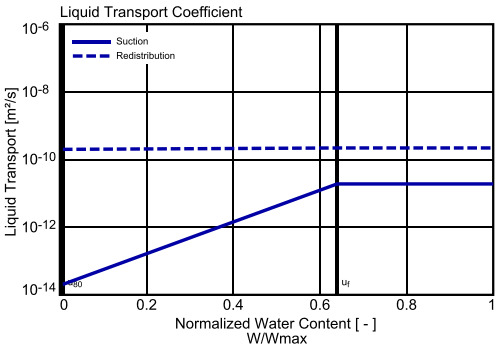

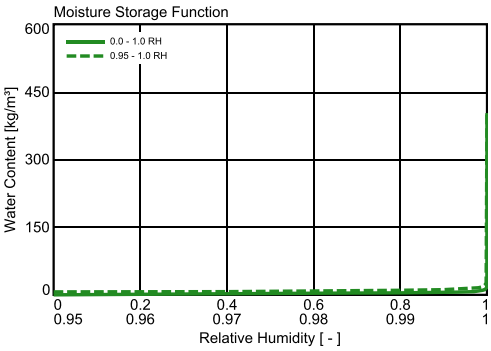

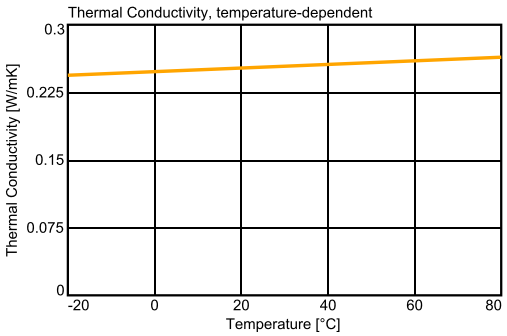

Surface and Boundary Conditions

Exterior Surface

Surface Transfer Coefficients

Property	Description	Unit	Value
Heat Transfer Coefficient		W/m²K	7.7
sd-Value		m	0
Short-Wave Radiation Absorptivity		-	0.8
Long-Wave Radiation Emissivity		-	0.9
Adhering Fraction of Rain		-	0.7
Radiative overcooling			No

Boundary Conditions

Weather file: BSIM_WUFI_DK_Referenceår2_DMI_Sjælsmark - Kopi.wac

Property	Description	Unit	Value
Temperature Shift		K	0

Interior Surface

Surface Transfer Coefficients

Property	Description	Unit	Value
Heat Transfer Coefficient		W/m²K	25
sd-Value		m	0

Boundary Conditions

Weather file: BSIM_WUFI_DK_Referenceår2_DMI_Sjælsmark - Kopi.wac

Property	Description	Unit	Value
Temperature Shift		K	0

Part III

Appendices for determination of material properties

Appendix P

VSA measurement schedule

This appendix contains our measurement schedule for the VSA measurements. If the sample is not used for a measurement, it is stored in the oven at 60℃. The *Duration test* variation was a test of the settings of the VSA, to figure out how we could get the longest measurements.

Table P.1. The schedule of our VSA measurements.

Material	**Variation**	**Start**	**End**
Ytong	10-90%	10/03	13/03
WFI	10%	13/03	16/03
HFI	10%	17/03	24/03
Ytong	10%	24/03	27/03
WFI	10-90%	27/03	03/04
HFI	10-90%	03/04	10/04
WFI	Setting test	10/04	14/04
WFI	10% slow	14/04	23/04
WFI	10-90% slow	23/04	07/05

Appendix Q

Analysis of hysteresis

This appendix contains all graphs created for the analysis of hysteresis in section 3.1. Furthermore, the raw, extracted values can be found in Table Q.1 and Q.2.

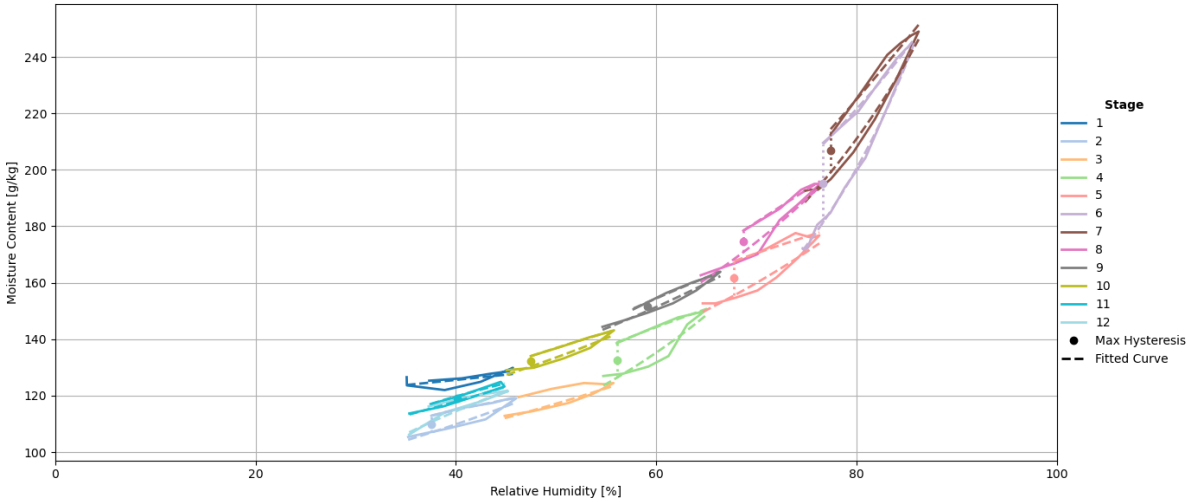

Figure Q.1. The GAB model fitted to the 10% variations for WFI.

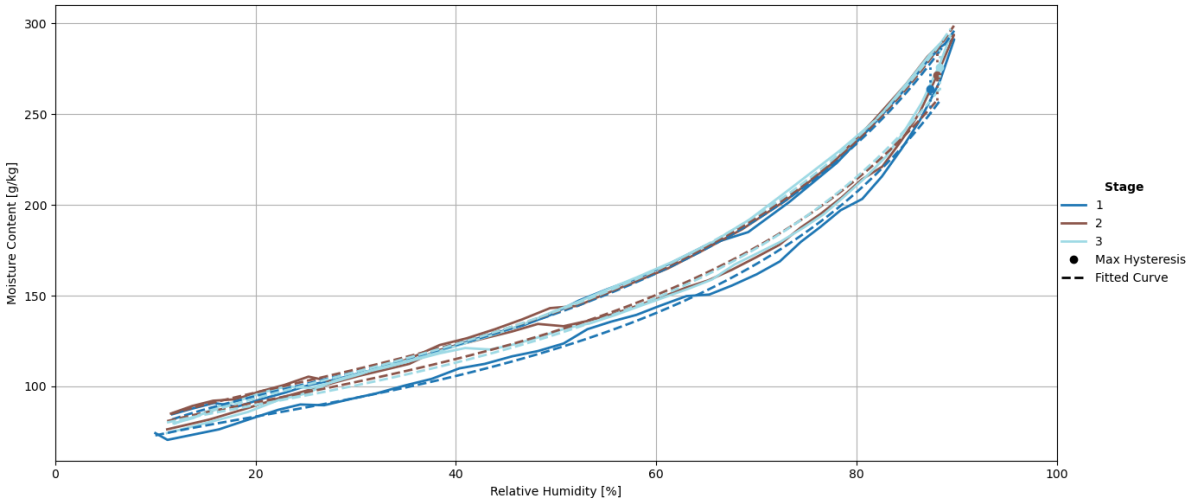

Figure Q.2. The GAB model fitted to 10-90% isotherms for WFI.

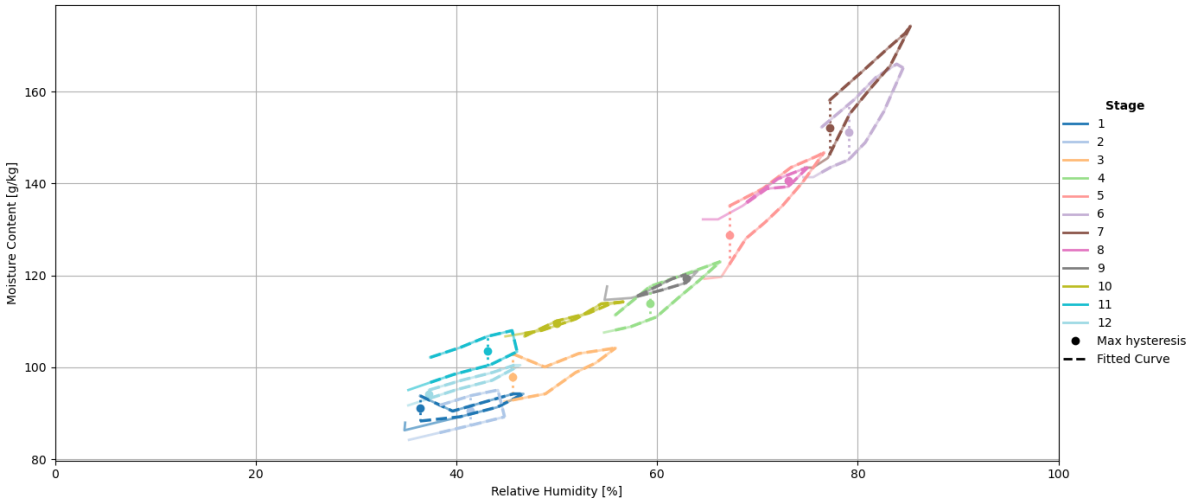

Figure Q.3. Linear interpolation used to fit to the 10% variations for HFI.

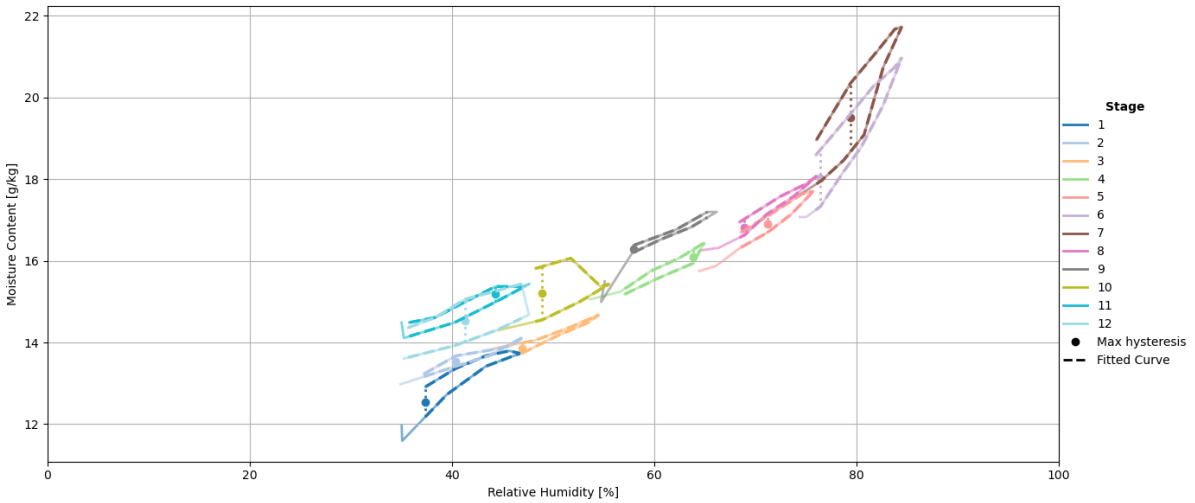

Figure Q.4. Linear interpolation used to fit to the 10% variations for ytong.

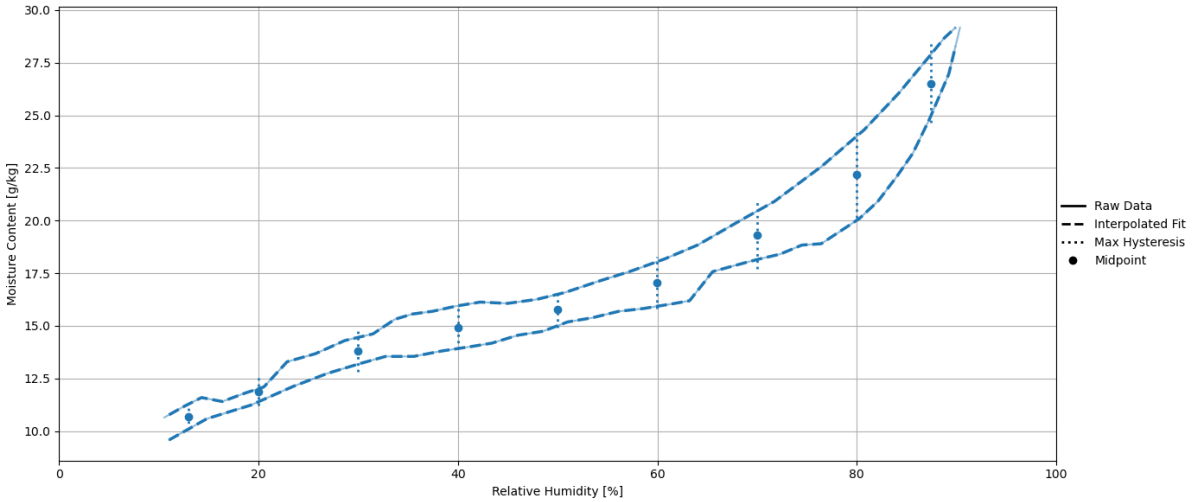

Figure Q.5. Linear interpolation used to fit to 10-90% isotherms for Ytong.

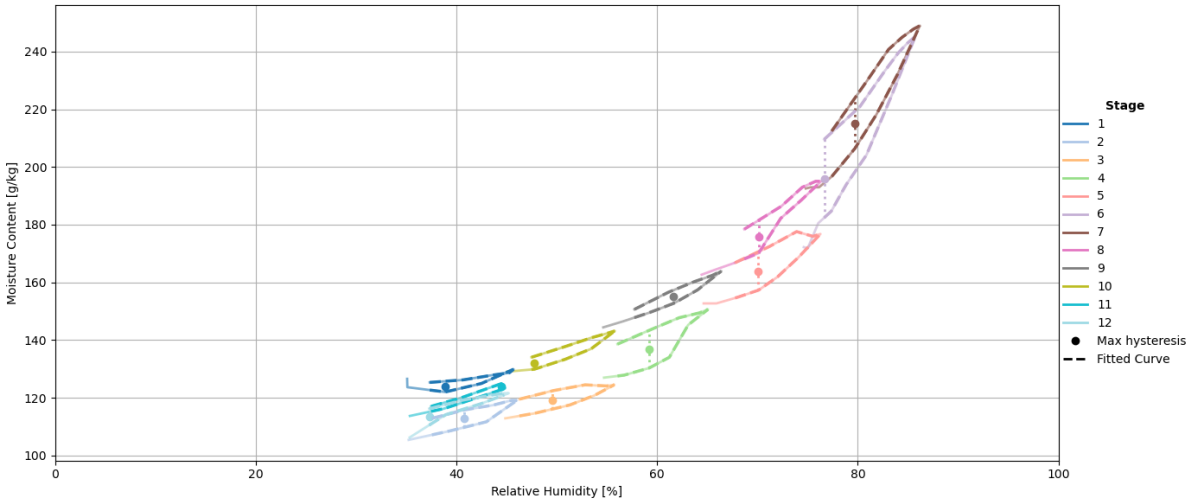

Figure Q.6. Linear interpolation used to fit to the fast 10% variations for WFI.

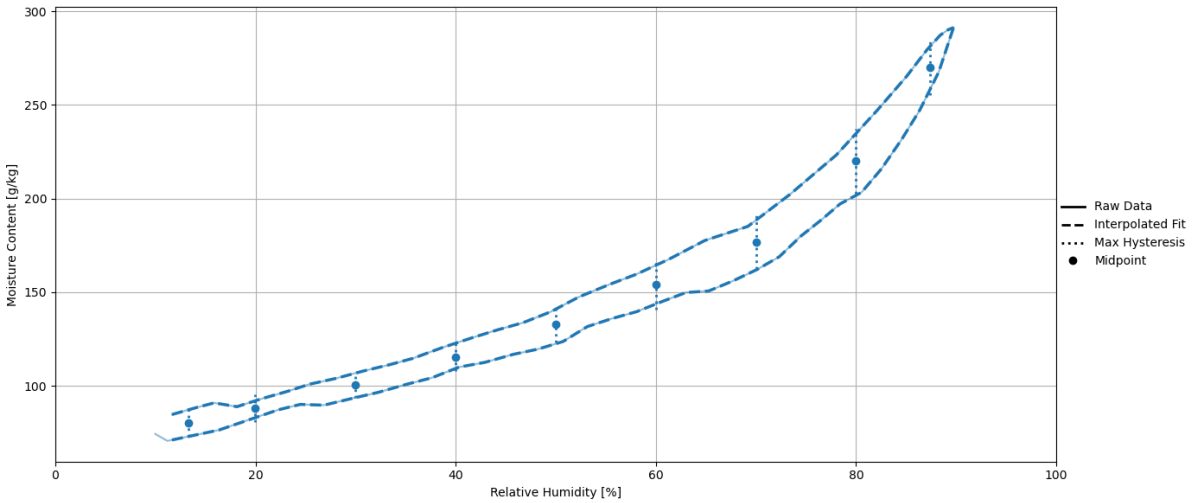

Figure Q.7. Linear interpolation used to fit to the fast 10-90% isotherms for WFI.

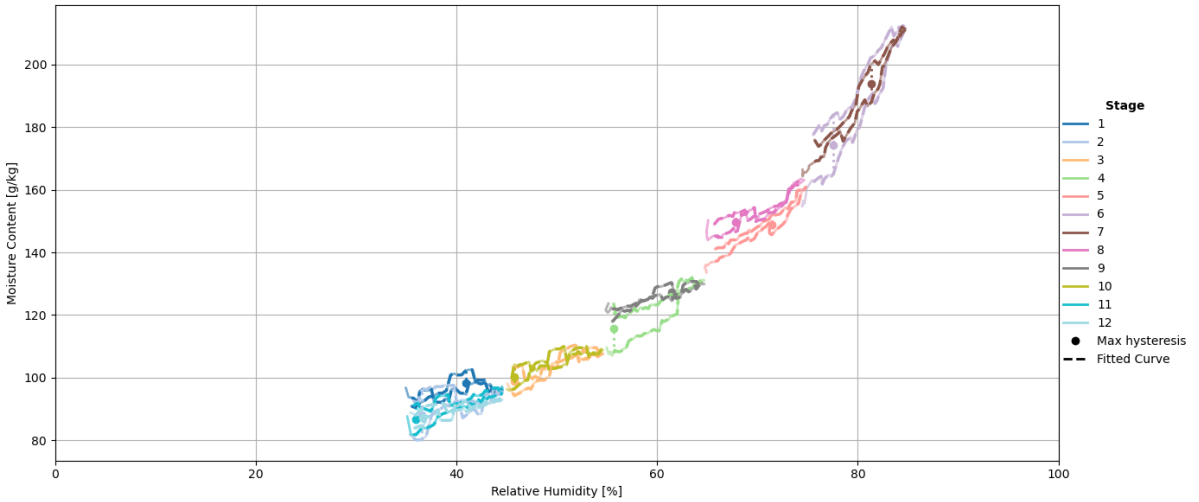

Figure Q.8. Linear interpolation used to fit to the slow 10% variations for WFI.

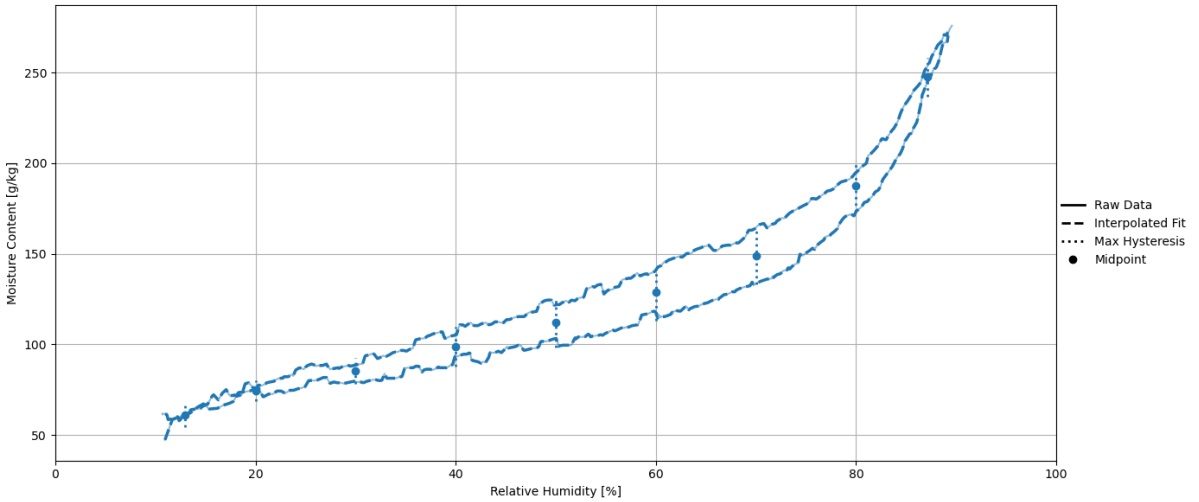

Figure Q.9. Linear interpolation used to fit to slow 10-90% isotherms for WFI.

From these graphs, the maximum and avg distance between the linear interpolation are found. The values can be seen in Table Q.1 and Q.2.

Table Q.1. The average and maximum hysteresis for each cycle and measurements for the small variation. The unit is g/kg

Cycles	1	2	3	4	5	6	7	8	9	10	11	12
RH	35-45%	35-45%	45-55%	55-65%	65-75%	75-85%	75-85%	65-75%	55-65%	45-55%	35-45%	35-45%
Ytong 1 hour												
Max hysteresis	0.7	0.3	0.3	0.3	0.4	1.4	1.7	0.4	1.7	1.3	0.4	1.0
Average hysteresis	0.4	0.1	0.1	0.2	0.3	1.0	1.2	0.2	0.1	0.9	0.3	0.9
HFI 1 hour												
Max hysteresis	5.5	6.5	10.1	7.2	12.7	12.0	11.8	2.6	1.8	1.0	6.4	1.9
Average hysteresis	2.1	5.9	4.9	4.4	6.6	9.5	5.5	1.1	1.2	0.5	5.5	1.6
WFI 1 hour												
Max hysteresis	3.7	6.0	6.4	13.1	13.3	27.2	17.4	11.4	4.6	4.5	2.1	5.7
Average hysteresis	2.2	4.8	4.9	9.1	9.9	16.9	13.5	6.0	3.2	3.6	1.9	2.9
WFI 6 hour												
Max hysteresis	7.5	15.6	9.1	15.7	6.6	18.9	12.0	6.2	5.8	7.8	9.9	9.6
Average hysteresis	2.8	5.7	3.1	6.7	2.9	11.7	4.6	2.5	1.8	3.0	3.8	2.3

Table Q.2. The average and maximum hysteresis for each cycle and measurements for the 10-90%. The unit is g/kg

RH	10-15%	15-25%	25-35%	35-45%	45-55%	55-65%	65-75%	75-85%	85-90%
Ytong 1 hour									
Max hysteresis	1.2	1.3	1.9	2.0	1.7	2.5	3.2	4.1	3.7
Average hysteresis	1.2	0.8	1.4	2.0	1.6	2.1	2.3	3.8	2.8
WFI 1 hour									
Max hysteresis	14.8	15.1	13.3	15.4	19.4	27.2	28.9	34.6	29.4
Average hysteresis	14.2	10.2	12.8	14.2	17.5	21.2	27.2	30.8	20.4
WFI 6 hour									
Max hysteresis	14.1	11.3	14.5	21.9	27.9	31.7	31.6	28.0	21.8
Average hysteresis	2.0	5.7	10.5	16.8	21.6	27.2	28.7	22.9	11.7

The data in the tables shows that hysteresis varies with relative humidity range, material type, and exposure duration. In general, larger RH ranges (10–90%) result in much higher hysteresis values than smaller variations. WFI consistently shows higher hysteresis than HFI and Ytong. In Table Q.1 hysteresis remains relatively low, with WFI reaching up to 13.5 g/kg and Ytong staying below 3.5 g/kg. In Table Q.2, WFI shows maximum hysteresis values as high as 29.4 g/kg, while Ytong peaks around 4.1 g/kg. Furthermore, it is seen from both of the variations that longer variations generally lead to slightly higher hysteresis for WFI, but with no pattern. Lastly, the average hysteresis values are lower than the maximum values but follow the same trends. Overall, the data clearly show that RH range, material, and time all influence hysteresis.

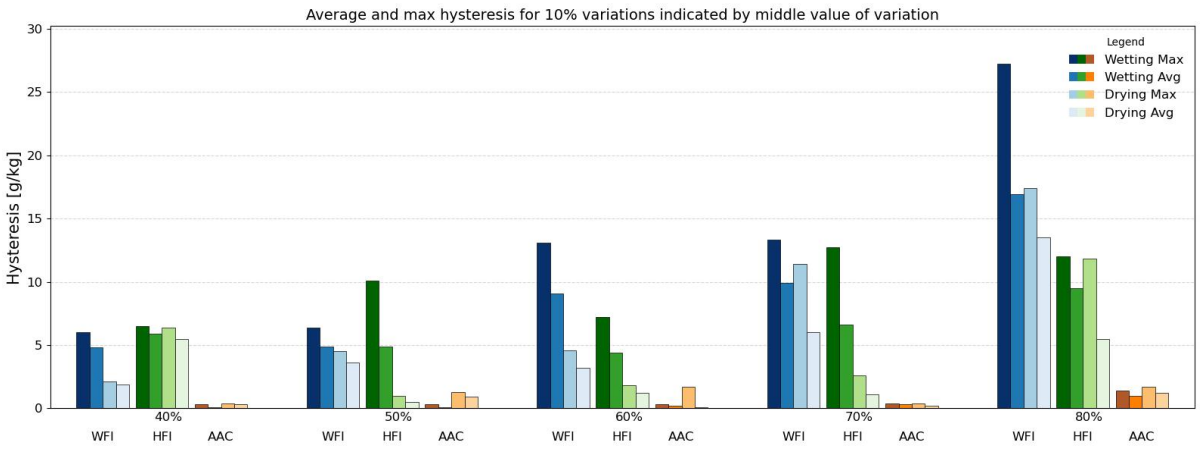

Figure Q.10. Average and max hysteresis of the Δ10% variations, divided into the wetting and drying cycle.

Appendix R

Determination of moisture content

To determine the starting conditions of the materials in the full-scale setup, one of the needed parameters is the moisture content. The measurement is done according to DS/EN ISO 12570 [57].

To determine the moisture content, firstly the material is weighed as quickly as possible, to secure that the moisture content is not changed. This is done for all of the samples. Afterwards, the samples are placed in an oven at 60℃, and weighed once a day, until the weight changes less than 0.1% for three days in a row.

The moisture content can be calculated with Equation R.1

$$u = \frac{m - m_0}{m_0} \tag{R.1}$$

where

m	Mass of sample before drying [g]
m_0	Mass of the sample after drying [g]

Pictures of the measurement are seen on Figure R.1 to R.3.

Figure R.1. Picture of the oven during the drying process

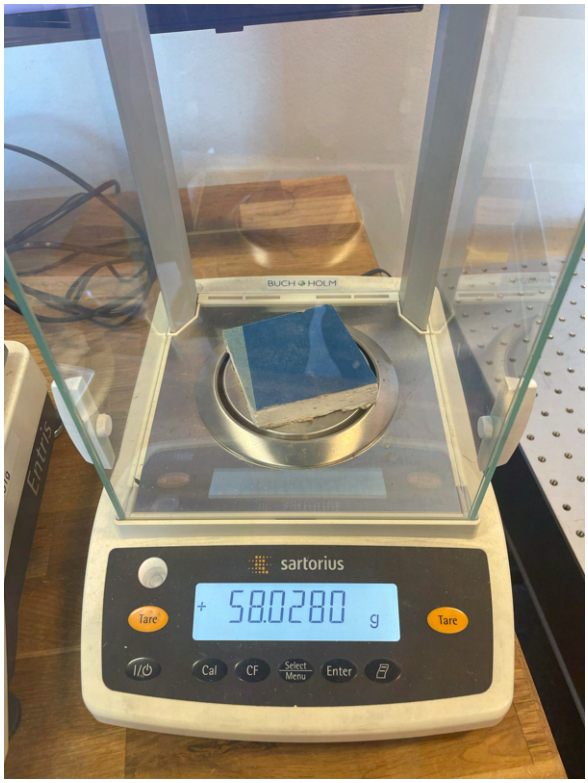

Figure R.2. Weighing of the gypsumboard

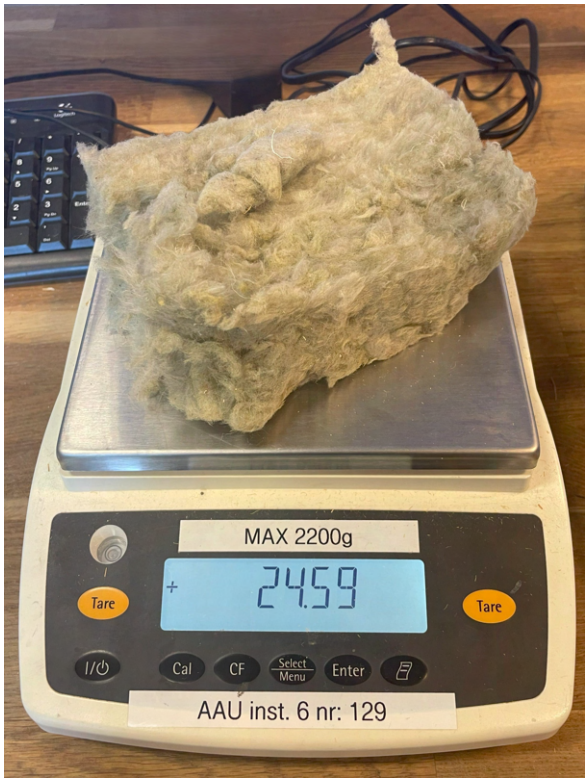

Figure R.3. Weighing of the mineral insulation.

The moisture content is seen in Table R.1.

Table R.1. Moisture content for the different materials

Material	OSB4	Gypsum	Timber	RW	WFI	HFI
Moisture Content [g/g]	0.079	0.010	0.128	0.009	0.117	0.080

Appendix S

Determination of thermal conductivity

NOTE: *The measurements in this appendix are not done by us. The measurements are planned by us, but done as a part of a biobased building material workshop for 8. semester.*

To get to know the building materials better, the thermal conductivity is determined. This is done with the Guarded Hot-Plate method, and the measurements are conducted in the EP500. The method uses a rewritten form of the Heat Equation to calculate the thermal conductivity. To perform the measurement, steady-state conditions are maintained at the top and bottom surfaces. These conditions secure a 1-dimensional heat flux throughout the material. The temperatures at the two plates, the heat supplied and the thickness of the sample are all monitored until steady-state is reached. When this state is obtained, the equipment calculates the thermal conductivity with Equation S.1.

$$\lambda = Q \cdot \frac{\Delta x}{(T_{Hot} - T_{Cold}) \cdot A} \tag{S.1}$$

where:

[H] Q	Heat flux [W]
Δx	Thickness of the sample [m]
T_{Hot}	Temperature at the hot plate [K]
T_{Cold}	Temperature at the cold plate [K]
A	Metering area of the test sample [m^2]

S.1 Measurements

The goal of this measurement campaign, is to correlate the thermal conductivity with the moisture content. This is done for three different insulation materials. Two biobased (Wood

Fiber Insulation and Hemp Fiber Insulation) and one mineral-based (RockWool). Each material is tested at three different relative humidities: 0, room level, and around 80%. The 0% test samples were kept in an oven, at 60 °C, until the weight did not vary more than 0.1 %, three days in a row. The 80% samples was kept in the climatic chamber used in Appendix E for at least two weeks. When doing the measurements the low and high RH samples are sealed in a thin plastic bag, to keep the RH-level the same throughout the measurement.

As a requirement for the measurements, the thermal conductivity has to vary by less than 1% for 60 minutes. The results for the three materials can be seen on Figure S.1.

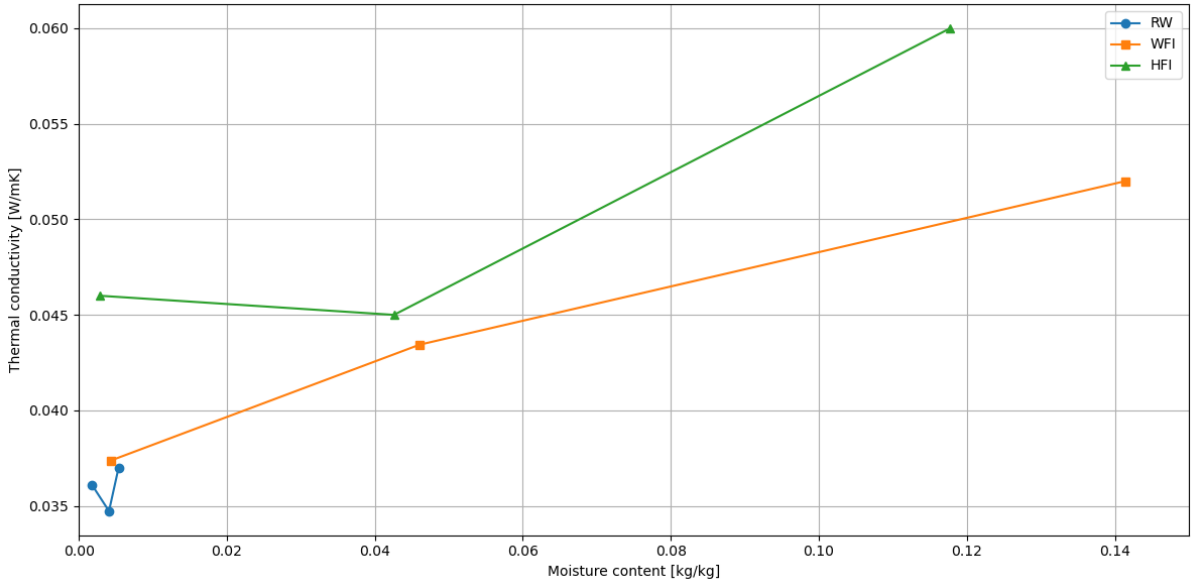

Figure S.1. Thermal conductivity as a function of moisture content for the three materials.

As seen in the plot, the RockWool shows very little variation in moisture content. This suggests that RW is not significantly affected by moisture uptake, likely due to its hygroscopic nature. Consequently, the thermal conductivity remains relatively constant across the measured moisture contents.

In contrast, both biobased insulation materials show a clear increase in moisture content. As the moisture content rises, their thermal conductivity also increases. This trend indicates that biobased materials are more susceptible to moisture uptake, which in turn has a noticeable effect on their thermal performance.

Appendix T

Air permeability

In order to expand the use of biobased building materials, it is essential to have a thorough knowledge of their properties. Here is the water vapour permeability, a key property needed for moisture simulations and moisture assessment of constructions. Understanding the dynamics of moisture and air is essential to prevent mold growth and ensure a healthy indoor environment. The current standard method to measure water vapour permeability is the wet cup and dry cup measurement, which takes up to weeks to make. BUILD at Aalborg University developed a new measurement method and ODA apparatus to measure oxygen diffusion [58]. [50] did extensive work in measuring material properties for a collection of building materials. One of their key findings was a linear relation between relative oxygen diffusion and water vapour permeability. This is a major finding because it only takes up to 3 hours to measure the oxygen diffusion, but the same accuracy is achieved. This sparked curiosity about how air permeability potentially also could be used as a proxy for the water vapour permeability and even further reduce the measurement time. Air permeability only takes around 3 minutes to measure. With a donation from Siemens Fonden it has been possible to conduct measurements of air permeability and add this material property to the collection of measurements by Nyborg, Mikkelsen, and Pedersen [50].

T.1 Measurement setup and method

We have conducted our measurements of air permeability on the apparatus developed by Per Schjønning and Michael Koppelgaard at Aarhus University Foulom (AU Foulum), described in [59]. We were guided by an experienced user of the apparatus, Jørgen Munksgaard Nielsen, when making the measurements. A diagram of the measurement setup is shown in Figure T.1 and a

photo of the apparatus and measurement setup on Figure T.2.

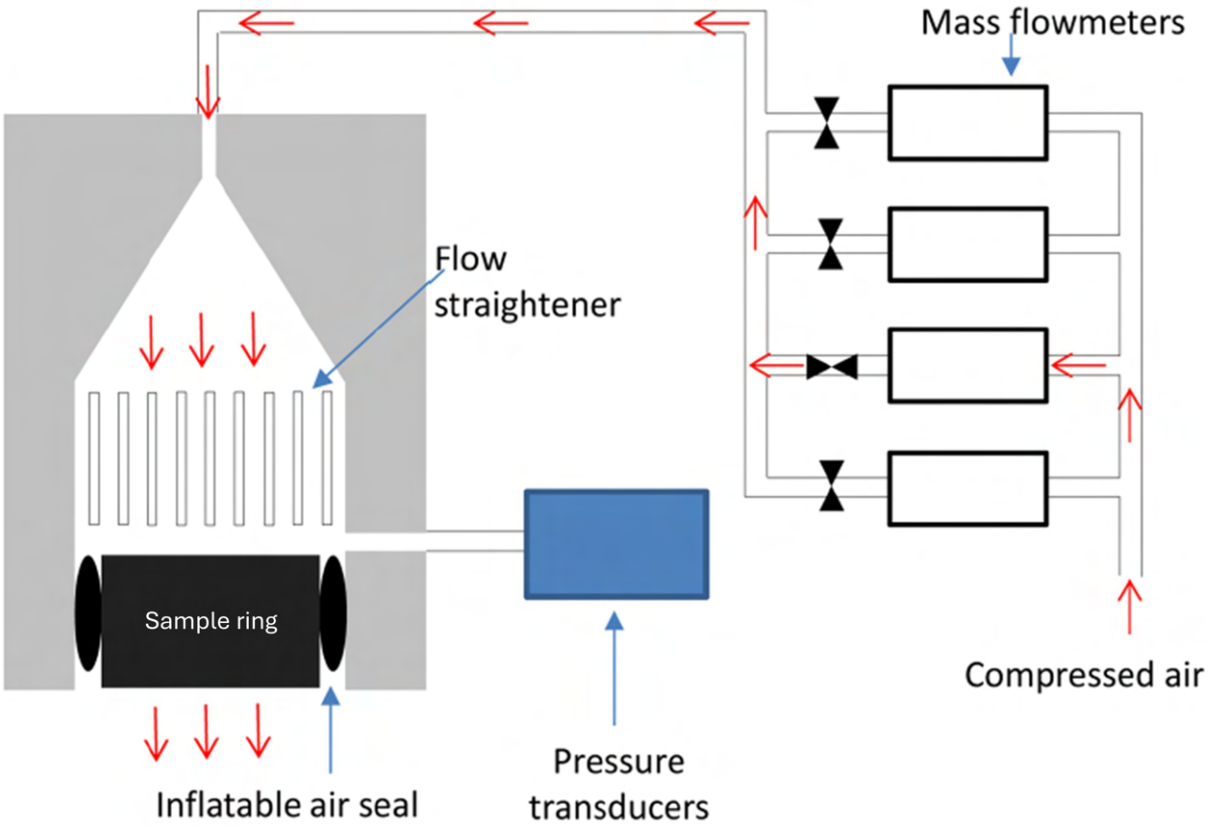

Figure T.1. Air permeameter apparatus schematic from [59].

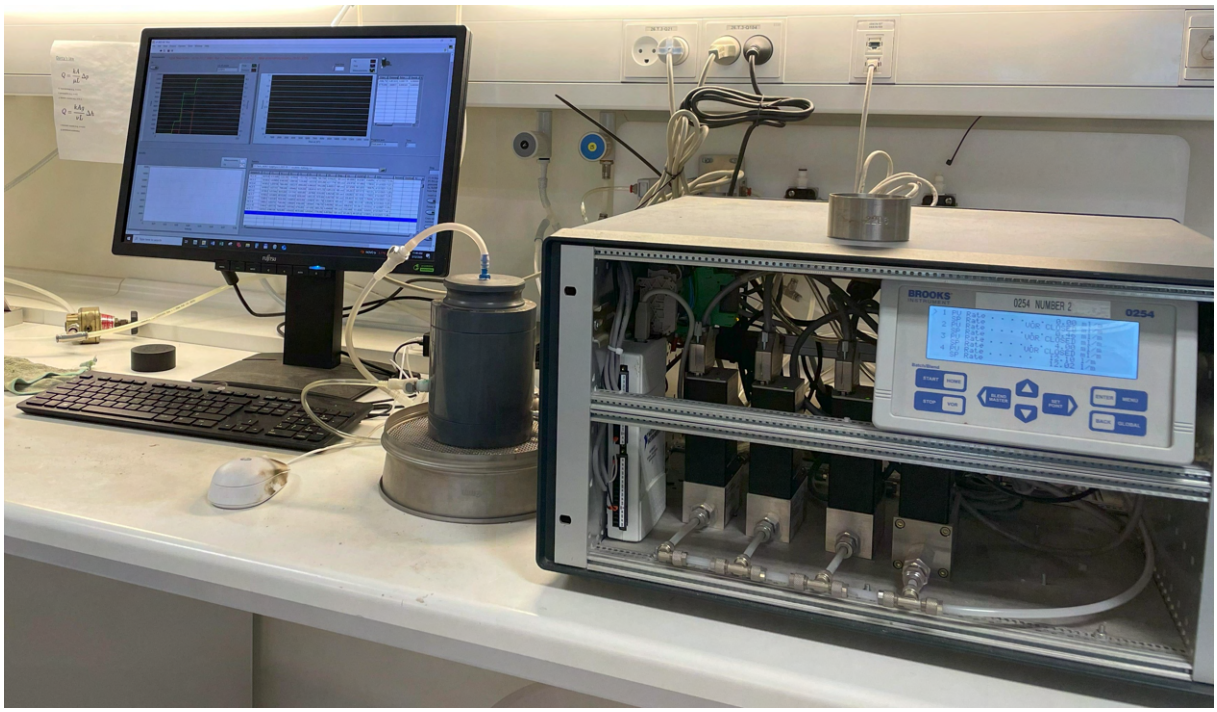

Figure T.2. Air permeameter apparatus [59].

Their setup is designed to measure on a differently sized sample ring, and we therefore needed an adapter for our sample rings. This is necessary in order to get an airtight seal of the measuring chamber, with the inflatable o-rings. The two different sample rings are shown on Figure T.3.

Figure T.3. Sample rings. Our sample ring to the left, and to the right the sample ring used at Aarhus University Foulum.

	Unit	AAU	AU Foulum
Outer diameter	mm	53	63.63
Inner diameter	mm	50	60.63
Radius	mm	25	30.32
Height	mm	51	34.82
Volume	cm^3	100.14	100.53
Surface area:	cm^2	19.63	28.87

Table T.1. Sample ring dimensions for the two different sample rings. [59]

Our sample ring is a type 0753SA from Royal Eijkelkamp. The apparatus is configured to obtain a pressure difference of 5 hPa, 2 hPa, 1 hPa and 0.5 hPa, by automatically adjusting the airflow until the four pairs of airflow and pressure difference are obtained.

We achieved an airtight seal by using a rubber conical casket, with some silicone sealant (Mykote high vacuum grease) on the inside of the casket to seal against the metal ring. Using a solid dummy, we tested our adapter solution and verified it worked, by the system not measuring any airflow and thereby failing the measurement. Figure T.3 show our sample ring with the rubber conical casket, and on Figure T.5 it is placed inside the sample ring from AU Foulum.

Figure T.4. Our sample ring with a rubber conical casket mounted.

Figure T.5. Our sample ring with rubber conical casket, inside the sample ring used at AU Foulum.

T.2 Sample materials and measurements

We conducted our measurements on the exact same measuring rings, made and used by Nyborg, Mikkelsen, and Pedersen [50]. We have used their sample rings, so our measurements of air permeability can be directly added to their sequence of material measurements. The prepared sample rings are shown on Figure T.6, with their labelling.

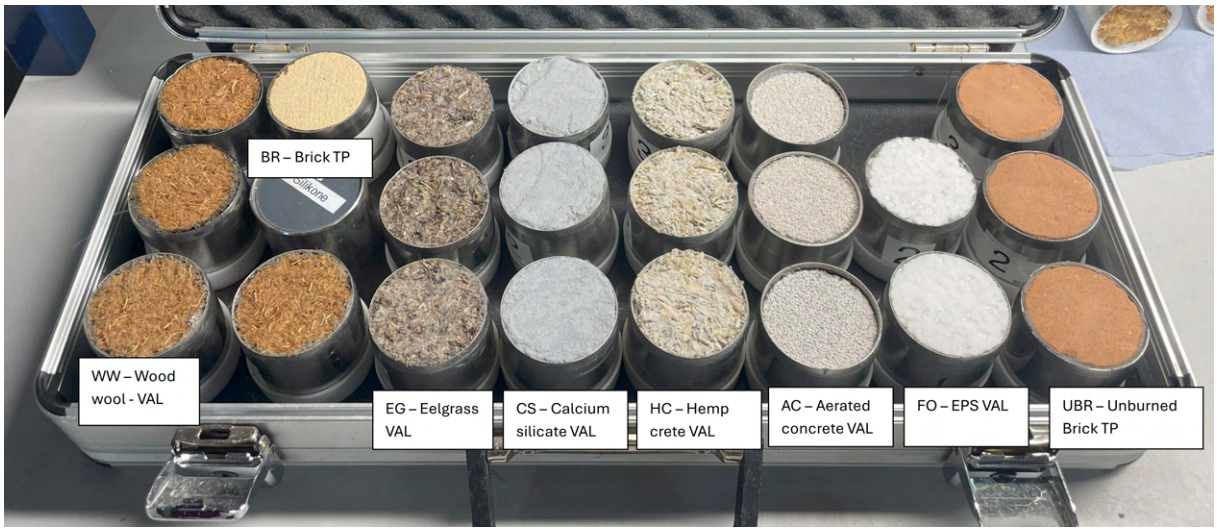

Figure T.6. Picture of tested materials in sample rings, made by Nyborg, Mikkelsen, and Pedersen [50].

Nyborg, Mikkelsen, and Pedersen [50] made measurements for Eelgrass, Calcium Silicate, Hempcrete, Aerated concrete, and EPS conditioned at four different humidities. They conditioned the samples at relative humidities of around 0%, 30%, 60% and 90%. The 30% was assumed to be the state of the room condition. The sample rings have since last time they were used, been stored in the transport case in Figure T.6. To match the measurements from [50], the samples have been stored as shown in Figure T.6, in order to condition them at room conditions of about 30% relative humidity and 22°C. They were stored open, exposed to the room for one and a half months prior to the measurements of air permeability.

Besides the samples on Figure T.6 we prepared three sample rings of the wood fiber insulation and hemp fiber insulation used in the wall elements as described in section 4.2. The used wood fiber insulation is the same product as for the samples made by [50]. One of the hemp fiber sample rings is shown on Figure T.7.

Figure T.7. Hempfiber sample ring prepared for measurements of air permeability and oxygen diffusion.

T.3 Results

In the used measurement setup, the LabView program automatically calculates the air permeability, $K_{a-Darcy}$ [μm^2] and saves the result. The Darcian air permeability is calculated based on a polynomial regression of the four measurement points. This calculation assumes the dimensions of their standard sample ring, and we therefore need to correct it for our sample ring size. The conversion is a simple scaling of the difference in the sample height and sample surface area in the K_a-equation. The equation for air permeability is Equation T.1 [60].

$$K_a = \frac{Q \cdot \eta \cdot L}{A \cdot t \cdot \Delta p} \tag{T.1}$$

Where	
Q	Airflow [mL/min]
Δp	Pressure difference [hPa]
η	Dynamic air viscosity [kg/$(m \cdot s)$]
L	Sample length [cm]
A	Sample surface area [cm^2]
t	time [s]

The correction factor for the sample length and sample surface area is shown in Equation T.2 and Equation T.3. The combined correction factor is shown in Equation T.4.

$$\text{Sample lenght correction} = \frac{L_{AAU}}{L_{Foulum}} = \frac{51mm}{34.84} = 1.46 \tag{T.2}$$

$$\text{Surface area correction} = \frac{A_{AAU}}{A_{Foulum}} = \frac{19.63cm^2}{28.87cm^2} = 0.68 \tag{T.3}$$

$$K_a\text{-corr} = K_a \cdot \frac{\text{Sample lenght correction}}{\text{Surface area correction}} = K_a \cdot 2.1537 \tag{T.4}$$

All the measured values of air permeability are shown in Table T.2. Here it should be noticed that there is no measurement of the wood wool samples or hemp fiber samples. For the wood wool and hemp fiber insulation samples, the measurement failed because the setup could not reach the high pressure difference. The wood wool and hemp fiber are too permeable for the setup. The Q-ΔP_a data pairs at the lower pressure differences could be used to calculate the air permeability, but this data was not saved when the system failed to perform all four measurement points. On the day of our measurements, we measured the air permeability of a black solid with holes, which was said to be the most permeable sample the system could measure. It was measured to have a permeability of 4345 μm^2, and it can be assumed that the wood wool and hemp fiber insulation will have an air permeability higher than this. Figure T.8 illustrates the higher relative diffusion of wood fiber and hemp fiber insulation, than eelgrass which was the most permeable material we measured.

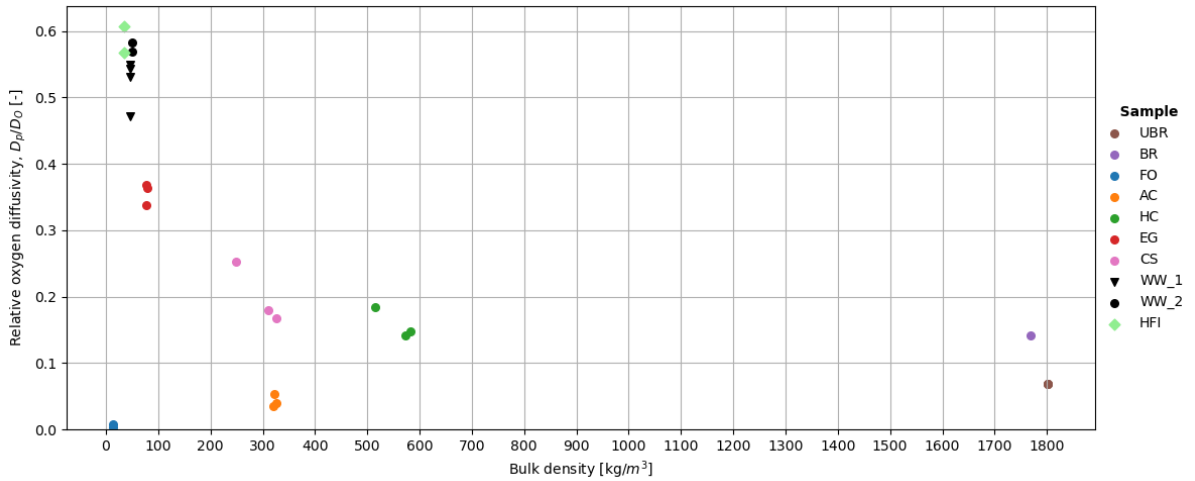

Figure T.8. Relative oxygen diffusion as function of bulk density. WW_1 is from [50]. WW_2 and HFI are our samples, on which we have measured oxygen diffusion with the ODA-apparatus as described in [50]. A general bulk density is used for WW_2 and HFI.

We did several consecutive measurements on the same sample rings, to investigate the reproducibility of a measurement result. We also did consecutive measurements on the same sample ring, but with changes in positions.

Table T.2. Measurements of air permeability $K_{a-darcy}$ [μm^2] at room conditions (30%RH and 20°C). [59].

Sampling series	Sample																
	EG1	EG2	EG3	CS1	CS2	CS3	AC1	AC2	FO1	FO2	HC1	HC2	HC3	UBR1	UBR2	UBR3	BR2
A	1310.0	1654.8	1546.7	4.3	0.4	16.4	168.0	132.9	32.9	93.1	102.7	163.1	651.7	13.4	13.2	20.9	122.6
B			1553.6	4.2			165.5					144.8	653.4				
			1552.8				165.5					146.3					
			1561.6				166.3					144.8					
			1569.5				167.5					149.9					
			1555.8				164.6					148.8					
			1562.9				167.5										
			1570.9														
C													699.9				
													706.1				
													711.3				
													706.6				
													707.7				
D													671.0				
													667.2				
													668.8				
E													648.4				
													645.2				
													642.1				
													643.7				
Avg:	1310.0	1654.8	1559.2	4.2	0.4	16.4	166.4	132.9	32.9	93.1	102.7	149.6	673.1	13.4	13.2	20.9	122.6
Std dev:			8.4	0.06			1.2					6.9	27.3				

In Table T.3 we have compiled an overview of the material properties measured on the samples. Here an average air permeability is stated for each sample, based on the measurements in Table T.2. The values in Table T.3 are compiled from multiple sources. General values for each material are provided in Table 2 of [50]. The values for UBR and BR are based on measurements reported by [61], and the rest are measured by Nyborg, Mikkelsen, and Pedersen [50].

The stated values for EG, AC, CS, HC, and FO of bulk density, air-filled porosity, pure oxygen Currie diffusion, relative oxygen diffusion, tortuosity, and air permeability are measured under room conditions (30%RH and 20°C). These values are hereby measured for the materials in the same state, to ensure comparability. The specific data at room conditions have been shared by Nyborg, Mikkelsen, and Pedersen [50]. The values for water vapour permeability are general values measured with the dry cup method [50]. For the thermal heat conductivity, the values are compiled from data sheets and literature and are general values.

Table T.3. Compiled material properties measured on the samples. [50] [61]

Sample	Thermal conductivity λ, $W/m \cdot K$	Bulk density kg/m^3	$K_{a-darcy}$ $[\mu m^2]$	Water vapour permeability, dry Cup $[kg/(m \cdot s \cdot GPa)]$	Air-filled porosity ϵ, $\frac{m^2 \text{ air}}{m^2 \text{ sample}}$	Pure O_2 currie diffusion D_P, cm^2/s	Air diffusion D_o, cm^2/s	Relative O_2 diffusion D_p/D_o, [-]
Ubr1	0.84[1]	1802	13.4	0.0186	0.32	0.01415	0.205	0.069
Ubr2	0.84[1]	1802	13.2	0.0186	0.32	0.01415	0.205	0.069
Ubr3	0.84[1]	1802	20.9	0.0186	0.32	0.01415	0.205	0.069
Br2	0.398[1]	1768	122.6	0.0244	0.35	0.02911	0.205	0.142
Eg1	0.037[2]	77.2	1310.0	0.0704	0.942	0.06935	0.205	0.338
Eg2	0.037[2]	77.6	1654.8	0.0704	0.942	0.07565	0.205	0.369
Eg3	0.037[2]	79.2	1559.2	0.0704	0.941	0.07472	0.205	0.364
Ac1	0.088[3]	322.9	166.4	0.0135	0.872	0.01097	0.205	0.054
Ac2	0.088[3]	326.9	132.9	0.0135	0.870	0.00822	0.205	0.040
Cs1	0.068[4]	311.4	4.2	0.0463	0.864	0.03671	0.205	0.179
Cs2	0.068[4]	325.3	0.4	0.0463	0.858	0.03426	0.205	0.167
Cs3	0.068[4]	248.7	16.4	0.0463	0.891	0.05175	0.205	0.252
HC1	0.135[5]	572.9	102.7	0.0341	0.749	0.02911	0.205	0.142
HC2	0.135[5]	582.0	149.6	0.0341	0.745	0.03028	0.205	0.148
HC3	0.135[5]	515.1	673.1	0.0341	0.773	0.03786	0.205	0.185
FO1	0.042[6]	13.7	32.9	0.0056	0.987	0.00058	0.205	0.003
FO2	0.042[6]	14.0	93.1	0.0056	0.987	0.00146	0.205	0.007

[1] Brick (25°C) and Clay unfired brick (25 °C) is from reference 1 in [36].
[2] Eelgrass from Læsø Zostera ApS [62].
[3] Ytong data sheet [63].
[4] Skamowall board data sheet [64] .
[5] The hempcrete sample is approx. 25% hemp shives and 75% lime. Hemp-lime mix 11 (20 °C) is from reference 37 in [36].
[6] EPS2 in [36] from [65].

It is interesting to visualize the relationship between air permeability, relative oxygen diffusion, and water vapour permeability as stated in the introduction. Figure T.9 shows the relationship between air permeability and relative oxygen diffusion.

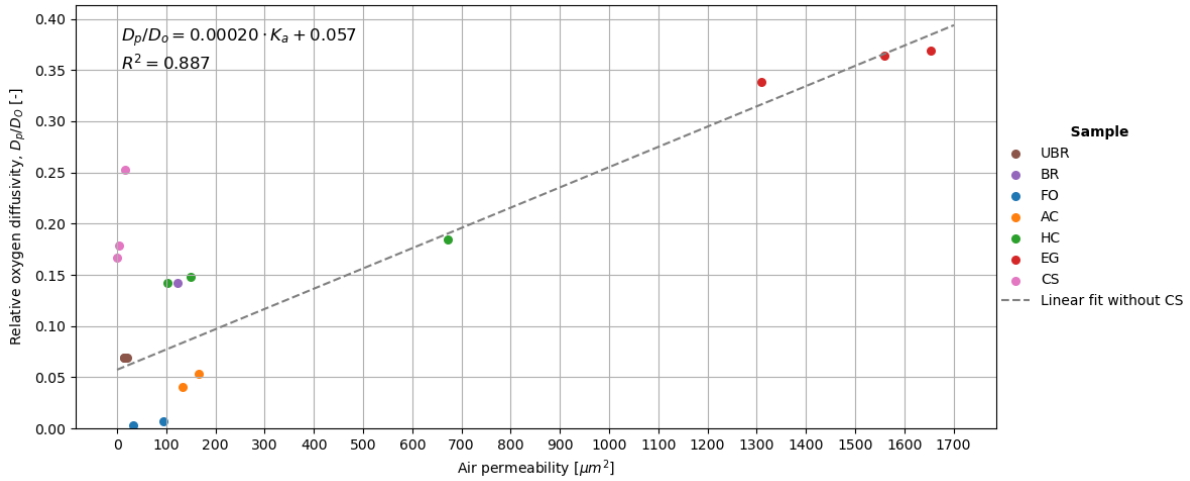

Figure T.9. Relative oxygen diffusion as function of air permeability.

The calcium silicate falls outside of the general tendency, for which we do not have a good explanation and is something to further investigate. We have fitted a linear function to the data, and excluded calcium silicate for now. Overall Figure T.10 shows a promising tendency

and indicates a possible linear correlation. The correlation is not as clear and significant as the one found between the water vapour permeability and relative oxygen diffusion by [50]. This serves as motivation for further investigation and to establish more data points and include more materials. An obvious next step, is to add the air permeability of the porous wood wool and hemp fiber insulation.

We have also plotted the water vapour permeability as a function of air permeability. This shows a similar tendency as expected due to the findings of [50].

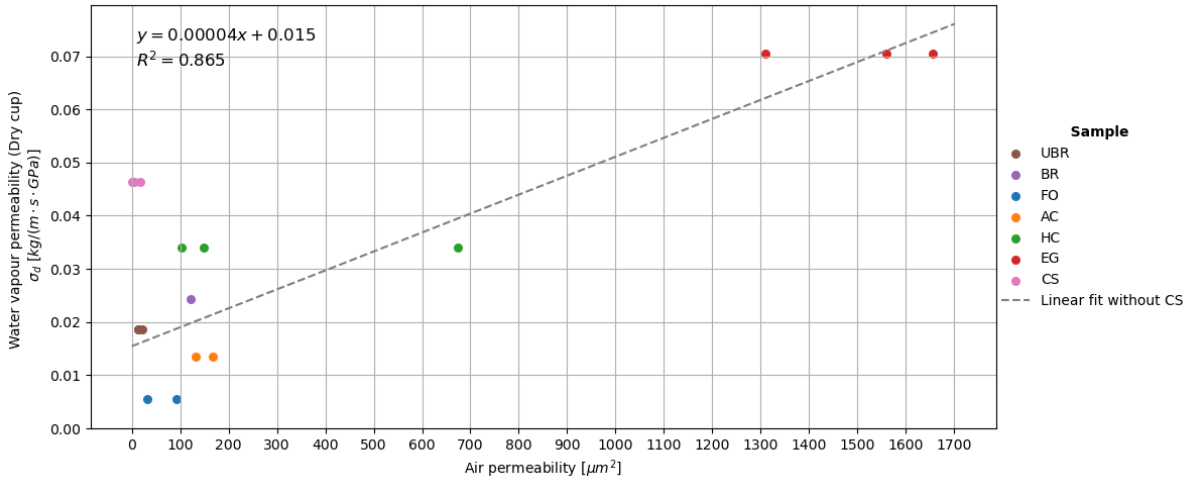

Figure T.10. Water vapour permeability as function of air permeability.

By our measurements of air permeability, we have added another material characteristic to the work of [50]. There is now a foundation for a deeper material analysis, which can provide a more detailed insight into building materials.

T.3.1 Reproducibility of air permeability

For the porous samples, it was a concern if they could be altered by the high airflows from the air permeameter apparatus. The concern arose with hempcrete, where lime dust was visually blown out during measurements. We therefore did several consecutive measurements on the same sample to check if the results would change.

Figure T.11 shows the deviation in the measurement result from the first measurement in a consecutive measurement series.

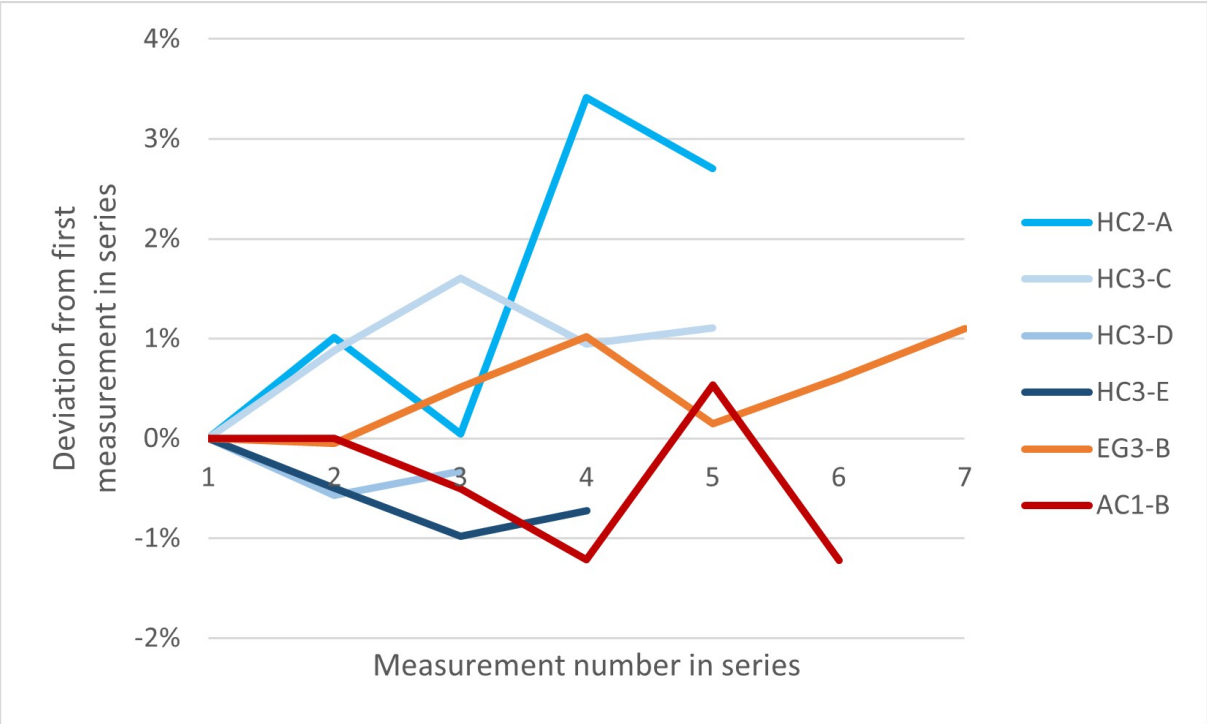

Figure T.11. Deviation in air permeability for a series of consecutive measurements.

Figure T.11 shows a good consistency in the measured result, indicating the samples are not altered during a measurement. Comparing the different measurement series, where the sample has been removed and reinserted into the measurement setup, there is a bigger deviation in the results. The deviation from the first measurement, and all measurements done on the same samples, is shown in Figure T.12.

Figure T.12. Deviation in air permeability for a series of consecutive measurements.

The largest deviation observed is 13%, but overall, there is a good level of reproducibility in the measurements for the same samples.

Appendix U

Analysis of RH

This appendix contains all of the boxplots used in the analysis of RH for WUFI simulations. The analysis is found in chapter 2. For all of the boxplots note the changing y-axis.

U.0.1 Distance plots

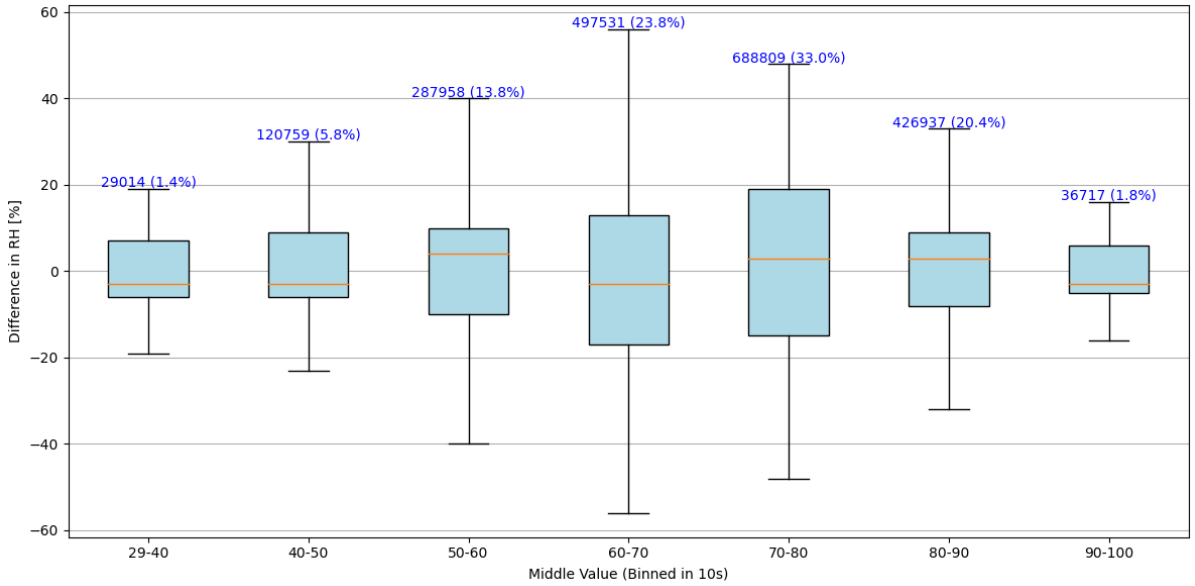

Figure U.1. The variation of RH for point 0.

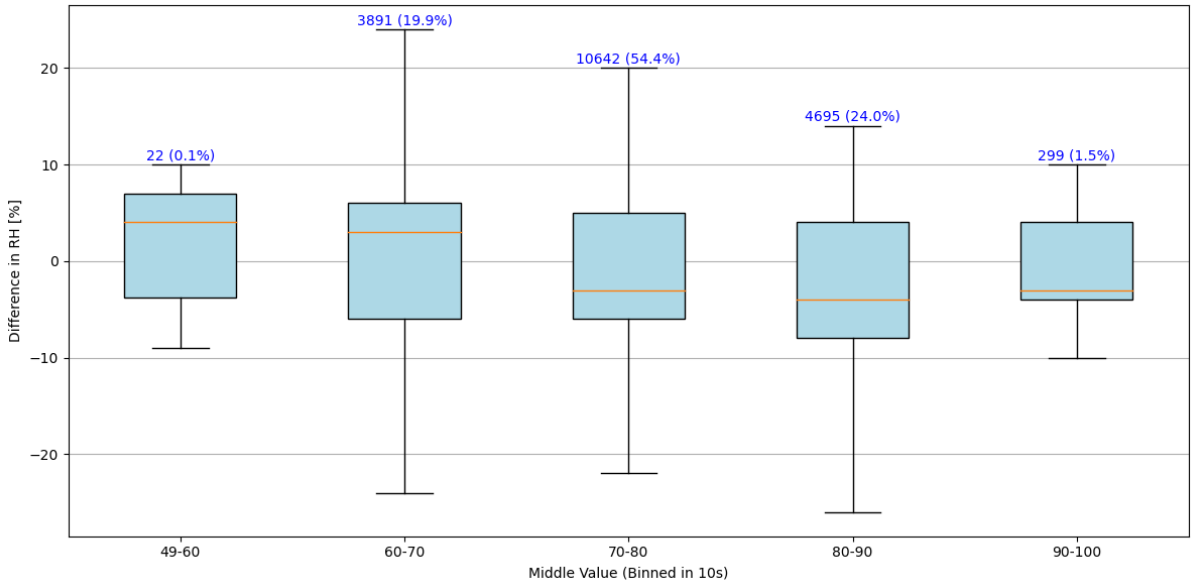

Figure U.2. The variation of RH for point 2.

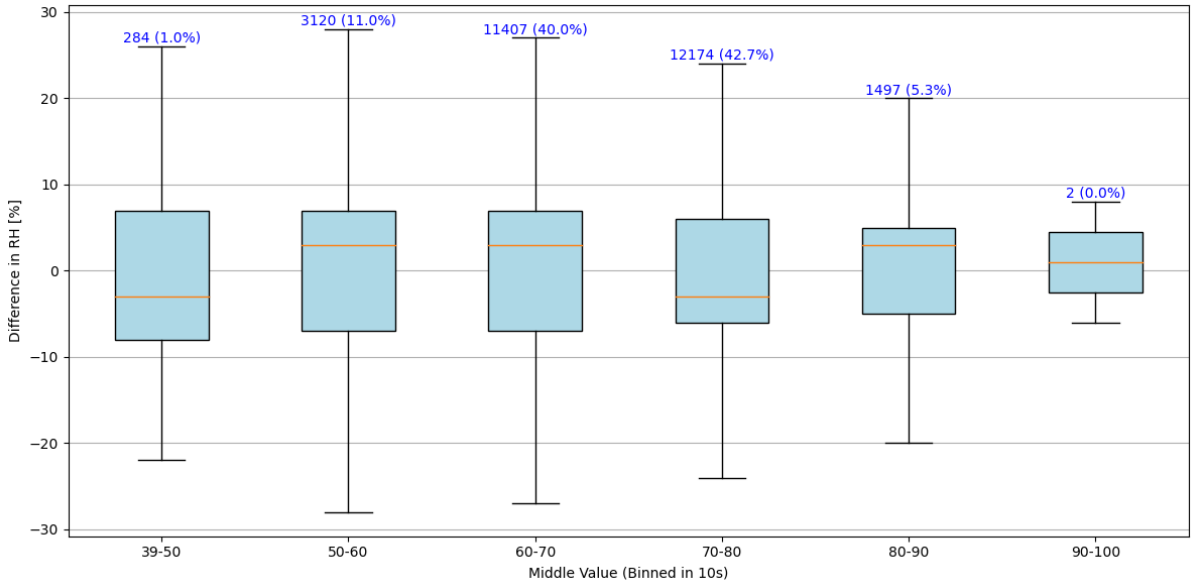

Figure U.3. The variation of RH for point 4.

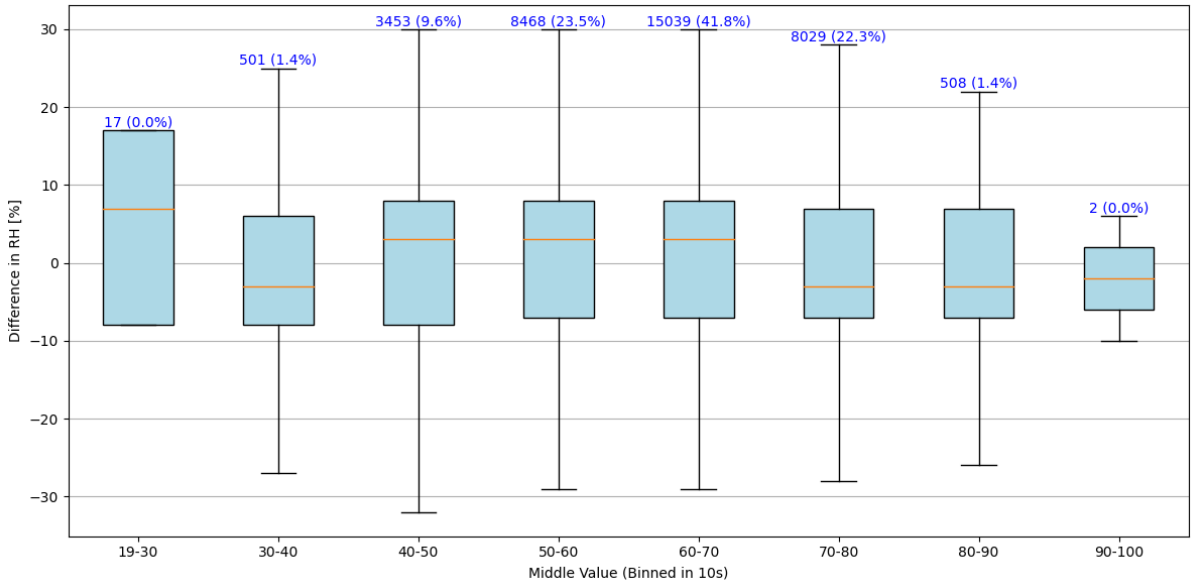

Figure U.4. The variation of RH for point 5.

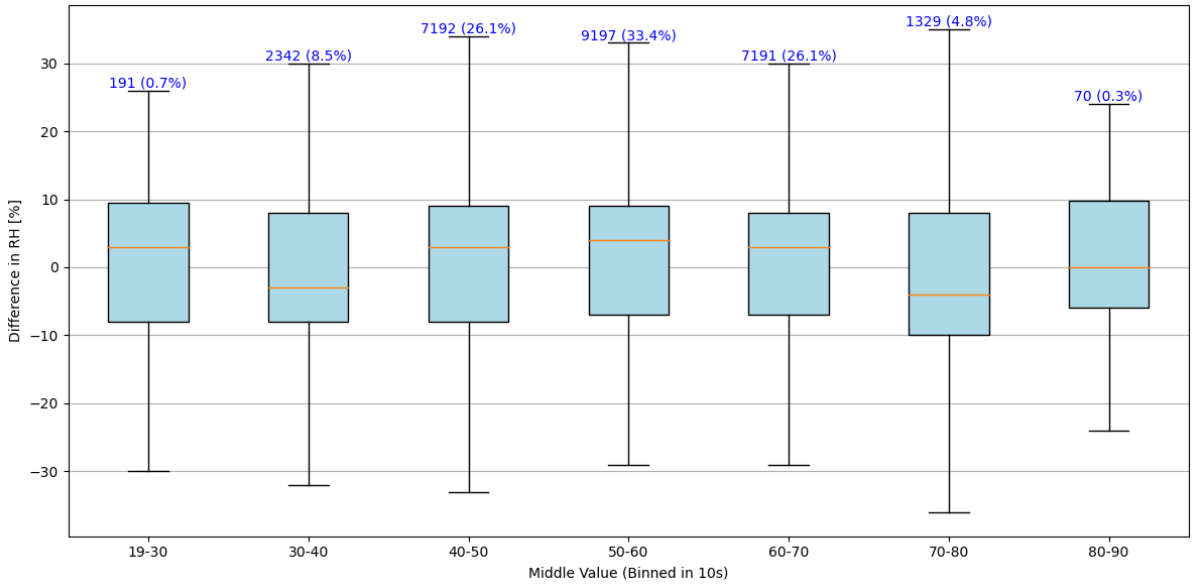

Figure U.5. The variation of RH for point 6.

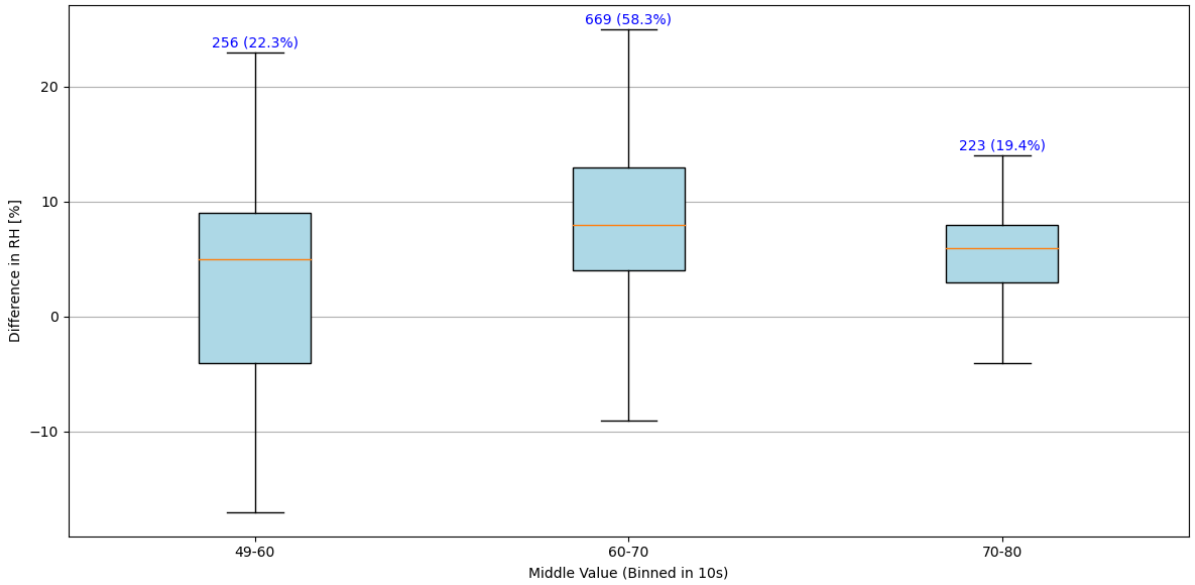

Figure U.6. The variation of RH for point 8.

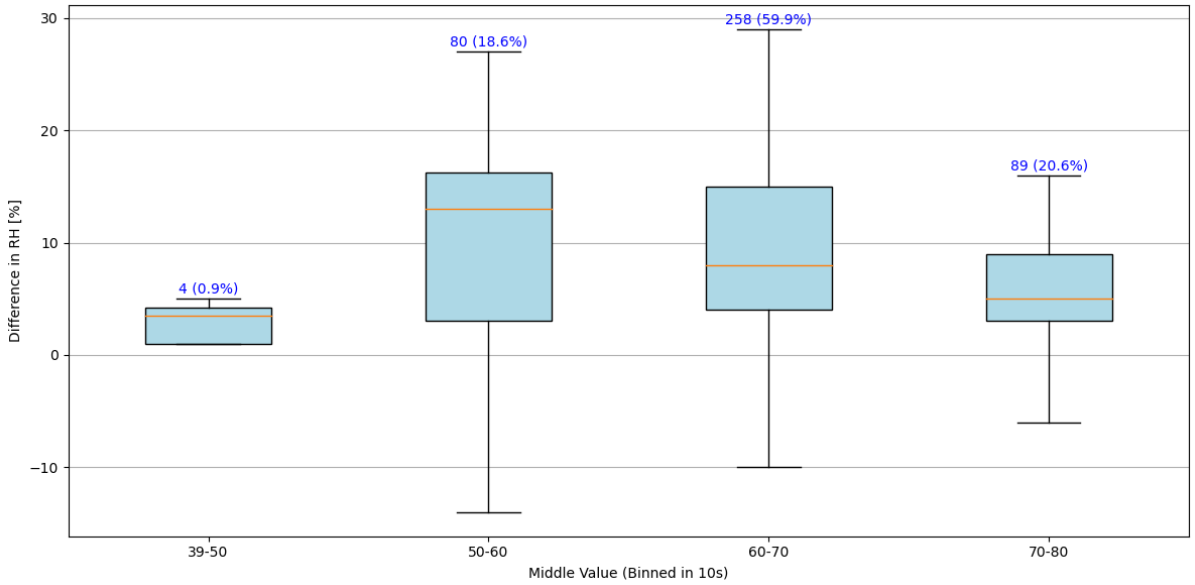

Figure U.7. The variation of RH for point 10.

U.0.2 Time plots

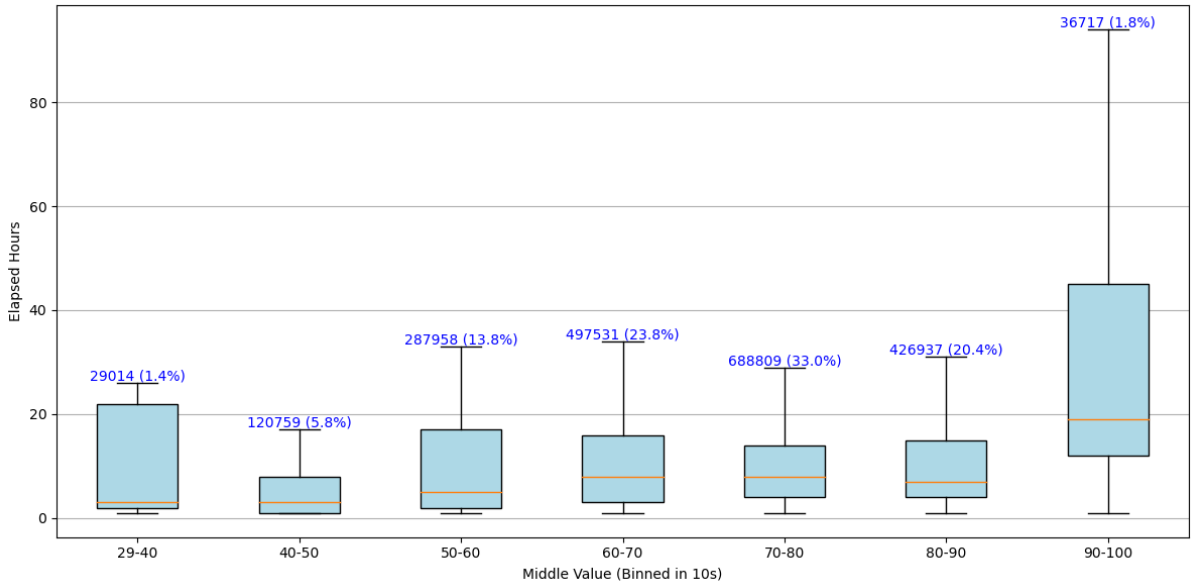

Figure U.8. The duration of the variation in RH for point 0.

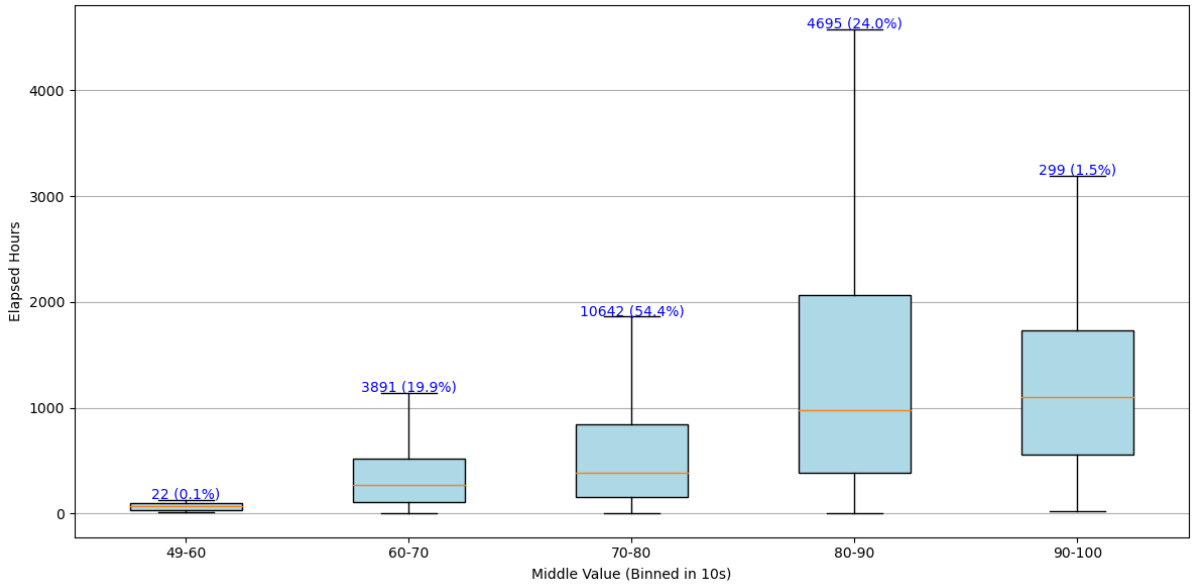

Figure U.9. The duration of the variation in RH for point 2.

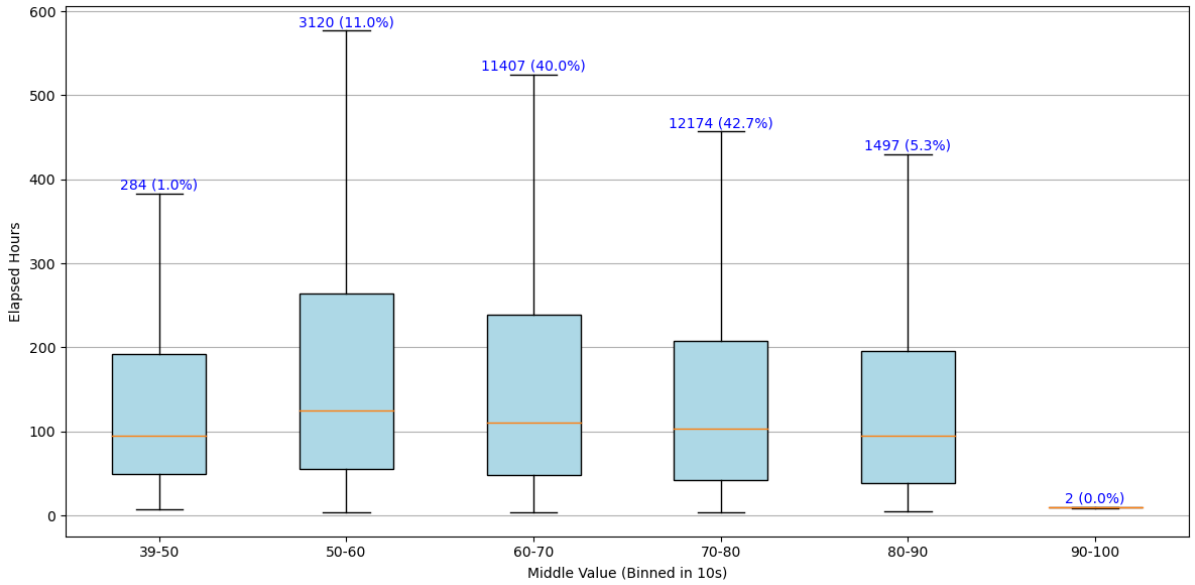

Figure U.10. The duration of the variation in RH for point 4.

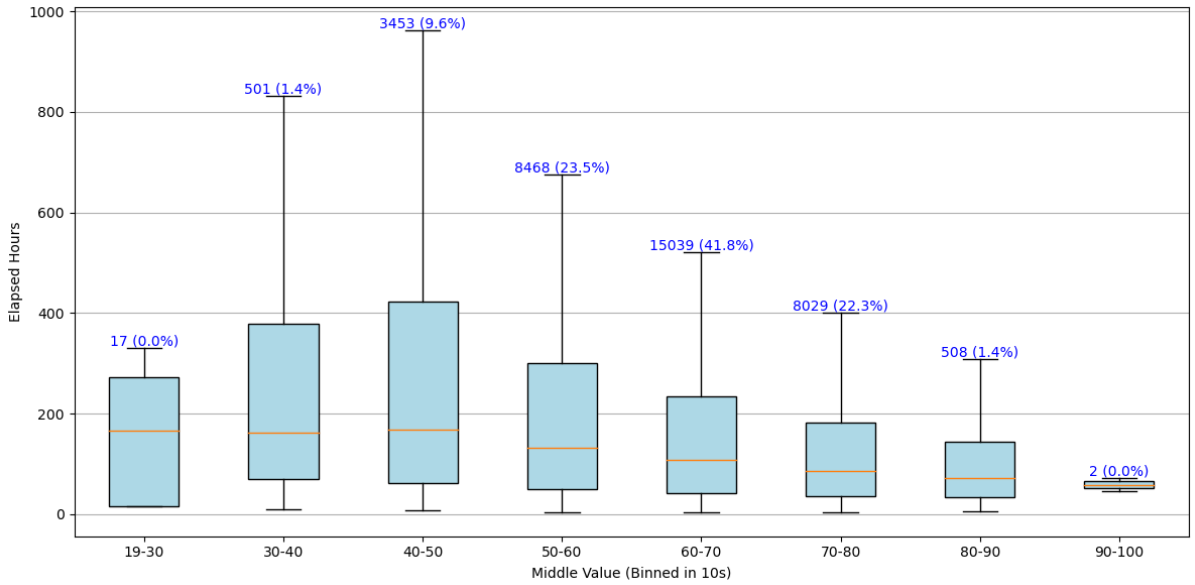

Figure U.11. The duration of the variation in RH for point 5.

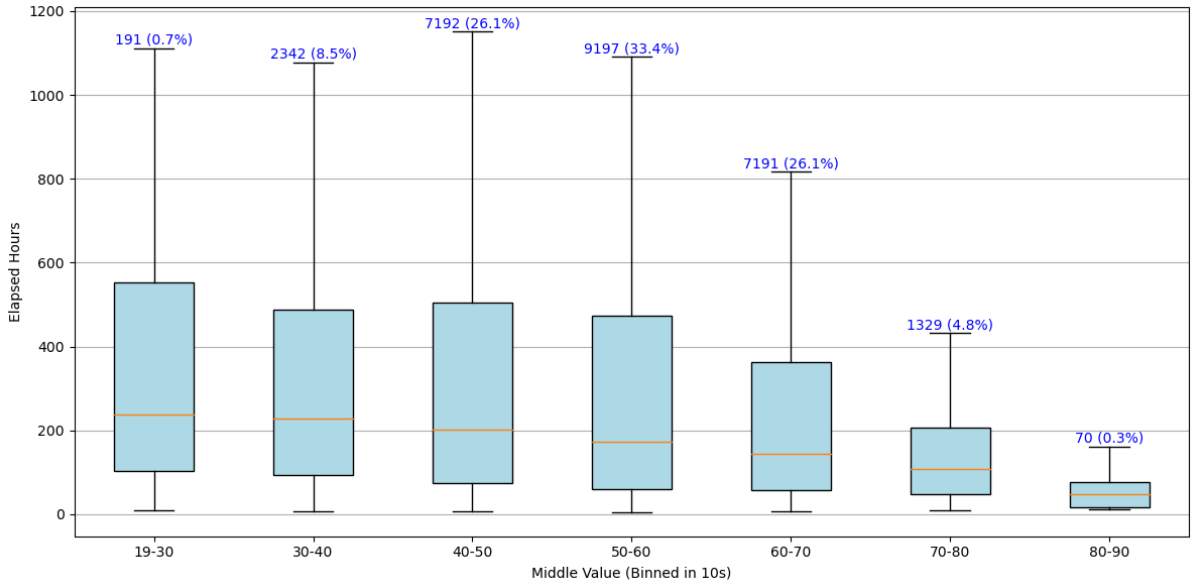

Figure U.12. The duration of the variation in RH for point 6.

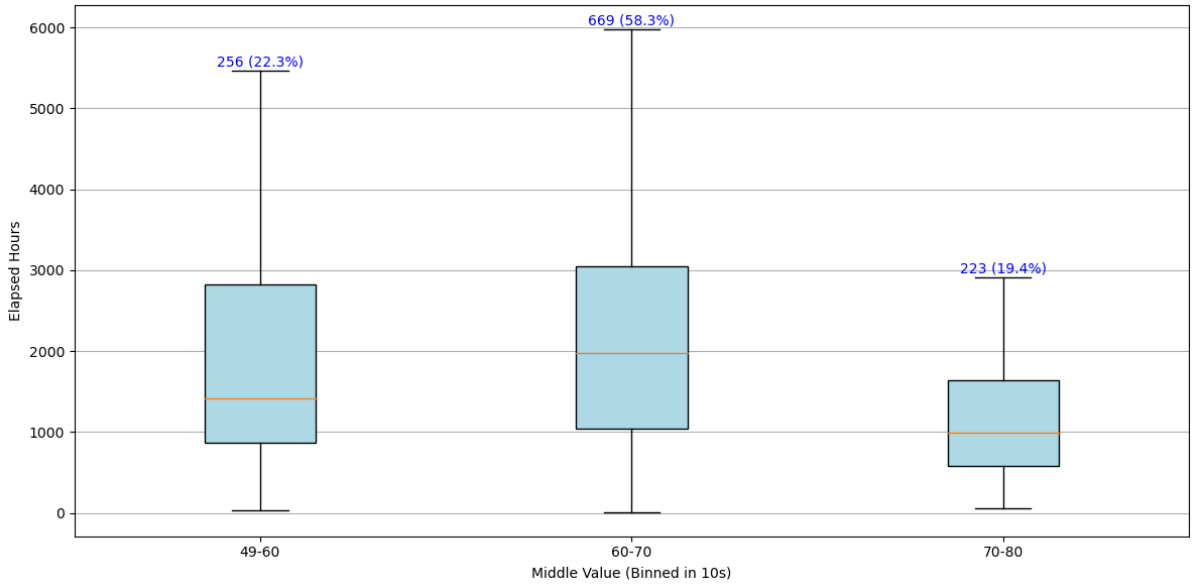

Figure U.13. The duration of the variation in RH for point 8.

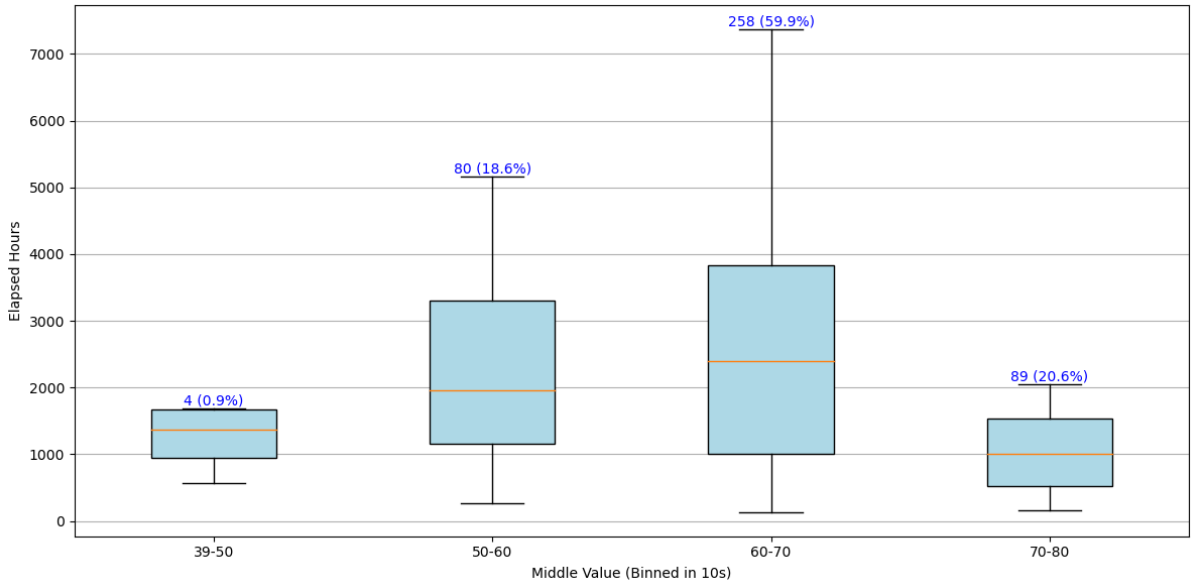

Figure U.14. The duration of the variation in RH for point 10.

Part IV

General appendices

Appendix V

Calibration of HygroDat

In order to check the accuracy of the DewMaster sensors, the HygroDat 100 is used. The HygroDat measures both temperature and relative humidity. To get precise results, the equipment needs to be calibrated for relative humidity. In order to do the calibration, the following equipment is needed:

- HygroDat 100
- Novasina calibration salts for RH
  - 11.3%
  - 32.8%
  - 53.3%
  - 75.5%
  - 90.1%
- F200 precision thermometer
- ISOTECH temperature well

The temperature measurements have been compared with the F200 precision thermometer, and measure within ±0.3℃. As the temperature measurements from the HygroDat are not used as a reference, this is close to the accuracy at ±0.2℃ specified, it is assumed good.

V.1 Relative humidity

The calibration for relative humidity is done using the calibration salt solutions. The solutions are mixed with a few drops of demineralised water, in order to obtain a mixture between salt crystals and water. The calibration is done for the five different humidities mentioned in the list

above. The setup used for the calibration can be seen in Figure V.1, and a close-up of the probe and salt on Figure V.2.

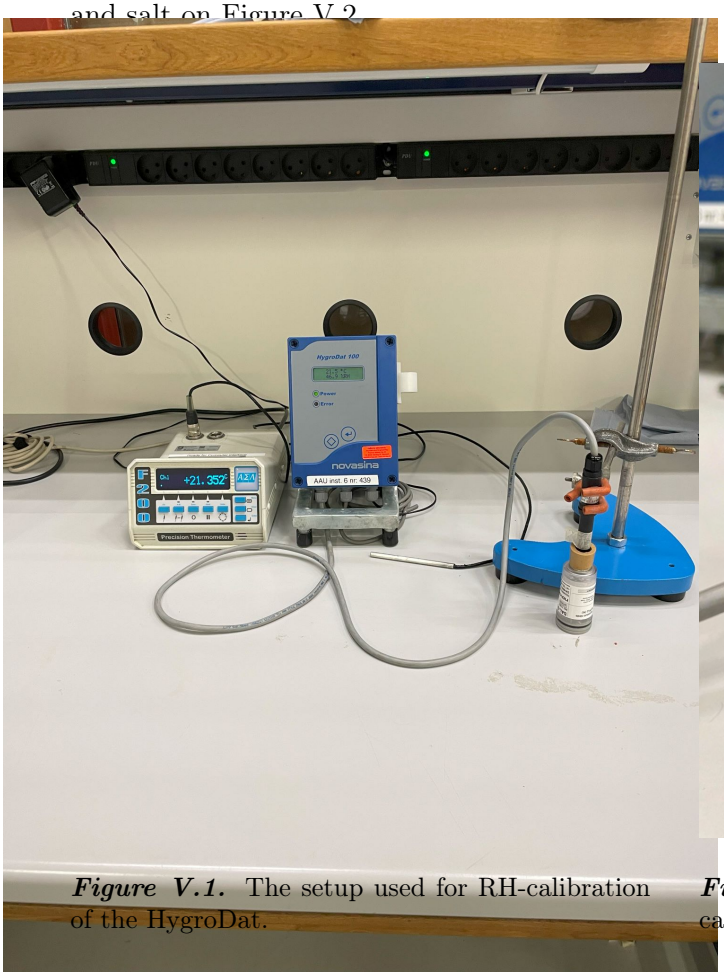

Figure V.1. The setup used for RH-calibration of the HygroDat.

Figure V.2. Close up of the probe attached to a calibration salt.

The HygroDat sensor is placed in a container with the salt solution. For each solution, the temperature and relative humidity are measured until the humidity is stabilized. The result of the calibration can be seen in Figure V.3.

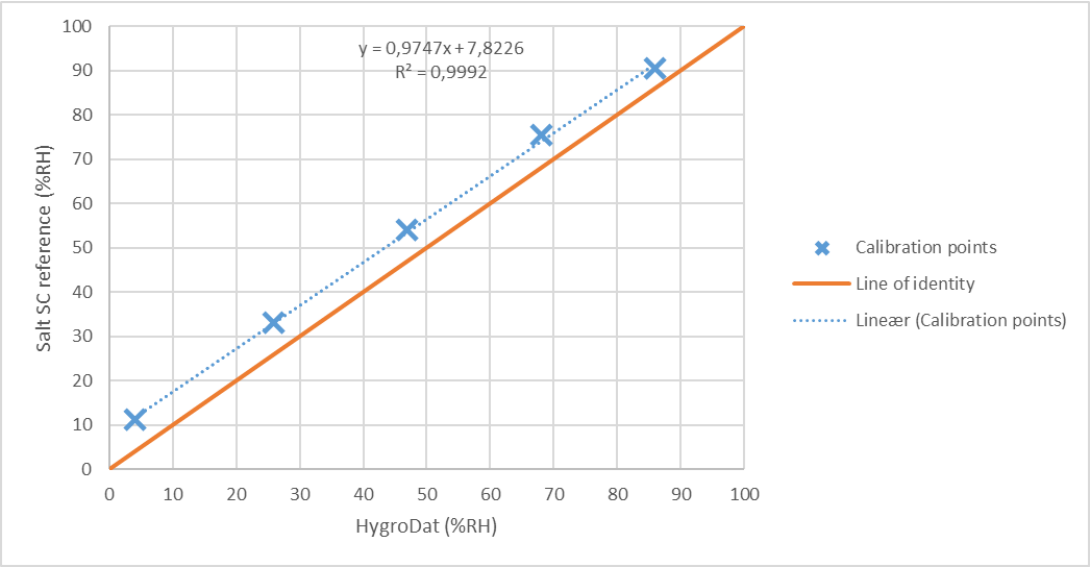

Figure V.3. Calibration graph for relative humidity.

As seen on the calibration graph, the RH measurements from the HygroDat follow the line of identity, albeit with a small offset.

Appendix W

F200 calibration certificate

KALIBRERINGSCERTIFIKAT

CERTIFIKATNR.:
200-T-24274

TEKNOLOGISK INSTITUT

Teknologiparken
Kongsvang Allé 29
Bygning 14
8000 Aarhus C
Tlf. +45 72 20 20 00
info@teknologisk.dk
www.teknologisk.dk

Side 1 af 3
Antal bilag: 0
Init: BJNI/DDS

Rekvirent: Aalborg Universitet, Institut for Byggeri, By og Miljø (Build)
Thomas Manns Vej 23
9220 Aalborg Øst

Emne: **Termoføler**

Fabrikat:	-	Id:	**Føler 1**
Type:	Pt-100	Diameter:	6 mm.
Tilbehør:	Termometer, digital (Id: Inst. 6/54192)		

Periode: Modtaget: 16-01-2025 Kalibreret: **20-01-2025**

Procedure: D1-2.2

Bemærkninger: Nominelt kalibreret område: -20...100 °C.
Kalibreringen er udført i væskebade ved sammenligning med et referencetermometer. Føleren har under kalibrering været indført i et tætsluttende glasrør, isoleret og neddyppet med minimum 15 gange diameteren. Føleren har været tilsluttet udlæseenhedens kanal 1.

Vilkår: Kalibreringen er udført akkrediteret i henhold til internationale krav (DS/EN ISO/IEC 17025:2017) og i henhold til Teknologisk Instituts almindelige vilkår. Kalibreringsresultater gælder udelukkende for det kalibrerede emne. Kalibreringscertifikatet må kun gengives i uddrag, hvis Teknologisk Institut skriftligt har godkendt uddraget.

Dette certifikat er i overensstemmelse med de måleevner, der er anført i Bilag C til CIPM MRA udarbejdet af CIPM. Under CIPM MRA anerkender alle deltagende institutter gyldigheden af hinandens kalibrerings- og målecertifikater for de målestørrelser, måleområder og måleusikkerheder, der er specificeret i KCDB (se detaljer her: https://www.bipm.org/kcdb/)

Kalibreret af: Bjørn Kjærsgaard Nielsen, 72203534, bjni@teknologisk.dk

Signatur: Dette dokument er kun gyldigt med digital signatur fra Teknologisk Institut. Udstedelsesdato fremgår af den digitale signatur. Godkendt og signeret af

Dennis Dam Sørensen
Faglig leder, ph.d., cand.polyt.

CIPM MRA

ilac-MRA DANAK
CAL Reg.nr. 200

TEMPERATURLABORATORIET

TEKNOLOGISK INSTITUT

Certifikat nr.: 200-T-24274 Side 2 af 3

KALIBRERINGSCERTIFIKAT
Resultater

Føler mærket: Føler 1

Reference-værdi °C	Aflæsning °C	Fejl °C	Usikkerhed °C	Note
-20,0436	-20,0700	-0,0264	0,0066	
-10,0253	-10,0410	-0,0157	0,0066	
-0,0063	-0,0115	-0,0052	0,0062	
9,9886	9,9925	0,0039	0,0061	
19,9887	19,9995	0,0108	0,0062	
29,9902	30,0060	0,0158	0,0062	
40,0558	40,0750	0,0192	0,0066	
50,0395	50,0610	0,0215	0,0061	
60,0264	60,0500	0,0236	0,0060	
70,0169	70,0415	0,0246	0,0064	
80,0096	80,0340	0,0244	0,0066	
90,0058	90,0285	0,0227	0,0068	
100,0043	100,0250	0,0207	0,0069	

Bemærkninger:
Aflæsning er middelværdien af flere aflæsninger på det kalibrerede måleinstrument.
Fejl = Aflæsning - referenceværdi.

Temperatur - 20240606

TEMPERATURLABORATORIET

TEKNOLOGISK INSTITUT

Certifikat nr.: 200-T-24274 Side 3 af 3

KALIBRERINGSCERTIFIKAT
Fejlkurve

Føler mærket: Føler 1

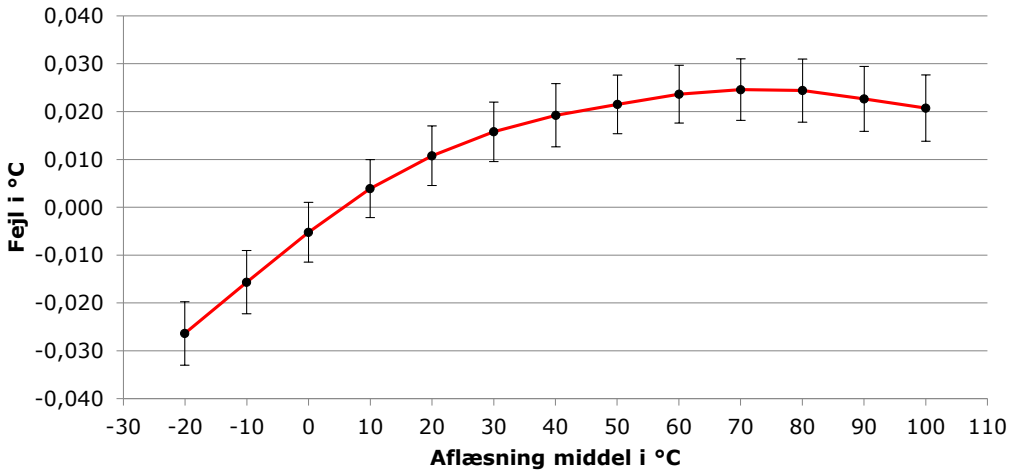

Kun de markerede punkter er målt.

Bemærkninger:
Aflæsning er middelværdien af flere aflæsninger på det kalibrerede måleinstrument.
Fejl = Aflæsning - referenceværdi.

Den rapporterede ekspanderede usikkerhed er angivet som standardusikkerheden af målingen multipliceret med dækningsfaktoren k =2, således at dækningssandsynligheden svarer til ca. 95 %.
Alle temperaturer er i henhold til ITS90.

Kalibreringsforhold:

Rumtemperatur:	22,0 °C ± 1,2 °C
Relativ fugtighed:	44,2 %rh ± 3,3 %rh
Barometerstand:	1014,1 mbar ± 2,4 mbar

Sporbarhed:
Dette kalibreringscertifikat er omfattet af DANAK akkreditering og EA's og ILAC's multilaterale aftaler for kalibrering, hvilket sikrer, at målingerne er sporbare til SI enhedssystemet.

Temperatur - 20240606

Appendix X

SHT-sensor calibration functions

Table X.1. Calibration function coefficients for temperature calibration.

	b	a0-Temp	a1-RH	R2
B1_S1	-0.22294	1.00166	0.0004293	0.999963
B1_S2	-0.13161	1.001389	0.0003833	0.999965
B1_S3	-0.12235	0.999793	0.0005975	0.999961
B1_S4	-0.16452	1.002112	0.0001616	0.999967
B1_S5	-0.01287	1.00315	0.0001299	0.999968
B1_S6	-0.13403	1.002036	0.0004260	0.999963
B1_S7	-0.18643	1.003005	0.0004083	0.999962
B1_S8	-0.2012	1.001537	0.0005450	0.999961
B1_S9	-0.09264	1.000471	-0.0000296	0.999969
B1_S10	-0.09247	1.000812	0.0002161	0.999965
B2_S1	-0.198	1.002559	0.0004841	0.999972
B2_S2	-0.11314	1.001635	0.0007472	0.999975
B2_S3	-0.18412	1.001892	0.0003342	0.999977
B2_S4	-0.05614	1.000692	-0.0007468	0.999991
B2_S5	-0.23807	1.00246	0.0006650	0.999976
B2_S6	-0.21743	1.00212	0.0004688	0.999976
B2_S7	-0.16379	1.002056	0.0006420	0.999974
B2_S8	-0.13108	1.002365	0.0000255	0.999986
B2_S9	-0.11439	1.001686	-0.0003250	0.999984
B2_S10	-0.21218	1.002745	0.0006014	0.999974

Continued on next page

Table X.1 – continued from previous page

	b	a0-Temp	a1-RH	R2
B3_S1	0.525376	0.992779	-0.0017808	0.999985
B3_S2	0.132667	0.998237	-0.0023297	0.999985
B3_S3	0.273071	0.993253	-0.0011008	0.999984
B3_S4	0.13613	1.003616	-0.0016362	0.999984
B3_S5	0.18361	1.008965	-0.0019779	0.999991
B3_S6	0.251947	0.991742	-0.0007297	0.999993
B3_S7	0.454041	0.999533	-0.0012972	0.99999
B3_S8	0.059366	0.998364	-0.0016244	0.999992
B3_S9	0.349722	0.99462	-0.0011368	0.999991
B3_S10	0.140911	1.0014	-0.0016612	0.999984
B4_S1	-0.20303	1.002422	0.0005018	0.999974
B4_S2	-0.1479	1.002276	0.0008140	0.999967
B4_S3	-0.26152	1.003277	0.0006969	0.999966
B4_S4	-0.24043	1.002924	0.0009383	0.999965
B4_S5	-0.17619	1.002274	0.0004560	0.999968
B4_S6	-0.20595	1.002254	0.0009861	0.999908
B4_S7	-0.19751	1.003391	0.0006129	0.99997
B4_S8	-0.15575	1.002545	0.0006345	0.999968
B4_S9	-0.22062	1.002209	0.0007576	0.999964
B4_S10	-0.12592	1.000802	0.0004443	0.999964
B5_S1	-0.3686	1.006499	0.0005027	0.99997
B5_S2	-0.34914	1.015232	0.0005025	0.999979
B5_S3	-0.3704	1.010162	0.0004723	0.999966
B5_S4	0.061766	1.004815	0.0002669	0.999974
B5_S5	-0.09499	1.007725	0.0008274	0.999965
B5_S6	-0.20581	1.008342	-0.0004738	0.999989
B5_S7	-0.23926	1.002488	0.0006545	0.999969
B5_S8	-0.10332	1.008814	-0.0002853	0.999987
B5_S9	-0.04223	1.005915	-0.0000316	0.999972
B5_S10	-0.26016	0.997514	0.0007448	0.999958
B6_S1	0.155551	0.995157	0.0006946	0.999976

Continued on next page

Table X.1 – continued from previous page

	b	a0-Temp	a1-RH	R2
B6_S2	-0.22349	1.000535	0.0009259	0.999966
B6_S3	0.144231	0.9998	0.0003784	0.999974
B6_S4	-0.16269	1.011849	0.0001498	0.999969
B6_S5	-0.11182	1.004807	0.0004856	0.999968
B6_S6	-0.25735	1.008178	0.0000415	0.999967
B6_S7	0.181428	0.989974	0.0009704	0.999968
B6_S8	-0.21707	1.006386	0.0008044	0.999962
B6_S9	-0.03913	1.00162	0.0007840	0.999976
B6_S10	0.048638	0.996717	0.0007353	0.999976
B7_S1	-0.39844	1.015389	0.0001881	0.999982
B7_S2	0.219461	0.995791	0.0005164	0.999967
B7_S3	-0.14501	1.000019	0.0006242	0.999962
B7_S4	-0.07352	0.998507	-0.0008944	0.99999
B7_S5	-0.30031	1.004074	0.0007606	0.999967
B7_S6	-0.12609	1.011228	-0.0001590	0.999985
B7_S7	0.461059	0.990604	-0.0002088	0.999984
B7_S8	0.104755	0.997604	0.0005039	0.999972
B7_S9	-0.44909	1.010782	0.0003969	0.999975
B7_S10	0.150259	0.997379	0.0009348	0.999965
B8_S1	0.305089	0.99224	-0.0011703	0.999972
B8_S2	0.095487	1.000771	-0.0013996	0.999968
B8_S3	-0.23736	1.008254	-0.0011971	0.999976
B8_S4	0.269465	1.006127	-0.0015808	0.999971
B8_S5	0.087891	0.996034	-0.0021229	0.999976
B8_S6	0.374863	0.995051	-0.0014143	0.99996
B8_S7	0.098867	0.999489	-0.0015549	0.999963
B8_S8	0.205283	0.994155	-0.0016894	0.99997
B8_S9	0.093098	0.994203	-0.0011850	0.999976
B8_S10	0.383336	0.993645	-0.0017530	0.999959
B9_S1	-0.23886	1.00253	0.0011883	0.999972
B9_S2	-0.14722	1.002536	0.0003952	0.99997

Continued on next page

Table X.1 – continued from previous page

	b	a0-Temp	a1-RH	R2
B9_S3	-0.24977	1.003263	0.0006112	0.999968
B9_S4	-0.27606	1.003	0.0008809	0.999973
B9_S5	-0.2467	1.002917	0.0010631	0.999967
B9_S6	-0.2733	1.002638	0.0004088	0.999969
B9_S7	-0.22319	1.002959	0.0007757	0.99997
B9_S8	-0.23491	1.002529	0.0012328	0.999968
B9_S9	0.0278	0.999648	-0.0014787	0.999986
B9_S10	-0.23854	1.002372	0.0012997	0.99997
B10_S1	-0.61299	1.013239	0.0003893	0.999973
B10_S2	0.121437	0.995978	-0.0002923	0.999984
B10_S3	-0.18432	1.006152	-0.0002242	0.999983
B10_S4	0.047214	0.999862	-0.0007032	0.999996
B10_S5	0.374343	0.999085	-0.0008242	0.999993
B10_S6	0.232321	0.995957	0.0000530	0.999977
B10_S7	-0.20353	1.005124	0.0001367	0.999976
B10_S8	-0.01937	0.997119	-0.0003091	0.99997
B10_S9	-0.11673	1.014545	-0.0000199	0.999972
B10_S10	-0.13933	1.005665	-0.0009731	0.999994
B11_S1	-0.22386	1.003861	0.0000462	0.999977
B11_S2	-0.26914	1.00367	0.0007383	0.999977
B11_S3	-0.19228	1.003008	0.0001012	0.999973
B11_S4	-0.2205	1.001452	0.0007805	0.99998
B11_S5	-0.21497	1.003732	-0.0003036	0.999979
B11_S6	-0.21218	1.003821	0.0004049	0.999977
B11_S7	-0.22497	1.004049	0.0002236	0.999977
B11_S8	-1.07552	0.998082	0.0066543	0.998416
B11_S9	-0.17661	1.003134	-0.0003806	0.999975
B11_S10	-0.21826	1.00326	0.0006150	0.999979
B12_S1	0.360112	1.000989	-0.0010068	0.999992
B12_S2	-0.0518	1.00543	-0.0018399	0.999977
B12_S3	0.345273	0.989577	-0.0005349	0.99999

Continued on next page

Table X.1 – continued from previous page

	b	a0-Temp	a1-RH	R2
B12_S4	0.210536	0.998548	-0.0009938	0.999991
B12_S5	0.465574	0.995793	-0.0019406	0.999975
B12_S6	0.196361	0.989466	-0.0005510	0.999994
B12_S7	0.169986	1.000481	-0.0007981	0.999983
B12_S8	0.400691	0.995035	-0.0010467	0.999992
B12_S9	-0.01601	1.011207	-0.0012227	0.999993
B12_S10	0.173122	0.998701	-0.0015182	0.999987
B13_S1	-0.14429	1.001084	0.0008394	0.999975
B13_S2	-0.18359	1.001873	0.0007740	0.99997
B13_S3	-0.24786	1.001844	0.0005215	0.999971
B13_S4	-0.15085	1.001904	-0.0006990	0.999975
B13_S5	-0.13623	1.003263	-0.0008390	0.99997
B13_S6	-0.12203	1.001716	0.0000742	0.99997
B13_S7	-0.19035	1.001143	0.0000735	0.999978
B13_S8	-0.12691	1.002855	-0.0003413	0.999968
B13_S9	-0.25592	1.002797	-0.0003672	0.999975
B13_S10	-0.16288	1.0011	0.0008904	0.999969
B14_S1	0.393427	0.99426	-0.0012482	0.999982
B14_S2	-0.01551	1.00615	-0.0008577	0.999986
B14_S3	-0.20501	1.010324	-0.0008382	0.999987
B14_S4	0.025538	0.998915	-0.0018927	0.999962
B14_S5	0.638136	0.988926	-0.0008594	0.999987
B14_S6	-0.03582	1.001515	-0.0011658	0.999985
B14_S7	-0.30312	1.012233	-0.0012157	0.999982
B14_S8	0.062726	0.998504	-0.0005293	0.999984
B14_S9	0.153719	1.002925	-0.0005296	0.999981
B14_S10	0.14659	0.997574	-0.0007229	0.999991
B15_S1	0.060171	0.994654	-0.0019962	0.999957
B15_S2	0.06178	0.994133	-0.0018716	0.999956
B15_S3	0.237715	0.990814	-0.0019234	0.999938
B15_S4	0.086914	0.993987	-0.0018682	0.999963

Continued on next page

Table X.1 – continued from previous page

	b	a0-Temp	a1-RH	R2
B15_S5	0.126048	0.9933	-0.0017109	0.999955
B15_S6	0.147137	0.99357	-0.0019051	0.999952
B15_S7	0.124758	0.994031	-0.0019705	0.999941
B15_S8	0.117277	0.993588	-0.0020472	0.999946
B15_S9	0.133568	0.992964	-0.0017240	0.999949
B15_S10	0.089355	0.994839	-0.0016987	0.999972
B16_S1	0.234353	0.990509	-0.0004086	0.999973
B16_S2	0.284099	0.995288	-0.0005328	0.999986
B16_S3	0.219354	0.997506	0.0001113	0.999979
B16_S4	0.082268	0.998103	-0.0005296	0.999976
B16_S5	0.153376	1.003368	-0.0007498	0.999988
B16_S6	0.02974	1.004382	0.0005183	0.999976
B16_S7	-0.03517	1.00177	0.0009822	0.999972
B16_S8	-0.05845	1.005936	0.0008021	0.999971
B16_S9	-0.28207	1.004195	0.0003540	0.999974
B16_S10	0.126981	1.002481	0.0006200	0.999974
B17_S1	-0.05941	1.004125	-0.0009001	0.999993
B17_S2	0.279226	0.99512	-0.0018567	0.999975
B17_S3	0.084234	1.003139	-0.0012420	0.999994
B17_S4	0.372454	0.994504	-0.0018104	0.999969
B17_S5	0.038902	1.004853	-0.0020388	0.999962
B17_S6	0.31168	0.992146	-0.0014640	0.999979
B17_S7	0.433501	0.991904	-0.0016865	0.999983
B17_S8	0.128799	1.001355	-0.0011347	0.999995
B17_S9	0.134062	0.998137	-0.0015009	0.99999
B17_S10	0.364687	0.99523	-0.0020407	0.999987
B18_S1	0.277523	0.998508	-0.0011781	0.999989
B18_S2	-0.09165	1.00234	-0.0008496	0.999984
B18_S3	0.009488	1.004128	-0.0008220	0.999981
B18_S4	-0.06285	0.998067	-0.0011285	0.999977
B18_S5	0.074535	0.990949	0.0002765	0.999972

Continued on next page

Table X.1 – continued from previous page

	b	a0-Temp	a1-RH	R2
B18_S6	0.173393	0.995457	0.0000161	0.999972
B18_S7	-0.07785	1.004601	-0.0001431	0.999973
B18_S8	-0.21331	1.005788	0.0001051	0.999975
B18_S9	0.055022	1.003867	-0.0002329	0.999972
B18_S10	0.132819	1.003171	-0.0012211	0.999984
B19_S1	0.036484	0.994876	-0.0018945	0.999963
B19_S2	-0.06108	0.999196	-0.0011485	0.999995
B19_S3	-0.02681	0.997165	-0.0012008	0.99998
B19_S4	-0.09651	1.000935	-0.0009028	0.999997
B19_S5	0.036636	0.995302	-0.0016237	0.999974
B19_S6	-0.07884	1.000759	-0.0010303	0.999997
B19_S7	-0.04309	0.998756	-0.0012607	0.999995
B19_S8	0.022758	0.996623	-0.0009846	0.99998
B19_S9	0.056415	0.996778	-0.0016619	0.999942
B19_S10	0.03287	0.998037	-0.0011480	0.999987
B20_S1	0.05848	0.999797	-0.0006020	0.999974
B20_S2	0.074077	0.99621	-0.0003239	0.999969
B20_S3	0.145248	1.000473	-0.0009848	0.999988
B20_S4	0.276767	0.992317	-0.0008186	0.999977
B20_S5	0.142622	0.997937	-0.0003699	0.999973
B20_S6	0.304686	0.993078	-0.0003374	0.999971
B20_S7	0.206251	1.002997	-0.0010815	0.999981
B20_S8	0.014553	0.994042	-0.0012220	0.999985
B20_S9	-0.0121	1.002443	-0.0007593	0.999975
B20_S10	0.079329	1.004268	-0.0001148	0.999978

Table X.2. Calibration function coefficients for relative humidity calibration.

	b	a0-Temp	a1-RH	R2
B1_S1	-2.52261	0.063248	0.998288	0.994609
B1_S2	-2.85679	0.063732	1.005918	0.994459
B1_S3	-3.71528	0.05763	1.011948	0.994397
B1_S4	-2.90557	0.059416	0.999884	0.994084
B1_S5	-5.62097	0.051328	1.052385	0.994018
B1_S6	-2.77143	0.059641	1.006506	0.994449
B1_S7	-3.13445	0.058932	1.009133	0.994372
B1_S8	-2.72243	0.061676	1.006794	0.99469
B1_S9	-4.104	0.055215	1.015637	0.993553
B1_S10	-2.47383	0.064471	0.998469	0.994431
B2_S1	-3.74632	0.063728	1.014679	0.994464
B2_S2	-3.46636	0.065203	1.018165	0.995058
B2_S3	-3.89172	0.064918	1.027905	0.994406
B2_S4	-4.32465	0.063049	1.031233	0.993671
B2_S5	-3.49038	0.065498	1.01818	0.995161
B2_S6	-3.37666	0.064917	1.018013	0.995059
B2_S7	-3.8701	0.060432	1.026754	0.995298
B2_S8	-3.55538	0.06323	1.016488	0.994511
B2_S9	-4.44792	0.060115	1.036511	0.99422
B2_S10	-3.4634	0.062579	1.016311	0.994896
B3_S1	-19.7518	0.255057	1.156579	0.994278
B3_S2	-20.2996	0.252307	1.163423	0.993991
B3_S3	-18.5491	0.242435	1.139485	0.994684
B3_S4	-20.0148	0.246612	1.156769	0.994405
B3_S5	-19.9178	0.260101	1.155547	0.993979
B3_S6	-19.9524	0.237663	1.16084	0.994985
B3_S7	-20.5136	0.250923	1.166292	0.994324
B3_S8	-19.6291	0.258918	1.1522	0.994451
B3_S9	-20.5214	0.244201	1.166163	0.994733
B3_S10	-20.3433	0.241148	1.164381	0.99438

Continued on next page

Table X.2 – continued from previous page

	b	a0-Temp	a1-RH	R2
B4_S1	-2.87406	0.065115	1.010995	0.994414
B4_S2	-2.96385	0.064866	1.010921	0.994465
B4_S3	-3.08318	0.064643	1.008824	0.994362
B4_S4	-3.11373	0.064697	1.011863	0.994648
B4_S5	-3.47188	0.063148	1.019125	0.993997
B4_S6	-3.62781	0.019611	1.030523	0.994699
B4_S7	-2.69013	0.066368	1.00946	0.994655
B4_S8	-3.29719	0.064218	1.016536	0.99433
B4_S9	-2.7917	0.064705	1.009646	0.994432
B4_S10	-3.1198	0.065294	1.014561	0.994161
B5_S1	-17.0421	0.241658	1.126275	0.995604
B5_S2	-16.7066	0.243833	1.117215	0.995479
B5_S3	-17.0197	0.2471	1.117756	0.995583
B5_S4	-16.9609	0.252833	1.119224	0.995548
B5_S5	-16.7382	0.253284	1.116413	0.995696
B5_S6	-17.584	0.253858	1.128227	0.995019
B5_S7	-17.7384	0.247255	1.123287	0.995571
B5_S8	-19.0571	0.256588	1.13912	0.994773
B5_S9	-18.1642	0.241043	1.134509	0.99523
B5_S10	-18.9662	0.237691	1.140538	0.995316
B6_S1	-18.9666	0.230942	1.140526	0.996582
B6_S2	-19.2176	0.237724	1.142893	0.996553
B6_S3	-18.629	0.231186	1.143368	0.996572
B6_S4	-19.6723	0.243562	1.147561	0.996487
B6_S5	-18.8494	0.235994	1.143516	0.996438
B6_S6	-19.5044	0.238411	1.144659	0.99634
B6_S7	-19.0252	0.238436	1.137558	0.99657
B6_S8	-19.1064	0.237677	1.144864	0.996543
B6_S9	-19.0656	0.240903	1.137662	0.996593
B6_S10	-19.5602	0.237281	1.146293	0.99651
B7_S1	-19.7348	0.24682	1.146132	0.996237

Continued on next page

Table X.2 – continued from previous page

	b	a0-Temp	a1-RH	R2
B7_S2	-18.6822	0.238293	1.139598	0.996237
B7_S3	-18.2633	0.241643	1.137617	0.996383
B7_S4	-19.2079	0.252034	1.142483	0.995683
B7_S5	-18.6242	0.236302	1.138801	0.996457
B7_S6	-20.142	0.249151	1.1573	0.995913
B7_S7	-18.3385	0.24171	1.138214	0.996238
B7_S8	-19.6068	0.239495	1.151734	0.996274
B7_S9	-17.8094	0.237821	1.13212	0.996091
B7_S10	-19.8543	0.243096	1.15049	0.996284
B8_S1	-18.9139	0.253223	1.138798	0.995393
B8_S2	-19.4626	0.256431	1.146811	0.995214
B8_S3	-19.1787	0.24906	1.151407	0.995457
B8_S4	-20.521	0.250207	1.169715	0.995083
B8_S5	-19.1948	0.247395	1.148782	0.995166
B8_S6	-18.8153	0.256261	1.151662	0.99537
B8_S7	-19.8274	0.249695	1.158652	0.995328
B8_S8	-19.6068	0.258767	1.150245	0.995316
B8_S9	-19.13	0.259444	1.144034	0.995418
B8_S10	-18.9017	0.251731	1.14859	0.994953
B9_S1	-3.57895	0.056805	1.013082	0.995287
B9_S2	-4.3421	0.04826	1.024999	0.99428
B9_S3	-4.08589	0.050135	1.026541	0.994629
B9_S4	-3.78608	0.053358	1.01492	0.995088
B9_S5	-4.59142	0.047822	1.029518	0.994699
B9_S6	-4.29745	0.048821	1.017713	0.994478
B9_S7	-4.63726	0.048271	1.026267	0.994477
B9_S8	-4.10353	0.053645	1.023287	0.995088
B9_S9	-4.94173	0.059524	1.02903	0.99225
B9_S10	-3.72273	0.056509	1.014781	0.995149
B10_S1	-18.5862	0.241977	1.140399	0.996437
B10_S2	-19.949	0.234835	1.154536	0.996287

Continued on next page

Table X.2 – continued from previous page

	b	a0-Temp	a1-RH	R2
B10_S3	-20.4032	0.229775	1.161151	0.996016
B10_S4	-20.4169	0.242394	1.15672	0.99594
B10_S5	-18.7485	0.248607	1.138463	0.995862
B10_S6	-17.8566	0.236345	1.13699	0.996385
B10_S7	-20.6643	0.239453	1.162198	0.996176
B10_S8	-18.1754	0.230847	1.141098	0.996198
B10_S9	-18.3257	0.23417	1.139661	0.996101
B10_S10	-18.9261	0.241344	1.140363	0.995718
B11_S1	-3.7433	0.057156	1.010839	0.9939
B11_S2	-3.38717	0.063871	1.020173	0.995269
B11_S3	-3.21705	0.059399	1.009047	0.994445
B11_S4	-4.0157	0.060124	1.019249	0.994829
B11_S5	-3.42287	0.059546	1.020308	0.994186
B11_S6	-3.62407	0.059268	1.019199	0.994767
B11_S7	-3.70485	0.057103	1.02064	0.994636
B11_S8	-1.71486	0.055156	1.023458	0.989671
B11_S9	-3.21488	0.056743	1.011191	0.994196
B11_S10	-3.90521	0.057404	1.008322	0.994673
B12_S1	-19.8911	0.242189	1.161284	0.994495
B12_S2	-20.8398	0.261692	1.165971	0.9938
B12_S3	-20.4614	0.234936	1.165395	0.995015
B12_S4	-19.9929	0.236669	1.157452	0.99497
B12_S5	-20.5076	0.25436	1.161792	0.993858
B12_S6	-20.1005	0.240304	1.156493	0.995131
B12_S7	-20.7195	0.234598	1.17511	0.9948
B12_S8	-20.6689	0.234576	1.169012	0.994603
B12_S9	-20.8389	0.243519	1.172774	0.994535
B12_S10	-20.767	0.244208	1.170518	0.994149
B13_S1	-4.22907	0.050267	1.029723	0.994451
B13_S2	-3.59675	0.05057	1.021641	0.99468
B13_S3	-3.88312	0.046402	1.028083	0.99408

Continued on next page

Table X.2 – continued from previous page

	b	a0-Temp	a1-RH	R2
B13_S4	-4.97647	0.04076	1.04603	0.992957
B13_S5	-4.83682	0.040259	1.044911	0.992684
B13_S6	-3.85463	0.046616	1.028969	0.99435
B13_S7	-4.90483	0.040556	1.041153	0.993695
B13_S8	-3.90922	0.044637	1.03097	0.993653
B13_S9	-3.95307	0.04713	1.024962	0.993888
B13_S10	-3.42907	0.048696	1.011699	0.993269
B14_S1	-20.5773	0.246737	1.168217	0.994373
B14_S2	-19.222	0.23652	1.150317	0.995103
B14_S3	-18.8217	0.225834	1.1498	0.995164
B14_S4	-17.9495	0.258325	1.136932	0.993824
B14_S5	-17.6558	0.232038	1.148759	0.995088
B14_S6	-19.7348	0.254578	1.157142	0.994452
B14_S7	-19.3772	0.245974	1.147865	0.99447
B14_S8	-19.0933	0.233107	1.152269	0.995389
B14_S9	-18.2386	0.241076	1.140002	0.99541
B14_S10	-18.381	0.243978	1.142577	0.995183
B15_S1	-5.15665	0.071135	1.039204	0.991466
B15_S2	-4.77499	0.077523	1.034356	0.991901
B15_S3	-5.18965	0.086082	1.036525	0.992166
B15_S4	-5.06811	0.074508	1.035032	0.991723
B15_S5	-5.67649	0.077456	1.035243	0.9912
B15_S6	-5.22601	0.076491	1.034382	0.991345
B15_S7	-4.85788	0.077397	1.034161	0.991643
B15_S8	-5.1835	0.074783	1.040384	0.991416
B15_S9	-4.97604	0.080331	1.03173	0.991769
B15_S10	-5.0673	0.076045	1.038073	0.99255
B16_S1	-18.6033	0.233283	1.140364	0.994848
B16_S2	-20.097	0.22918	1.162768	0.99471
B16_S3	-20.277	0.232571	1.167941	0.995261
B16_S4	-19.7613	0.225318	1.158954	0.994688

Continued on next page

Table X.2 – continued from previous page

	b	a0-Temp	a1-RH	R2
B16_S5	-19.0908	0.246565	1.151733	0.995131
B16_S6	-19.3807	0.230878	1.152855	0.995743
B16_S7	-17.9643	0.244292	1.132223	0.995902
B16_S8	-19.0658	0.238024	1.149266	0.995414
B16_S9	-20.0694	0.235087	1.160929	0.995122
B16_S10	-17.8776	0.238249	1.133023	0.995907
B17_S1	-18.1989	0.243963	1.139839	0.995093
B17_S2	-20.3878	0.2527	1.154653	0.994193
B17_S3	-20.0023	0.249309	1.156307	0.995102
B17_S4	-20.5406	0.259967	1.164935	0.994282
B17_S5	-21.1664	0.263989	1.168516	0.993994
B17_S6	-20.3838	0.253295	1.163765	0.994466
B17_S7	-20.7387	0.253077	1.155639	0.994345
B17_S8	-18.9332	0.2448	1.144349	0.995113
B17_S9	-18.99	0.253958	1.13879	0.994944
B17_S10	-18.5183	0.251606	1.135509	0.994747
B18_S1	-18.0093	0.244089	1.135471	0.994527
B18_S2	-18.752	0.245356	1.14851	0.994529
B18_S3	-17.7208	0.23797	1.135796	0.994697
B18_S4	-17.7658	0.243181	1.127262	0.994333
B18_S5	-17.1819	0.229211	1.124549	0.995366
B18_S6	-19.8791	0.232233	1.157239	0.995146
B18_S7	-16.8261	0.239914	1.115508	0.995178
B18_S8	-17.4035	0.238979	1.12972	0.995377
B18_S9	-17.471	0.244452	1.122469	0.994969
B18_S10	-18.2582	0.244478	1.130131	0.994339
B19_S1	-4.38633	0.084394	1.022266	0.991965
B19_S2	-4.2412	0.065146	1.029813	0.99376
B19_S3	-4.41623	0.067905	1.020446	0.992454
B19_S4	-3.69941	0.062128	1.021361	0.994086
B19_S5	-4.41931	0.07683	1.022314	0.992477

Continued on next page

Table X.2 – continued from previous page

	b	a0-Temp	a1-RH	R2
B19_S6	-3.93632	0.062068	1.02384	0.993718
B19_S7	-5.01501	0.061043	1.031603	0.992991
B19_S8	-3.99281	0.075793	1.017409	0.993483
B19_S9	-4.3552	0.099719	1.030241	0.993705
B19_S10	-3.84477	0.069792	1.021464	0.993865
B20_S1	-17.356	0.237423	1.132666	0.995359
B20_S2	-17.5126	0.235586	1.135437	0.995528
B20_S3	-17.6594	0.239514	1.137084	0.995319
B20_S4	-18.2187	0.236059	1.143432	0.994711
B20_S5	-17.7948	0.242299	1.137911	0.99551
B20_S6	-17	0.225746	1.129139	0.995741
B20_S7	-17.2229	0.243179	1.134708	0.995096
B20_S8	-17.826	0.241047	1.136771	0.995071
B20_S9	-18.8956	0.239198	1.150328	0.995084
B20_S10	-17.3161	0.24038	1.126198	0.995805